Perturbative and Nonperturbative Aspects of Jet Quenching in Near-Critical Quark-Gluon Plasmas

Jiechen Xu

Submitted in partial fulfillment of the

requirements for the degree of

Doctor of Philosophy

in the Graduate School of Arts and Sciences

Columbia University

2016

Abstract

Perturbative and Nonperturbative Aspects of Jet Quenching in Near-Critical Quark-Gluon Plasmas

Jiechen Xu

In this thesis, we construct two QCD based energy loss models to perform quantitative analysis of jet quenching observables in ultra-relativistic nucleus-nucleus collisions at RHIC and the LHC.

We first build up a perturbative QCD based CUJET2.0 jet flavor tomography model that couples the dynamical running coupling DGLV opacity series to bulk data constrained relativistic viscous hydrodynamic backgrounds. It solves the strong heavy quark energy loss puzzle at RHIC and explains the surprising transparency of the quark-gluon plasma (QGP) at the LHC. The observed azimuthal anisotropy of hard leading hadrons requires a path dependent jet-medium coupling in CUJET2.0 that implies physics of nonperturbative origin.

To explore the nonperturbative chromo-electric and chromo-magnetic structure of the strongly-coupled QGP through jet probes, we build up a new CUJET3.0 framework that includes in CUJET2.0 both Polyakov loop suppressed semi-QGP chromo-electric charges and emergent chromo-magnetic monopoles in the critical transition regime. CUJET3.0 quantitatively describes the anisotropic hadron suppression at RHIC and the LHC. More significantly, it provides a robust connection between the long wavelength "perfect fluidity" of the QGP and the short distance jet transport in the QGP. This framework paves the way for "measuring" both perturbative and nonperturbative properties of the QGP, and more importantly for probing color confinement through jet quenching.

Contents

List of Figures

List of Tables

Acknowledgments

I thank my parents. Their teachings and examples have been helping me sailing determinedly and confidently in the ocean of life: thank you so much for always pointing me to the right direction. My most heartfelt appreciations to your total, unconditional supports throughout all these years. I am so grateful for your full trust and firm belief in my life choices.

I thank my advisor, Professor Miklos Gyulassy, for the invaluable supports, advices and encouragements that I received during these exciting years of doctoral research at Columbia University. Miklos, I am so obliged to you for your teaching and experience. My path from a student to a physicist (though far from complete), would have been impossible without your guidance and help.

I thank Jinfeng Liao, for leading me into the exciting world of chromo-magnetic monopoles, and for enlightening the insightful discussions we had over the years.

The completion of this thesis would have not been possible without the support of the US DOE Grant No. DE-FG02-93ER40764 and of the JET Collaboration: many thanks to Xin-Nian Wang for directing the topical collaboration.

Also thank you to all the members of the nuclear theory group at Columbia: Barbara Betz, Alessandro Buzzatti, Andrej Ficnar, Mohammed Mia, Jorge Noronha, Jaki Noronha-Hostler, Giorgio Torrieri, for your friendship and very insightful discussions.

I am extremely grateful to Uli Heinz, Jinfeng Liao, Xin-Nian Wang, Bill Zajc, and

especially Miklos, for writing the reference letters for me.

I am thankful to Brian Cole, Gabriel Denicol, Adrian Dumitru, Magdalena Djordjevic, Angelo Esposito, Kenji Fukushima, Charles Gale, Steve Gubser, John Harris, Uli Heinz, Will Horowitz, Xu-Guang Huang, Lam Hui, Edmond Iancu, Jiangyong Jia, Sangyong Jeon, Zhongbo Kang, Dima Kharzeev, Yuri Kovchegov, Shu Lin, Zi-Wei Lin, Al Mueller, Alberto Nicolis, Abhay Pasupathy, Peter Petreczky, Rob Pisarski, Guang-You Qin, Ralf Rapp, Dirk Rischke, Paul Romatschke, Chun Shen, Ed Shuryak, Tomo Uemura, Ivan Vitev, Xin-Nian Wang, Bin Wu, Bo-Wen Xiao, Hongxi Xing, Nu Xu, Yi Yin, Bill Zajc, and Pengfei Zhuang for very helpful conversations about all kinds of physics. I have learnt so much from you guys. Thanks Denes Molnar for raising interesting questions every time we met and for climbing Mt. Fuji with me in October 2015.

I am thankful to my officemates in the Pupin Hall: Angelo Esposito, Andrej Ficnar, Sebastian Garcia-Saenz, Jonghee Kang, Zhe Liu, Ali Masoumi, Andrea Petri, Chiara Toldo, Junpu Wang, Xiao Xiao – You guys made up such an enjoyable environment for "good looking" young theorists. Thanks for making our blackboards crowded all the time. I cherished the days spent with you.

My nearly 4 years 4 months of doctorate at Columbia University, however, would have been rather insignificant if I did not have a chance to live New York City at its fullest, or without the company of some of my close friends: Ziyuan Bai, Alessandro Buzzatti, Ben Frandsen, Andrej Ficnar, Xiaoqian Gui, Luchang Jin, Zhe Liu, Shuang Lu, Tingting Wang, Yang Zha, Daiqian Zhang, Shuo Zhang. Knowing someone to have fun with is easy, but meeting friends who one can count on "no-matter-what" is a rare event. I was lucky, and you guys deserve all my gratitude. A special thank you to Guangyuan Yang, my lifetime friend, for discussing the ultimate meaning of life with me, at countless places in the world.

To my parents, Yuanyuan Xu and Lili Xie, with gratitude

Outline

In Chapter 1, we first present a general introduction to the fundamental theory of Quantum Chromodynamics (QCD) in Section 1.1. Following that, we show how one can explore the QCD phase diagram with ultra-relativistic nucleus-nucleus collisions at the Brookhaven National Laboratory (BNL) Relativistic Heavy Ion Collider (RHIC) and the European Organization for Nuclear Research (CERN) Large Hadron Collider (LHC) in Section 1.2. We will illustrate signatures for the formation of a new state of matter – Quark-Gluon Plasma (QGP) – under the extremely hot/dense conditions in such reactions, and introduce the jet quenching phenomenon and key observables of our interests.

In Chapter 2, we review two fundamental energy loss mechanism for jet quenching in the QGP – collisional (Section 2.1) and radiative (Section 2.2). The former is easy to calculate while the latter requires detailed modeling. Within the radiative sector, we focus specially on the DGLV opacity expansion theory and its developments (Section 2.3), including: (1) multiple gluon emission, (2) multiple scatterings, (3) energy loss and geometry fluctuations, (4) dynamical medium effects, and (5) running of the QCD coupling constant.

In Chapter 3, we construct the perturbative QCD (pQCD) based CUJET2.0 jet energy loss model from the dynamical running coupling DGLV opacity series coupled with long distance hadron spectra and bulk flow data constrained relativistic viscous hydrodynamical backgrounds (Section 3.1). Within this model, it is found that the suppression

of heavy flavor decay electrons can be well-described (Section 3.2.1), the jet opacity's dependence on medium density is data-compatible (Section 3.2.2), and the average jet transverse momentum transfer per unit length in the QGP is determined to a remarkable precision when combined with four other pQCD models in the US Department of Energy Topical JET Collaboration (Section 3.3). However, in this model we find a "high p_T v_2 puzzle" that can only be explained by introducing path dependent coupling strength (Section 3.4). The solution implies that physics of nonperturbative QCD origin plays an important role in jet quenching studies.

In Chapter 4, we explore possible non-perturbative descriptions of the strongly-coupled QGP (sQGP) in the critical confinement/deconfinement transition region. We particularly focus on the magnetic scenario of sQGP because this framework naturally gives rise to an enhanced jet-medium coupling in the critical regime that is required by the large azimuthal anisotropy data (Section 4.1). We will explore the foundations of this scenario, and study how the particle-monopoles will emerge and influence the properties of the QGP in the regime near the critical transition temperature T_c, based on quantitative evidences from lattice QCD calculations (Section 4.2, 4.3 and **??**). We see however in the presence of non-zero Polyakov loop this scenario missed the "semi-QGP" suppression of color electric degrees of freedom (Section 4.4). Therefore more quantitative considerations regarding both electric and magnetic sector in the near T_c regime are necessary.

In Chapter 5, we explore the full nonperturbative chromo-electric and chromo-magnetic structure of the near-critical QGP, as well as the solution to the "high p_T v_2 puzzle" and the reconciliation of the discrepancy between the long wavelength "perfect fluidity" of the QGP and the short distance jet quenching in the QGP (Section 5.1.1). We first build up a microscopic semi-Quark-Gluon-Monopole Plasma (sQGMP) model that has Polyakov loop suppressed semi-QGP chromo-electric charges (Section 5.1.2) and emergent chromo-magnetic monopoles (Section 5.1.3) in the critical transition region, then implement it

into a new jet quenching framework CUJET3.0 (Section 5.1.4) that has a CUJET2.0 perturbative energy loss kernel upgraded with nonperturbative features. We show that CUJET3.0 can explain light hadrons' and open heavy flavors' nuclear modification factors and azimuthal anisotropies at RHIC and the LHC simultaneously, and more importantly, it builds up for the first time among all jet quenching models a quantitative connection between the long distance bulk shear viscous transport properties and the short distance jet transport coefficient $\hat{q}$ at all temperatures above T_c (Section 5.2).

In order to apply CUJET3.0 to do robust quantitative analysis of both perturbative and nonperturbative properties of the QGP, key theoretical uncertainties originated from different interpretations of the lattice QCD data on the color electric and magnetic components of the near-critical QGP are systematically studied (Section 5.3 and 5.5). The path length dependence of jet energy loss in sQGMP for both light and heavy flavor are also extracted. (Section 5.4).

In Chapter 6, we will utilize the CUJET3.0 framework to compute more jet quenching observables that are being or will be measured at RHIC and the LHC. In particular, we will show results from CUJET3.0 on the centrality dependence of R_{AA} and R_{cp} for prompt D mesons (Section 6.1), a systematic analysis of the suppression of open heavy flavors and heavy flavor decay electrons in A+A collisions (Section 6.2), and possible jet quenching effects in proton-nucleus collisions (Section 6.3 and 6.4).

We summarize the main results of this thesis in Concluding Remarks.

Chapter 1

Introduction

We start with a brief overview of Quantum Chromodynamics (QCD) in Section 1.1, and discuss both the perturbative and nonperturbative aspects of strong force. We will see the underlying symmetry breaking/restoration leads hadronic matter to have a deconfinement transition to a Quark-Gluon Plasma (QGP) phase at extremely hot/dense condition. The QGP is a primordial phase of matter a microsecond after the Big Bang, and it now has been recreated in high-energy nuclear collisions at the BNL Relativistic Heavy-Ion Collider (RHIC) and the CERN Large Hadron Collider (LHC). In Section 1.2, we focus on the thermalization, evolution and hadronization of QGP in heavy-ion collisions. Specifically, its collective behavior and impacts on high energy jets will be considered. Finally, we introduce the nuclear modification factor and azimuthal anisotropy, the main set of observables of our interests.

1.1 Quantum chromodynamics

The strong nuclear force in nature is described in the Standard Model (SM) by Quantum Chromodynamics (QCD). The history of this theory dated from 1960s – motivated by

the successful classification of subatomic baryons and mesons through the eightfold way by Gell-Mann and Ne'eman [1] and the discovery of Ω^- hyperon [2], Gell-Mann, Zweig, Han, Nambu, and Fritzsch, postulated that hadrons may be made of quarks and gluons [3–6]. These hypotheses were thereafter validated by the deep inelastic scattering (DIS) experiment at SLAC [7, 8] and the three jet events at PETRA [9]. Subsequent observations of the running coupling, vector boson production [10] and Bjorken scaling violation [11], furthermore established QCD as the fundamental theory of strong interactions.

Formally, QCD is a non-Abelian $SU(N_c = 3)$ gauge theory, consists of $N_f = 6$ spin-1/2 fermions (quarks) in the fundamental and $N_c^2 - 1 = 8$ spin-1 gauge bosons (gluons) in the adjoint representation of the color group. Its gauge-invariant Lagrangian density reads

$$\mathcal{L}_{\mathcal{QCD}} = \sum_f \bar{q}_f^{\alpha}(i\,\gamma^\mu D_\mu - m_f)_{\alpha\beta}\, q_f^{\beta} - \frac{1}{4} F^a_{\mu\nu} F_a^{\mu\nu} \quad , \tag{1.1}$$

where the quark flavor f = u (up), d (down), s (strange), c (charm), b (bottom), t (top). The covariant derivative $(D_\mu)_{\alpha\beta}$, quark mass term $(m_f)_{\alpha\beta}$ and field strength tensor $F^a_{\alpha\beta}$ are defined as

$$\begin{aligned} (D_\mu)_{\alpha\beta} &\equiv \partial_\mu \delta_{\alpha\beta} + ig(T_a)_{\alpha\beta} A^a_\mu \\ (m_f)_{\alpha\beta} &\equiv m_f \delta_{\alpha\beta} \\ F^a_{\mu\nu} &= \partial_\mu A^a_\nu - \partial_\nu A^a_\mu - g f^{abc} A^b_\mu A^c_\nu \quad . \end{aligned} \tag{1.2}$$

The gauge coupling strength is governed by the coupling constant g. Quark fields $q_f^{\alpha=1,2,3}$ are in the $SU(3)$ triplet while gluon fields $A_\mu^{a=1,\cdots,8}$ are in octet. In the fundamental representation of $SU(3)$, the group generators T_a's are represented by traceless hermitian 3×3 matrices that satisfy the relation

$$[T_a, T_b] = i f_{abc} T_c \quad . \tag{1.3}$$

Here f_{abc}[1] are the structure constants and are antisymmetric in all indices. Unlike Abelian Quantum Electrodynamics (QED), the intrinsic non-abelian nature of QCD leads to a self-coupling term of gauge bosons, i.e. three-gluon vertex, that results in rich QCD phenomenology.

1.1.1 Asymptotic freedom

Because of gluon self-interactions, the renormalization of QCD is drastically different from QED. For a non-Abelian theory with gauge group $G = SU(N_c)$ and N_f Dirac fermions in the "R" representation of G, the one-loop beta function was independently calculated by Gross and Wilczek [12], Politzer[2] [13], and 't Hooft [14], it has the form

$$\beta(g) \equiv \frac{\partial g}{\partial \log \mu} = -\left(\frac{11}{3}C_2(G) - \frac{4}{3}N_f C(R)\right)\frac{g^3}{16\pi^2}\,. \tag{1.4}$$

Here $C_2(G)$ is the quardratic Casimir of G, and $C_2(G) = N_c$ for adjoint gauge gluons. $C(R)$ is an Casimir invariant that satisfies $Tr(T_R^a T_R^b) = C(R)\delta^{ab}$, and $C(R) = 1/2$ for fundamental fermions. For QCD, $N_c = 3$, the above reduces to:

$$\beta(g) = -\left(11 - \frac{2}{3}N_f\right)\frac{g^3}{16\pi^2}\,. \tag{1.5}$$

When $N_f \leq 16$, $\beta(g)$ is negative. The strong coupling $\alpha_s = g^2/4\pi$ reads [15]:

$$\alpha_s(Q^2) = \frac{4\pi}{(11 - \frac{2}{3}N_f)\log(Q^2/\Lambda^2_{QCD})}\,. \tag{1.6}$$

[1]Note that the rules to raise or lower the a, b, c indices are trivial $(+, \cdots, +)$ so that $f_{abc} = f^{abc}$. On the other hand, for Lorentz μ, ν indices, one transforms according to the metric signature, for what Minkovski $(+,-,-,-)$ is used throughout this thesis.

[2]With indelible contributions from Sidney Coleman and Erick Weinberg.

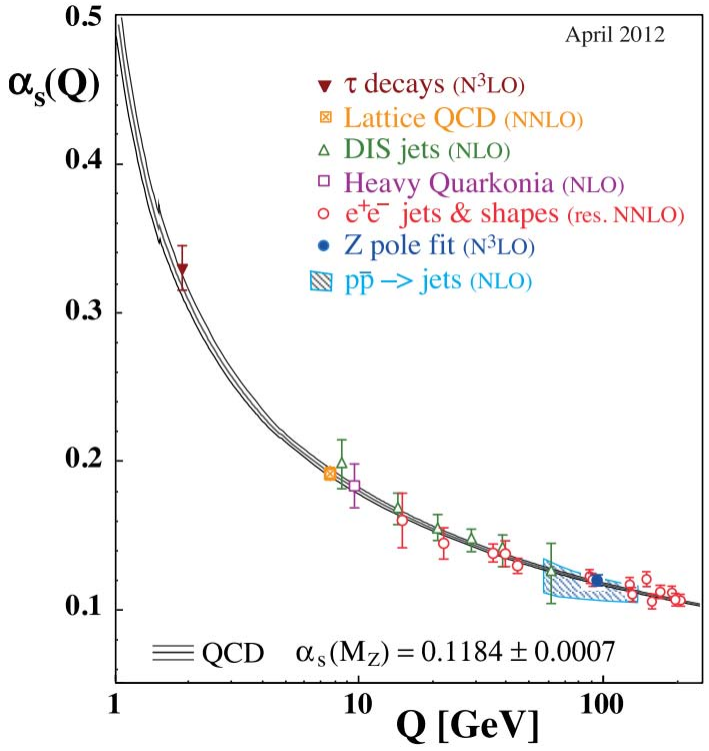

Figure 1.1: *Summary of measurements of α_s as a function of the respective energy scale Q from [16]. The strong coupling strength clearly goes down as the momentum transfer increases.*

One sees that after the inclusion of quantum corrections, α_s will "run" in such a way that its strength decreases as one increases the energy scale Q^2 (or decreases the length scale). This is the famous phenomenon of asymptotic freedom, it is a direct outcome of the renormalization group equation for QCD. Fig. 1.1 shows a recent summary of α_s from the Particle Data Group (PDG) based on relevant experimental measurements. The mass scale Λ_{QCD}, which is experimentally fixed to ~ 200 MeV, sets a parameter used to determine the validity of the perturbative expansion.

For various processes at high energy, or more precisely, high momentum transfers $Q^2 \gg \Lambda^2_{QCD}$, also known as "hard" processes, the theory is asymptotically free and the quarks are treated as a weakly-coupled gas, one may use the standard perturbation

theory to calculate the corresponding scattering amplitudes. This has given rise to the phenomenologically very successful method of perturbative QCD (pQCD), that has been applied to make predictions of observables in a wide range of high energy experiments. A side note is that when Q^2 is extremely large, both the coupling α_s and the beta function of QCD vanish, the theory reaches a ultraviolet fixed point and QCD becomes conformal.

On the other hand, at low energies (long distances), the coupling becomes extremely large, and QCD is strongly coupled, i.e. non-perturbative. In this case perturbation theory is no longer applicable. Therefore, one needs to use different approaches apart from pQCD to calculate low Q^2 or "soft" processes. Among them are the Nambu-Jona-Lasinio (NJL) model [17–19], Chiral perturbation theory [20–22], QCD sum rules [23, 24], Lattice QCD [25], and the AdS/CFT correspondence [26–30]. As we will see in later chapters, the non-perturbative aspects of QCD in fact play an unexpected role in maintaining the consistency between theory predictions and experimental observables within a broad energy range, and it is critical to include their contributions in various phenomenological models.

1.1.2 Color confinement/deconfinement

The biggest mystery of QCD is color confinement, the phenomenon that color charged particles (quarks and gluons) cannot be isolated singularly, they are confined in hadrons instead, and therefore cannot be directly observed. There exists no analytic proof that QCD should be confining. However phenomenologically, the "string-breaking" model has received significant recognition in explaining the nature of confinement. It is rooted in postulating quarks being bounded by color flux tubes [31]. Drawing an analogy with the ground state of a superconductor that consists of a condensate of Cooper pairs, due to translation invariance, one expects that a quark anti-quark pair ($q\bar{q}$) in such a medium

will have strongly localized color electric flux lines connecting them, resembling a tube-like region with a constant energy density of gluon fields. Thus the $q\bar{q}$ potential at long distances should depend linearly on the separation r between the pair, i.e.

$$V(r) \to \sigma r \,, \tag{1.7}$$

where σ is the so-called string tension, $\sigma \sim 1$ GeV/fm. When one keeps pulling the string, in order to minimize the free energy, at some point it will become more favorable for the string to break and another $q\bar{q}$ pair spontaneously appears. As a result, hadronization (or fragmentation) occurs.

While the $q\bar{q}$ potential has the string form (1.7) at large distances, at small distances it will exhibit a Coulomb-like $\sim 1/r$. Putting them together, one gets the Cornell potential:

$$V_{\bar{q}q}(r) = -\frac{a}{r} + \sigma r \,. \tag{1.8}$$

At one-loop order, $a = 4\alpha_s/3$. These effective potentials can be extracted from the Wilson loop that measures the spacetime path traced out by a $q\bar{q}$ pair created at one point, propagated through a closed curve C then annihilated,

$$W_R(C) = \mathrm{Tr}_\mathrm{R}\left[\mathcal{P}\exp\left(ig\oint_C A^\mu dx_\mu\right)\right] = \mathrm{Tr}_\mathrm{R}\left[Hol(A,C)\right] \,, \tag{1.9}$$

where $\mathcal{P}$ is the path ordering operator, R is the representation of gauge fields A in the Yang-Mills theory, Hol is the holonomy. If one takes C to be the oriented boundary of a rectangular $r \times t$ area in spacetime, for $t \gg r$, the vacuum expectation value of (1.9) is dominated by the ground state, and this value determines the interaction energy $V(r)$ of static quarks:

$$\langle W_R(r,t)\rangle \to \exp\left\{-V(r)t\right\} \,. \tag{1.10}$$

At short distances, one can use the perturbative approaches to evaluate $\langle W_R(r,t)\rangle$, while at long distances (1.10) it can be computed on the lattice (see Section 1.1.4). In the confining phase, $\langle W_R(r,t)\rangle$ displays an area law, suggests a linear $q\bar{q}$ potential.

Bag model

To grasp the different behavior of QCD in the confined phase and in the asymptotically free regime, one can look at the MIT bag model developed in 1970s [32–34]. It provides a simple picture incorporating both. This model consists of hadrons that are finite "bags" of perturbative vacuum, inside them massless quarks and gluons are free due to asymptotic freedom. Confinement is accomplished in a Lorentz-invariant way by assuming that the bag possesses a constant positive energy density B – the bag constant. Physically, B should be equal to the energy density of the QCD vacuum at zero temperature, $B = -\epsilon_{\text{vac}}$. In the simplest picture, the mass of a hadron is the sum of the energy associated with the creation of the finite-volume perturbative bag in a non-perturbative vacuum and the kinetic energy of quarks inside the bag. Assuming that the bag is a sphere with radius r_B and that the kinetic energy is proportional to $\sim 1/r_B$ coming from the uncertainty principle, the hadron energy reads

$$M_h \approx \frac{4\pi r_B^3}{3} B + \frac{A}{r_B}\,, \tag{1.11}$$

where A is some constant. Fitting the mass of light hadrons fixes the bag constant to the empirical value $B^{1/4} \sim 145$ MeV [33], however, the difference between the vacuum and QCD ground energy is constrained by other models and renders a larger value for B, $B^{1/4} \sim 250$ MeV, see e.g. [35].

In the hadronic phase, assuming massless quarks, the dominant excitations are massless pions. This phase is characterized by the spontaneous breaking of chiral symmetry

and the appearance of $d_\pi = (2^2 - 1) = 3$ Goldstone bosons (massless pions). The pressure, energy density follows from Bose-Einstein statistics:

$$\begin{aligned} p_\pi &= d_\pi \frac{\pi^2}{90} T^4 \ , \\ \epsilon_\pi &= 3 d_\pi \frac{\pi^2}{90} T^4 \ . \end{aligned} \tag{1.12}$$

At high temperature $T \gg \Lambda_{QCD}$, the system is asymptotically free and treated as a non interacting gas of quarks and gluons, its thermodynamic properties are governed by Fermi-Dirac and Bose-Einstein statistics [3]:

$$\begin{aligned} p_{q+g} &= d_{q+g} \frac{\pi^2}{90} T^4 - B \ , \\ \epsilon_{q+g} &= 3 d_{q+g} \frac{\pi^2}{90} T^4 + B \ , \end{aligned} \tag{1.13}$$

where the degeneracies

$$\begin{aligned} d_{q+g} &= d_g + \frac{7}{8} d_q = 16 + 10.5 N_f \ , \\ d_g &= 2_{helicity} \times (3^2_{color} - 1) = 16 \ , \\ d_q &= 2_{spin} \times 2_{q,\bar{q}} \times 3_{color} \times N_f = 12 N_f \ . \end{aligned} \tag{1.14}$$

Note that it is straightforward to get the entropy density via $s = (p + \epsilon)/T$ [4]. At low temperature, the bag constant makes $p_\pi > p_{q+g}$ and the hadronic state wins out; at high temperature, a large number of color degrees of freedom ($d_{q+g} = 37$ for $N_f = 2$) are

[3] It is obvious that for a hot relativistic ($T \gg m$) or massless ($m = 0$) gas of parton species i, the number density ($-$ for bosons, $+$ for fermions) $n_i = \int \frac{d^3 p_i}{(2\pi)^3} \frac{1}{e^{\beta E_i} \pm 1} = (1_-, 3/4_+)\zeta(3) T^3/\pi^2$, where $\beta = 1/k_B T$, and the energy density $\epsilon_i = \int \frac{d^3 p_i}{(2\pi)^3} \frac{E_i}{e^{\beta E_i} \pm 1} = (1_-, 7/8_+)\pi^2 T^4/30$.

[4] There is another assumption here, that $T \gg \Lambda_{QCD}$ guarantees that the baryon chemical potential is much less than T.

present. This suggests a phase transition may occur at $p_\pi(T_c) = p_{q+g}(T_c)$, and

$$T_c = \left(\frac{90}{\pi^2}\frac{B}{d_{q+g} - d_\pi}\right)^{\frac{1}{4}} \quad . \tag{1.15}$$

Plugging in $N_f = 2$ and $B^{1/4} = 250$ MeV, one gets $T_c \sim 180$ MeV. One can also estimate the critical energy density required to realize a "plasma" of quarks and gluons, $\epsilon_c = \epsilon_{q+g}(T_c) \sim 4.25B \sim 2.08$ GeV/fm^3,[5] which is an order of magnitude larger than $\epsilon_\pi(T_c) \sim 0.13$ GeV/fm^3.

Deconfinement and Debye screening

Another interesting unsolved question is how exactly the transition from a confined phase to a deconfined one happens. Generally speaking, one may compress the baryonic matter while fixing the temperature until a critical density is achieved and the QCD matter dissolves into a deconfined state of quarks and gluons. This is the case for compact neutron stars. Alternatively, one can "heat up" the QCD vacuum, above some critical temperature, thermal excitations may overlap, a dense but baryon-neutral system is obtained, and it is referred to as a deconfined plasma of quarks and gluons. This plasma is recreated in ultrarelativistic heavy-ion collisions which will be discussed in Section 1.2.

There is a useful concept – Debye screening – in understanding the general behavior of dense system of charged particles. Take a QED plasma for example, the electric field induced by a point-like electric charge will polarize the medium, and effectively screens the charge itself. Similarly in a QCD plasma, color charges will be screened, this leads to an effective reduction in the range of the strong force.

The screening length $\lambda_D(T)$ is inversely proportional to the density of the plasma, and the Debye mass is defined via $\mu_D = 1/\lambda_D$. The screening effectively shortens the range of

[5] Plugging in $N_f = 3$ and $B^{1/4} = 250$ MeV, one gets $T_c \sim 168.2$ MeV and $\epsilon_c = \epsilon_{q+g}(T_c) \sim 3.20B \sim 1.56$ GeV/fm^3.

the binding potential:

$$V_{q\bar{q}}(r) \approx -\frac{4\alpha_s}{3}\frac{\mathrm{e}^{-\mu_D r}}{r} + \sigma\, r\left(\frac{1-\mathrm{e}^{-\mu_D r}}{\mu_D r}\right) \quad . \tag{1.16}$$

The damping of the binding force wipes out all long-range interactions among color charges. At sufficiently high temperatures, this mechanism is responsible for the melting of heavy hadrons [36].

1.1.3 Chiral symmetry breaking

The QCD Lagrangian possesses more symmetries than local $SU(3)$ gauge invariance. For instance, take $m_u = m_d \approx 0$ and neglect heavier flavors, the theory is invariant under global $U(2)_L \times U(2)_R$ transformations as one can rotate left- and right-handed quark fields $q_{R,L} = \frac{1}{2}(1 \pm \gamma_5)q$ independently and make no difference to the Lagrangian. In general, in the presence of N_f light flavors, the QCD Lagrangian has a global $U(N_f)_L \times (N_f)_R$ symmetry that can be decomposed into $SU(N_f)_L \times SU(N_f)_R \times U(1)_V \times U(1)_A$. For $N_f = 2$, i.e. u and d, this is called chiral symmetry; for $N_f = 3$, i.e. u, d, and s, this is called flavor-chiral symmetry. Single vector $U(1)_V$ rotates $q_{L,R}$ by the same angle, this symmetry corresponds to baryon number conservation. Axial $U(1)_A$ rotates $q_{L,R}$ by opposite angles, it is explicitly violated due to a quantum anomaly, i.e. $\partial^\mu j_{5\mu} \neq 0$.

Chiral symmetry is spontaneously broken in the ground state of QCD. This mechanism is responsible for generating 99% mass of nucleons (hence the bulk of all visible matter) out of very light quarks. In the non-perturbative QCD vacuum there is a non-vanishing chiral condensate $\langle\bar{q}q\rangle$, it breaks $SU(2)_L \times SU(2)_R \to SU(2)_V$ isospin symmetry. This spontaneous symmetry breaking (SSB) also involves the generation of $2^2 - 1 = 3$ massless Goldstone bosons (pions). In addition to SSB, the chiral symmetry is explicitly broken

by finite quark masses, which gives mass to the pions:

$$m_\pi^2 = (m_u + m_d)\frac{\langle \bar{q}q \rangle}{f_\pi^2} \,. \tag{1.17}$$

Since the mass of the pions is $m_\pi \sim 140$ MeV and $m_{u,d} \sim$ a few MeV, most of the pion mass in fact comes from chiral symmetry breaking. If $m_u = m_d = 0$, one would still have $\langle \bar{q}q \rangle \neq 0$, but the pions now become true massless Goldstone bosons[6].

To identify the transition between the chiral symmetry broken phase at low temperature and the chiral symmetry restored phase at high temperature, notice that the mass term in the QCD Lagrangian hence the corresponding operator $q\bar{q} = (q_R\bar{q}_L + q_L\bar{q}_R)$ is not invariant under chiral rotation, one can take the chiral condensate $\langle q\bar{q} \rangle$ as the order parameter of chiral symmetry breaking or restoration [7]:

$$\begin{aligned} \langle q\bar{q} \rangle &\neq 0 \;:\; \text{hadron gas} \\ \langle q\bar{q} \rangle &= 0 \;:\; \text{quark–gluon plasma} \;. \end{aligned}$$

As the temperature increases, the $\langle q\bar{q} \rangle$ condensate is dissociated by thermal fluctuations, and a 'plasma' of quarks and gluons forms and evolves at very high temperature to an asymptotically free gas. Simulations with $m_u = m_d = m_s = 0$ show chiral symmetry restores at $T_{chiral} \sim 150$ MeV [42]. Taking into account the physical masses, latest lattice QCD simulations show that $T_{chiral} \sim 145 - 163$ MeV [44].

Masses of u, d, s quarks significantly influence the chiral phase transition point and

[6] Motivated by the BCS theory of superconductivity [37], Nambu [38] and Nambu and Jona-Lasinio [17, 18] first postulated that chiral symmetry is spontaneously broken as a dynamical effect. According to the Goldstone theorem [39], a massless boson appears for every symmetry violated by the vacuum. In the case of $SU(2)_L \times SU(2)_R \to SU(2)_V$, the $SU(2)$ axial symmetry is spontaneously broken, three "conserved charges" are generated, and the Goldstone bosons are identified with three massless pions. More details on SSB can be found in [40] or [41], where an approach based on the Nambu-Jona-Lasinio (NJL) model is outlined.

[7] As T increases, phase transitions responsible for (1) deconfinement and (2) chiral symmetry restoration occur. Whether or not the two are intercorrelated remains an open question [42, 43].

its order, as shown in Fig. 1.2. For three massless quarks, the transformation cannot be

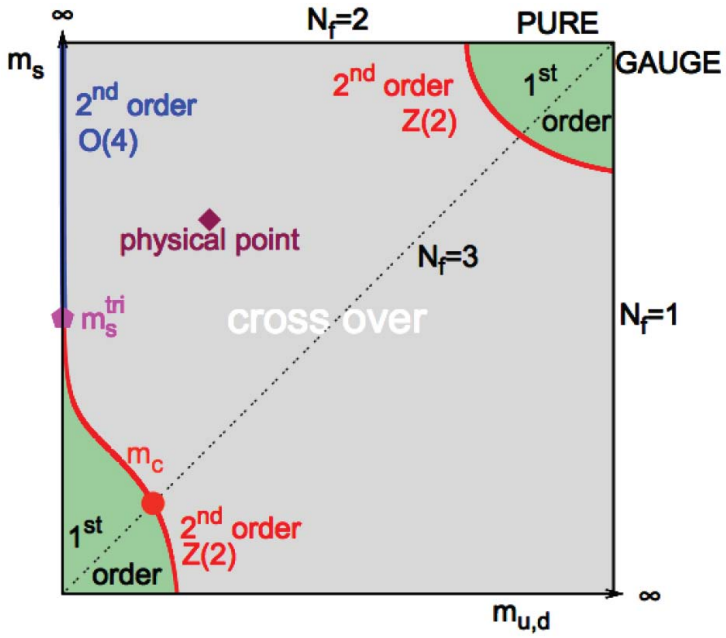

Figure 1.2: *"Columbia plot" [45]: a schematic phase transition behavior of $N_f = 2 + 1$ QCD as quark masses ($m_{u,d,s}$) vary at zero baryochemical potential. Two critical lines separate the regions of first-order transitions from the crossover region in the middle that encloses the physical point.*

second order [46], and the system must then experience a first order chiral restoration transition. For two massless quarks, instead, the transition can be either first or second order, depending on the particular value of the strange quark mass. Finally, when all quarks acquire finite mass, the second order transition is replaced by a crossover.

1.1.4 Lattice formulations of QCD

The phase structure of quark matter is one of the most fundamental questions of QCD. The non-perturbative nature of the $SU(3)$ gauge theory leads to many aspects of it yet to be understood. A variety of first-principle or energy effective theory studies have been performed to fully understand the QCD phase transition in the continuum limit. Besides

these continuum approaches, there is a powerful tool in discretized spacetime – lattice QCD.

Lattice QCD is constructed from Feynman path-integral approach, it is first proposed by Wilson in 1974 [25], and is now a standard ab initio approach to study non-perturbative phenomena associated with strong interactions. In this section, we present a brief summary of the main results of the theory. Comprehensive reviews on lattice QCD are widely available, e.g. [47].

To discretize the QCD Lagrangian Eq. (1.1) on the lattice[8], one must replace the partial derivatives with finite differences and the action becomes non-local. In the lattice action, to preserve gauge invariance, the gauge field is described by link variables of $SU(3)$ matrices that connects the fermion fields sitting on lattice sites. The relation between the link variables $U_\mu(x)$ (Wilson lines) and the continuum field $A_\mu(x)$ is given by

$$U_\mu(x) \equiv U(x, x+\mu) = \mathcal{P} \exp\left(ig \int_x^{x+\mu} A_\nu(z) dz^\nu \right) \quad . \tag{1.18}$$

Denote by a the lattice spacing and $\hat{\mu}$ one of the 4 unit four-vectors along the 4 possible directions on lattice, when a is small, $U_{\hat{\mu}}(x) = e^{igaA_\mu(x)}$. It is straightforward to prove that the sandwiched two-point function (quark bilinear) $\bar{q}(x)U_\mu(x)q(x+\mu)$ and the Wilson loop $W(C) = \mathrm{Tr}\left(U_\mu(x)U_\nu(x+\mu)U_\mu^\dagger(x+\nu)U_\nu^\dagger(x)\right)$ is manifestly invariant under local $SU(3)$ gauge transformations. And they constitute the fundamental building blocks for the quark (S_q) and gluon (S_g) action respectively.

For S_g, think of the simplest Wilson loop $W_{\mu\nu}^{1\times1}$, an elementary 1×1 plaquette that is given by

$$W_{\mu\nu}^{1\times1} = U_{\hat{\mu}}(x)U_{\hat{\nu}}(x+\hat{\mu})U_{\hat{\mu}}^\dagger(x+\hat{\nu})U_{\hat{\nu}}^\dagger(x) \quad . \tag{1.19}$$

[8] In Euclidean space. A Wick rotation $t \to -i\tau$ connects it to Minkowski space.

Expand about $x + (\hat{\mu} + \hat{\nu})/2$, suppress the color indices, one gets

$$W_{\mu\nu}^{1\times1} = 1 + ia^2 g F_{\mu\nu} - \frac{a^4 g^2}{2} F_{\mu\nu}F^{\mu\nu} + O(a^6) + \cdots \quad . \tag{1.20}$$

Note the above μ, ν indices are uncontracted. After proper reorderings and summations, to lowest order in a, the gauge action reads

$$S_g^W[U] = \frac{6}{g^2}\sum_x \sum_{\mu<\nu} \text{Re Tr } [\frac{1}{3}(1 - W_{\mu\nu}^{1\times1})] = \frac{a^4}{4}\sum_x \sum_{\mu,\nu} F_{\mu\nu}F^{\mu\nu} \to \frac{1}{4}\int d^4x F^2 \quad . \tag{1.21}$$

This is the famous Wilson action [25]. However, the above is not the unique discretization scheme for the gauge action, and it has been found in several studies [48] that lattice calculations with the Wilson gauge action deviate appreciably from the continuum theory. Improvements can be made by adding planar 1×2 rectangular plaquettes $W_{\mu\nu}^{1\times2}(x)$[9], forming the Iwasaki gauge action [49]:

$$S_g^I[U] = \frac{6}{g^2}\sum_x \sum_{\mu<\nu}(1 - \frac{c_0}{3}\text{ Re Tr } W_{\mu\nu}^{1\times1}) + \frac{6}{g^2}\sum_x \sum_{\mu\neq\nu}(1 - \frac{c_1}{3}\text{ Re Tr } W_{\mu\nu}^{1\times2}) \quad . \tag{1.22}$$

Note that $c_0 = 1 - 8c_1$ is imposed to ensure a correct continuum limit. Iwasaki uses $c_1 = -0.331$. The improved action has better rotational and chiral symmetry properties, and is widely adopted by most lattice calculations in studying QCD thermodynamics.

For quarks, simple discretization of the continuum fermion action induces the "fermion doubling" problem. The naive lattice formulation of S_q takes the form

$$S_q^N = \sum_{x,y} \bar{q}(x)\left(\frac{1}{2}\sum_\mu(\gamma_\mu\delta_{x+\hat{\mu},y} - \gamma_\mu\delta_{x-\hat{\mu},y}) + m\delta_{x,y}\right)q(y) \quad . \tag{1.23}$$

Take a hypercube of extent N in all directions, in the continuum $a \to 0$ ($N \to \infty$), the

[9] $W_{\mu\nu}^{1\times2} = U_{\hat{\mu}}(x)U_{\hat{\mu}}(x+\hat{\mu})U_{\hat{\nu}}(x+2\hat{\mu})U_{\hat{\mu}}^\dagger(x+\hat{\mu}+\hat{\nu})U_{\hat{\mu}}^\dagger(x+\hat{\nu})U_{\hat{\nu}}^\dagger(x)$.

fermion propagator in the momentum space becomes an integral within the first Brillouin zone (B),

$$\langle q(x)\bar{q}(y)\rangle = \frac{1}{Z}\int \mathcal{D}\bar{q}\mathcal{D}q\; q(x)\bar{q}(y)e^{-S_q^N} = \int_B \frac{d^4p}{(2\pi)^4}\frac{-\frac{i}{a}\sum_\mu \gamma_\mu \sin(p_\mu a)+m}{\frac{1}{a^2}\sum_\mu \sin^2(p_\mu a)+m^2}e^{ip(x-y)}\ . \tag{1.24}$$

When the continuum limit is taken, the propagator receives a proper contribution from $p_\mu \approx 0$ in the origin. However, it also receives contributions from the boundary of B where $p_\mu \approx \pm\pi/a$. Thus the naive fermion action in fact represents $2^4 = 16$ degenerate fermion species instead of one.

To maintain good chiral symmetry and avoid the fermion doubling problem, the most commonly used method is the "Domain Wall Fermions" (DWF) proposed by Kaplan [50, 51]. This is achieved by introducing an extra dimension s ($s = 0, 1, \cdots, L_s - 1$) into the action,

$$S_q^{DWF} = \sum_{x,s;x',s'} \bar{\psi}(x,s)D^{DWF}(x,s;x',s')\psi(x',s')\ . \tag{1.25}$$

Where the domain wall Dirac operator is given by

$$D^{DWF}(x,s;x',s') = (\delta_{x,x'} + D^W(x,x'))\delta_{s,s'} - m(s)P_R\delta_{s,s'+1} - m(s+1)P_L\delta_{s,s'-1}\ . \tag{1.26}$$

The $P_{R,L} = (1 \pm \gamma_5)/2$ is the right (left) handed projection operator. The 4D quark field $q, \bar{q}$ is constructed from 5D DWF field $\psi, \bar{\psi}$ via $q(x) = P_L\psi(x,0) + P_R\psi(x, L_s - 1)$ and $\bar{q}(x) = \bar{\psi}(x, L_s - 1)P_L + \bar{\psi}(x,0)P_R$. The $m(s) = -m_f$ for $s = 0$ and $m(s) = 1$ otherwise. D^W is the Wilson Dirac operator with a special mass M_5, defined as

$$D^W(x,x';U) = (4 + M_5)\delta_{x,x'} - \frac{1}{2}\sum_\mu \left[(1-\gamma_\mu)U_{\hat{\mu}}(x)\delta_{x+\hat{\mu},y} + (1+\gamma_\mu)U^\dagger_{\hat{\mu}}(x)\delta_{x-\hat{\mu},y}\right]\ . \tag{1.27}$$

Note that DWF has L_s doublers, among them $L_s - 1$ flavors are at the order of the UV

cutoff and can be canceled out through adding a Pauli-Villars term

$$S_q^{PV} = \sum_{x,s;x',s'} \phi^\dagger(x,s) D^{DWF}(x,s;x',s';m_f=1)\phi(x',s') \tag{1.28}$$

to the DWF action.

In most lattice QCD calculations, the sum of Eq. (1.22),(1.25),(1.28) is adopted as the action. It is then quantized using the Feynman path-integral method. The resulting partition function is given by an integral over pure gauge configurations,

$$Z = \int \mathcal{D}U\ \mathcal{D}\bar{q}\ \mathcal{D}q\ \mathrm{e}^{-S_g[U]-S_q[\bar{q},q,U]} = \int \mathcal{D}U \det M\ \mathrm{e}^{-S_g(U)}\ , \tag{1.29}$$

with $\mathcal{D}$U the Haar measure and $\det M$ a determinant that contains all the fermionic contributions. A "quenched" approximation is frequently used to simplify numerical integrations, under which $\det M = const$ and vacuum polarization effects are neglected. However even then the computational expense looks formidable: the total number of gluon integrations $\int \mathcal{D}U$, is already significant for moderately sized lattices. The solution to this is using Monte Carlo methods. Details on some of the algorithms used can be found in [52] and [53].

At finite temperature, the partition function of a system is given by $Z = \mathrm{Tr}\ \mathrm{e}^{-H/T}$ where H is an appropriate Hamiltonian that has a corresponding Lagrangian density $\mathcal{L}$. Going to the action formulation, Z can be recast as a functional integral over a finite Euclidean time interval $1/T$ with periodic (anti-periodic) boundary conditions for bosonic (fermionic) fields[10], and the action is given by $S = \int_0^{1/T} d\tau_E \int d^3x \mathcal{L}$. The lattice in this case has N_t points in the time direction that satisfy $T^{-1} = N_t a$, and N_s points in other spatial directions. In particular, boundaries conditions for the gauge link and fermion

[10]Note that there are also periodic boundary conditions in the spatial directions.

fields are

$$U_\mu(\mathbf{x}, \tau_E + N_t a) = U_\mu(\mathbf{x}, \tau_E) \quad , \quad q(\mathbf{x}, \tau_E + N_t a) = -q(\mathbf{x}, \tau_E) \quad . \tag{1.30}$$

The thermodynamic limit corresponds to $N_s \to \infty$ with N_t fixed. Practically N_s is always finite, and this limit is approximated by keeping $N_s \gg N_t$. On the other hand $N_t \geq N_s$ approximates the zero temperature field theory. Thermodynamic quantities are obtained by taking derivatives of the logarithm of the partition function as in the continuum.

Applying numerical methods, one can then compute thermodynamic variables such as pressure $p(T)$, energy density $\epsilon(T)$, entropy density $s(T)$, and study the equation of state of the system near the critical point T_c. Results from a recent computation by the

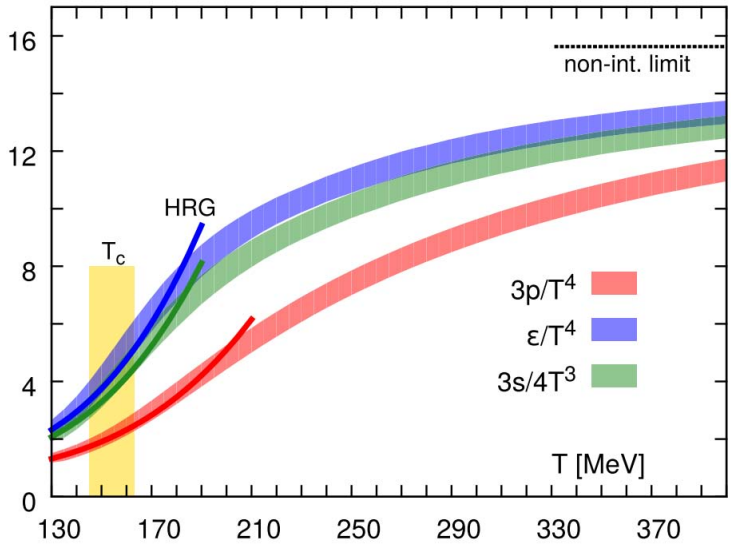

Figure 1.3: *Equation of state for $N_f = 2 + 1$ QCD from the hotQCD collaboration [44]. The error bands indicate uncertainties from statistical and systematic errors. The horizontal line at $95\pi^2/60$ in the right panel corresponds to the ideal gas (Stefan-Boltzmann) limit for the energy density and the vertical band marks the crossover region with $T_c = 154 \pm 9$ MeV.*

hotQCD collaboration [44] are shown in Fig. 1.3. The rapid increase of the energy density

near the critical temperature is evidence of a phase transition where the system develops a large number of new degrees of freedom. On the other hand, the pressure increases rather slowly and indicates a sudden decrease of the speed of sound $c_s^2 = \partial p/\partial \epsilon$ in a narrow region near T_c as shown in Fig. 1.4. The resutls shown are with physical quark

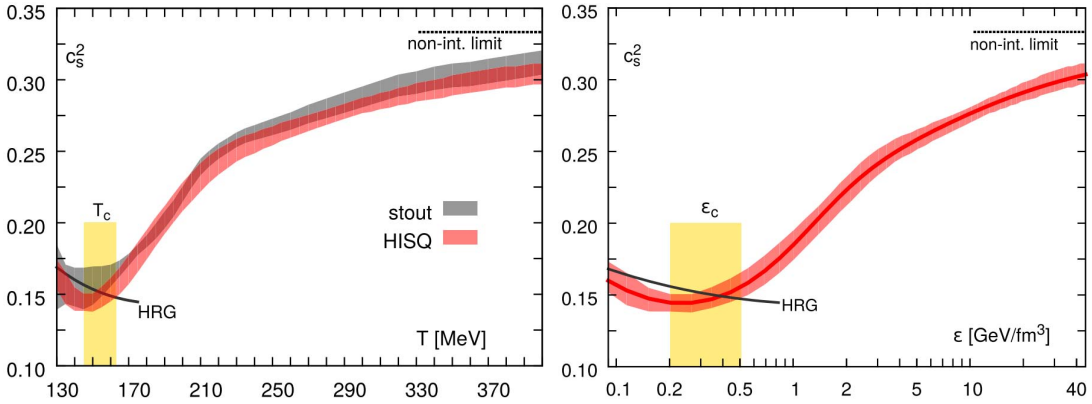

Figure 1.4: *The speed of sound squared from lattice QCD and the HRG model versus temperature (left) and energy density (right) for $N_f = 2+1$ QCD from the hotQCD collaboration [44]. The vertical band marks the location of the crossover region $T_c = 154 \pm 9$ MeV and the corresponding range in energy density, $\epsilon_c = 0.18 - 0.5$ GeV/fm^3.*

masses, for the massless limit, the critical temperature for different N_f can be extracted as $T_c(N_f = 0, 2, 3) = 273,\ 175,\ 155$ MeV [48].

1.1.5 QCD phase diagram

It is difficult to perform lattice calculations at finite baryon chemical potential (μ_B) because of the sign problem [54]. Therefore, most of the analysis and discussions up to this point have been limited to a vanishing μ_B. The full phase diagram of QCD mixes solid experimental results and first-principle calculations, as well as reasonable speculations from various models. Fig. 1.5 shows a sketch of it represented in the direction of temperature (T) and μ_B. In this diagram, the lattice QCD results shown so far sit along the T axis, where there is a smooth crossover transition from a hadron gas to a quark-gluon plasma

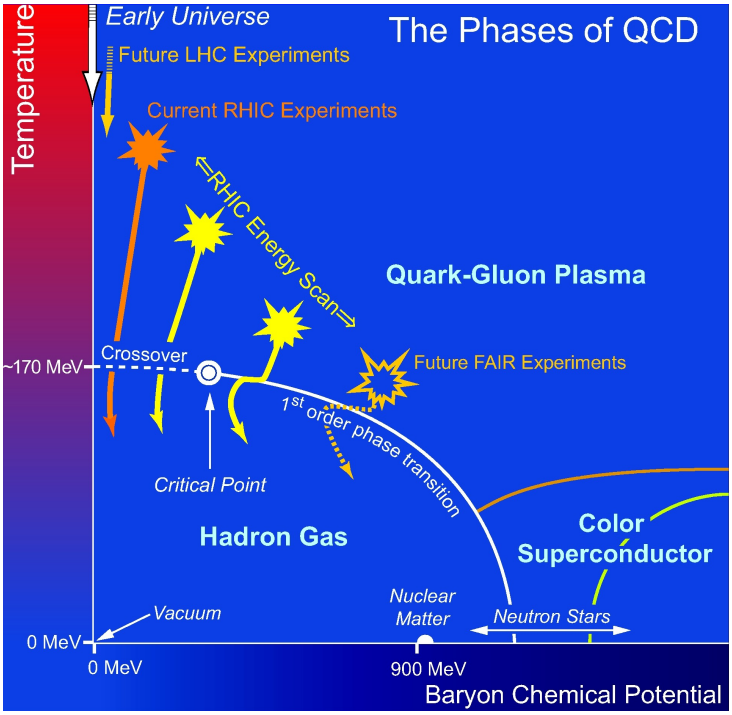

Figure 1.5: *QCD Phase diagram represented in the direction of temperature and baryon chemical potential. Taken from NSAC Long Range Plan 2007 [55].*

(QGP) once dynamical massive quarks are taken into account.

Several other important observations can be drawn from this figure: in the baryon rich regime, neutron stars provide ideal laboratories to study the QCD phase structure, however very limited measurements of their properties are presently available. On the other hand, in lower μ_B regime where T is high, high energy heavy-ion collisions at the Facility for Antiproton and Ion Research (FAIR), the Brookhaven National Laboratories (BNL) Relativistic Heavy Ion Collider (RHIC), and the CERN Large Hadron Collider (LHC) are generating enormous amount of experimental data for investigating QCD matter at extreme hot/dense conditions.

One notices that for increasing values of μ_B, the crossover between the hadron gas and the quark-gluon plasma is replaced by a first order transition. On the edge of this first order transition line there is a critical end point (CEP) that is crucial for understanding

the complete phase structure of QCD, and it has stimulated numerous theoretical investigations. The RHIC Beam Energy Scan (BES) is the current experimental frontier of studying the CEP.

A dramatic feature of Fig. 1.5 is that the quark-gluon plasma (QGP) occupies almost the entire phase space at high temperature $T > 170$ MeV because of the asymptotic freedom of strong interactions. Therefore the early universe was filled with QGP when it was sufficiently hot, and this condition is satisfied at time shorter than 10^{-5} seconds after the Big Bang, as illustrated in the left panel of Fig. 1.6. However, the primordial

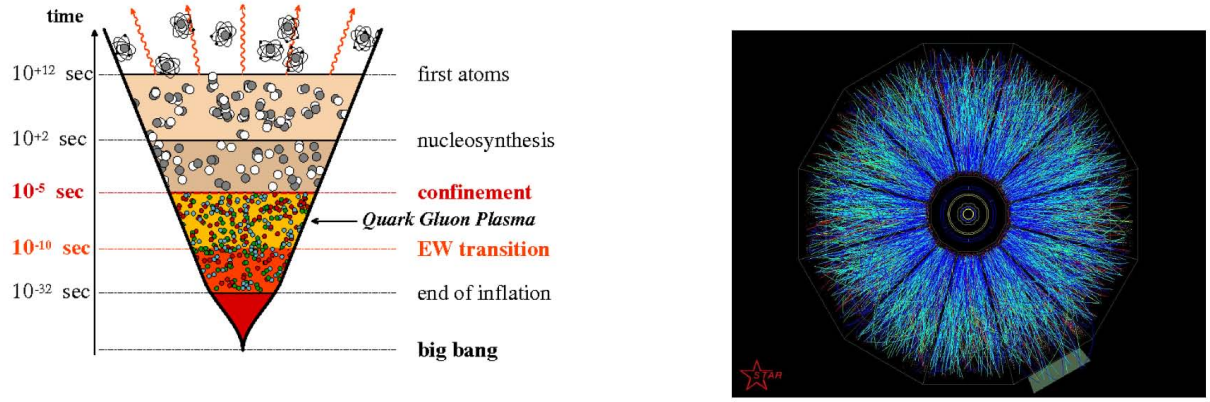

Figure 1.6: *(Taken from [56]) Left: the quark gluon plasma in the early universe. Right: event display of a heavy ion collision at RHIC (STAR collaboration).*

confinement/deconfinement transition seems to be too weak to have left any imprint that can be observed nowadays through astronomical approaches. Therefore one must seek ways to study this primordial nuclear matter in the laboratory. Fortunately, QGPs have now been recreated in ultra-relativistic nucleus-nucleus collisions at BNL RHIC and the CERN LHC, respectively at a center of mass energy of 200 GeV and 2.76 TeV per nucleon pair. The right panel of Fig. 1.6 shows one typical event at the RHIC STAR detector.

One can infer from a glimpse of this event that complicated particle/jet phenomena in these collisions must have encoded rich fundamental information about both the per-

turbative and non-perturbative aspects of QCD. And to decode such imprints is exactly the goal of this thesis. The next section will serve as a general introduction to heavy-ion collisions and quark-gluon plasmas. This thesis will be dedicated to building up a QCD framework that incorporates physics in both the strong and weak coupling limit, and that can be applied to make reliable quantitative predictions of particle/jet observables in high-energy nuclear collisions at RHIC and the LHC.

1.2 Heavy-ion collisions and quark-gluon plasmas

Generally speaking, there are three major stages of relativistic heavy ion collisions as time evolves: (1) the initial stage and a brief period of time afterwards – Color Glass Condensate (CGC) and Glasma; (2) a longer stage where the matter is close to local thermal equilibrium – strongly-coupled Quark Gluon Plasma (sQGP); (3) the final stage during which the matter has become too dilute to remain in equilibrium – Hadron Gas. They are illustrated in the cartoon in Fig. 1.7.

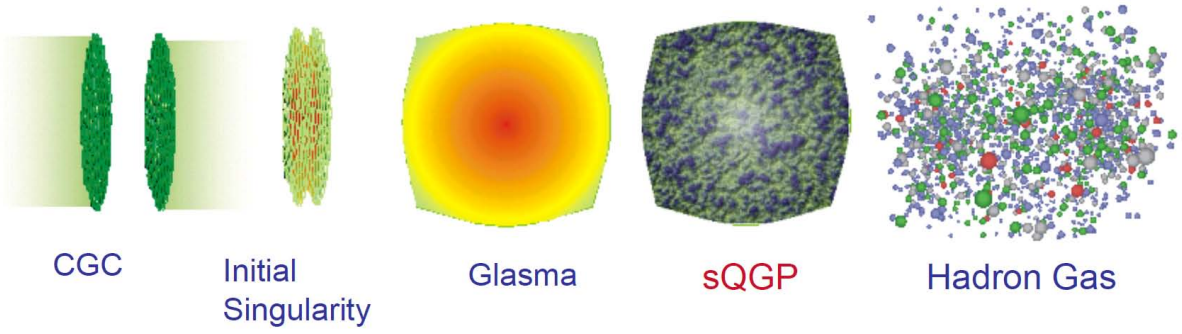

Figure 1.7: *A cartoon of the collision of two high-energy heavy nuclei from [57].*

Before the impact, the two nuclei travel at relativistic speeds and are Lorentz-contracted in the laboratory frame. Valence partons are surrounded by a dense cloud of gluons that can be described by a superposition of coherent classical color-electric and color-magnetic fields, and this is called the Color Glass Condensate.

Upon the collision, the nuclei penetrate each other mostly unchanged and carry away the baryonic matter. At the same time, they acquire a net color charge and leave behind a color-rich and baryon-free region known as Glasma. This region is described by longitudinal color flux-tubes that connect the two receding nuclei. It eventually thermalizes into a plasma of quarks and gluons.

Fig. 1.7 illustrates from an different angle the stages of a heavy-ion collision, i.e. in the beam axis (z) vs time (t) plane. After a time shorter than 1 fm/c from the initial impact,

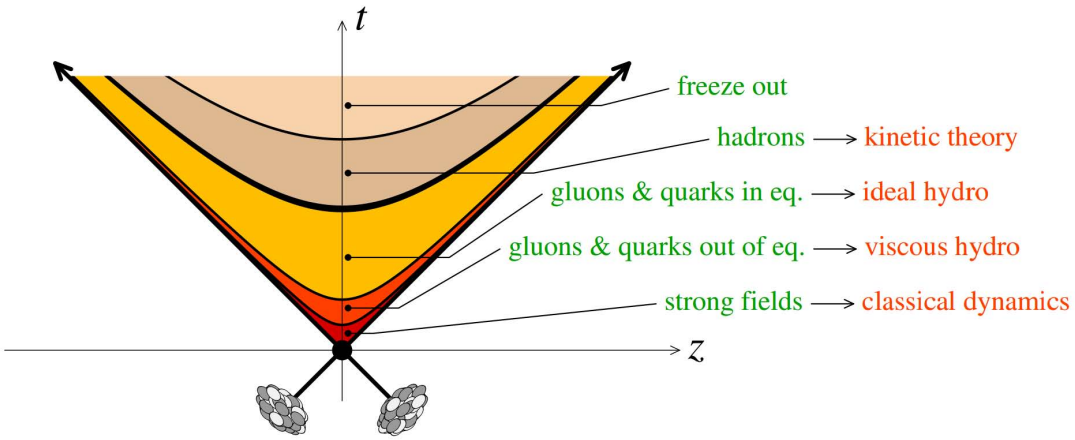

Figure 1.8: *Stages of a heavy-ion collision in the beam axis (z) vs time (t) plane. Taken from [56].*

a strongly-coupled quark-gluon plasma consists of deconfined quarks and gluons in or slightly out of equilibrium is created. At RHIC and LHC energies, the QGP behaves as a "perfect" fluid with a shear viscosity to entropy density ratio approaching the quantum bound, and its evolution is governed by the laws of relativistic hydrodynamics.

As time evolves, the system expands and cools down. When the medium reaches

a certain critical temperature, it will experiences a confinement transition to a hadronic state. This state will goes through a kinetic freeze-out shortly, and result in the formation of a Hadron Gas. This is the final stage of the collision, and are directly measured via the detectors.

1.2.1 Color glass condensate

The hadronic constituents of a nucleon include valence partons (quarks), and wee partons (sea quarks and gluons) whose nature is highly non-perturbative. In heavy ion collisions, the partons generating the bulk of the final state carry a very small fraction x of the momentum of their parent nucleon[11], $x = E_{\text{parton}}/E_{\text{nucleon}} \sim p_T/\sqrt{s}$,[12] where p_T is the transverse momentum of a typical final state particle and $\sqrt{s}$ the center of mass energy per nucleon pair. This value ranges from $x \sim 10^{-2}$ (RHIC) to $x \sim 10^{-4}$ (LHC). The left panel of Fig. 1.9 shows a measurement of the parton distributions in a proton from HERA [64, 65][13]. At low values of x, the nucleon content is predominantly made of gluons. This increase of the gluon density at low x is due to the large emission probability of soft gluons. The differential probability behaves like $dP \sim \alpha_s dx/x$.

However, this increase in gluon density cannot continue forever. When the gluon occupation number becomes of the order of the inverse coupling $1/\alpha_s$ and they start to overlap

[11] Note that the formal definition of the scaling variable x (Lorentz invariant) is rooted in deep inelastic scatterings (DIS). At lowest order in perturbation theory, it corresponds to the longitudinal momentum fraction carried by a parton in the hadron. Denote by $q^2 = -Q^2 < 0$ the virtual photon four-momentum squared, y the ratio of the photon energy to the electron energy in the hadron rest frame, s the center of mass energy squared, then $xy = Q^2/s$.

[12] It is useful to consider two asymptotic limits in DIS that better illustrate the QCD dynamics of high energy hadron wavefunctions for fixed y. The first is called the Bjorken limit, corresponds to fix x, let $Q^2 \to \infty$ and $s \to \infty$. The evolution of the separation of hard and soft scales is given by the renormalization group (RG) called DGLAP (Dokshitzer-Gribov-Lipatov-Altarelli-Parisi) equation [58–60]. The second is the Regge-Gribov limit, corresponds to fix Q^2, let $x \to 0$ and $s \to \infty$. The rapid rise of the gluon distribution at small x is given by BFKL (Balitsky-Fadin-Kuraev-Lipatov) equation [61–63]. They are shown in the right panel of Fig. 1.9.

[13] In the simplest possible words, the parton distribution function (PDF) measures the probability of finding at scale Q a parton with a momentum faction x of the parent nucleon.

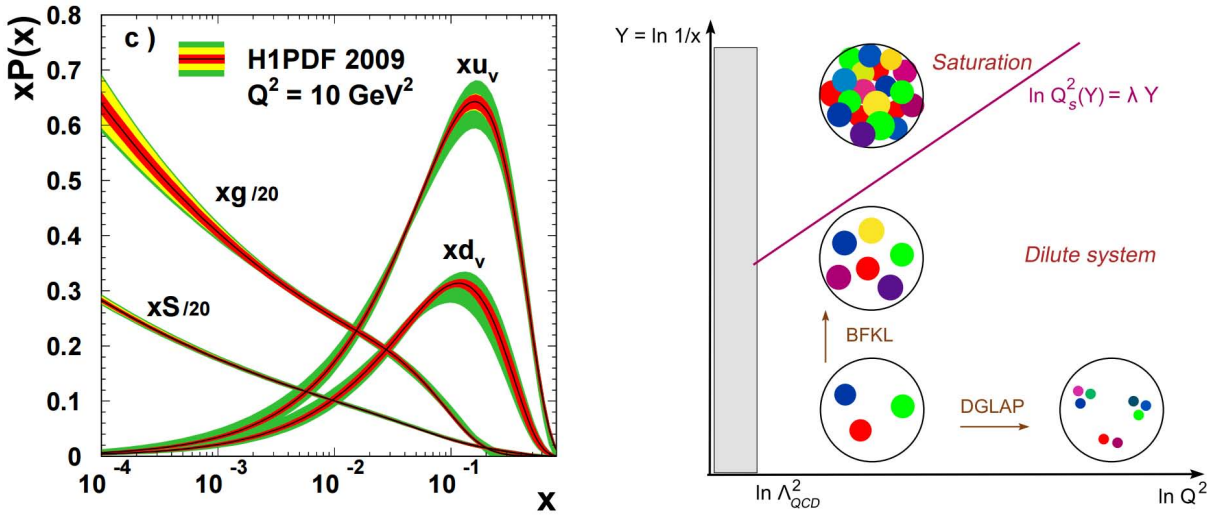

Figure 1.9: *Left: the x-evolution of valence quark, sea quark, and gluon distributions for $Q^2 = 10$ GeV^2 measured at HERA [64, 65]. Right: the "phase diagram" for QCD evolution. Each colored dot represents a parton in the infinite momentum frame with transverse area $\delta S_\perp \sim 1/Q^2$ and momentum $k^+ = xP^+$. Taken from [66].*

each other, the reverse process that two gluons recombine possesses a higher probability [67, 68]. It leads to a saturation of the gluon density [69–71]. This saturation mechanism generates a dynamical momentum scale – the saturation momentum Q_s. For gluons with transverse momentum $k_\perp \leq Q_s$, saturation effects are important. The $Q_s(x, A)$ is defined such that, the gluon density (ρ_g) which grows rapidly with decreasing x (when ρ_g is low), saturates at $\sim 1/\alpha_s(Q_s)$, and thereafter it grows only logarithmically with x. Generally speaking, $Q_s(x, A)$ increases at small momentum fraction x and increases with the mass number A of a nucleus, as shown in the left panel of Fig. 1.10. This is the reason that saturation is expected to play a more important role in heavy-ion collisions than in proton-proton collisions, and even more so at higher energies at the LHC.

Gluon densities of order $1/\alpha_s$ lead to a breakdown of the perturbative expansion, make the saturation region non-perturbative. The resummation of the infinite series of relevant graphs can be extremely cumbersome if one used standard Feynman rules. The Colour

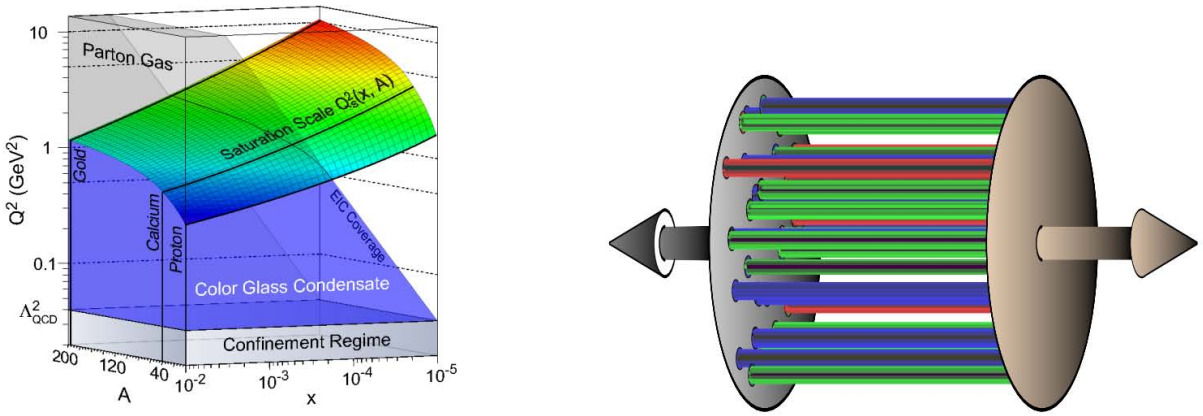

Figure 1.10: *Left: Saturation momentum Q_s (from [72]). Right: "Glasma" flux tubes – gauge field configurations of longitudinal chromo-electric and chromo-magnetic fields screened on transverse scales $1/Q_s$ (from [56]).*

Glass Condensate (CGC) [73, 74] is an effective theory based on QCD that reorganizes the perturbative expansion to simplify this resummation. The effective action in CGC neglects the quarks and treats the large x fast partons as static color sources J moving along the trajectories of the two projectiles, i.e. $S = -\frac{1}{4}\int F_{\mu\nu}F^{\mu\nu} + \int (J_1^\mu + J_2^\mu)A_\mu$. In the saturated regime, these sources are large and must be resummed to all orders. However, the advantage of this formulation is that quantum fields sourced by a large current behave classically in a first approximation. Thus at Leading Order (LO) in α_s, observables in CGC can be calculated through solving the classical Yang-Mills equations[14]:

$$[D_\mu, F^{\mu\nu}] = J_1^\nu + J_2^\nu \ , \ \lim_{t\to-\infty} A^\mu(t, \mathbf{x}) \ . \tag{1.31}$$

The resulting classical solution has a unique feature imposed by the geometry of the

[14] If the small x gluons can be described by classical fields, on the contrary large x gluons can be treated as their sources, which evolve slowly in time due to relativistic dilation effects (Glass). The distinction between the two scales is entirely arbitrary, and a correct description of the small x physics is achieved only after applying renormalization group analysis [75]. It turns out that the evolution equations are diffusive and have universal solutions: the color glass condensate indeed represents the universal form of high-energy QCD wavefunctions at small x.

collision: at a proper time $\tau = 0^+$, the lines of the chromo-electric and chromo-magnetic fields are all parallel to the collision axis as illustrated in the right panel of Fig. 1.10. These fields form color flux tubes with a typical transverse size of order Q_s^{-1} in the beam axis, and this configuration is called the Glasma. The energy-momentum tensor of such a color field configuration has a negative longitudinal pressure, thus this matter is very far from local thermal equilibrium. The evolution of the Glasma into a thermalized Quark-Gluon Plasma as well as the interaction of hard probes with the Glasma is not understood, and this is a subject of ongoing studies [76].

Experimental evidence of CGC

The description of the initial conditions in terms of coherent classical color fields must be validated by experiments before the CGC framework can be firmly established. There are growing pieces of evidence in a variety of measurements carried out in different collider experiments. For instance, the CGC hypothesis is generally supported by electron-proton scattering measurements, which can probe the physics of small $x \leq 10^{-2}$ [69–71].

In heavy ion collisions, evidence is expected be found in several observables, for example, particle multiplicity in A+A collisions [77–79], forward rapidity intermediate p_T hadron-spectrum suppression in deuteron-gold (d+A) collisions [80–82], suppression of forward azimuthal back-to-back correlations in d+A [83, 84], long-range rapidity correlations in A+A known as the "ridge" [85], etc. However at current stage, for most of them there are only after-the-fact *postdictions* that claim to be due to CGC.

An example of the CGC *prediction* that is validated by data is the particle multiplicity in A+A collisions, as shown in Fig. 1.11, where the pseudorapidity densities of charged particles predicted by CGC models (black curves with yellow bands) are in agreement with data from A+A collisions at RHIC.

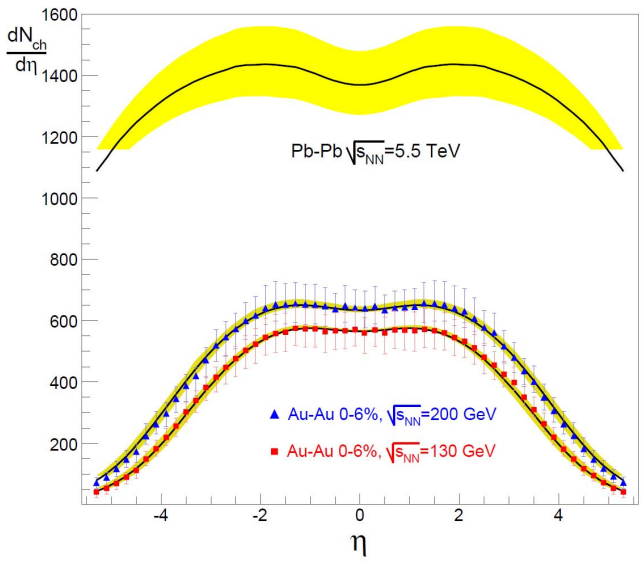

Figure 1.11: *Multiplicities of charged particles produced at RHIC at different center-of-mass energies $\sqrt{s_{NN}}$ (blue triangles and red squares) are compatible with CGC predictions (black curves with yellow bands). The upper band represents the CGC predictions of Pb-Pb collisions at the LHC. Taken from [78].*

1.2.2 Towards a thermalized QGP

The idea of ultra-relativistic heavy ion collisions originates from T.D. Lee in 1970s, he suggested that it is interesting to "investigate ... phenomena by distributing high energy or high nucleon density over a relatively large volume" [86]. The restoration of the broken symmetries in the QCD vacuum will make ultra-dense states of nuclear matter accessible through experiments of colliding heavy nuclei with high center-of-mass (c.o.m.) energies $\sqrt{s}$ [87, 88].

Dated back to the 1980s and 1990s, the earliest heavy ion collisions aimed at creating the quark-gluon plasma (QGP) started at the CERN's Super Proton Synchrotron (SPS). The SPS c.o.m. energies reached $\sqrt{s_{NN}} \approx 20$ GeV per nucleon pair and the data displayed several signatures that hinted the onset of a "new state of matter" [89]. Built upon these efforts, the Relativistic Heavy Ion Collider (RHIC) at the Brookhaven National

Laboratory (BNL) started its heavy ion program in 2000 by colliding Cu-Cu and Au-Au nuclei that reached $\sqrt{s_{NN}} = 200$ GeV. These energies are sufficient to create the QCD matter well above the deconfinement transition point, and a wide range of experimental data from the BRAHMS [90], PHENIX [91], PHOBOS [92] and STAR [93] collaboration suggest that the QGP has indeed been created at RHIC [94]. Further experimental efforts have also started at the CERN's Large Hadron Collider (LHC) in 2010, where Pb-Pb nuclei are collided at $\sqrt{s_{NN}} = 2.76$ TeV or above.

To estimate the energy density of the system being created in a heavy-ion collision, one can measure the number of detected charged particles as a function of the polar angle θ with respect to the beam direction z. This is the so-called multiplicity distribution and is shown in Fig. 1.12 for several beam energies at RHIC.

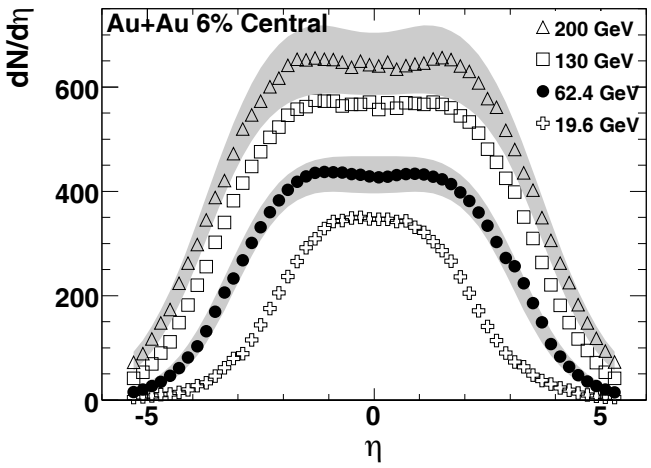

Figure 1.12: *Multiplicity distributions of charged particles as a function of pseudorapidity* (1.32)*, measured at RHIC at several different beam energies. (Taken from [95].)*

The results here are plotted as a function of the pseudorapidity[15],

$$\eta = -\log\tan\left(\theta/2\right) \ . \tag{1.32}$$

Note that $\eta = 0$ corresponds to $\theta = \pi/2$, i.e. the direction perpendicular to the beam axis, and this is called midrapidity. A notable feature in Fig. 1.12 is the plateau around midrapidity is $dN_{\rm ch}/d\eta \approx 700$ at $\sqrt{s_{NN}} = 200$ GeV ($dN_{\rm ch}/d\eta \approx 1584$ at LHC $\sqrt{s_{NN}} = 2.76$ TeV [96]). This translates into a total number of charged particles around 5000. Approximate all observed particles to be pions, then $dN/d\eta = (3/2)dN_{\rm ch}/d\eta$. This means around 8000 particles are produced.

To estimate the energy density ϵ of the medium, a simple geometric approach was proposed by Bjorken [97]. Assume that at $\tau = 0$ nuclei of radius R inter-penetrate each other, then at some $\tau = \tau_0$, the volume of the system will be roughly $2\tau_0\pi R^2$, if there is a longitudinal expansion and no radial expansion. The energy contained in that system is at least the total transverse energy between $\eta = -1$ and $\eta = 1$ in the plateau, i.e. $2 \cdot dE_T/d\eta|_{\eta=0}$. Thus one has

$$\epsilon \cdot 2\tau_0\pi R^2 = 2 \cdot dE_T/d\eta|_{\eta=0} \ . \tag{1.33}$$

Choosing $\tau_0 = 1$ fm/c[16], this relation gives one $\epsilon \sim 5$ GeV/fm^3 for $\sqrt{s_{NN}} = 200$ GeV. This conservative estimate is an order of magnitude larger than the critical energy density $\epsilon_c \sim 0.5$ GeV/fm^3 as shown in Fig. 1.4. At such an energy density the deconfinement transition must happen, and the system must undergo a crossover from the hadronic phase to the quark-gluon plasma (QGP) phase.

[15]The rapidity y of a particle is defined as $y = \frac{1}{2}\ln\frac{E+p_z}{E-p_z} = \frac{1}{2}\ln\frac{p_+}{p_-}$. It is related to the pseudorapidity η via $\sqrt{1+\frac{m^2}{p_T^2}}\sinh y = \sinh\eta$. In the massless limit, the two are the same, $y = \eta = -\ln\tan\frac{\theta}{2}$.

[16]At this point, this value is only a rough estimate of a typical size of the system, but, as we will soon see, the elliptic flow data in fact indicates that after about ~ 1 fm/c, the system is in thermal equilibrium.

More realistically, the QGP is an ultra-dense, strongly-coupled, deconfined form of matter that is formed at energy densities $\epsilon \sim 2$ GeV/fm^3, evolving from an initial state of $\epsilon \sim 20 - 30$ GeV/fm^3 to a mixed partonic and hadronic plasma after a time $\tau \sim 5$ fm/c [94]. Decouplings and hadronizations occur at later time $\tau \sim 10$ fm/c, as shown in the diagram of Fig. 1.13.

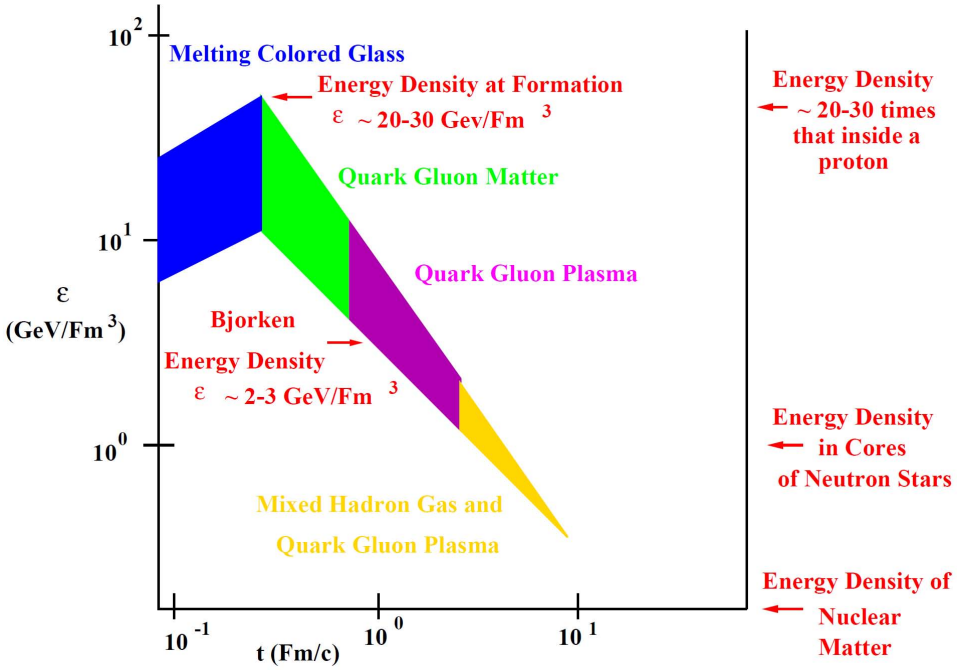

Figure 1.13: *Energy density bounds as a function of time in heavy ion collisions. From [94].*

Of course the multiplicity estimate is not a most direct experimental proof that the QGP has been created in RHIC A+A $\sqrt{s_{NN}} = 200$ GeV collisions. The first strong indication in fact came from the spectra of the "soft" particles with transverse momenta smaller than $p_T \sim 2 - 5$ GeV that comprise the bulk of the observed hadrons. These spectra drop exponentially with $\exp(-\sqrt{p_T^2 + m^2}/T_{\text{eff}})$, as opposed to the "hard" particles, whose spectra possess a power law shape. The exponentially falling spectra also show up

in the case of proton-proton (pp) collisions[17], but what is different in AA collisions is that the effective temperature T_{eff} extracted from these spectra strongly depend on the particle species, see e.g. [98]. This dependence is consistent with having a system of thermally equilibrated particles that radially expands, so that all particle species have the same radial velocity (which is about $0.6c$ in central collisions [93]), but because of their different masses, different momentum boosts occur in the final spectra.

The properties and dynamics of the locally thermal equilibrated QGP can be described by collective, macroscopic theories such as relativistic hydrodynamics. The characteristics of this "fluid" and the phenomenological consequences in terms of experimental measurements will be discussed in detail in the next section.

1.2.3 QGP: collective flow and perfect fluidity

The underlying microscopic theory of the quark-gluon plasma is QCD at finite temperature (see appendix C). Macroscopically, the thermalized plasma behaves as a fluid and obeys the laws of hydrodynamics (see appendix A and B).

The macroscopic hydrodynamic picture[18] is expected to hold after a time $\tau_0 \sim 0.3 - 1$ fm/c from the initial impact, when the plasma is sufficiently hot, and before a mixed gluonic-hadronic state is formed at $\tau_f \sim 3 - 5$ fm/c. The connection between hydrodynamics and finite temperature QCD is built through computing from the microscopic theory the quantities such as the transport coefficients using Kubo formulae [101, 102], and the equations of state (EOS) using lattice QCD. An example of lattice QCD calculations of EOS has been given in Section 1.1.4, and Fig. 1.14 is another illustration. In addition to what has already been shown in Fig. 1.3 and Fig. 1.4, here the trace anomaly,

[17] The pp spectrum is the standard baseline for comparison.

[18] To simulate the evolution of the system in a relativistic hydrodynamical framework, the knowledge of the initial conditions (determined by CGC or by the Glauber model [99] elaborated in appendix B) and the equation of state are necessary. A review on applying hydrodynamics to heavy ion collisions can be found in e.g. Pasi Huovinen and P.Vesa Ruuskanen [100].

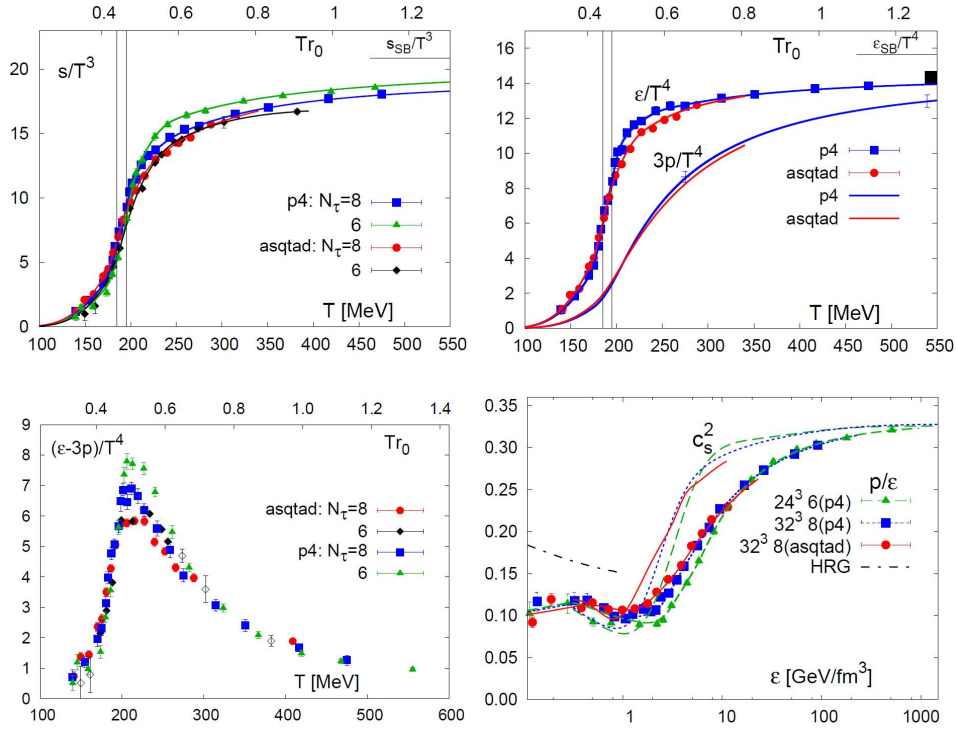

Figure 1.14: *A recent lattice calculation of $N_f = 2 + 1$ QCD equations of state with physical quarks from the HotQCD collaboration [103]. From the top-left, clockwise: the entropy density, the energy density and pressure, the speed of sound and the trace anomaly.*

$T^\mu_\mu = \epsilon - 3p$ is plotted. This quantity indicates the deviation from a conformal theory [30], a limit reached by QCD for $T \gg \Lambda_{QCD}$.

An observable directly related to the formation of a strongly-coupled QGP is the azimuthally anisotropic flow (or the azimuthal anisotropy for hard particles) in non-central collisions [104]. This is a critical observable that this thesis studies and will be discussed at length in the following.

From a simple view of a heavy-ion collision, one can imagine two Lorentz-contracted "pancakes" collide with each other in the beam direction at some impact parameter b, as illustrated in Fig. 1.15. Depending on the size of b, one can have central, semi-peripheral or peripheral collisions. However in an experiment it is impossible to select the exact impact parameter, therefore, in reality one orders the events according to their

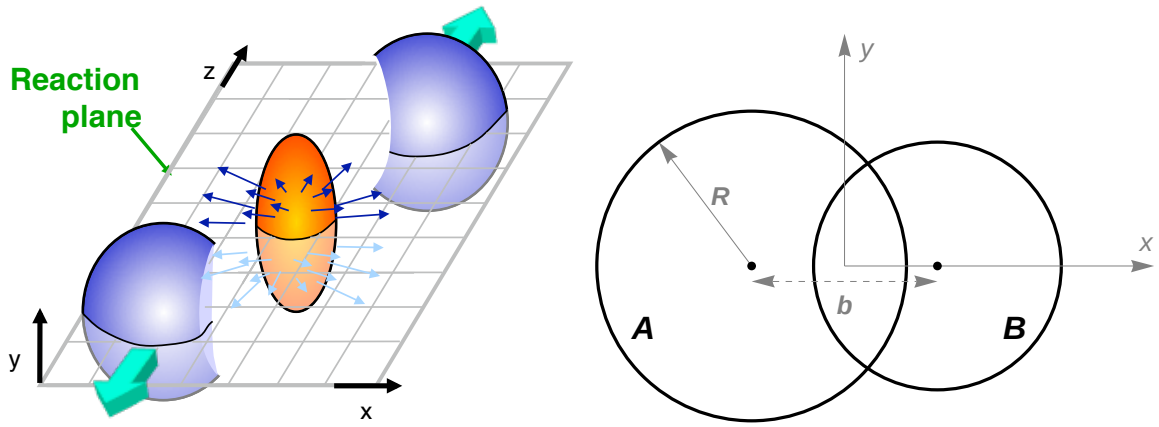

Figure 1.15: *An cartoon of a non-central collision with impact parameter b of two nuclei with mass numbers A and B. (Taken from [105].)*

multiplicities and classifies them in so-called centrality bins. For example, a collection of 5% of the events with highest multiplicities is called the "0-5% centrality bin". Generally speaking, the smaller the impact parameter, the larger the participant multiplicity. With a particular model (such as the Glauber model in appendix B), it is possible to quantify them.

Now one can turn to the particle spectrum that depends on a particle's transverse momentum p_T, the spacetime rapidity y, and the azimuthal angle ϕ. The spacetime rapidity y is defined as

$$y = \frac{1}{2} \log \left(\frac{t + z}{t - z} \right) , \tag{1.34}$$

where t is the time in the laboratory frame and z is the beam axis. It is closely related to the pseudorapidity defined in Eq. (1.32):

$$y = \frac{1}{2} \log \left(\frac{E + p_z}{E - p_z} \right) = \eta - 2 \frac{\cot \theta}{\sin \theta} \frac{m^2}{4p^2} . \tag{1.35}$$

Note that $p_z = p\cos\theta$ is used, and the observed particle has non-vanishing mass m. Thus,

$$\left.\frac{d\eta}{dy}\right|_{\theta=\pi/2} = 1 + \frac{m^2}{2p^2}\,. \tag{1.36}$$

When $p \gg m$, one can approximate $y = \eta$. The azimuthal angle ϕ in the particle distribution is measured with respect to the x-axis in Fig. 1.15. The particle spectrum is analyzed using a Fourier decomposition in ϕ:

$$\frac{dN}{p_T dp_T d\phi dy} = \frac{1}{2\pi}\frac{dN}{p_T dp_T dy}\left[1 + 2v_1(p_T)\cos\left(\phi - \Psi_1\right) + 2v_2(p_T)\cos\left(2(\phi - \Psi_2)\right) + ...\right]\,, \tag{1.37}$$

where Φ_n is the azimuthal orientation of the reaction plane. Denote by v_n the harmonic coefficients, then

$$v_n \equiv \left\langle e^{in(\phi - \Psi_n)} \right\rangle\,, \tag{1.38}$$

and it is called the "n-th order harmonics". v_n's and $dN/dp_T dy$ implicitly depend on the rapidity y, the impact parameter b (centrality), and the particle species. At high p_T, v_n's describe the azimuthal anisotropies of hard particles. At low p_T, they characterize the collective flow. In particular, v_1 is the direct flow, v_2 the elliptic flow, and v_3 the triangular flow.

At suggested by Fig. 1.15, for collisions of identical nuclei at midrapidity $y = 0$, the odd flow coefficients v_{2n+1} should vanish due to the $\phi \to \phi + \pi$ symmetry of the almond-shaped region[19]. Therefore, on average the first non-vanishing flow coefficient in the particle distribution is the elliptic flow v_2. It characterizes the asymmetry of the particles measured in the x-direction versus the particles measured in the y-direction in Fig. 1.15. Measurements of the angular asymmetries at RHIC are shown in Fig. 1.16, the magnitudes of v_2's are significant. At the LHC at $\sqrt{s_{NN}} = 2.76$ TeV, these angular

[19] On an event-by-event basis they will generally be non-zero.

asymmetries are similarly large [96, 106, 107]. The elliptic flow has a clear dependence

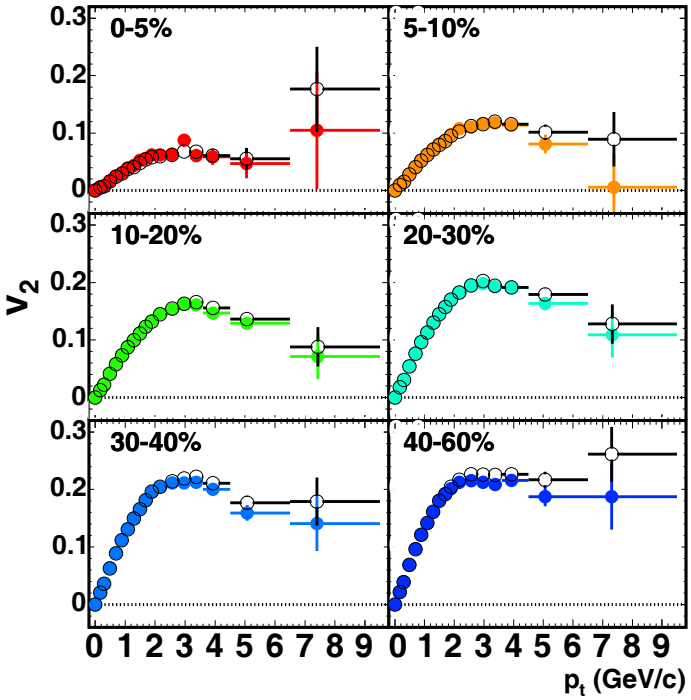

Figure 1.16: *Elliptic flow v_2 versus transverse momentum p_T for charged hadrons at different centralities in Au+Au collisions at RHIC $\sqrt{s_{NN}} = 200$ GeV. (Taken from [108].)*

on the centrality of the collision. This is a strong indication of collective behaviors. If the observed particles came from independent pp collisions, one would find symmetric azimuthal distribution, and all flow coefficients would vanish. Therefore must be some strong correlation effects at play in these systems.

For these reasons, the next natural step is to test if relativistic hydrodynamics can quantitatively describe/predict the azimuthal flow data in high-energy heavy-ion collisions. As shown in Fig. 1.17, there is indeed a remarkable agreement between the elliptic flow v_2 predicted by hydrodynamical models and what has been measured at RHIC. This is one of the strong pieces of evidence of the QGP formation at RHIC (and the LHC)[20].

[20]There are still some arguments on this point, since it relies on the subtle arguments demonstrating that one cannot reproduce this behavior with hadrons, and even if one could, the required densities exceed those at which hadrons could exist.

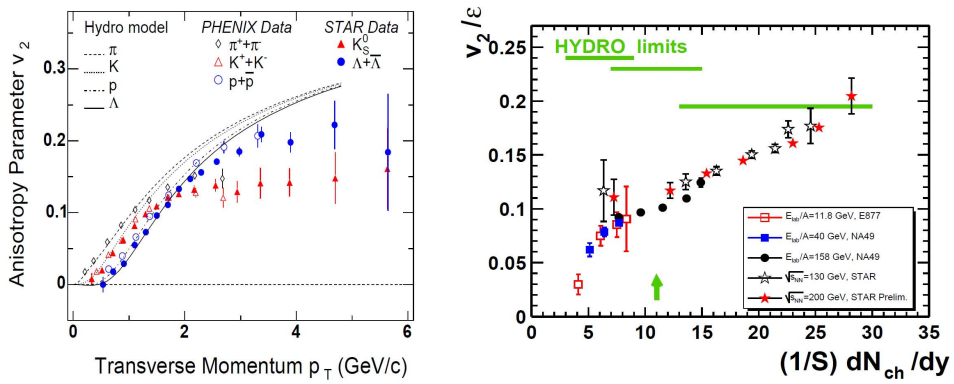

Figure 1.17: *The bulk collective flow as strong evidence for QGP formations in high-energy heavy-ion collisions. Left: RHIC measurements of the azimuthal elliptic flow $v_2(p_T)$ are shown to agree with the predicted ideal hydro flow in bulk $p_\perp \lesssim 1$ GeV domain. Right: $v_2(p_\perp)$ as a function of the charged particle rapidity density. When dN/dy drops below the values achieved at RHIC, the v_2 falls below the hydro predictions. Taken from [94].*

Telling from the left panel of Fig. 1.17, one notice that the collective flow breaks down at high values of transverse momentum $p_\perp \gtrsim 2$ GeV. The reason is clear: for such short wavelength components of the QGP, local equilibrium cannot be sustained because the coupling strength becomes too weak due to QCD asymptotic freedom. The right panel of Fig. 1.17 shows that the collective flow breaks down at small multiplicity, where there is a substantial deviation from the hydro limit is observed. The reason is also clear: at lower densities, or lower temperatures temperatures approaching T_c, a mixed gluonic-hadronic phase comes into play and hadronic dissipation takes control [109].

Another notable feature of the QGP created in heavy-ion collisions is the "perfect fluidity" [110–112]. It is characterized by a small shear viscosity to entropy density ratio η/s close to the quantum bound [113, 114] that is partially caused by a spiked increase of the number of degrees of freedom in the color-deconfined phase. Fig. 1.18 shows an example of collective flow results from first order dissipative hydrodynamics calculations. One can see from this figure that the η/s needed in viscous hydrodynamics in order to

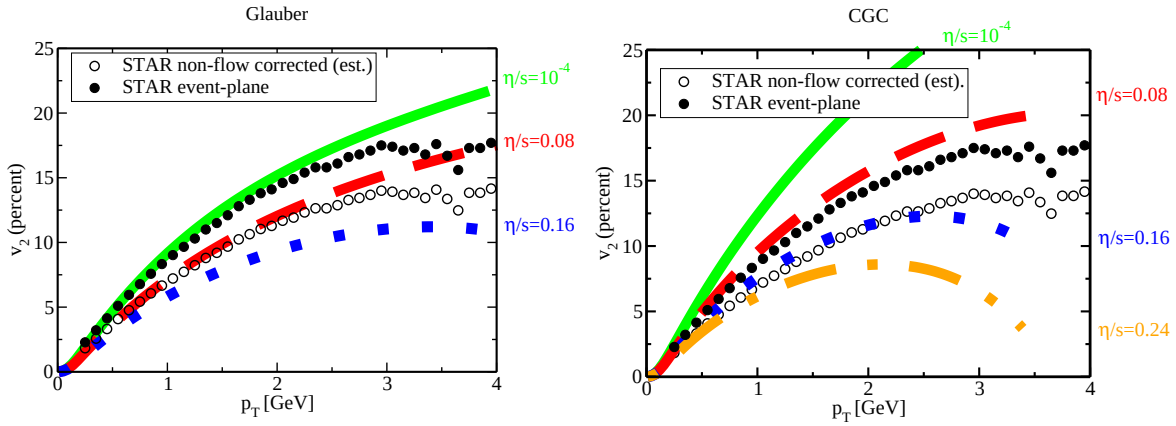

Figure 1.18: *Comparison of a conformal relativistic viscous hydrodynamic model [115] to experimental data on charged hadron elliptic flow in minimum bias events at STAR [116], for two different sets of initial conditions (CGC and Glauber). (Taken from [115].)*

achieve fits with data is small, $\eta/s \ll 1$. It implies that the medium created is indeed a near-perfect fluid.

Perfect fluidity generally implies a strong coupling feature of the underlying theory, for the following reasons: in a standard quasiparticle picture, shear viscosity describes the system's efficiency of transporting e.g. a $y-$directed momentum in the x direction. Large shear viscosity therefore indicates large mean free paths and hence weak coupling[21]. On the other hand, low η/s suggests that the momentum cannot be efficiently transported over distances of the order of $s^{-1/3}$. Consequently, there are no quasiparticles possessing long mean free paths, and this directly leads to strong coupling. A side note is that the AdS/CFT calculation (extremely strong coupling limit) for η/s agrees very well with the values from Fig. 1.18 [30]. Another insight that can be drawn is that local thermal equilibrium must established very soon after the collision, because otherwise the almond shaped region in Fig. 1.15 will have enough time to isotropize and the angular asymmetries will not be as significant as measured in Fig. 1.16. In fact, various hydrodynamic simulations

[21] Computations of the shear viscosity using the Kubo formula show that at high temperatures, QCD asymptotic freedom leads to a divergence in the shear viscosity, see e.g. [117]. At low temperatures, the hadron gas is weakly-coupled, the shear viscosity also diverges.

have suggested that τ_{eq} is on the order of 1 fm/c [118].

All the results presented point to the following conclusion: the medium produced in ultra-relativistic heavy-ion collisions at RHIC and the LHC is a strongly-coupled, near-perfect fluid, that reaches an approximate local thermal equilibrium within about 1 fm/c after the collision – this is exactly the Quark-Gluon Plasma.

Besides the collective flow, there is in fact much more data measured in RHIC and the LHC AA collisions that exhibit different features from scaled pp collisions. They provide additional evidence to support the formation of Quark-Gluon Plasmas in high-energy heavy-ion collisions. The J/ψ suppression[22] [119] and the strangeness enhancement[23] [120] are good examples.

1.2.4 Hadronization and freeze-out

As the fireball of the deconfined quark-gluon plasma expands, it cools down and to some point it will undergo a phase transition to a hadron gas phase. The hadronic bound states are formed starting from the outer and colder region of the plasma, known as the corona.

The hadronization take places through the processes of recombination and fragmentation, depending on the p_T range of the partons. In the low to intermediate p_T regime, i.e. the soft sector up to ~ 5 GeV, hadrons are formed by recombination (or coalescence) [121, 122] of partons thermal quarks and antiquarks. In the high p_T regime, i.e. the hard sector above ~ 5 GeV, hadronization takes place through fragmentation.

During the hadronization, a mixed gluonic and hadronic phase coexists while the

[22] J/ψ is the lightest of the $c\bar{c}$ mesons. In a deconfined QGP, the $q\bar{q}$ potential (1.8) is replaced by a Debye-screened one, if the screening length $\lambda_D \sim 1/\mu$ falls below an analogy of the Bohr radius for J/ψ, one expects to see the dissociation of the meson. Therefore, fewer J/ψ's will be observed in heavy-ion collisions than in scaled pp collisions.

[23] Strangeness enhancement is the phenomenon that more hadrons containing s and $\bar{s}$ quarks are produced in heavy-ion collisions than in scaled pp collisions. One proposal to explain this is that, due to the restoration of chiral symmetry in the quark-gluon plasma and a high density of gluons, the production of $s\bar{s}$ pairs through processes like the gluon fusion $gg \to s\bar{s}$ becomes more probable.

system continues to expand until the matter has fully hadronized. After that, the hadronic matter keeps diluting while interacting and at some point the inelastic hadron-hadron collisions become weak enough such that the hadronic content of the matter no longer changes [123, 124]. The temperature at which this is achieved is called the chemical freeze-out temperature and is about 155-180 MeV at RHIC at $\sqrt{s_{NN}} = 200$ GeV [123].

Finally, as the system keeps evolving, the hadronic matter becomes so dilute that the particle mean free path gets larger than the system size. In such a state even elastic interactions become negligible: hadrons from thereon free stream and the momentum distributions do not change anymore – a non-interacting hadron gas is formed. The temperature at which this happens is called the kinetic freeze-out temperature, which is about 90 MeV at RHIC [93].

Recombination/coalescence, fragmentation, freeze-out will be discussed in detail in this section in the following.

Recombination/Coalescence

In the low and intermediate p_T range, hadrons are mostly formed by recombination (coalescence) mechanisms [121, 122, 125]. In this picture, thermal quarks and anti-quarks combine to form mesons and baryons. The hadron production spectra can be written as

$$E\frac{dN_h}{d^3p} \propto \int_\Sigma p \cdot d\Sigma \int \prod_{i=1}^{n} \left(d^3x_i d^3p_i f(x_i, p_i)\right) W_n(p, x) \quad . \tag{1.39}$$

Here $f(x_i, p_i)$ is the phase-space distribution of the constituent q_i or $\bar{q}_i$ and $W_n(p, x)$ is the Wigner function of the recombined meson ($n = 2$) or baryon ($n = 3$). Recombination takes place on the hypersurface Σ.

Taking into account the steep fall off of the momentum distribution function, only a limited portion of the constituent phase-space with low p_T is dense enough to allow any

coalescence process to occur. In this scenario, the production of baryons or mesons is expected to scale with the quark constituents, take the elliptic flow $v_2(p_T)$ for example, one expects $v_{2,B}(p_T) \simeq 3v_{2,q}(p_T/3)$ for baryons and $v_{2,M}(p_T) \simeq 2v_{2,q}(p_T/2)$ for mesons. This scaling behavior has been confirmed in experimental measurements [126], as shown in Fig 1.19.

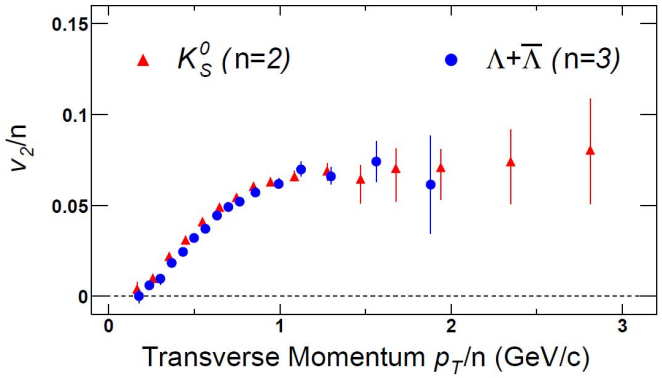

Figure 1.19: *The elliptic flow v_2 for K mesons and Λ baryons scaled by the number of constituent quarks n overlap each other. Taken from [127].*

Fragmentation

High p_T particles above $\sim$ 5 GeV hadronize mostly by fragmentation processes [128, 129]. In this scenario, the parent parton i with momentum p_i fragments into a hadron h with momentum $p_h = zp_i$, $z < 1$:

$$E_h \frac{d\sigma^h}{d^3p_h}(p_h) = \sum_i \int_0^1 \frac{dz}{z^2} E_i \frac{d\sigma^{q_i}}{d^3p_i} D^{q_i \to h}(z, Q^2) \ , \tag{1.40}$$

where $E_i d\sigma_i/d^3p_i$ is the invariant differential production cross-section for the parton i (the same for hadron h). The fragmentation function $D^{q_i \to h}(z, Q^2)$ can be interpreted as the probability for the partons i, either quarks or gluons with virtuality Q, to fragment

into a hadron h which carries a fraction z of the parton energy. From QCD factorization, the soft hadronization is factorized from the hard process, and the factorization scale is Q[24]. Fragmentation functions (FF) evolve with Q^2 as given by the DGLAP equations [58–60]. At a fixed Q^2, they generally have a simple form: for example, the KKP fragmentation functions [130] that describe the fragmentation of light quarks and gluons can be parametrized at standard $Q_0^2 = 2$ GeV^2 as:

$$D^{q_i \to h}(z, Q_0^2) = N z^\alpha (1-z)^\beta \,, \tag{1.41}$$

where α, β and N are tabulated and can be evolved to other Q^2. The FFs $D^{q_i \to h}$ are universal[25], i.e. once determined, they are applicable to any process, and they have been studied in detail in e^+e^-, $p\bar{p}$ and pp collisions.

A side note is that one can rewrite Eq. (1.40) in a more practical way:

$$\frac{dN^h}{dp_h} = \sum_i \int_0^1 \frac{dz}{z} D^{q_i \to h}(z, Q^2) \frac{dN^{q_i}}{dp_i}\bigg|_{p_i = p_h/z} . \tag{1.42}$$

This form will be extensively used in this thesis.

Freeze-out

The description of the freeze-out process is given by the Cooper-Frye formalism [131]: the transition of a locally thermal equilibrated many-body system to a free streaming state happens on a spacetime hypersurface $\Sigma(x)$. The observed momentum distribution is given

[24] In a process like $e^+ + e^- \to h + X$, the scale Q is on the order of c.o.m. energy $\sqrt{s}$, but in our context one typically takes it to be between p_i and $2p_i$.

[25] One can tell from the form of $D^{i \to h}$ that since $E_i d\sigma_i / d^3 p_i$ has a power-law fall off for high p_T, the high p_T hadron spectrum will exhibit a power-law behavior as well.

by

$$E\frac{dN}{d^3p} \propto \int_\Sigma f(x,p)p \cdot d\Sigma \ , \tag{1.43}$$

where $f(x,p)p \cdot d\Sigma$ represents the local flux of particles with momentum p through the infinitesimal surface $d\Sigma$. The distribution $f(x,p)$ is given by equilibrium Maxwell-Boltzmann statistics with the 4-momentum shifted by the local fluid 4-velocity $u_\mu(x)$.

1.2.5 Nuclear effects on hard probes

Up to now discussions about the experimental observables in relativistic heavy-ion collisions that are imprinted by quark-gluon plasmas have been focused on the low transverse momentum p_T regime. These soft particles are directly associated with the bulk medium, hence possess an "internal" nature – information about the QGP are "encapsulated" in them and are difficult to be inferred from them. On the other end of the spectra, there are high p_T hard particles that provide possibilities to study the QGP using "external" sources. They are referred to as "hard probes". These hard probes constitute one of the most powerful tools in heavy-ion phenomenology.

Hard probes pave a unique way to investigate jet-medium interactions in the sQGP, and they act as an independent and indispensable approach to study the properties of QGP. Hard partons with large virtualities are produced at the early stage of the collision before the formation of the medium. They traverse the entire bulk evolution, interact with thermal quarks and gluons, and lose energy via scattering processes that are computable because of QCD factorization – one can separate the soft non-perturbative parts (PDFs, FFs) from the hard perturbative processes (scattering cross-sections) [132, 133]. At the final stage, the hard partons fragment into energetic hadron streams known as jets. Through study the modification of jet/leading hadron spectra in the presence of the medium, one can deduce important properties of the QGP such as the coupling strength,

screening mass, transport coefficients, etc.

Hard partons produced in A+A collisions are subject to nuclear effects which can be divided in two categories: (1) Initial state or cold nuclear matter (CNM) effects. These are effects that influence the initial momentum distribution of partons, which is modified with respect to the distribution in rescaled p+p collisions. They are due to the modification of the parton distribution functions (PDFs) inside the nucleus, and are visible in asymmetric p+A events. For the CNM, shadowing/anti-shadowing and Cronin effect will be discussed in this section. (2) Final state or hot nuclear matter effects. These effects are directly related to the presence of a hot deconfined quark-gluon plasma, they are visible mostly in A+A collisions. Modifications to the observed hadronic distribution due to final state effects can be utilized to study several properties of the QGP if initial state effects have been correctly singled out and the initial hard parton distributions can be reliably calculated. Energy loss is the most important hot nuclear matter effect, it is the topic of next chapter. In this section it will be skimmed over, but it will be discussed somewhat at length in the next section.

Shadowing/Anti-shadowing

The difference between PDFs in a free and a bound nucleon can be characterized by the nuclear ratio

$$R^A_{F_2}(x,Q^2) = \frac{F_2^A(x,Q^2)}{A\ F_2^N(x,Q^2)} \quad , \tag{1.44}$$

where $F_2(x,Q^2)$ are structure functions, N stands for nucleon, and A is the nuclear mass number. Since the structure functions are functionals of the PDFs, nuclear effects in the ratio $R^A_{F_2}$ are applicable to the parton distributions. The results shown in Fig. 1.20 identify four separate regions where these effects take place: (1) Shadowing: $R^A_{F_2} < 1$ for $x \lesssim 0.1$; (2) Anti-shadowing: $R^A_{F_2} > 1$ for $0.1 \lesssim x \lesssim 0.3$; (3) EMC: $R^A_{F_2} < 1$ for

$0.3 \lesssim x \lesssim 0.8$; (4) Fermi motion: $R_{F_2}^A > 1$ for $x \gtrsim 0.8$.

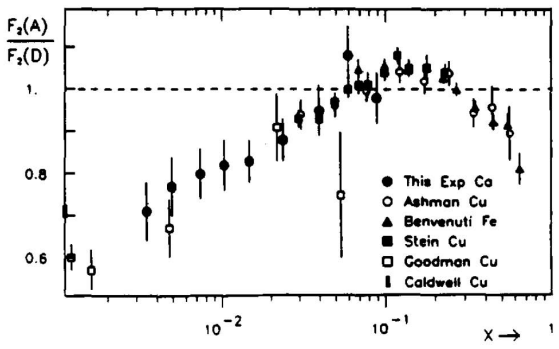

Figure 1.20: *Results for $R_{F_2}^A$ for different nuclear species, taken from [134].*

Providing a unique theoretical description of these effects is an ongoing research effort. The depletion of partons (shadowing) in the low x kinematic region is particularly relevant to experiments at RHIC and the LHC, because they probe the physics of nuclear collisions at increasingly higher energies and smaller x. Such depletions will lead to a reduction of the hadron yield in the high p_T region.

Notable features of the shadowing effect [135] include: (1) an enhancement of shadowing with decreasing x, although at very small x experimental data is compatible with either saturation or a mild weakening; (2) an enhancement of shadowing with A; (3) a weakening of shadowing with increasing Q^2.

Several phenomenological explanations of shadowing have been proposed [136–139]. Underlying is the concept of gluon fusion and gluon saturation that occurs at very low x for very dense systems [140], a phenomenon addressed theoretically in the CGC framework presented in Section 1.2.1.

Cronin effect

The Cronin effect [141] refers to the enhancement of the production cross section of hadrons in p+A compared to p+p collisions. It has been experimentally observed in the

transverse momentum range $1 < p_\perp < 7$ GeV.

This effect can be studied in a model of multiple parton scatterings [142]. In this model, when incident partons pass through the target nucleus A, they undergo multiple soft scatterings prior to the hard one. Each of the scatterings provide a transverse momentum kick which broadens the Gaussian distribution of the beam partons k_T by a factor $\langle \Delta k_T^2 \rangle_A$, i.e.

$$g_A(k_T) = \frac{1}{\pi \langle k_T^2 \rangle_A} \mathrm{e}^{-k_T^2/\langle k_T^2 \rangle_A} \quad , \tag{1.45}$$

with width $\langle k_T^2 \rangle_A = \langle k_T^2 \rangle + \langle \Delta k_T^2 \rangle_A$. The broadening is assumed to be proportional to the number of scatterings the projectile suffers inside the nucleus. This k_T broadening overrides the interference absorption between successive scatterings, and result in an enhancement in the hadron yield within a specific p_T range.

Energy loss

Energy loss is a final state effect, and is experienced by hard partons (jets) that interact with the thermal particles [133, 143]. Both elastic and inelastic collisions may occur [144, 145]. The knowledge of the hadron distribution if jet-medium interactions are absent allows one to determine the properties of the quark-gluon plasma by making observations of the modified hadron distribution in A+A collisions. Suppressed high p_T leading hadron/jet yields in AA collisions comparing to scaled pp collisions is strong evidence for the formation of a hot deconfined medium. This phenomenon, called "jet quenching", will be discussed in detail in the following section. And it is the main subject that this thesis will study.

1.2.6 Jet quenching

In relativistic heavy-ion collisions, jets are generally referred to a collection of particles in the $y - \phi$ space surrounding some energetic leading hadrons, and a particular jet clustering algorithm such as anti-k_T [146] is utilized to identify them. On the theory side, the term "jet quenching" may be simplified to the energy loss of the leading hadron, i.e. one considers under eikonal approximation high p_T quarks/gluons that pass through the strongly-coupled quark-gluon plasma created in AA collisions, lose energy through radiative and collisional processes, and eventually fragment into high p_T hadrons with reduced yields compared to those in rescaled pp collisions. This will be the convention of this thesis unless otherwise restated. And experimental observables of interests will be at single particle level.

Jet quenching is one of the most decisive signals for formation of the quark-gluon plasma in heavy-ion collisions [133]. The two-particle correlations in Au+Au vs p+p collisions at the same c.o.m. energy at RHIC is a clear example to manifest this effect, as shown in Fig. 1.21.

In this measurement, the trigger momentum is chosen between 4 and 6 GeV and the associated momentum has range Δp_T, i.e. once a particle with the momentum equal to the trigger momentum is detected, one then looks for other particles that have momentum within the Δp_T range and plot their relative azimuthal angle and pseudorapidity dependence with respect to the trigger particle. The lower left panel in Fig. 1.21 demonstrates the jet quenching phenomenon: in the pp collision one clearly sees two peaks at $\Delta\phi = 0$ and $\Delta\phi = \pi$, this indicates two back-to-back jets. However in the AA collision, the away-side peak ($\Delta\phi = \pi$) is missing. This clearly indicates jet quenching, because the energy of the energetic parton has been transferred to the thermal constituents of the plasma. A side proof is that the soft particles with $p_T < 2$ GeV in the upper left panel have a

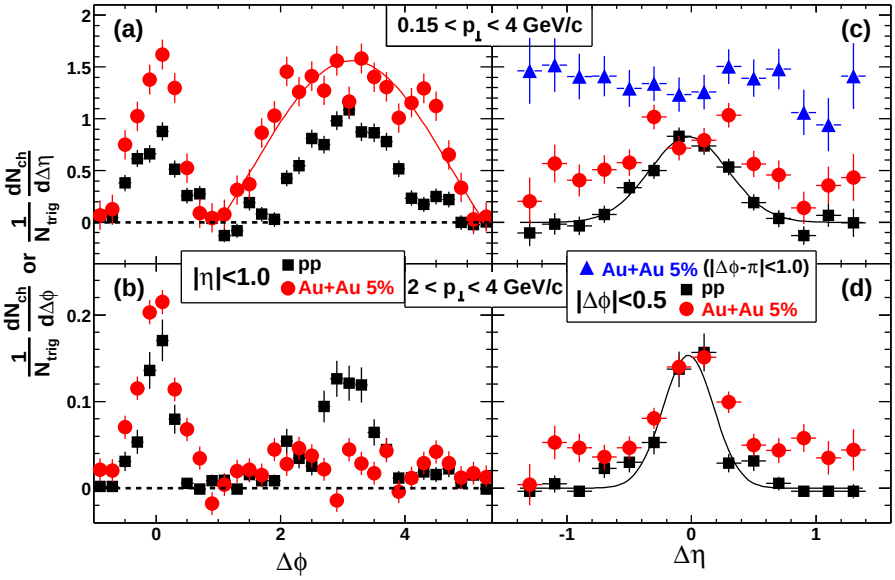

Figure 1.21: *Two-particle azimuthal $\Delta\phi$ and pseudorapidity $\Delta\eta$ correlations (with background subtracted) in central Au-Au collisons at RHIC at $\sqrt{s_{NN}} = 200$ GeV (colored dots), compared to the pp results (black dots). The trigger momentum was $4 < p_T^{\text{trig.}} < 6$ GeV and the associated momentum ranges are indicated. (From STAR collaboration [147].)*

broadened away-side peak. Note that for observed back-to-back jets, there is a surface bias[26] that leads to one twin parton must traverse much longer distances in the medium and hence lose more energy than the other one, Fig. 1.22 is an illustration of this.

To analyze the phenomenon of jet quenching more quantitatively, one may start with *pp* collisions, which is the benchmark for *AA* data. In *pp* collisions, partons rarely scatter with a large momentum transfer Q. These high-Q processes result in the production of highly energetic, back-to-back hadrons with p_T of several GeV. At such high Q, perturbative QCD is particularly successful in calculating the production rate because QCD factorization states that the soft and hard scales can be separated. Schematically, the

[26]The surface bias comes from jet quenching combined with a steeply falling spectrum – this means the most likely way to get a high momentum jet is from surface production with its partner being quenched.

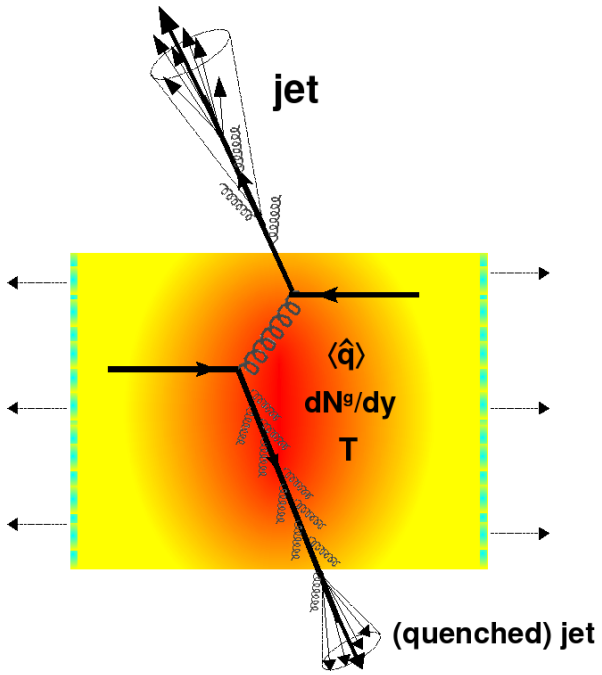

Figure 1.22: *An illustration of jet quenching in a heavy ion collision. After a hard scattering of two partons, one of them goes directly to the vacuum and hadronizes, while the other one must propagate through the strongly-coupled quark-gluon plasma. It interacts with the medium, loses energy through medium-induced gluon radiation and finally hadronizes. (Taken from [148].)*

cross section for production of a high-p_T hadron h is

$$d\sigma_{pp\to h} = \sum_{i,j,k} f_{i/p}(x_i, Q^2) \otimes f_{j/p}(x_j, Q^2) \otimes d\sigma^{\text{hard}}_{ij\to k}(x_i, x_j, Q^2) \otimes D_{k\to h}(z, Q^2)\,. \qquad (1.46)$$

Here $f_{i/p}(x, Q^2)$ is the parton distribution function (PDF) that characterizes the probability of finding the parton i with momentum fraction x_i inside the proton p. $D_{k\to h}(z, Q^2)$ is the fragmentation function (FF) that characterizes the probability for the parton k to fragment into the hadron h with fractional momentum z. In this factorized formula, PDFs and FFs constitute the soft non-perturbative part, they are process-independent and can be measured experimentally. The $d\sigma^{\text{hard}}_{ij\to k}(x_i, x_j, Q^2)$ is the cross-section for a hard

process $ij \to k$ that is computable in perturbative QCD.

For a collision of two heavy nuclei with mass numbers A and B, Eq. (1.46) will be modified to:

$$d\sigma_{AB\to h} = \sum_{i,j,k} f_{i/A}(x_i, Q^2) \otimes f_{j/B}(x_j, Q^2) \otimes d\sigma^{\text{hard}}_{ij\to k}(x_i, x_j, Q^2) \otimes P_k(\Delta E) \otimes D_{k\to h}(z, Q^2)\,. \tag{1.47}$$

One now has nuclear PDFs $f_{i/A}(x_i, Q^2)$. The $P_k(\Delta E)$ characterizes the probability for a parton c to lose energy ΔE from interactions with the medium. It is assumed that the hard process $d\sigma^{\text{hard}}_{ij\to k}(x_i, x_j, Q^2)$ remains unchanged in A+B collisions because it occurs on a scale $\sim 1/Q$ that is too short to be resolved in the medium. The combination $P_k \otimes D_{k\to h}$ is referred to as the modified fragmentation function. One can approximate the nuclear PDF's with the proton PDF's, although in reality nuclear PDF's are modified by initial state shadowing/anti-shadowing effects [135]. If the hot medium effects are negligible in (1.47), then the only difference between $d\sigma^{\text{hard}}_{AB\to h}$ and $d\sigma^{\text{hard}}_{pp\to h}$ is the effective number of inelastic binary nucleon-nucleon collisions $N_{\text{bin}}(b)$[27] at a given impact parameter b. From this perspective, in order to quantify the medium effects, one should take the ratio of the AA cross-section (or particle yield) over the pp one, and scale it with the number of binary collisions:

$$R^h_{AB}(p_T; b) = \frac{\frac{dN_{AB\to h}}{p_T dp_T d\eta}}{N_{\text{bin}}(b)\frac{dN_{pp\to h}}{p_T dp_T d\eta}}\,. \tag{1.48}$$

Here $dN_{AB\to h}/p_T dp_T d\eta$ is the particle yield of hadron h as measured in a $A+B$ collision and $dN_{pp\to h}/p_T dp_T d\eta$ denotes the particle yield at the same p_T, η, and $\sqrt{s_{NN}}$ in a $p+p$ collision. Note that this definition can also be applied to a parton of species i to get a partonic R_{AB}.

Combine Eq. (1.46)(1.47)(1.48), one can arrive at a hadronic R_{AB} expressed in terms

[27] For derivation from simple geometrical considerations see appendix B.

of the partonic one:

$$R^h_{AB}(p_h) = \frac{\sum_i \int_0^1 \frac{dz}{z} D^h_i(z,Q^2)\,(dN_{pp\to i}/dp_i)\,|_{p_i=p_h/z} R^i_{AB}(p_h/z)}{\sum_i \int_0^1 \frac{dz}{z} D^h_i(z,Q^2)\,(dN_{pp\to i}/dp_i)\,|_{p_i=p_h/z}}\,. \tag{1.49}$$

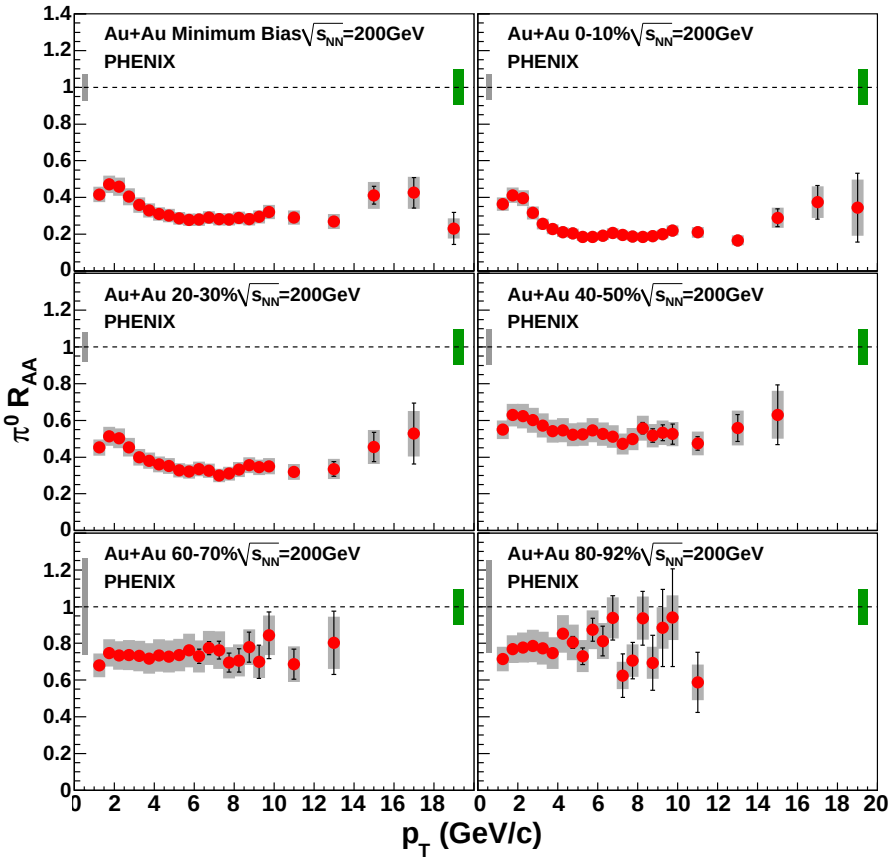

Figure 1.23: *Nuclear modification factor R_{AA} for neutral pions as a function of momentum in Au-Au collisons at RHIC at $\sqrt{s_{NN}} = 200$ GeV, for various centrality bins. (Taken from [149].)*

The quantity R_{AB}[28] is called the nuclear modification factor and it is one of main observables of interests in this thesis. It is clear from previous discussions that if one neglects the medium and initial state effects and think of the nucleus-nucleus collision

[28]Besides p_T, R_{AB} is also a function of c.o.m. energy $\sqrt{s_{NN}}$ and pseudorapidity η, for simplicity, we do not write them out explicitly, and take the mid-rapidity regime unless otherwise restated.

as a collection of N_{bin} incoherent nucleon-nucleon collisions, R_{AB} will approximately be equal to 1. However, at highest RHIC energies, the first results [147, 150, 151] indicate very strong suppressions: as one can see from Fig. 1.23, in the most central collisions at RHIC, $R_{AA} \approx 0.2$, this is a clear signature of strong jet quenching. Jet quenching remains significant at even higher energies that are accessible at the LHC [152, 153].

It is clear in Fig. 1.23 that the nuclear modification factor shows a strong centrality dependence. This is consistent with the interpretation that as the impact parameter increases the size and temperature of the medium decreases and hence the jet quenching effects weaken. It is also important to notice that at high p_T, R_{AA} is approximately independent of momentum and hadron species [147, 154], this suggests hard partons lose energy in the medium and hadronize outside the medium.

Chapter 2

Parton energy loss

Two main mechanisms are responsible for the energy loss of a parton traversing the hot deconfined quark-gluon plasma: the collisional energy loss due to elastic processes, and the radiative energy loss due to inelastic processes. Effects of other energy loss mechanisms, such as synchrotron or Cherenkov radiation, are generally less important compared with these two. For this reason, the "jet quenching" we refer to is the collisional process between hard partons and thermal quanta that results in a loss of energy of the original parton, and this process includes elastic collisions and inelastic color bremsstrahlung.

Assuming valid QCD factorization in ultra-relativistic nucleus-nucleus reactions, the interaction between the jet and the medium can be separated from non-perturbative initial and final states of the heavy-ion collision and computed perturbatively. In the past two decades, several models of jet quenching have been formulated in the perturbative QCD (pQCD) paradigm and applied to explain or predict high p_T observables at RHIC and the LHC.

The concentration of this section will be on the detailed mechanism of parton energy loss, and in particular, to introduce a pQCD based framework for computing radiative energy loss – the Djordjevic-Gyulassy-Levai-Vitev (DGLV) opacity expansion theory. As

noted before, we will focus on partons that have high transverse momentum $p_T \gg \Lambda_{\rm QCD}$. They originate from "hard" scatterings with $Q^2 \gg \Lambda^2_{\rm QCD}$, and are well-described by perturbative QCD because of asymptotic freedom. After this hard scattering, the large virtuality parton travels through the quark-gluon plasma with a velocity close to the speed of light along a straight line (eikonal approximation), loses energy through elastic and inelastic interactions with the medium, and eventually fragments non-perturbatively into a set of final state hadrons. The main underlying assumption in applying pQCD to study parton energy loss is that the jet and the medium are weakly-coupled because the typical exchanged momentum is high, $\langle q^2 \rangle \gg \Lambda^2_{\rm QCD}$, while the medium is still considered to be strongly coupled.

Let us start from the collisional (elastic) energy loss.

2.1 Collisional energy loss

Purely elastic collisions in a color medium, originally described in [133], were subsequently found to play a relevant role especially in the case of heavy quark jet quenching [155–157]. An in-depth analysis of the elastic contribution to the energy loss was performed by Wicks in [158], and the implementation into our CUJET model will be described in Chapter 3. The collisional energy loss originates from elastic scatterings of the parton with the medium constituents and is generally more important at low momenta.

The first estimation for collisional energy loss in a quark gluon plasma was made by Bjorken [133]. His work still constitutes the benchmark against which any computation of this kind should be compared. Here we briefly outline his derivation.

In the limit $E \gg k$, where k the momentum of the target particle in the medium, we

can approximate the quark-quark, quark-gluon and gluon-gluon elastic cross sections as

$$\frac{d\sigma_{i,j}}{d\hat{t}} = \frac{2\pi\alpha^2}{\hat{t}^2} c_{i,j} \quad , \tag{2.1}$$

where $c_{i,j}$ is a numerical factor equal to 4/9, 1, 9/4 for $\{i,j\} = \{q,q\}$, $\{q,g\}$ or $\{g,g\}$ respectively. The energy loss per unit length can be written as

$$\frac{dE}{dx} = \int d^3k \; \rho_i(k) \Phi \int_{\hat{t}_{MIN}}^{\hat{t}_{MAX}} d\hat{t} \frac{d\sigma_{i,j}}{d\hat{t}} \cdot (E - E') \quad . \tag{2.2}$$

Here $E - E'$ represents the energy lost in the collision, $\rho_i(k)$ is the quark or gluon number density, and Φ is the flux factor that accounts for the relative orientation of the target and projectile. Defining θ as the angle between the momentum of the incoming parton and that of the target,

$$\begin{aligned} E - E' &= -\frac{\hat{t}}{2k(1-\cos\theta)} \\ \Phi &= 1 - \cos\theta \quad . \end{aligned} \tag{2.3}$$

Integrating (2.2) over $d\hat{t}$, we obtain

$$\frac{dE}{dL} = \int d^3k \; \rho_i(k) \left(-\frac{\pi\alpha^2}{k} c_{i,j} \log B \right) \quad , \tag{2.4}$$

where B is determined by the integration limits $\hat{t}_{MAX}$ and $\hat{t}_{MIN}$. Assuming B is independent of k for simplicity, one can set $\hat{t}_{MAX} \approx 2 \langle k \rangle E \approx 4TE$ and $\hat{t}_{MIN} = \mu^2$, with μ being the Debye screening mass of the plasma, and in this case $B = 4ET/\mu^2$.

If we further write the quark and gluon number densities as

$$\begin{aligned} \rho_q(k) &= \frac{12N_f}{(2\pi)^3} \frac{1}{e^{\beta k} + 1} \\ \rho_g(k) &= \frac{16}{(2\pi)^3} \frac{1}{e^{\beta k} - 1} \quad , \end{aligned} \tag{2.5}$$

we can perform the last integration over all momenta d^3k and finally get to the Bjorken energy loss formula

$$\frac{dE}{dL} = -\pi C_R \frac{\alpha^2}{\beta^2}\left(1 + \frac{N_f}{6}\right)\log B \quad . \tag{2.6}$$

Where C_R is the quadratic Casimir of the hard parton ($C_R = 4/3$ for quark and $C_R = 3$ for gluon). This result tells us that the collisional energy loss is path independent and that it depends on the energy of the jet only logarithmically. In order to derive this short analytic result, several approximations were made in the way that infrared and ultraviolet divergences are regulated, i.e. $\hat{t}_{MIN}$ and $\hat{t}_{MAX}$. Such divergences are physically related to the absence of collective medium effects (soft scattering) and recoil (hard scattering) in the derivation of the theory. Improvements over this formula has been achieved by numerous works, including more careful treatment of the IR divergences [159], UV divergences [160, 161], the inclusion of the running of the coupling [162, 163] and many more.

2.2 Radiative energy loss

Radiative energy loss is rooted in the inelastic interactions between the parton and the medium. It dominates at high momentum. Inelastic scatterings lead to the highly virtual parton splitting into a parton and a gluon. This process is equivalent to a hard parton radiates a soft gluon in the thermal bath, and is called medium-induced color bremsstrahlung. The energy/momentum carried by the soft gluon is the lost energy/momentum of the parton from interacting inelastically with the medium. Therefore, the radiative energy loss is typically written as the gluon radiation spectrum as a function of emitted gluon energy ω and (two dimensional) transverse momentum $\mathbf{k}_\perp$, $dI_{\text{rad}}/d\omega d\mathbf{k}_\perp$. The medium-induced multiple gluon emission is the dominant mechanism for parton energy loss in the quark-

gluon plasma[1].

2.2.1 Vacuum radiation

A high p_T parton produced in a hard process has large virtuality, i.e. strong off-shellness. Towards a stable on-shell state, it will radiate gluons even in vacuum. This process is called vacuum splitting. Denote by $x \equiv \omega/E$ the energy fraction of the emitted gluon to the hard parton. For radiations in vacuum, splitting functions, $P_{q\to q+g}(x)$ and $P_{g\to g+g}(x)$, characterize the probability for the inelastic $q \to q + g$ and $g \to g + g$ process to happen in vacuum. The distribution of gluons radiated from a massless parton in the x-$\mathbf{k}_\perp$ space is given by [15]

$$x\frac{dN_g^{(0)}}{dxd\mathbf{k}_\perp} = \frac{\alpha_s}{2\pi}\frac{xP_{a\to a+g}(x)}{\mathrm{k}_\perp^2}\,. \tag{2.7}$$

Here we denote by dN_g the number of radiated gluons such that $\omega dN_g = dI_{\rm rad}$ and by (0) the vacuum radiation. For soft gluon radiations, $x \ll 1$, the splitting functions for $a = q\ , g$ differ only by the color Casimir factor, $P_{(q,g)\to(q,g)+g} \approx 2C_R/x$, where $R = F$ stands for the fundamental representation and $R = A$ stands for the adjoint. In this limit, Eq. (2.7) is approximately x independent, With properly chosen kinematic bounds, one can integrate Eq. (2.7) and get the energy loss outside a jet cone of radius $\sim 1/\mu$ ($\mathrm{k}_\perp > \mu$),

$$\Delta E^{(0)} = \frac{4C_R\alpha_s}{3\pi}E\log\left(\frac{E}{\mu}\right)\,. \tag{2.8}$$

For a heavy quark jet, the radiated gluon spectrum is different from Eq. (2.7) due to kinematic constraints. This radiation is suppressed at angles smaller than $\theta_0 = M/E$

[1]Recent developments [164] have shown that the collisional energy loss may play a significant role especially for heavy quarks. This will be discussed in Chapter 3. In fact, in the language of the jet quenching parameter $\hat{q}$, $dE_{rad}/dL \propto \hat{q}L$ and $dE_{el}/dL \propto \hat{q}/T$, thus the relative magnitude of the two depends on $T \times L$ times some constant of $\mathcal{O}(1)$.

where M is the mass of the quark, under soft approximation (small x),

$$x\frac{dN^{(0)}}{dxd\mathbf{k}_\perp} = \frac{C_F\alpha_s}{\pi}\frac{\mathrm{k}_\perp^2}{(\mathrm{k}_\perp^2 + x^2M^2)^2}\,. \tag{2.9}$$

This is the dead cone effect [165] that results in the reduction of the gluon radiation intensity by heavy quarks. One will see later that the vacuum radiation is in fact the dominant component of the full gluon radiation spectrum. Medium-induced effects generate small corrections to the radiation spectrum Eq. (2.7), and while their magnitudes are limited, they are of physical importance.

2.2.2 LPM effect

Quantum mechanically, it takes a finite amount of time for fluctuations to evolve such that the wavefunction of a radiated gluon decouples from the parent parton. This time period is called the formation time, τ_f. Intuitively, τ_f will be small for soft and non-collinearly radiated gluons since they can be resolved from the high virtuality parton more easily. For gluon radiations in a thermal medium, another length scale comes into play: the mean free path λ. If τ_f is larger than λ, interferences taking place among successive scatterings in the medium becomes (destructively) coherent. The overall induced gluon radiation spectrum will be suppressed. The QED equivalent of this effect is referred to as the Landau-Pomeranchuck-Migdal (LPM) effect. LPM's non-Abelian version plays a crucial role in computing parton energy loss in the QGP[2] [166, 167].

To consider soft gluon radiations in the presence of a deconfined plasma, an eikonal approximation is usually made. This is an assumption that the hard parton has high enough energy to travel along an unaltered z direction. The medium is modeled as a collection of static scattering centers in which the kth kick on the jet occur at position

[2]In this thesis, the LPM effect we refer to is the QCD version of it, unless otherwise restated.

z_k, and $|z_{k+1} - z_k| = \lambda$, where λ is the mean free path of the parton in the QGP. There is a certain scattering potential associated with each interaction between the jet and the medium. This will lead to induced gluon radiation. The mean free path $\lambda = (\rho\sigma_{\rm el})^{-1}$, where ρ is the density of the medium and $\sigma_{\rm el}$ is the elastic cross-section for the particle-medium interaction. For a system of length L, one can define the opacity as $\bar{N} \equiv L/\lambda$, i.e. the mean number of collisions in the medium.

Coherent multiple inelastic scatterings lead to the LPM effect that is responsible for destructive interferences and non-trivial reductions of the radiated gluon spectrum. To get a simple flavor of this effect, consider in QED the amplitude current $J^\mu(k)$ of a massless particle that experiences n collisions in spacetime. At x_i^μ, the particle's momentum changes from p_{i-1}^μ to p_i^μ, and

$$J^\mu(k) = \sum_{i=1}^{n} J_i^\mu(k) = ie \sum_{i=1}^{n} e^{ik\cdot x_i} \left(\frac{p_i^\mu}{k\cdot p_i} - \frac{p_{i-1}^\mu}{k\cdot p_{i-1}} \right) . \tag{2.10}$$

The radiated photon (γ) spectrum is obtained by squaring $J^\mu(k)\varepsilon_\mu$ (ε_μ is the photon's polarization vector) and summing over all polarizations, and the final result will be $\omega dN_\gamma/d^3k \propto |J(k)|^2$. The size of the off-diagonal terms in this summation is governed by the phase factors:

$$e^{ik\cdot(x_i - x_j)} = \exp\left(i\left(\omega - \sqrt{\omega^2 - k_\perp^2} \right)(z_i - z_j) \right) \approx \exp\left(i\frac{k_\perp^2}{2\omega}(z_i - z_j) \right) = \exp\left(i\frac{\Delta z_i}{\tau_f} \right) . \tag{2.11}$$

Here the collinear approximation $k_\perp \ll \omega, k_z$ is assumed. The formation time

$$\tau_f = \frac{2\omega}{k_\perp^2} \tag{2.12}$$

can be understood as the minimal time $\sim 1/\Delta E$ required to resolve a transverse pho-

ton/gluon wavepacket of size $\Delta x_\perp \sim 1/k_\perp$ from the wavepacket of the high energy parent particle. Because on the average, $\Delta z_i \sim \lambda$, from Eq. (2.11) one can get two extremes: (1) the incoherent multiple scattering limit where $\lambda \gg \tau_f$ and (2) the factorization limit where $\lambda \ll \tau_f$. The incoherent limit will be discussed in the next section. In the factorization limit, the phase factors are ~ 1, causing cancellations in the sum in $|J(k)|^2$, the only left-over contributions are the radiations from the initial and final lines. Between these two limits, the interplay between λ and τ_f will affect the distribution of radiated gluons non-trivially. This is illustrated in Fig. 2.1, where $\tau_f \sim 3\lambda$. Physically speaking, the formation time is the time it takes for the radiated gluon to become on-shell, and during this period one can have interference LPM effects.

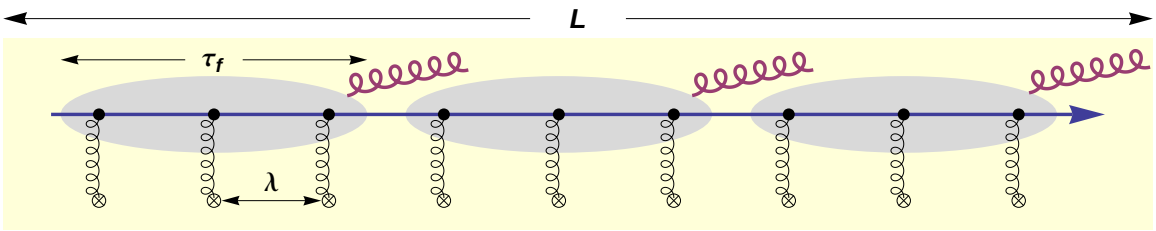

Figure 2.1: *Illustration of the LPM effect in a QCD medium of length L. The formation time τ_f is around 3 times the mean free path λ. (Taken from [168].)*

2.2.3 Gunion-Bertsch incoherent radiation

In the incoherent multiple scattering limit, the mean free path λ is much larger than the formation time τ_f, the phase factors in Eq. (2.11) are large and the off-diagonal elements average to 0. There are then only diagonal components left. Physically, this limit assumes no interference effects among successive scatterings of the hard parton traversing the medium (incoherent) and considers the incoming jet being on-shell (asymptotic), in this way further interferences between the vertex and induced radiation can be neglected. This limit is the non-Abelian QCD equivalent of the incoherent Bethe-Heitler (BH) limit in

QED [169]. The gluon spectrum in this regime was first calculated by Gunion and Bertsch [143] and is named after them. The incoherent Gunion-Bertsch (GB) radiation spectrum is

$$x\frac{dN_g^{\rm GB}}{dxd\mathbf{k}_\perp} = \frac{C_A\alpha_s}{\pi^2}\frac{\mathbf{q}_\perp^2}{\mathbf{k}_\perp^2(\mathbf{q}_\perp-\mathbf{k}_\perp)^2}\,. \tag{2.13}$$

where $\mathbf{q}_\perp$ is the transverse momentum transfer from the medium. It is the reference for any medium-induced radiative jet energy loss computation.

After performing the transformation $x\frac{d}{dx} = \frac{d}{dy}$, where y is the rapidity of the gluon, Eq. (2.13) shows the existence of a central region uniform in rapidity, i.e. a plateau, and a spectrum that falls as a power-law $1/k_\perp^4$ at large $k_\perp$. To get the final gluon spectrum from Eq. (2.13), one needs to average over $\mathbf{q}_\perp$, for which one needs a distribution of color dipoles in the medium. More about this will be specified in Section 2.2.5. Just to get a glimpse at a rough final spectrum, assume the momentum transfer between the parton and the medium has a probability distribution that resembles a color-screened Yukawa potential in momentum space,

$$\frac{dP}{d\mathbf{q}_\perp} = \frac{1}{\pi}\frac{\mu^2}{(\mathbf{q}_\perp^2+\mu^2)^2}\quad. \tag{2.14}$$

Here $\mu \equiv \mu_D$ is the Debye screening mass of the QGP. In order to regulate the $\mathbf{k}_\perp \to \mathbf{q}_\perp$ and $\mathbf{k}_\perp \to 0$ infrared divergences, a physical soft $\mathrm{k}_\perp$ scale χ must be determined, it turns out to be related to the dynamically generated mass that the gluon acquires in a thermal plasma [170]. Therefore, the incoherent asymptotic gluon radiation spectrum for a hard parton traversing a deconfined thermal medium with length L and mean free path λ is given by

$$x\frac{dN_g}{dxd\mathbf{k}} = \frac{C_A\alpha_s}{\pi^2}\frac{L}{\lambda}\int d\mathbf{q}_\perp \frac{\mu^2}{\pi(\mathbf{q}_\perp^2+\mu^2)^2}\frac{\mathbf{q}_\perp^2}{(\mathbf{k}_\perp^2+\chi^2)((\mathbf{q}_\perp-\mathbf{k}_\perp)^2+\chi^2)}\quad. \tag{2.15}$$

2.2.4 Perturbative QCD energy loss models

Having studied the medium-induced radiative energy loss in the incoherent limit and the factorization limit, a natural next step is to explore the coherent regime in between. However, theoretical calculations of radiated gluon spectra in this phase space is significantly complicated by non-trivial interplays between different physical scales. Complex interference effects among vacuum radiation, vertex radiation and gluon rescattering also come into play.

In the perturbative QCD paradigm, there are 4 major energy loss models on the market. They are all based on QCD factorization Eq. (1.47), but differ mainly in assumptions about the scale hierarchy and the QGP modeling[3]. Effectively, the calculated energy loss results in modifications of the vacuum fragmentation functions. In this section, some general features of these models will be briefly discussed. Comprehensive reviews of these models and jet quenching in general can be found in [144, 145, 148, 172]. Detailed quantitative comparisons among these models can be found in [171, 173].

In the Baier-Dokshitzer-Mueller-Peigne-Schiff (BDMPS) model [145, 174–183], the radiated gluon distribution is computed in a plasma modeled by static color scattering centers. A multiple soft scattering (MSS) approximation is imposed, in this limit, the hard parton is subject to Brownian motion and it experiences a Gaussian diffusion in the p_T space. The scattering properties of medium is encoded in the jet transport coefficient,

$$\hat{q} = \rho \int d^2\mathrm{q}_\perp \mathrm{q}_\perp^2 \frac{d\sigma}{d^2\mathrm{q}_\perp}\,, \tag{2.16}$$

where ρ is the density of the medium and $d\sigma/d^2\mathrm{q}_\perp$ is the differential parton-medium scat-

[3]The differences among these models are not limited to the assumptions of the medium, but extend to the inclusion of specific features of the medium-induced radiation. In [171], it is shown that the largest quantitative discrepancies arise from the way approximations are carried out throughout the calculations and how specific kinematic limits are imposed.

tering cross-section. Physically, $\hat{q}$ is the average transverse momentum transfer squared per unit length and can be expressed as $\hat{q} \sim \mu^2/\lambda$. The BDMPS approach is equivalent to Zakharov's light-cone path integral (LCPI) formalism for jet energy loss [179–182, 184] in the dipole approximation. The two frameworks are generally combined together and be referred to as BDMPS-Z. In the MSS limit, the Armesto-Salgado-Wiedemann (ASW) [185–188] model implements Poisson probability distributions for the fractional parton energy loss due to variable quenching weights, convolutes them with the vacuum fragmentation functions (FFs), and generates medium-modified FFs.

In the higher twist (HT) model [189–193], the medium-modified fragmentation function is directly calculated from power corrections to the leading-twist cross-section for parton scattering processes. The medium-modified FF differs from the vacuum one by an additive part that is calculated from the medium-modified splitting function which is connected to the properties of the medium through the jet transport coefficient $\hat{q}$.

In the Arnold-Moore-Yaffe (AMY) model [102, 194–199], one starts from a well-defined, thermally-equilibrated QGP made of quark and gluon quasiparticles. Properties of the medium such as the dispersion relations are given by the hard thermal loop (HTL) [200–205] approximation in the finite temperature field theory. The distribution of partons is calculated from the transition rates of parton $\rightarrow$ parton + gluon, through a Fokker-Planck like equation using the HTL effective theory and assuming high temperature. This distribution is thereafter convoluted with the vacuum FFs to get the medium-modified ones.

In the Gyulassy-Levai-Vitev (GLV) model [206–210], the radiated gluon distribution is formulated as an expansion in opacity. The opacity series can be calculated to an arbitrary order using a recursive diagrammatic procedure called the reaction operator approach. The medium is modeled as static color screened scattering centers, its properties depend non-trivially on the Debye screening mass μ^2 and the mean free path λ. The GLV

approach abandons the MSS approximation, i.e. it computes single hard radiation spectrum and uses that to arrive at the full multiple scattering spectrum through a recursive procedure. After taking into account Poisson energy loss fluctuations, medium modified fragmentation functions are obtained. Djordjevic and Gyulassy further generalized GLV to include effects coming from finite quark masses and gluon plasmon masses, and established the DGLV theory [170]. The DGLV approach will be the topic for the rest of this chapter. The foundation of the GLV opacity expansion theory is the Gyulassy-Wang model, it will be discussed in the next section.

2.2.5 Gyulassy-Wang model

Before one moves on to compute the induced gluon bremsstrahlung in the QGP, some kinematic approximations generally made by pQCD parton energy loss models referred to in the previous section shall be noted:

1. Eikonal approximation: both the hard parton energy E and the emitted gluon energy ω are much larger than the transverse momentum transfer $\mathrm{q}_\perp \equiv |\mathbf{q}_\perp|$ between the jet and the medium: $E \gg \mathrm{q}_\perp$, $\omega \gg \mathrm{q}_\perp$. The physical picture underneath is that a highly energetic jet will travel through the QGP without changing its direction.

2. Soft approximation: the emitted gluon is soft compared with the parent parton, i.e. $\omega \ll E$.

3. Collinear approximation: gluons are emitted at small angles with respect to the parent parton: $\omega \gg \mathrm{k}_\perp$, where $\mathrm{k}_\perp \equiv |\mathbf{k}_\perp|$ represents the transverse momentum of the gluon[4].

[4]Note the insights gained from the Gunion-Bertsch (GB) limit is that the radiation spectrum has a power-law tail at large $\mathrm{k}_\perp$ that falls off rapidly. On the other hand, the formation time $\tau_f = 2\omega/\mathrm{k}_\perp^2$ for collinearly radiated gluons is more likely to be longer, thus they are more likely to be in the coherent regime and to make corrections to the incoherent GB spectrum.)

4. Well-separated scattering centers: the mean free path λ is much larger than the Debye screening length $\lambda_D = 1/\mu$, $\lambda \gg \lambda_D$, such that the scattering centers in the hot deconfined medium are discrete and independent of each other.

Even though the results are valid only within the range of approximations specified above, the common way to proceed is to extrapolate the computation to the other regions. This procedure leads to results that must be carefully interpreted, and possible issues must be addressed at least numerically.

The Gyulassy-Wang (GW) model [166] is the foundation of the Gyulassy-Levai-Vitev (GLV) [206, 207] energy loss framework. The gluon radiation features of the GLV theory are all embedded in the GW model. In GW, a Debye color screened potential $V_i^a(\vec{q})$ with screening mass μ is introduced in the QGP to model the interaction with a static target parton (scattering center) localized at $\vec{x}_i$ (three dimensional space) and carrying color c:

$$V_i^a(\vec{q}) = g(T_i^a)_{c,c'} \frac{\mathrm{e}^{-i\vec{q}\cdot\vec{x}_i}}{\vec{q}^2 + \mu^2} \quad , \tag{2.17}$$

where T_i^a's are the $SU(3)$ generators in the representation of the target parton i. Under high temperature and static approximation, the average energy loss per elastic scattering $q_0 \sim q_z \sim g^2 T$ can be neglected compared to the average transverse momentum transfer $q_\perp \sim \mu \sim gT$ (assuming $g \ll 1$). In addition, at high T the mean free path $\lambda \sim 1/g^2 T$ is much larger than the screening length $1/\mu \sim 1/gT$, thus the scattering centers are assumed to be well-separated.

We start by studying a single scattering in the potential Eq. (2.17). The amplitude for a scattering at $\vec{x}_i$ from an incident jet momentum p_{i-1}^μ to p_i^μ is given by

$$M_i(p_i, p_{i-1}) = 2\pi\delta(p_i^0 - p_{i-1}^0) A_i(\vec{q}_i) e^{-i\vec{q}_i\cdot\vec{x}_i} \, , \tag{2.18}$$

where $\vec{q}_i \equiv \vec{p}_i - \vec{p}_{i-1}$. This form is the same as the analogous QED amplitude, except that A_i carries non-trivial color information,

$$A_i(\vec{q}_i) = -2igET^a V_i^a(\vec{q}_i)\,. \tag{2.19}$$

Here T^a's are the $SU(3)$ generators in the representation of the incoming parton/jet (projectile). From amplitude (2.18), by standard averaging over the initial states and summing over the final states, we can get the elastic cross section between the jet and the target parton in the low momentum transfer limit:

$$\frac{d\sigma_{\mathrm{el},i}}{d^2q_{\perp i}} \approx \frac{C_2(P)C_2(T_i)}{d_A}\frac{|v(\vec{q}_{\perp i})|^2}{(2\pi)^2}\,, \tag{2.20}$$

where

$$v(\vec{q}_\perp) = \frac{4\pi\alpha_s}{q_\perp^2 + \mu^2}\,, \tag{2.21}$$

and where $d_A = N_c^2 - 1 = 8$ and $C_2(P)$ and $C_2(T_i)$ is the quadratic Casimir of the projectile and the target parton i, respectively. Note that for quarks $C_F \equiv C_2(\mathbf{3}) = 4/3$ and for gluons $C_A \equiv C_2(\mathbf{8}) = 3$.

If we denote an intermediate jet parton propagator by $\Delta(p_i)$, the amplitude for multiple elastic collisions takes the form

$$\begin{aligned} M_{j,i}(p_j, p_{i-1}) \propto \int d^4p_{j-1}d^4p_i\; M_j(p_j, p_{j-1}) \\ \times\, \Delta(p_{j-1})\cdots\Delta(p_i)M_i(p_i, p_{i-1})\;\;, \end{aligned} \tag{2.22}$$

whereas the amplitude for radiating a gluon with four momentum k, polarization vector ϵ_μ and color c, at the mth intermediate jet line, becomes

$$M^c_{j,i;m}(p_j, p_{i-1}; k) \propto \int d^4p_m \; M_{j,m+1}(p_j, p_m - k) \\ \times \{\Delta(p_m - k)(g\epsilon_\mu p_j^\mu T^c)\Delta(p_m)\} M_{m,i}(p_m, p_{i-1}) \quad . \tag{2.23}$$

The latter expression represents a jet that undergoes multiple scatterings in the medium and radiates one gluon, and the radiation comes from internal jet lines. However, it is also possible for the radiated gluon to scatter multiple times with the medium, adding another set of amplitudes that include three gluon vertices. This corresponds to multiple final state interactions of the emitted gluon (cascading). If the intermediate gluon lines are on-shell, the cascading becomes classical and the only effect of this is then the broadening of the final $\mathrm{k}_\perp$ radiation distribution.

In the eikonal limit, the total radiation amplitude for n scatterings, Eq. (57)-(59) of [166] is:

$$M^c_n(p_n, p_0; k) \propto (g)^n \int \prod_{m=1}^{n} \left[d\mathbf{q}_{\perp m} \; \mathrm{e}^{-i\mathbf{q}_{\perp m}\cdot\mathbf{x}_{\perp m}} V^{a_m}_m(\mathbf{q}_{\perp m}) \right] \\ \times \left(\epsilon \cdot \mathbf{J}^c_{a_1\cdots a_n}(\mathbf{q}_{\perp 1} \cdots \mathbf{q}_{\perp n}; k) \right) \quad , \tag{2.24}$$

with the effective color current

$$\mathbf{J}^c_{a_1\cdots a_n}(\mathbf{q}_{\perp 1} \cdots \mathbf{q}_{\perp n}; k) = 2ig \sum_{i=1}^{n} \mathrm{e}^{ikx_i} \left(\frac{\mathbf{k}_\perp}{\mathbf{k}_\perp^2} + \frac{\mathbf{q}_{\perp i} - \mathbf{k}_\perp}{(\mathbf{q}_{\perp i} - \mathbf{k}_\perp)^2} \right) \\ \times (T^{a_n} \cdots [c, T^{a_i}] \cdots T^{a_1}) \quad , \tag{2.25}$$

where $\mathbf{q}_\perp$'s are medium-induced transverse momenta transfers. From this expression, one can obtain the spectrum of soft induced gluon bremsstrahlung as the modulus square of the amplitude averaged over initial and summed over final colors and polarizations. The

result is the coherent analog of asymptotic incoherent Gunion-Bertsch spectrum [143]. The Gunion-Bertsch radiation spectrum Eq. (2.15) is recovered from the GW model in the limit $n = 1$.

The LPM effect in QCD [166, 167] manifests itself in the phase factors of Eq. 2.24. When squared, $|J|^2$ gives rise to n diagonal terms where the phase factors drop out, and $n(n-1)$ off-diagonal terms where the phase factors take the form $\exp\left(ik(x_i - x_j)\right)$. Noticed the similarity between this form and the one in Section 2.2.2, one can immediately retrieve three limits: incoherent, factorization, and LPM. And all of them have been extensively discussed in Section 2.2.2 and 2.2.3.

Denote by L the size of the medium ($L > \lambda$, λ is the mean free path), one can immediately see that interference effects are dominant in the region $\lambda < \tau_f < L$ ($\tau_f = 2\omega/\mathrm{k}_\perp^2$ is the gluon formation time as usual), whereas the incoherent and factorization limits are obtained in the regions $\tau_f < \lambda < L$ and $\lambda < L < \tau_f$ respectively.

2.2.6 DGLV opacity expansion

To establish a pQCD model for calculating medium-induced gluon radiation spectra, besides the kinematic approximations discussed in Section 2.2.5, more assumptions about the QGP are generally required. Among them are the "thin" and the "thick" plasma approximation, the two identify very different jet-medium scattering limits. The former assumes one or several "hard" scatterings for the jet traversing the QGP, while the latter assumes an infinite number of "soft" scatterings in the medium. There was a simple estimate from [207] shown that, for relevant conditions at RHIC and the LHC, the mean number of collisions in the medium, the opacity $\bar{N} = L/\lambda$, is moderate, i.e. $\bar{N} < 10$. Therefore, it is necessary to develop a vastly different approach from multiple soft scattering (MSS) models to handle this realistic "mesoscopic" problem. The problem has been

successfully solved by the GLV opacity expansion theory [170, 206, 207]. This approach was later generalized to DGLV [170] to include finite masses of quarks and effective gluon masses.

Built upon the foundation of the Gyulassy-Wang model introduced in the previous section, the GLV opacity expansion theory includes various interference effects between or among: (1) vacuum radiation; (2) vertex radiations; and (3) gluon rescatterings (quantum cascade). The model is formulated as a series expansion in opacity L/λ, and it provides an expression of the all-order result in closed form as a sum of integrals. At first order in opacity, the DGLV integral can be evaluated analytically; at higher orders, the full integral can only be evaluated numerically, which is performed through order-by-order iterations.

Fig. 2.2 illustrates a typical diagram involved in deriving the opacity series. In this figure, $M_{n_s,m,l}$ denotes the amplitude that involves n_s scattering centers, the gluon is emitted between site z_m and z_{m+1}. The jet-medium scattering pattern is encoded in $l \equiv \sum_{i=1}^{n_s} \sigma_i 2^{i-m-1}$, where $\sigma_i = 1$ if a gluon rescattering occurs at site z_i and $\sigma_i = 0$ otherwise.

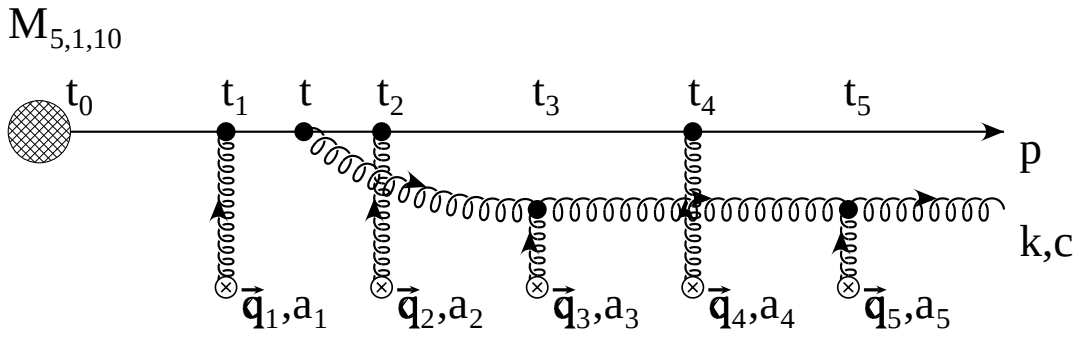

Figure 2.2: *An amplitude contributing to fifth (and higher) orders in opacity in the GLV opacity expansion of radiative energy loss. The crosses denote the Debye-screened Yukawa interactions and the blob at t_0 is the initial hard jet amplitude. (Taken from [206].)*

However, in order to preserve unitarity, in addition to the single Born scattering

("direct") diagrams as shown in Fig. 2.2, one also needs to include double Born ("virtual") diagrams [183] that are composed of contact interactions in which $z_{i-1} \to z_i$. Fig. 2.3 is an illustration of the two different type of diagrams.

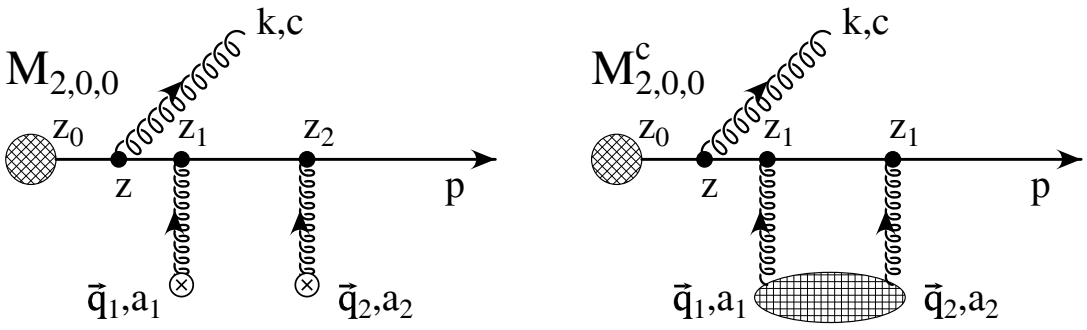

Figure 2.3: *The $M_{2,0,0}$ "direct" diagram that contributes to the second order in opacity, and its contact limit $z_1 = z_2$ ("virtual") diagram, that can contribute to the first order in opacity as well. (Taken from [207].)*

In the GLV theory, the hard probe is assumed to be produced inside the plasma at some finite time at position z_0[5]. The amplitude for this initial hard production and the gluon radiation associated is

$$G_0 = -2ig\frac{\boldsymbol{\epsilon}_\perp \cdot \mathbf{k}_\perp}{\mathrm{k}_\perp^2} e^{i\omega_0 z_0} c\,. \tag{2.26}$$

ϵ^μ and c are the polarization and the color of the radiated gluon respectively. The notation for this process is $G_0 = M_{0,0,0}$. Note that at the first order in opacity, even if there is only one scattering in the medium, one can have interference effects between G_0 and the first hard scattering.

The essence of GLV is to organize diagrams into classes of order n in opacity by defining suitable operators $\hat{D}_m$ or $\hat{V}_m$ that stand for the insertion of a direct or a virtual interaction at a scattering center m with implicit summations over all possible kinds of

[5] As opposed to the Gunion-Bertsch or BDMPS-Z, where the jet is prepared in the remote past.

interactions. Bare this in mind, one can describe the diagram class in a symbolic way,

$$\mathcal{A}_{i_1\cdots i_n} = \prod_{m=1}^{n} \left(\delta_{0,i_m} + \delta_{1,i_m}\hat{D}_m + \delta_{2,i_m}\hat{V}_m\right) G_0 \,, \tag{2.27}$$

where $i_m = 0, 1, 2$ indicates the exact scattering process occurred at site m. Note that diagrams in a given class n have different powers of the coupling α_s, but if one includes a complementary class of diagrams $\bar{\mathcal{A}}$ such that

$$\bar{\mathcal{A}}_{i_1\cdots i_n} = \prod_{m=1}^{n} \left(\delta_{0,i_m}\hat{V}_m + \delta_{1,i_m}\hat{D}_m + \delta_{2,i_m}\right) G_0 \,, \tag{2.28}$$

then one can define a "probability" distribution at n-th order in opacity,

$$P_n = \bar{\mathcal{A}}^{i_1\cdots i_n}\mathcal{A}_{i_1\cdots i_n} \,. \tag{2.29}$$

Every term in Eq. (2.29) contributes with at same order, α_s^{2n+1}. The "1" power of α_s comes from the gluon radiation vertex and the remaining "2n" powers of α_s comes from the n scatterings. It was first proposed in [207] that P_n can constructed recursively from classes of diagrams of lower opacities through the "reaction operator"

$$\hat{R}_m \equiv \hat{D}_m^\dagger\hat{D}_m + \hat{V}_m + \hat{V}_m^\dagger \quad , \tag{2.30}$$

and such that

$$P_n = \bar{\mathcal{A}}^{i_1\cdots i_{n-1}}\hat{R}_n\mathcal{A}_{i_1\cdots i_{n-1}} \,. \tag{2.31}$$

Because of a specific relationship between the operators $\hat{V}_m$ and $\hat{D}_m$, the authors in [207] were able to sum all the probabilities in a closed form recursively. This leads to the final integral form of inclusive gluon radiation spectra at all orders in opacity.

An important extension of the GLV formalism is to include effects of gluon plasmon

masses and finite quark masses. Djordjevic and Gyulassy [211] studied the QCD analog of the Ter-Mikayelian effect in the QGP. This is an effect in which the gluon radiation associated with hard processes is modified by the dielectric properties of the medium. It results in an effective mass for the gluon which regulates infrared divergences. They studied the impacts of this effect on the radiative energy loss, and found that the gluon propagator can be approximated by using a gluon plasmon mass of $m_g = \mu/\sqrt{2}$. In [170] Djordjevic and Gyulassy further calculated the roles of finite quark masses and found that they modify the GLV radiation amplitudes and phase factors in a simple way. The DGLV formula for the double-differential multiplicity distribution of inclusive gluon radiations is thus established:

$$\begin{aligned} x_+\frac{dN_g^{(n)}}{dx_+ d\mathbf{k}_\perp} = \frac{C_R\alpha_s}{\pi^2}\frac{1}{n!}\int\prod_{i=1}^{n}\left(d\mathbf{q}_{\perp i}\frac{L}{\lambda_g(i)}\left[|\bar{v}(\mathbf{q}_{\perp i})|^2-\delta^2(\mathbf{q}_{\perp i})\right]\right) \\ \times\left(-2\,\mathbf{C}_{(1\cdots n)}\cdot\sum_{m=1}^{n}\mathbf{B}_{(m+1\cdots n)(m\cdots n)}\right) \\ \times\left[\cos\left(\sum_{k=2}^{m}\Omega_{(k\cdots n)}\Delta z_k\right)-\cos\left(\sum_{k=1}^{m}\Omega_{(k\cdots n)}\Delta z_k\right)\right]\ . \end{aligned} \tag{2.32}$$

Here $\Delta z_k = z_k - z_{k-1}$ represents the distance between the scattering points z_k and z_{k-1} (z_0 is the position of the production vertex). C_R is the quadratic Casimir of the jet: for quark jets, $C_F = 4/3$; for gluon jets, $C_A = 3$. The strong coupling constant is $\alpha_s = g^2/4\pi$. The "cascade" (related to the rescattering of the radiated gluon), "Hard" (related to initial hard amplitude Eq. (2.26)) and "Gunion-Bertsch" (related to the incoherent gluon

radiation Eq. (2.13)) terms are:

$$\begin{aligned}
\mathbf{C}_{(1\cdots n)} &= \frac{\mathbf{k}_\perp - \mathbf{q}_{\perp 1} - \cdots - \mathbf{q}_{\perp n}}{(\mathbf{k}_\perp - \mathbf{q}_{\perp 1} - \cdots - \mathbf{q}_{\perp n}) + \chi^2} \ , \\
\mathbf{H} &= \frac{\mathbf{k}_\perp}{\mathbf{k}_\perp^2 + \chi^2} \ , \\
\mathbf{B}_{(i)} &= \mathbf{H} - \mathbf{C}_{(i)} \ , \\
\mathbf{B}_{(1\cdots m)(1\cdots n)} &= \mathbf{C}_{(1\cdots m)} - \mathbf{C}_{(1\cdots n)} \ .
\end{aligned} \tag{2.33}$$

Implicitly, $\sum_2^1 \equiv 0$ and $\mathbf{B}_{(n+1\cdots n)(n)} \equiv \mathbf{B}_{(n)}$. The inverse formation time Ω is given by

$$\Omega_{(m\cdots n)} = \frac{(\mathbf{k} - \mathbf{q}_{\perp m} - \cdots - \mathbf{q}_{\perp n}) + \chi^2}{2x_+ E} \ . \tag{2.34}$$

It controls the LPM destructive interferences[6]. Note that in the soft eikonal kinematics (c.f. Section 2.2.5) where DGLV is derived, the 4-momentum for the incoming jet (p), the radiated gluon (k) and the exchanged gluon (q) are

$$\begin{aligned}
p &= (E, E, 0) = [2E, 0, 0] \ , \\
k &= (\omega = x_E E, \sqrt{(x_E E)^2 - \mathbf{k}_\perp^2}, \mathbf{k}_\perp) = [x_+ E^+, \tfrac{\mathbf{k}_\perp^2}{x_+ E^+}, \mathbf{k}_\perp] \ , \\
q &= (q_0, q_z, \mathbf{q}_\perp) \ .
\end{aligned} \tag{2.35}$$

Here parenthesis and square brackets denote Minkowski and light-cone coordinates respectively. The radiated gluon's fractional energy $x_E \equiv \omega/E$ and fractional plus-momentum $x_+ \equiv k^+/E^+$ are connected via $x_+ = x_E[1 + \sqrt{1 - (\mathrm{k}_\perp/x_E E)^2}]/2$. Note that in Eq. (2.33) and (2.34), $\chi^2 = M^2 x_+^2 + m_g^2(1 - x_+)$, it encodes the effect of the finite quark mass M and gluon plasmon mass $m_g = \mu/\sqrt{2}$.

Note that in Eq. (2.32) the opacity is written in terms of the gluon mean free path λ_g rather than the jet mean free path. This simplification comes from the color algebra

[6] $\Omega \cdot \Delta z$ is the LPM phase factor.

known as "color triviality" [207]. It comes as follows: in Eq. (2.32), $\bar{v}(\mathbf{q}_{\perp i})$ is the normalized, static, color-screened Yukawa potential from the GW model (c.f. Section 2.2.5), $\int d\mathbf{q}_{\perp i}|\bar{v}(\mathbf{q}_{\perp i})|^2 = 1$. One has

$$|\bar{v}(\mathbf{q}_{\perp i})|^2 = \frac{\mu^2}{\pi(\mathbf{q}_{\perp i}^2 + \mu^2)^2} \quad . \tag{2.36}$$

Therefore, at each order in opacity there is a multiplying factor of $\sigma_{\rm el}$, and one may expect to get a complicated combination of jet and radiated gluon elastic cross-sections in the final sum. However, as shown in [207], after summing all direct and virtual diagrams and consider $C_R\sigma_g = C_A\sigma_{\rm el}$ (c.f. Eq. (2.20)), one gets a simple factor of $C_A C_2(T)/d_A$ at each order in opacity. This implies that in the DGLV formula, the opacity is determined by $N\sigma_g/A_\perp$, where N is the number of scattering centers in the medium and $A_\perp$ is the transverse area of the medium (perpendicular to the jet propagating direction z). Note that $N = \rho \cdot A_\perp \cdot L$ and $\rho\sigma_g = 1/\lambda_g$, where ρ is the number density of thermal quanta and L is the jet path length along z, the opacity hence becomes L/λ_g. In general, gluon elastic cross sections can vary along the jet path, therefore $\lambda_g(i)$ appears in Eq. (2.32).

Notice also in Eq. (2.32) that a forward scattering probability $\delta^2(\mathbf{q}_{\perp i})$ is subtracted to ensure unitarity; the $1/n!$ factor acts to avoid double-countings in permutations of the n scatterings; and the $\left(\mathbf{C}_{(1\cdots n)} \cdot \sum_{m=1}^{n} \mathbf{B}_{(m+1\cdots n)(m\cdots n)}\right)$ term is generally referred to as the "color antenna".

The total energy ΔE carried away by the emitted gluons is obtained by integrating the radiation spectrum Eq. (2.32). Assume no further jet-medium interactions, this can be interpreted as the energy loss that the jet experiences as it propagates through a hot deconfined plasma:

$$\frac{\Delta E}{E} = \int dx_+ \int d\mathbf{k}_\perp \; x_+ \frac{dN_g^{(1)+\cdots+(n)}}{dx_+ d\mathbf{k}_\perp} \quad . \tag{2.37}$$

At first order in opacity ($n = 1$), assuming no kinematic bounds on $\mathbf{q}_\perp$ and $\mathbf{k}_\perp$ and the parton is massless, one gets an asymptotic result

$$\Delta E^{(1)} = \frac{C_R \alpha_s}{4} \frac{L^2 \mu^2}{\lambda_g} \log \frac{E}{\mu} \quad . \tag{2.38}$$

The quadratic dependence of the energy loss on the size of the medium L is a characteristic of the LPM regime ($\Delta E \propto L^2$), this is different from the linear L dependence in the incoherent limit ($\Delta E \propto L$), i.e. Eq. (2.15). One can tell that when E is large, $\Delta E^{(1)}$ is a subleading effect compared to the vacuum radiation $\Delta E^{(0)}$, i.e. Eq. (2.8). This expression is directly compared with the BDMPS-Z result [175]:

$$\Delta E_{\text{BDMPS}} = \frac{C_R \alpha_s}{8} \frac{L^2 \mu^2}{\lambda_g} \log \left(\frac{L}{\lambda_g} \right) . \tag{2.39}$$

Both demonstrate a quadratic dependence of the energy loss on L.

Compare Eq. (2.6) with Eq. (2.38), one sees that the collisional energy loss is suppressed by one power of α_s with respect to the radiative one[7], therefore radiative energy loss generally dominates. However, for heavy quarks, because of the dead cone suppression Eq. (2.9), the collisional energy loss will play a significant role. More careful treatments of this issue led the authors in [164] to go beyond the assumption of static color scattering centers. This will be discussed in the next chapter.

Moreover, in setting up the DGLV framework, only leading-oder (LO) diagrams are considered (one external gluon line). Treating the induced gluon radiation as a stochastic process, multiple gluon emissions are generally taken into account incoherently, and they are assumed to be distributed following a Poisson ansatz [212, 213]. This will be discussed in the next section.

[7] Some physical estimations give $dE_{\text{el}}/dL \sim \mathcal{O}(2\,\text{GeV/fm})$ and $dE_{\text{rad}}/dL \sim \mathcal{O}(10\,\text{GeV/fm})$ [207].

2.3 Developments of DGLV

Several crucial improvements over the DGLV theory have been made in the past decade to address critical phenomenological issues and to make the the framework more powerful in predicting jet quenching observables in relativistic heavy-ion collisions at RHIC and the LHC. In this section, effects of multiple gluon emissions, the finite opacity, path length fluctuations, the dynamical QCD medium, and running coupling will be discussed.

2.3.1 Multiple gluon emission

Generally speaking, there will be more than one gluon emitted in the jet-medium interaction process. To account for the multiple gluon emission effect, authors in [212, 213] proposed that, a simple procedure can be implemented by the opacity expansion model: incoherently add up the emissions assuming the number of radiated gluons follows a Poisson distribution:

$$\mathcal{P}(N = N_g) = \frac{\langle N_g \rangle^{N_g}}{N_g!} \mathrm{e}^{-\langle N_g \rangle} \quad . \tag{2.40}$$

In practice, this is carried out as follows: the mean number of radiated gluons $\langle N_g \rangle$ is given by the integral of the gluon radiation spectrum $\langle N_g \rangle = \int dx \frac{dN_g}{dx}(x)$. Since the gluon radiation can be treated as a stochastic process, and it is applicable to assume a probability distribution $P(\epsilon)$ for a jet to lose a fraction $\epsilon \equiv \Delta E/E$ of its energy in the QGP, assume zero jet mass, then

$$P(\epsilon) = P^{null}\delta(\epsilon) + \sum_{n=1}^{\infty} P_n(\epsilon) + P^{full}\delta(\epsilon - 1) \quad . \tag{2.41}$$

This probability distribution is split in three parts: the first term corresponds to the probability of zero radiation, $P^{null} \equiv P_0 = \mathrm{e}^{-\langle N_g \rangle}$. Terms in the summation in Eq. (2.41)

are given by

$$\begin{aligned} P_1(\epsilon) &= P_0 \frac{dN_g}{dx}(x=\epsilon) \ , \\ P_{n+1}(\epsilon) &= \frac{1}{n+1}\int_0^1 dx_n P_n(\epsilon - x_n)\frac{dN_g}{dx}(x=x_n) \ . \end{aligned} \tag{2.42}$$

The last term represents the probability of total quenching. In the soft limit, the radiated gluon energy ω is much smaller than the initial jet energy E, hence $x \ll 1$. Consequently, the energy of the outgoing parton E' is approximately equal to the incoming parton E. When x_n's are integrated up to the kinematic limit $x_n = 1$, a leakage error coming from the unphysical region $P(\epsilon > 1) \neq 0$ appears, and it is absorbed into $P^{full} = \int_1^\infty d\epsilon \, P(\epsilon)$.

As an illustration, Fig. 2.4 demonstrates the radiative energy loss probability distribution for single and multiple gluon emissions in the WHDG model [212]. The left panel shows is the single radiation case and the red curve in right panel is the result with multiple gluon emissions included according to Eq. (2.41). The two have very different shape,

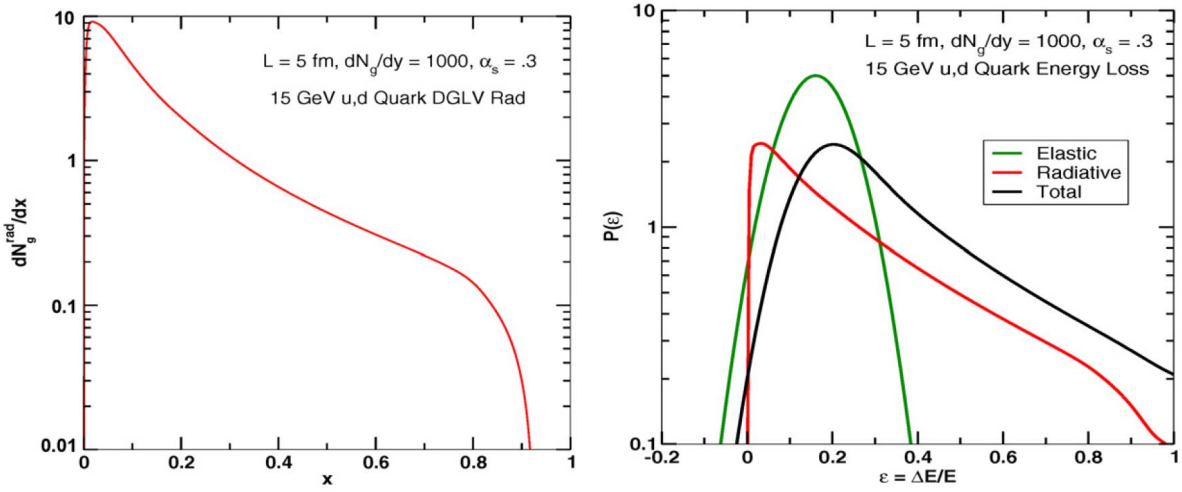

Figure 2.4: *Left: the single gluon radiation radiation spectrum. It is equivalent to the energy loss probability distribution with one gluon emitted, except for proper normalizations. Right: (red curve) the radiative energy loss distribution assuming a Poisson probability for multiple gluon emissions. Note its distinctive shape from the single emission case, and the different tail behavior at large x or (ϵ). (Taken from [212].)*

and the tail behaviors are distinguishable at large x (or (ϵ)). Multiple gluon emissions

boost the probability for larger energy loss, as intuitively expected.

The radiative energy loss distribution Eq. (2.41) will be slightly modified in the finite mass limit, this issue together with the fast Fourier transform techniques for getting the resulting distribution and the elastic energy loss fluctuations will be discussed in the next chapter.

2.3.2 Finite opacity

To interpolate between the "thin" (opacity order $n = 1$) and "thick" ($n = \infty$) plasma limit and solve the "mesoscopic" problem is one of the most important motivations that led to the development of the full DGLV opacity series. The "thin" plasma approximation assumes one single hard scattering and the"thick" plasma approximation assumes an infinite number of soft scatterings in the medium.

The BDMPS/ASW model [175, 176, 179, 180, 186] studied the induced gluon radiation spectrum in the multiple soft scattering (MSS) limit, i.e. under the "thick" plasma approximation. Assuming the length of the medium L is much larger than the mean free path λ, the incoming parton is expected to perform a Gaussian diffusion in the transverse momentum space. In this model, the jet transport coefficient $\hat{q}$ determines the medium effects on the jet, and is in analogy to μ^2/λ in the DGLV framework.

One will see that there are several problems in the MSS limit of BDMPS/ASW. Neglect the kinematic bounds on the gluon transverse momentum $\mathrm{k}_\perp$ and integrate it out, the BDMPS formula predicts a scaling behavior of the induced x-spectrum with $\hat{q}$ via the variable z:

$$\omega \frac{d}{d\omega}(I - I_{\mathrm{vac}}) = \frac{\alpha_s}{\pi} x P_{p\to p+g}(x) \ln \left| \cos\left(\sqrt{-iz}\right) \right| , \tag{2.43}$$

where the energy of the gluon is $\omega = xE$ and $P_{p\to p+g}(x)$ is the splitting function. The z

is defined as:

$$z \equiv \left|\omega_0^2\right| L^2, \quad \omega_0^2 \equiv -i\frac{\left[(1-x)C_A + x^2 C_s\right]\hat{q}}{2x(1-x)E}\,. \tag{2.44}$$

For small x, one has $z \sim (\mu^2 L^2)/(\lambda x E) \sim L/\tau_f$. As shown in [214], one can make a Taylor expansion of the BDMPS formula in z, and it can be interpreted as an opacity series:

$$\ln\left|\cos\left(\sqrt{-iz}\right)\right| = \frac{1}{12}z^2 - \frac{17}{2520}z^4 + \frac{691}{935550}z^6 - \ldots\,. \tag{2.45}$$

However, it was shown in [214] that the z scaling behavior of the spectrum is violated up to 100%. This scaling violation indicates that the gluon radiation spectrum at intermediate opacity depends on both the screening mass μ and mean free path λ, rather than only the ratio $\mu^2/\lambda \sim \hat{q}$. Moreover, in the Taylor expansion Eq. (2.45)[8], the first order in opacity contribution is missing, i.e. there is no term $\propto z$; for comparison, the first hard scattering in the GLV opacity series is the dominant contribution.

Furthermore, calculations reported in [185] which include the kinematic limits neglected in Eq. (2.43), showed that the BDMPS/ASW approach can fit the experimental data only by using a enormous $\hat{q}$ value that is too much larger than the expected $\hat{q} \sim \mu^2/\lambda$. As will be presented later, the GLV solution without the MSS approximation can fit the data with much more physical opacity parameters. To better understand the differences between DGLV and BDMPS/ASW, one can compare the radiated gluon $\mathrm{k}_\perp$-distribution from DGLV at various orders in opacity and from BDMPS/ASW in the MSS limit [187]. Fig. 2.5 shows such a comparison for a heavy quark jet with initial energy 20 GeV. Here one sees how the finite opacity DGLV successfully interpolates between the thin ($n = 1$) and thick ($n = \infty$) plasma approximations.

In general, one expect that at when $\mathrm{k}_\perp$ is small, the gluon distribution is better approximated by the Gaussian diffusion of the BDMPS/ASW in the MSS limit; on the

[8] Curiously, it has only even powers and alternating signs.

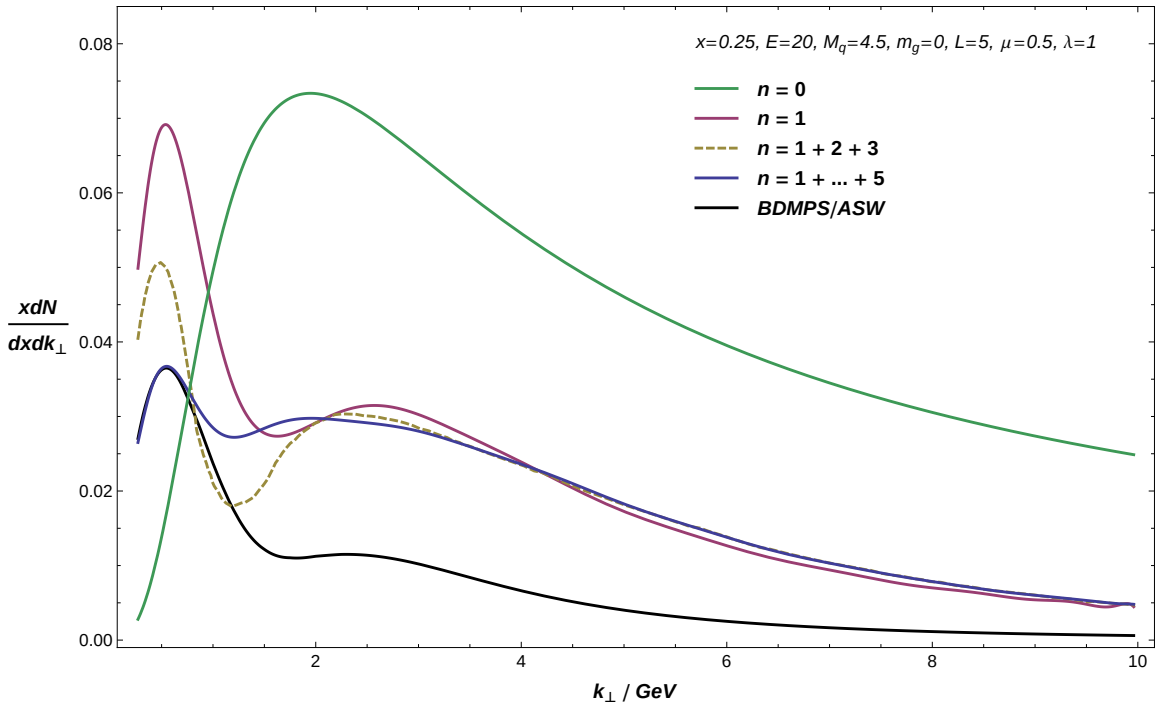

Figure 2.5: *The radiated gluon spectrum as a function of* $\mathrm{k}_\perp$ *for a heavy quark jet of energy 20 GeV, compared to the BDMPS/ASW limit. Colored curves are the DGLV results at various orders in opacity (in particular, red is the "thin plasma" approximation), and the black curve is the ASW distribution in the MSS limit (the "thick plasma" approximation). (Taken from [168], c.f. also [215, 216].)*

other hand, one can clearly see in Fig. 2.5 that the DGLV opacity series with $n = 5$ has converged to this limit. However, when $\mathrm{k}_\perp$ is large, DGLV should better describe the expected hard power-law tail. In Fig. 2.5 one does see the DGLV spectrum is harder at high $k_\perp$ than the MSS limit. This suggests that the missing of the first order in opacity term in BDMPS/ASW causes an unphysical softening of the spectrum for less collinear gluons, and the inclusion of the first hard scattering in pQCD energy loss models is indeed crucial.

In this figure one can also see that the dead cone effect at $n = 0$, i.e. a low multiplicity for small $\mathrm{k}_\perp$ (collinearly emitted) gluons, c.f. Eq. (2.9), and how this dead cone is "filled" at first order in opacity by the medium-induced gluon radiation. At intermediate to large

$k_\perp$, the DGLV series at all orders in opacity show a good convergence. One can thus imagine that as the gluon fraction energy x decreases, the curves with different opacity orders will converge at an even lower $k_\perp$. This suggests in practice one can compute the energy loss to the first order in opacity ($n = 1$), and the final approximate result will contain only very limited systematic errors compared to the exact result from computing the opacity series to infinite order, detailed discussions regarding this issue can be found in [158].

2.3.3 Path length fluctuations

Up to this point all the energy loss frameworks introduced assume a fixed path length L for jets in the QGP. Apparently this is not a realistic condition, and it may limit the prediction power for the pQCD model. Therefore, the roles of geometric fluctuations in the computation of parton energy loss must be studied more carefully.

In the Wicks-Horowitz-Djordjevic-Gyulassy (WHDG) model [212], the effects of these fluctuations have been systematically investigated within the DGLV framework. There, geometric path length fluctuations are accounted for as follows: the total energy loss probability is

$$P(E_i \to E_i - \Delta_{\rm rad} - \Delta_{\rm el}) = \int \frac{d\phi}{2\pi} \int \frac{d^2\vec{x}_\perp}{N_{\rm bin}(b)} T_{AA}(\vec{x}_\perp, \vec{b}) \otimes P_{\rm rad}(\Delta_{\rm rad}; L(\vec{x}_\perp, \phi)) \otimes P_{\rm el}(\Delta_{\rm el}; L(\vec{x}_\perp, \phi)) \quad . \tag{2.46}$$

And $L(\vec{x}_\perp, \phi)$ is the locally determined effective path length of the jet given its initial production point $\vec{x}_\perp$ in the transverse plane (relative to the beam axis)and its initial azimuthal direction ϕ relative to the reaction plane. $L(\vec{x}_\perp, \phi)$ is given by

$$L(\vec{x}_\perp, \phi) = \int d\tau \rho_p(\vec{x}_\perp + \tau\hat{n}(\phi)) / \langle \rho_p \rangle \quad . \tag{2.47}$$

The participant transverse density $\rho_p(\vec{x}_\perp)$ is constructed from thickness functions in the Glauber model with diffuse Woods-Saxon nuclear density profiles [212][9]. The left panel of Fig. 2.6 shows the transverse coordinate $(x, 0)$ distribution of surviving jets moving in $+x$ direction.

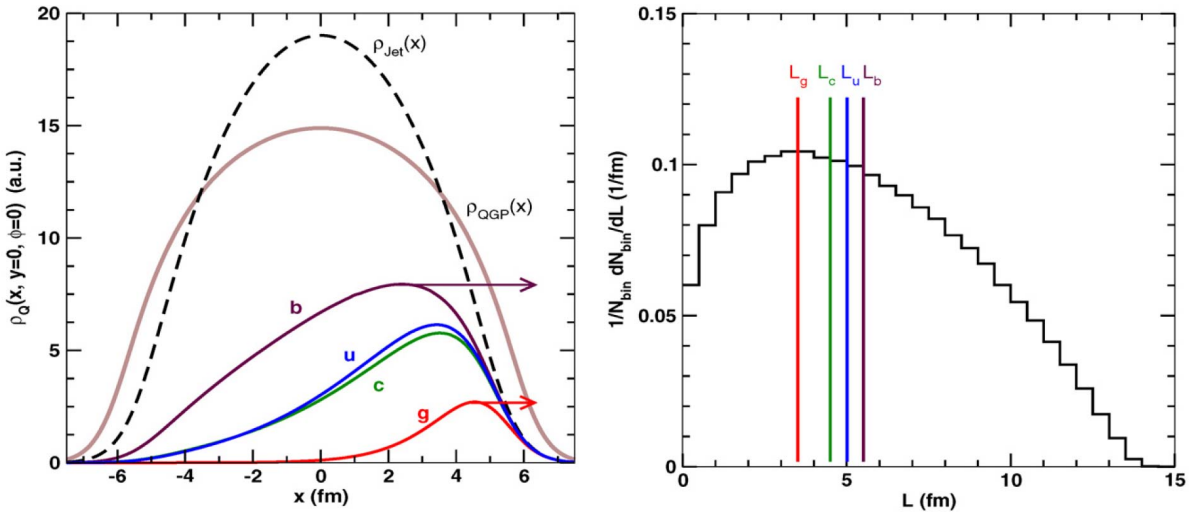

Figure 2.6: *Left: The transverse coordinate* $(x, 0)$ *distribution of surviving* $p_T = 15$ *GeV,* $Q = g,u,c,b$ *jets moving in direction* $\phi = 0$ *as indicated by the arrows. Right: Distribution of path lengths traversed by hard scatterers in 0-5% most central collisions. The lengths* $L(\vec{x}_\perp, \phi)$ *are weighted by the probability of production and averaged over azimuth. Color lines are the single, representative path lengths,* L_Q*. (Taken from [212].)*

A first observation is that the surviving gluon jets are distributed closer to the edge than the quark jets. And for surviving quark jets, if ordered by the distance from the edge, with longer ones come first, the sequence is then: bottom, up, charm[10]. This is a clear indication that due to different energy loss probabilities, different flavor jets have different effective path lengths in the QGP. This hierarchy is reinforced by the color lines

[9]In principle, on an event-by-event basis, the local density has large fluctuations. As a simplification, event-averaged, smooth profiles are usually embedded. This will bring very limited uncertainties to energy loss studies, c.f. e.g. [217, 218].

[10]Note that the u quark energy loss falls between b and c, which contradicts the naive b, c, u ordering. This breaking of the mass hierarchy originates from complicated interplays between the color antenna Eq. (2.33), the LPM effect Eq. (2.34), and the elastic energy loss Eq. (2.6).

in the right panel of Fig. 2.6.

Furthermore, for a given flavor, telling from the left panel of Fig. 2.6, the distribution of survived jets deviates significantly from the distribution of initial jet productions. This is strong evidence that there is a non-trivial distribution of effective jet path lengths in computing gluon radiation spectra. It comes from the complicated interplays among the distribution of initial binary collisions, thermal quanta, and energy loss probabilities. Indeed, this distribution is extracted from DGLV and plotted as a black curve in the right panel of Fig. 2.6.[11]

All the above results show that there are strong path length fluctuations in heavy-ion collisions, and they must be treated with care. This topic will be discussed further in the next chapter.

2.3.4 Dynamical QCD medium

As proposed by Djordjevic in [164]: "The computation of radiative energy loss in a dynamically screened QCD medium is a key ingredient for obtaining reliable predictions for jet quenching in ultra-relativistic heavy ion collisions. [...] The currently available studies suffer from one crucial drawback: the medium induced radiative energy loss is computed in a QCD medium consisting of randomly distributed but static scattering centers (static QCD medium). In such a medium the collisional energy loss is exactly zero. [...] Recent calculations showed that the collisional contribution is important and comparable to the radiative energy loss. The static approximation is thus qualitatively wrong as far as the computation of collisional energy loss is concerned and should therefore also be revisited in the context of radiative energy loss."

To include the effects of the dynamical medium into the parton energy loss theory, di-

[11] The distribution $1/N_{\rm bin}dN_{\rm bin}/dL$ in the right panel of Fig. 2.6 is a purely geometric quantity, it is the same for all jet varieties. In WHDG [212], the partonic nuclear modification $R_Q = \int dL(1/N_{\rm bin}dN_{\rm bin}/dL)\int d\epsilon(1-\epsilon)^n P_Q(\epsilon;L)$.

agrams in the finite temperature QCD framework must be calculated, with Hard Thermal Loop resummed propagators [200–205] for all gluons. Details of relevant computations can be found in the original papers [164, 219, 220], in one word, these dynamical effects result in a change in the mean free path λ and the effective parton-medium interaction potential $\pi|\bar{v}(\mathbf{q}_\perp)|^2$ in Eq. (2.32):

$$\begin{aligned} \lambda_{stat} &\Longrightarrow \lambda_{dyn} \quad , \\ \left[\frac{\mu^2}{(\mathbf{q}_\perp^2+\mu^2)^2}\right]_{stat} &\Longrightarrow \left[\frac{\mu^2}{\mathbf{q}_\perp^2(\mathbf{q}_\perp^2+\mu^2)}\right]_{dyn} \quad . \end{aligned} \tag{2.48}$$

And the effective dynamical mean free path λ_{dyn} is given by $\lambda_{dyn}^{-1} \equiv 3\alpha_s T$. It is related to its static counterpart via $\lambda_{dyn} = c(N_f)\lambda_{stat}$. Here $c(N_f) = 6\frac{1.202}{\pi^2}\frac{1+N_f/4}{1+N_f/6}$ [164, 219], it varies between $c(0) \approx 0.73$ and $c(\infty) = 1.09$. For a typical value $N_f = 2.5$, $c(2.5) \approx 0.84 \sim 1$.

As noted in the original paper [219], the combined effect of an enhanced cross section and a reduced mean free path leads to a significant increase in parton energy loss within the dynamical framework.

In the DGLV based CUJET1.0 model developed by Buzzatti and Gyulassy [221], an effective scattering potential that interpolates between the static and dynamical limit is included, and gluon radiation spectra are computed at first order in opacity. The rest of this section will concentrate on discussing the physical impacts of the dynamical QCD medium on the jet energy loss, based on results from the CUJET1.0 framework [215].

In Fig. 2.7 the comparison between the radiated gluon distribution for a static and a dynamical plasma of temperature $\sim$ 250 MeV within CUJET1.0 is shown. The enhancement of energy loss in the dynamical scenario is significant. Fig. 2.8 further shows the energy loss of the jet as a function of E and L within the CUJET1.0 model. Regardless of the medium being static or dynamical, there is a transition in $\Delta E/E$ from linear to quadratic L dependence as L increases, and there is a similarity between light and charm

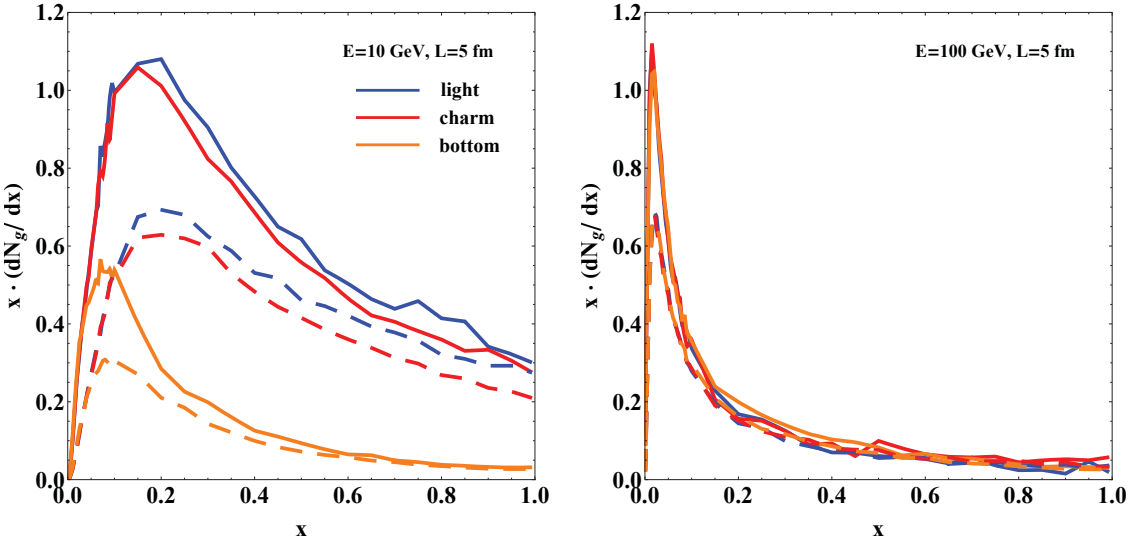

Figure 2.7: *CUJET1.0: Comparison between dynamical (solid) and static (dashed) radiated gluon distribution, computed at first order in opacity. The initial jet energy is* 10 *GeV (left) or* 100 *GeV (right). One sees that the radiation enhancement is strong, especially for low x gluons. (Taken from [215].)*

quark jets across a broad range of energies and path lengths.

From a first look, the enhancement in gluon radiation spectrum coming from dynamical effects could be equally obtained by the rescaling of the effective coupling α_s. However in [219] it has been suggested that the energy loss is enhanced in a flavor dependent way. The CUJET1.0 results on the ratio of light to bottom quark energy loss are shown in Fig. 2.9. Quantitatively speaking, if the suppression of light quark jets is enhanced by 100% in the dynamical medium compared with static one, then for heavy quark jets, this magnitude is $\sim$ 110%. This 10% difference is modest, but it plays an indispensable role in solving the so-called "heavy quark energy loss puzzle" at RHIC. Details about this will be discussed in the next chapter.

In Section 2.3.2, one sees that the first order approximation to the GLV opacity expansion is sufficient for computing inclusive gluon radiation spectra. In the presence of

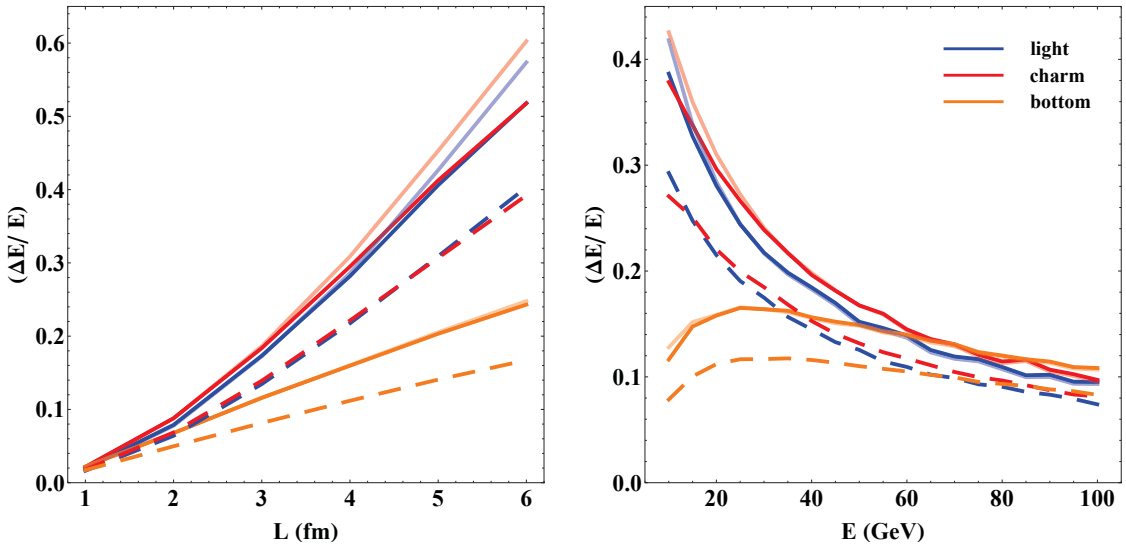

Figure 2.8: *CUJET1.0: The energy loss $\Delta E/E$ for light, charm and bottom quark jets, computed in the dynamical framework at first order in opacity, including fluctuation effects (solid lines). Opaque curves represent the same dynamical computation without fluctuation effects. Dashed curves represent the static DGLV results. Left: $E = 20$ GeV; Right: $L = 4$ fm. (Taken from [215].)*

dynamical medium effects, it is interesting to explore the convergence of the opacity series and see whether or not the first order approximation is still valid. To achieve this goal, in [222], a hybrid interaction potential is introduced

$$|\bar{v}(\mathbf{q}_\perp)|^2 = \frac{\mathcal{N}}{\pi} \frac{\mu_E^2}{(\mathbf{q}_\perp^2 + \mu_E^2)(\mathbf{q}_\perp^2 + \mu_M^2)} \quad , \tag{2.49}$$

where $\mu_E = r_m \mu_M$ and $\mathcal{N}$ is a normalization factor.

In Fig. 2.10 (c.f. also [222]), the energy loss ratios $\Delta E_l/\Delta E_b$ for three different r_m values are shown. The DGLV series is computed up to fifth order in opacity. The decrease in r_m diminishes the magnetic screening mass, makes the medium less static, and brings $\Delta E_l/\Delta E_b$ down. This is consistent with the previous conclusion about the dynamical medium effect, i.e. it suppresses heavy quarks relatively more than light ones. Higher

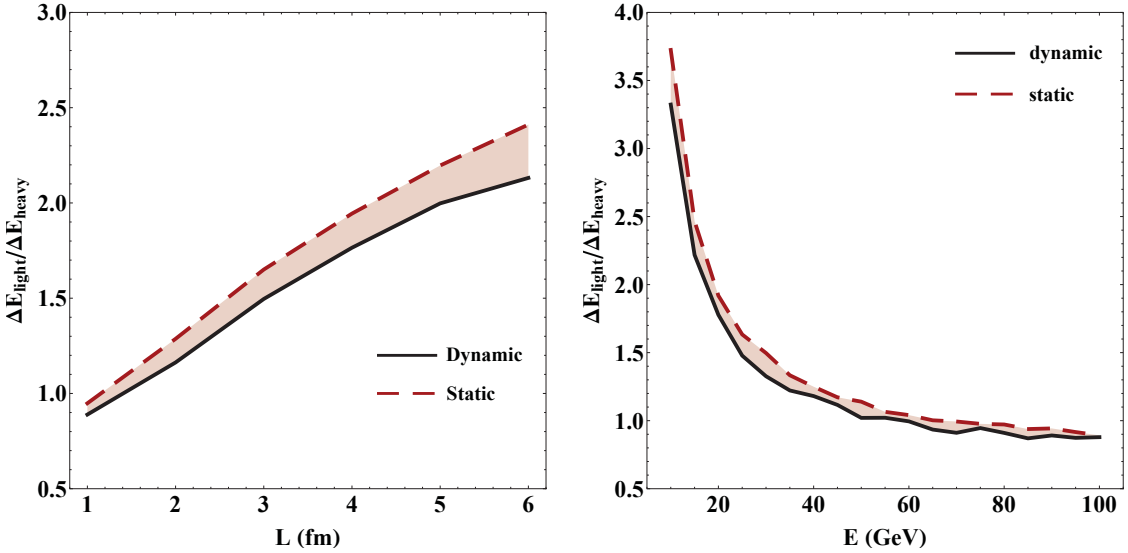

Figure 2.9: *CUJET1.0: Energy loss ratio $\Delta E_{light}/\Delta E_{heavy}$ between light and bottom quarks, for a dynamical (solid) and a static (dashed) potential, including fluctuations. Left: $E = 20$ GeV; Right: $L = 4$ fm. The light to heavy quark energy loss ratio is suppressed in the dynamical scenario for large L and small E, with $\sim 10-15\%$ reduction compared to static DGLV. (Taken from [215].)*

order corrections to the $n = 1$ result are never larger than $\sim 5 - 10\%$. Fig. 2.10 again illustrates that the dynamical medium effect depends in a non-trivial way on the energy and the length of the medium.

2.3.5 Running coupling

The motivation of introducing running strong coupling into computations of inclusive gluon radiation spectra can be inferred from Fig. 2.11. As one can tell from this figure, in a general way, for a fixed coupling pQCD energy loss model, after its parameters have been constrained at RHIC energies, its extrapolation to the LHC energies tends to underestimate the R_{AA}, i.e. the experimentally observed energy loss is less than theoretical calculations. Intuitively, since the LHC is probing more ultraviolet (UV) regime hence

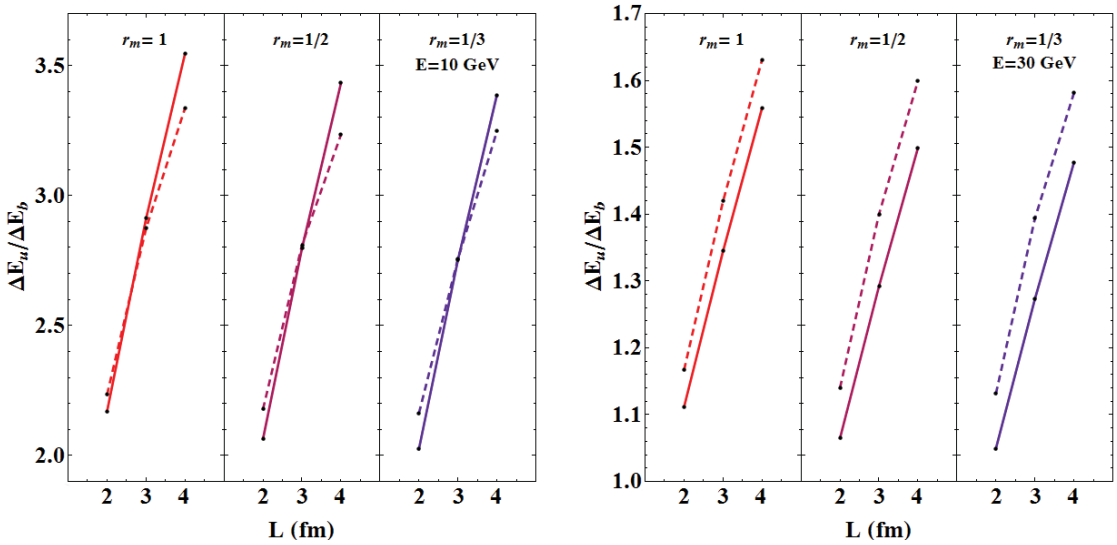

Figure 2.10: *Energy loss ratio between light and bottom quarks as a function of L, for different values of* $\mu_m = \mu_e, \mu_e/2$ and $\mu_e/3$ *(left to right subpanels). Solid lines refer to the* $n = 1$ *approximation, dashed lines show instead computations up to fifth order in opacity. The left figure assumes* $E = 10$ *GeV, the right figure* $E = 30$ *GeV. The variation between* $n = 1$ *and* $n = 5$ *is never bigger than* $\sim 5 - 10\%$*. (Taken from [215])*

smaller length scales, asymptotic freedom of QCD suggests a weaker coupling should appear at TeV heavy-ion collisions compared to the sub-TeV ones.

The problem then becomes how to introduce running coupling effects in a specific energy loss framework. Strictly speaking, for leading-order (LO) pQCD energy loss models on the market, it is necessary to carry out rigorous next-to-leading order (NLO) calculations in order to pin down the exact running scales. In [223], the authors proposed a physically motivated running scheme for the DGLV theory Eq. (2.32) at first order in opacity. Three distinct physical scales $Q_i (i = 1, 2, 3)$ are identified [216]:

1. There are two powers of α_s originating from the jet-medium interaction vertices with the exchanged transverse momentum being $\mathbf{q}_\perp$, and for them one can simply set the scale $Q_1^2 = \mathbf{q}_\perp^2$.

2. There is one power of α_s from the gluon radiation vertex. The off-shellness in the

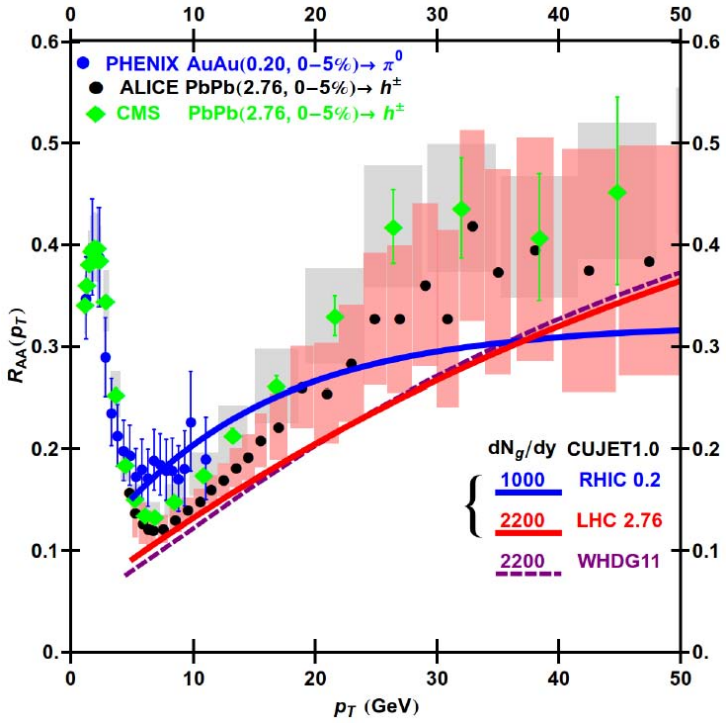

Figure 2.11: *The CUJET1.0/DGLV result of the nuclear modification factor R_{AA} at RHIC and the LHC. After its α_s parameter (fixed coupling strength) has been constrained at RHIC, the CUJET1.0's extrapolation to the LHC underpredicts the experimental R_{AA}. This suggests a necessity for introducing running coupling effects into energy loss computations. (Taken from [221].)*

intermediate quark propagator for the diagram where the gluon is emitted after the scattering is

$$Q_2^2 = q^2 - M^2 = \frac{\mathbf{k}_\perp^2}{x_+(1-x_+)} + \frac{x_+ M^2}{1-x_+} + \frac{m_g^2}{x_+} \quad . \tag{2.50}$$

Here $\mathbf{k}_\perp$ is the transverse momentum of the radiated gluon, M is the mass of the on-shell quark and m_g is the plasmon mass of gluon. An ambiguity may arise from other amplitudes, but in the limit when $\mathrm{k}_\perp \gg \mathrm{q}_\perp$ and mass effects are negligible, their differences are negligible, and the running scale

$$Q_2^2 \approx \frac{\mathbf{k}^2}{x_+(1-x_+)} \quad , \tag{2.51}$$

as in DGLAP radiative splitting.

3. The thermal coupling arises from the Debye mass $\mu(\alpha_s(Q^2);T)$ and the gluon plasmon mass. One thus set the scale for its running as $Q_3^2 = (3T)^2$[12].

In the elastic energy loss sector, one can include running coupling effects following the work of Peigné and Peshier [162]: both powers of α_s in the Bjorken formula for collisional energy loss, i.e. Eq. (2.1), run with $\hat{t}$. When integrating over $d\hat{t}$ in Eq. (2.2), one can obtain

$$\alpha_s^2 \int_{\mu^2}^{6ET} \frac{d\hat{t}}{\hat{t}} \longrightarrow \int_{\mu^2}^{6ET} \frac{d\hat{t}}{\hat{t}} \alpha_s^2(\hat{t}) \ , \tag{2.52}$$

and therefore,

$$\alpha_s^2 \log \frac{6ET}{\mu^2} \longrightarrow \alpha_s(\mu^2)\alpha_s(6ET) \log \frac{6ET}{\mu^2(\alpha_s((3T)^2);T)} \ . \tag{2.53}$$

Here the limits of $\hat{t}$ are $\hat{t}_{\rm MIN} = \mu^2$ and $\hat{t}_{\rm MAX} = 6ET$[13].

One can quantify the running coupling's influences on jet quenching by using a phenomenological a-b-c model by Gyulassy and Horowitz [224], and later Betz and Gyulassy [225]. In these works, a simple power law is assumed for jet energy loss

$$\frac{dE}{dL} = -\kappa E^a L^b T^{2-a+b} \ , \tag{2.54}$$

where dE/dL corresponds to the energy loss per unit length for a massless jet passing though a plasma with local temperature T. The power of T is constrained by simple dimensional analysis, and for fixed coupling, the index a and b can be set by the asymptotic

[12] Thermal quanta in the medium have an average energy $\sim N_f T \sim 3T$.

[13] For a projectile with energy E scattering off a target with energy $3T$, in the center of momentum frame, the total energy is $\sqrt{2 \cdot E \cdot 3T} = \sqrt{6ET}$. And the momentum transfer should be harder than the Debye mass μ for a color-screened interaction potential.

LPM behavior of the GLV model:

$$\Delta E \propto \log(E/T) L^2 T^3 \quad . \tag{2.55}$$

Obviously, from matching the a-b-c model with this limit, the b parameter is fixed to be 1, and in fact this quadratic dependence $\Delta E \propto L^2$ is general for pQCD radiative energy loss models. For the range of energies of interest, one can approximate the $\log(E/T)$ dependence as E^a, with $a \sim 1/3 - 1/4$.

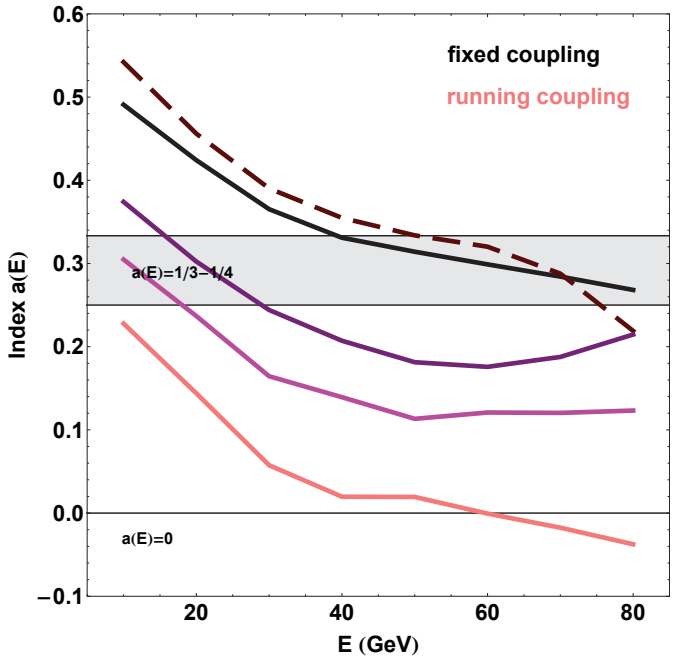

Figure 2.12: *The index $a(E)$ in the a-b-c model extracted from different running coupling schemes. Black: fixed $\alpha_s = 0.3$; Dashed red: thermal running only; Purple: $\alpha_s^2(\mathbf{q}_\perp^2)$ running only; Magenta: $\alpha_s^2(\mathbf{k}_\perp^2/(x_+(1-x_+)))$ running only; Pink: all couplings run. (Taken from [216].)*

In Fig. 2.12 the values of the index a as a function of the jet energy E, for five different cases are shown: α_s fixed, only $\alpha_s(4T^2)$ running, only $\alpha_s^2(\mathbf{q}_\perp^2)$ running, only $\alpha_s(\mathbf{k}_\perp^2/(x(1-x))$ running and finally all couplings run. The results are insightful:

- As expected, the fixed case shows $a \sim 1/3 - 1/4$.
- By introducing the thermal coupling, only the absolute value of the energy loss is affected and the energy dependence of the index remains unaltered. The scale at which the thermal α_s is evaluated is in fact independent of E. Not noticeable in this plot, at very high temperatures the reduced thermal coupling causes a stronger quenching compared to the fixed coupling case, since the smaller Debye mass diminishes the screening in the plasma. This running effect is however small.
- The couplings $\alpha_s^2(\mathbf{q}_\perp^2)$ and $\alpha_s(\mathbf{k}_\perp^2/(x_+(1-x_+))$ significantly reduce the dependence of ΔE on E, and as a consequence the value of the index a gets smaller and closer to 0. The $\alpha_s^2(\mathbf{q}_\perp^2)$ contribution is smaller since the $\mathrm{q}_\perp$ distribution is peaked at small values of $\mathrm{q}_\perp$, as opposed to the $\alpha_s(\mathbf{k}_\perp^2/(x_+(1-x_+))$ contribution which is larger due to the high tails of the $k_\perp$ distribution.
- The all-running case shows almost no dependence of ΔE on E, and $a(E) \approx 0$.

More discussions about the running coupling effect will be carried out in the next chapter. One will see that it is the critical component for explaining the "surprising transparency of the QGP" at the LHC [224].

Chapter 3

Azimuthal jet flavor tomography of QGP

"Tomography refers to imaging by sections or sectioning, through the use of any kind of penetrating wave. The method is used in radiology, archaeology, biology, atmospheric science, geophysics, oceanography, plasma physics, materials science, astrophysics, quantum information, and other sciences. [...] In conventional medical X-ray tomography, [...] make a sectional image through a body by moving an X-ray source and the film in opposite directions during the exposure. Consequently, structures in the focal plane appear sharper, while structures in other planes appear blurred. By modifying the direction and extent of the movement, operators can select different focal planes which contain the structures of interest." (Wikipedia, [226].)

Jet tomography is analogous to X-ray tomography except that in this method: the body of interests is the quark-gluon plasma (QGP); the X-ray is replaced by the jet; and the focal plane is adjusted through observing different transverse momenta (p_T), pseudo-rapidities (η), and azimuthal angles (ϕ) at the detector. It is applied to study the hot deconfined QCD matter in ultra-relativistic nucleus-nucleus collisions at RHIC and the

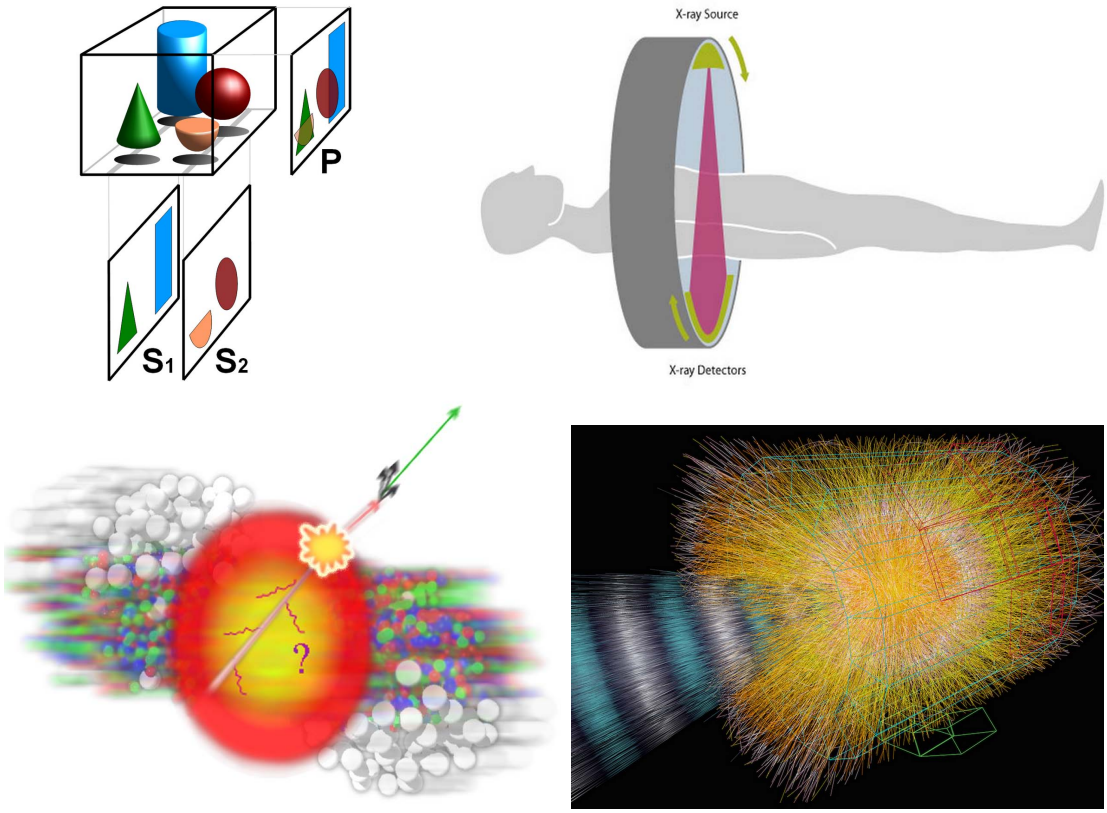

Figure 3.1: *An illustration of tomography (upper left, from [226]), X-ray tomography (upper right, from [227]), jet tomography (lower left, from [228]), ultra-relativistic nucleus-nucleus collision events at the ALICE detector (lower right, from [229]).*

LHC energies. Illustrations of these ideas are shown in Fig. 3.1.

In general, there are two fundamental assumptions in jet tomography: (1) The initial production of hard jets occurs before the formation of the QGP, and the cross section for this process can be reliably predicted through collinear factorized perturbative QCD (pQCD). (2) Thermally equilibrated quarks and gluons have final state interactions, and jet-medium scattering processes can be calculated via pQCD multiple collision theory. Based on these, the depletion or quenching of the initial rates of jet fragments as a function of $(p_T, y, \phi; A, b, \sqrt{s}, M)$[1] can be used to probe the dynamical properties of the

[1] p_T is the transverse momentum, y is the rapidity, ϕ is the azimuthal angle; A is the nuclear mass number, b is the impact parameter, $\sqrt{s}$ is the center of mass energy, M is the particle mass.

QGP at short wavelengths[2].

3.1 The CUJET2.0 model

The CUJET2.0 model [216] is an extension of the pQCD based DGLV opacity expansion theory (c.f. Section 2.2.6) for applications to azimuthal jet flavor tomography of the QGP produced at RHIC and the LHC. Its predecessor CUJET1.0 [215, 221] is a Monte Carlo code that implemented numerically the DGLV opacity series and featured (1) hybrid jet-medium interaction potentials that can interpolate between the pure hard thermal loop (HTL) [200–205] dynamically screened chromo-magnetic and static chromo-electric screening limits; (2) the ability to calculate high order opacity corrections to radiative energy loss up to ninth order; (3) full jet path proper time integrations over diffuse nuclear geometries with Bjorken expansion; (4) inclusions of fluctuating elastic energy loss; (5) the convolution over numerical tables of $\sqrt{s}$ dependent pQCD initial jet production spectra for all flavors; and (6) the convolution over fragmentation functions and semi-leptonic decay distributions.

The critical improvements of CUJET2.0 over the CUJET1.0 model include: (1) multi-scale running strong coupling effects in the DGLV opacity series; and (2) full 2+1D transverse and longitudinal expanding viscous hydrodynamical profiles for the QGP. Applied to heavy-ion phenomenology, the CUJET2.0 model explained the anomalous high quenching of non-photonic electrons (the "heavy quark energy loss puzzle", c.f. Section 3.2.1 in this chapter), and quantitatively described the "surprising transparency of the QGP" at the LHC (c.f. Section 3.2.2 in this chapter). However, as one will see in this chapter, CUJET2.0 poses a "high p_T v_2 puzzle" that applies to all pQCD energy loss models in general. The solution to this puzzle suggests non-trivial interplays between perturbative

[2]The term "azimuthal" in the title of this chapter emphasizes the ϕ dependence, while the term "flavor" emphasizes the M dependence.

and non-perturbative aspects of QCD in jet quenching studies, and it will be further investigated in Chapter 4 and 5.

3.1.1 Dynamical running coupling DGLV

The kernel of CUJET2.0 is the dynamical running coupling DGLV opacity expansion theory [166, 170, 207, 212, 216, 219, 221]. To arrive at it, one should first take into account generic spacetime dependent plasma geometries in Eq. (2.32). Consider a jet created at $\mathbf{x}_{\perp 0} \equiv (x_0,y_0)$ pointing along the azimuthal direction $\hat{\mathbf{n}}_\perp \equiv (\cos\phi, \sin\phi)$ that is transverse to the beam axis z, define

$$\mathbf{z} \equiv \mathbf{x}_{\perp 0} + \hat{\mathbf{n}}_\perp(\phi)\tau = (x_0 + \tau\cos\phi, y_0 + \tau\sin\phi) \tag{3.1}$$

as its transverse coordinates after it has traveled a proper time $\tau \equiv \sqrt{t^2 - z^2}$ at the speed of light[3]. The medium seen by the jet possesses a total quasi-particle number density $\rho(\mathbf{z})$. In a static hot deconfined plasma, the opacity can be expressed as

$$\frac{L}{\lambda_g} \longrightarrow \int_0^L d\tau\ \rho(\mathbf{z})\sigma_g^{el}(\mathbf{z}) \ , \tag{3.2}$$

and at higher orders,

$$\frac{1}{n!}\left(\frac{L}{\lambda_g}\right)^n \longrightarrow \int_0^L d\tau_1\ \rho(\mathbf{z}_1)\sigma_g^{el}(\mathbf{z}_1) \cdots \int_{\tau_{n-1}}^L d\tau_n\ \rho(\mathbf{z}_n)\sigma_g^{el}(\mathbf{z}_n) \ . \tag{3.3}$$

[3]Let (t,z) be the time that the jet parton has traveled in the lab frame and the coordinate of it along the beam axis, define rapidity $y \equiv \frac{1}{2}\ln\frac{t+z}{t-z} = \frac{1}{2}\ln\frac{E+p_z}{E-p_z}$ and proper time $\tau \equiv \sqrt{t^2-z^2}$, then $t = \tau\cosh y$, $z = \tau\sinh y$, and $E = \sqrt{p_T^2+m^2}\cosh y$, $p_z = \sqrt{p_T^2+m^2}\sinh y$. For a particle with 4-velocity u^μ, $u^2 = 1 - v_z^2 - v_T^2$, therefore $v_T = \sqrt{1-v_z^2-u^2} = \frac{\sqrt{t^2-z^2-u^2t^2}}{t}$. If the particle is lightlike, then $u^2 = 0$ and $v_T = \tau/t$, and its transverse coordinate $(x,y) = (v_T t\cos\phi, v_T t\sin\phi) = (\tau\cos\phi, \tau\sin\phi)$. More derivations can be found in [230].

Here L is the jet path length, and the elastic cross section for gluon $\sigma_g^{el}(\mathbf{z})$ can be split into gluon-quark and gluon-gluon terms, i.e.

$$\frac{1}{\lambda_g} = \sigma_g^{el}(\mathbf{z})\rho(\mathbf{z}) = \sigma_{gq}(\mathbf{z})\rho_q(\mathbf{z}) + \sigma_{gg}(\mathbf{z})\rho_g(\mathbf{z}) = \frac{2\pi\ \alpha_s^2}{\mu^2(\mathbf{z})}\rho_q(\mathbf{z}) + \frac{9}{4}\frac{2\pi\ \alpha_s^2}{\mu^2(\mathbf{z})}\rho_g(\mathbf{z}) \quad , \tag{3.4}$$

where

$$\mu^2(\mathbf{z}) = g^2 T(\mathbf{z})^2\,(1 + N_f/6) = 4\pi\alpha_s T(\mathbf{z})^2\,(1 + N_f/6) \tag{3.5}$$

is the squared HTL chromo-electric Debye screening mass in an N_f flavor QGP [200, 203]. In Stefan-Boltzmann limit, the QGP is a non-interacting ideal gas, from Bose-Einstein/Fermi-Dirac statistics, one can obtain the local number density of quark $\rho_q(\mathbf{z})$ and gluon $\rho_g(\mathbf{z})$, i.e.

$$\begin{aligned} \rho_q(\mathbf{z}) &= (9N_f)\cdot\frac{\zeta(3)}{\pi^2}T^3(\mathbf{z}) \quad , \\ \rho_g(\mathbf{z}) &= (16)\cdot\frac{\zeta(3)}{\pi^2}T^3(\mathbf{z}) \quad . \end{aligned} \tag{3.6}$$

Combining Eq. (3.4) and (3.6), noted that $\rho(\mathbf{z}) \equiv \rho_q(\mathbf{z}) + \rho_g(\mathbf{z})$, one gets

$$\frac{1}{\lambda_g} = 18\frac{\pi\ \alpha_s^2}{\mu^2(\mathbf{z})}\frac{4+N_f}{16+9N_f}\rho(\mathbf{z}) = 3\alpha_s\ T(\mathbf{z})\left(6\frac{\zeta(3)}{\pi^2}\frac{1+N_f/4}{1+N_f/6}\right) \quad . \tag{3.7}$$

Combined the wisdom of the dynamical QCD medium effects in Section 2.3.4 Eq. (2.49) and the multi-scale running coupling in Section 2.3.5, plug Eq. (2.49) into Eq. (2.32) and take $n = 1$, one can arrive at the inclusive gluon radiation spectrum at the first order in

opacity in dynamical running coupling DGLV opacity expansion theory [216, 231–233]:

$$
\begin{aligned}
x_E \frac{dN_g^{(1)}}{dx_E} &= \frac{18C_R}{\pi^2}\frac{4+N_f}{16+9N_f}\int d\tau\ \rho(\mathbf{z})\Gamma(\mathbf{z})\ \int d^2k_\perp \\
&\times\ \alpha_s\Big(\frac{\mathbf{k}_\perp^2}{x_+(1-x_+)}\Big)\ \int d^2q_\perp \frac{f_E^2\alpha_s^2(\mathbf{q}_\perp^2)}{(\mathbf{q}_\perp^2+f_E^2\mu^2(\mathbf{z}))(\mathbf{q}_\perp^2+f_M^2\mu^2(\mathbf{z}))} \\
&\times\ \frac{-2(\mathbf{k}_\perp-\mathbf{q}_\perp)}{(\mathbf{k}_\perp-\mathbf{q}_\perp)^2+\chi^2(\mathbf{z})}\left[\frac{\mathbf{k}_\perp}{\mathbf{k}_\perp^2+\chi^2(\mathbf{z})}-\frac{(\mathbf{k}_\perp-\mathbf{q}_\perp)}{(\mathbf{k}_\perp-\mathbf{q}_\perp)^2+\chi^2(\mathbf{z})}\right] \\
&\times\ \left[1-\cos\left(\frac{(\mathbf{k}_\perp-\mathbf{q}_\perp)^2+\chi^2(\mathbf{z})}{2x_+E}\tau\right)\right]\left(\frac{x_E}{x_+}\right)\left|\frac{dx_+}{dx_E}\right| \quad . \qquad (3.8)
\end{aligned}
$$

Here the (f_E, f_M) are HTL chromo-electric and chromo-magnetic deformation parameters that interpolate between the static $(1,1)$ and dynamical $(1,0)$ limit. $C_R = 4/3$ or 3 is the quadratic Casimir of the quark or gluon jet as usual. The local temperature is $T(\mathbf{z})$. In the presence of flow fields with 4-velocity $u_f^\mu(\mathbf{z})$, one must boost the energy loss computed in the co-moving back to the lab frame, and a relativistic correction $\Gamma(\mathbf{z}) = u_f^\mu u_{j\mu}$ must be multiplied [234, 235], where the flow 4-velocity $u_f^\mu = \gamma_f(1, \vec{\beta}_f)$ and null jet parton 4-velocity $u_j^\mu = (1, \vec{\beta}_j)$[4]. E is the energy of the jet in the lab frame. The kinematic bounds for the transverse momentum of the radiated gluon $\mathbf{k}_\perp$ and the transverse momentum transfer $\mathbf{q}_\perp$ is $|\mathbf{k}_\perp| \leq x_E E \cdot \Gamma(\mathbf{z})$ and $|\mathbf{q}_\perp| \leq 6T(\mathbf{z})E \cdot \Gamma(\mathbf{z})$ (c.f. Section 2.3.5), respectively. As in Eq. (2.32), $\chi^2(\mathbf{z}) = M^2x_+^2 + m_g^2(\mathbf{z})(1-x_+)$ regulates the soft collinear divergences in the color antennae and controls the LPM phase. The gluon plasmon mass $m_g(\mathbf{z}) = f_E\mu(\mathbf{z})/\sqrt{2}$, and the gluon fractional energy x_E and fractional plus-momentum x_+ are connected via $x_+(x_E) = x_E[1+\sqrt{1-(k_\perp/x_EE)^2}]/2$.

In the CUJET2.0 model, Zakharov's 1-loop pQCD running scheme is used [216, 236, 237]. This running is cutoff in the infrared when the strong coupling strength reaches a

[4]At mid-rapidity, $\Gamma(\mathbf{z}) = \gamma_f(1-\vec{\beta}_{\perp_f}\cdot\vec{\beta}_{\perp_j}) = (1-u_{fx}\cos\phi - u_{fy}\sin\phi)/(\sqrt{1-u_{fx}^2-u_{fy}^2})$.

maximum value α_{max} for $Q \leq Q_{min}$:

$$\alpha_s(Q^2) = \begin{cases} \alpha_{max} & \text{if } Q \leq Q_{min} \ , \\ \dfrac{4\pi}{9\log(Q^2/\Lambda^2_{QCD})} & \text{if } Q > Q_{min} \ . \end{cases} \tag{3.9}$$

where the minimum running scale Q_{min} is fixed by α_{max} via $Q_{min} = \Lambda_{QCD} \exp\{2\pi/9\alpha_{max}\}$, with $\Lambda_{QCD} = 200$ MeV. Note that following Section 2.3.5, the one power of α_s originating from the gluon radiation vertex runs with the virtuality $k^2_\perp/[x_+(1-x_+)]$, the two powers of α_s originated from parton-medium scatterings run with the transverse momentum exchange $q^2_\perp$, and the thermal coupling in Eq. (3.5) runs with $(3T)^2$, i.e.

$$\mu^2(\mathbf{z}) = 4\pi \times \alpha_s([3T(\mathbf{z})]^2) \times T(\mathbf{z})^2 \left(1 + \frac{N_f}{6}\right) \ . \tag{3.10}$$

3.1.2 Elastic energy loss

The assumption that pQCD elastic energy loss is negligible compared to radiative is questionable. In [156, 157], the authors found that radiative and elastic average energy losses for heavy quarks were in fact comparable over a very wide kinematic range accessible at the RHIC. In [212], the authors confirm these previous findings and extend them to the light quark sector, showing that elastic contributions to the total energy loss can be of the same order of magnitude of radiative ones. It is then clear that quantitative tomographic predictions cannot ignore such large contributions to jet quenching, and elastic effects must be included in any pQCD based parton energy loss models.

In the CUJET2.0 framework, the Thoma-Gyulassy (TG) model [159] is used for the elastic energy loss. Their work was based on Bjorken's estimation of collisional energy loss in the QGP (cf. Section 2.1 in Chapter 2). By using the HTL gluon propagators that provide a more natural infrared regulator, the TG computation leads to the following

leading logarithm result:

$$\frac{dE}{d\tau} = -C_R \pi \alpha_s^2 T^2 \left(1 + \frac{N_f}{6}\right) \left(\frac{1}{v} + \frac{v^2 - 1}{2v^2} \log \frac{1+v}{1-v}\right) \log \left(\frac{k_{max}}{\mu}\right) \quad . \tag{3.11}$$

Where L is the jet path. For ultra-relativistic particles, the velocity v can be approximated to 1 and the v-dependent factor in parenthesis becomes approximately 1. The integral over the momentum exchange is infrared finite due to the Debye screening mass in the denominator, but a maximal momentum k_{max} must be set in order to screen the otherwise ultraviolet divergent logarithm. Assuming that the maximal momentum transfer comes from forward scattering against target particles with average momenta $q \approx 3T$ is much smaller than the projectile momentum, the value of k_{max} is $2pq/(E-p+2q) \approx 6Tp/(E-p+6T)$, with $p = \sqrt{E^2 - M^2}$[5].

One immediately sees that this model yields a result that is very similar to the Bjorken computation, Eq. (2.6), i.e.

$$\frac{dE}{d\tau} = -C_R \pi \alpha_s^2 T^2 \left(1 + \frac{N_f}{6}\right) \log B \quad . \tag{3.12}$$

The different between them is that a Coulomb log reflecting the more natural momentum cutoffs is being used now, i.e. in Eq. (3.11):

$$\log \left(\frac{k_{max}}{\mu}\right) = \log \left(\frac{6Tp}{E-p+6T} \frac{1}{\mu}\right) \quad . \tag{3.13}$$

Combined Eq. (3.11), (3.12) and (3.13), taken into account the running coupling effects in the elastic sector (as in [162], c.f. Section 2.3.5), noted that the hard parton's local

[5]Despite its improvement over the Bjorken result, the TG model leaves the ultraviolet region unbounded, because the classical calculation has no knowledge about the particle nature of the medium and particle recoil, which becomes important when the momentum transfer q is large. The hard momentum transfer contribution is more naturally taken into account by Braaten and Thoma in [160, 161], but relevant analysis shows that the differences in practical applications are almost negligible.

coordinate $\mathbf{z} = (x_0 + \tau\cos\phi, y_0 + \tau\sin\phi)$, one gets the following equation for collisional energy loss in CUJET2.0:

$$\begin{aligned}\frac{d[\Gamma(\mathbf{z})E(\mathbf{z})]}{d\tau} =& - C_R\pi \times \alpha_s(\mu(\mathbf{z})^2) \times \alpha_s(6\Gamma(\mathbf{z})E(\mathbf{z})T(\mathbf{z})) \times T(\mathbf{z})^2 \left(1 + \frac{N_f}{6}\right) \\ & \times \Theta\left(\Gamma(\mathbf{z})E(\mathbf{z}) - M\right) \\ & \times \log\left(\frac{6T(\mathbf{z})\sqrt{\Gamma(\mathbf{z})^2E(\mathbf{z})^2 - M^2}}{\Gamma(\mathbf{z})E(\mathbf{z}) - \sqrt{\Gamma(\mathbf{z})^2E(\mathbf{z})^2 - M^2} + 6T(\mathbf{z})}\frac{1}{\mu(\mathbf{z})}\right) \quad ,\end{aligned} \tag{3.14}$$

where $\Theta(x) = 1$ $(x > 0)$, 0 $(x \leq 0)$ is a step function. The mean number of collisions is

$$\langle N_c\rangle = \int_0^{\tau_{max}} d\tau\Gamma(\mathbf{z})\frac{18\zeta(3)}{\pi}(4 + N_f)\frac{\alpha_s(\mu(\mathbf{z})^2) \times \alpha_s(6\Gamma(\mathbf{z})E(\mathbf{z})T(\mathbf{z}))}{\mu(\mathbf{z})^2}T(\mathbf{z})^3 \quad . \tag{3.15}$$

Here C_R is the quadratic Casimir of the jet parton ($C_F = 4/3$ for quarks, $C_A = 3$ for gluons), $\mathbf{z}$ and $\mu(\mathbf{z})$ is defined via Eq. (3.1) and (3.10) respectively, $T(\mathbf{z})$ is temperature profile of the medium. To get the elastic energy loss for a hard parton $(\mathbf{x}_{0\perp}, \phi; M, E_0)$, Eq. (3.14) should be solved recursively to get its $E(\mathbf{z})$, after this has been computed, the average number of collisions $\langle N_c\rangle$ follows from Eq. (3.15).

3.1.3 Viscous hydrodynamical background

The QGP evolution profiles generated from the Glauber model with longitudinal Bjorken expansion (c.f. Appendix B) are known to be inconsistent with data of soft particle spectra and harmonic flow coefficients at RHIC and the LHC [238]. As one had seen in Section 1.2.3, the collective behavior of the hot deconfined QCD matter is well-described by hydrodynamical simulations with a near vanishing η/s, and this was one of strongest pieces of evidence that the strongly-coupled QGP is a "perfect fluid". The value of η/s approaches the Kovtun-Son-Starinets (KSS) bound $1/4\pi$ [114], ranges from $1/4\pi \sim 3/4\pi$

in most viscous hydrodynamical simulations for RHIC and the LHC energies [239]. Albeit this ratio is small, dissipative effects are non-negligible and it is necessary to take them into account in hydro simulations[6].

The past decade has witnessed significant progresses in the developments of viscous hydrodynamical models [115, 240–242]. These 2+1D or 3+1D hydro frameworks have demonstrated remarkable successes in heavy-ion phenomenology. Fig. 3.2 is an example of the impressive consistency between viscous hydro results and experimental measurements.

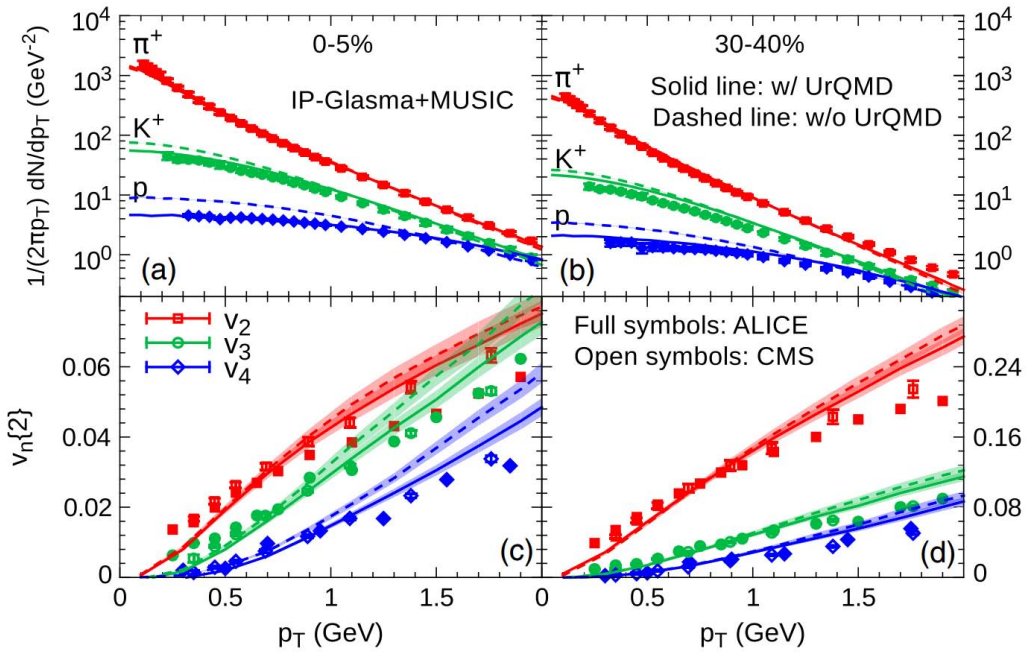

Figure 3.2: *Results from viscous hydrodynamical simulations show remarkable consistencies with data of low transverse momentum (p_T) spectra (upper panels) and harmonic flow coefficients (lower panels) of pions, kaons, and protons measured at relativistic heavy-ion collisions. (Taken from [243].)*

In the CUJET2.0 kernel, Eq. (3.8), one can tell that the local quasi-particle number density ρ, temperature T, and flow velocity u_f^μ of the thermally equilibrated medium all play important roles in the computation of parton energy loss. Therefore, to achieve the

[6]Note that it is always the ratio η/s that enters into the equations for damping (not η individually), as η measures a "force" and s (really sT) measures inertia.

goal of doing rigorous azimuthal jet flavor tomography of the QGP and making reliable predictions about jet quenching observables in ultra-relativistic heavy-ion collisions at RHIC and the LHC, it is crucial to embed a state-of-the-art viscous hydrodynamical evolving background in CUJET2.0.

The CUJET2.0 code has adaptive functions for hydro grid embedding, therefore a wide range of hydro backgrounds can be included in this framework. The current choice is 2+1D viscous profiles from the VISH2+1 model developed by the Ohio State University group [238, 241, 244–246]. Generally speaking, hydrodynamic equations arise from the local conservation of energy and momentum,

$$\partial_\mu T^{\mu\nu}(x) = 0 \ , \tag{3.16}$$

where the stress-energy tensor has the decomposition

$$T^{\mu\nu} = \epsilon u^\mu u^\nu - (p + \Pi)\Delta^{\mu\nu} + \pi^{\mu\nu} \ . \tag{3.17}$$

Here ϵ is the local energy density, and u^μ is the timelike, normalized 4-velocity of the energy flow. The projector $\Delta^{\mu\nu} = g^{\mu\nu} - u^\mu u^\nu$ is transverse to the flow velocity. Π is the bulk viscous pressure; combine it with the thermal pressure p and one can get the total bulk pressure. $\pi^{\mu\nu}$ is the traceless shear viscous stress tensor, and $\pi^{\mu\nu}u_\nu = 0$. In the local fluid rest frame (LRF), both the second and third term in Eq. (3.17) are purely spacelike. For ideal fluids, both Π and $\pi^{\mu\nu}$ vanish, and the leftover dynamical fields are $\epsilon(x)$, $p(x)$ and $u^\mu(x)$. For dissipative fluids without heat conduction, Π and $\pi^{\mu\nu}$ enter as additional dynamical variables and in relativistic Navier-Stokes theory, their evolution equations are given by

$$\Pi = -\zeta \nabla \cdot u \ \ , \pi^{\mu\nu} = 2\eta \nabla^{\langle\mu} u^{\nu\rangle} \ \ , \tag{3.18}$$

where these dissipative flows are expressed in terms of the local expansion rate $\theta \equiv \nabla \cdot u$ and velocity shear tensor $\sigma^{\mu\nu} \equiv \nabla^{\langle\mu} u^{\nu\rangle}$; ζ and η is the bulk and shear viscosity (both ≥ 0), respectively. $\nabla^\mu \equiv \Delta^{\mu\nu}\partial_\nu$ is the gradient in the LRF, and $\nabla^{\langle\mu} u^{\nu\rangle} \equiv \nabla^{(\mu} u^{\nu)} - \frac{1}{3}(\nabla \cdot u)\Delta^{\mu\nu}$ where $\nabla^{(\mu} u^{\nu)} \equiv \frac{1}{2}(\nabla^\mu u^\nu + \nabla^\nu u^\mu)$. Eq. (3.18) is a instantaneous identification and leads to causality problems. To avoid these issues, in VISH2+1 [241], the Israel-Stewart approach [247] is used, where the new kinetic transport equations are

$$D\Pi = -\frac{1}{\tau_\Pi}(\Pi + \zeta\nabla \cdot u) \ , \tag{3.19}$$

$$D\pi^{\mu\nu} = -\frac{1}{\tau_\pi}(\pi^{\mu\nu} - 2\eta\nabla^{\langle\mu} u^{\nu\rangle}) - 2u^{(\mu}\pi^{\nu)\alpha} Du_\alpha \ . \tag{3.20}$$

Here $D = u^\mu\partial_\mu$ is the time derivative in the LRF. τ_Π and τ_π are relaxation times and are related to the second-order expansion coefficients in the entropy current. In general the equation of motion for second order viscous hydrodynamics must be supplemented by an evolution equation (conservation law) for the baryon current $\partial_\mu j^\mu = \partial_\mu(nu^\mu) = 0$. These hydrodynamic equations need to be solved together with a given equation of state (EOS). In VISH2+1, the lattice s95p-v0-PCE (partial chemical equilibrium) EOS [245] is used, as shown in the left panel of Fig. 3.3. It has a smooth cross-over transition in the near T_c regime, fits well the thermodynamic quantities from lattice QCD calculations at high temperature, and recovers the hadron resonance gas (HRG) limit at low temperature [245, 246].

In the VISH2+1 [244, 246, 248] version adapted by CUJET2.0, MC-Glauber initial conditions are used, the Cooper-Frye algorithm [131] along a hypersurface of constant temperature $T_f = 120$ MeV is utilized to describe hadronic rescatterings, and a sharp transition from viscous fluids to free-streaming particles is generated in the kinetic freeze-out process. The input parameters in these viscous hydro simulations are adjusted to fit final hadron spectra and elliptic flow in low transverse momentum $p_T < 1.5(2.5)$

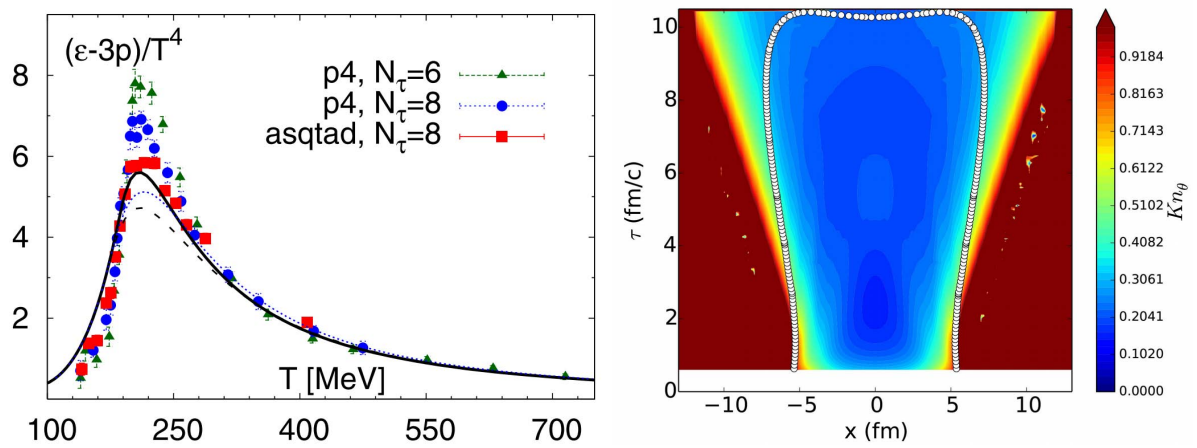

Figure 3.3: *Left: The EOS used in VISH2+1 (s95p, solid black line) describes well the lattice results of the trace anomaly. (Taken from [245].) Right: Contour plot for the evolution of the Knudsen number in VISH2+1 at LHC 20-30% Pb+Pb collisions. Small Knudsen numbers indicate valid hydro calculations. White points form the kinetic freeze-out surface at $T_{\rm dec}$ = 120 MeV. One can tell from its shape that the QGP experiences a clear transverse expansion. Note that the Knudson number $Kn_\theta = \frac{\lambda_{\rm mfp}}{L_{\rm hydro}} = \tau_\pi\theta = 5\frac{\eta\theta}{sT}$. (Taken from [238].)*

GeV/c region in [248]. In particular, experimental data of pion and proton spectra in $\sqrt{s_{NN}}$ = 200GeV Au+Au central collisions (0-5% centrality, b=2.33 fm), pion, proton and charged hadron elliptic flow $v_2(p_T)$ in semi-peripheral collisions (20-30% centrality, b=7.5 fm) are compared. With MC-Glauber initial conditions, s95p-PCE EOS and 120MeV freeze-out temperature, for a QGP with number of quark flavors $n_f = 2.5$, the starting time τ_0 at which the system is sufficiently close to local thermal equilibrium so that viscous hydrodynamics is applicable is calculated to be $\tau_0 = 0.6$ fm/c[7], and the QGP's shear viscosity to entropy density ratio η/s is phenomenologically extracted to be $\eta/s = 0.08$[8].

[7]In CUJET2.0 calculations one sets $\tau_0 = 0.6$ fm/c to match the orginal hydro setting. For the pre-thermal stage one uses a linear scheme, systematic uncertainties resulted from the choosing different thermalization parametrizations can be found in [231].

[8]Event-by-event fluctuations as considered in the recent iEBE-VISHNU [238] extension of viscous hydrodynamics are not included in studies of this thesis. But they will be added to future research with an event-by-event CUJET4.0 yet to be constructed.

3.1.4 Fluctuations and convolutions

It has been noted in the DGLV/WHDG framework [212] that fluctuations of radiative and collisional energy loss both play important roles in making the model predictions in line with data at RHIC and the LHC. These fluctuations are due to multiple gluon emissions or multiple parton collisions, and lead to broadened probability distributions of parton energy loss (c.f. e.g. Section 2.3.1 Fig. 2.4). In this section, the details of how energy loss fluctuations in the inelastic and elastic sector are considered, as well as how convolutions over initial jet productions and final jet fragmentations are performed within the CUJET2.0 model will be discussed.

Fluctuations: radiative energy loss

In the radiative energy loss sector, for multiple gluon emissions, a Poisson ansatz[9] is applied (c.f. Section 2.3.1), i.e. the number of radiated gluons is assumed to follow a Poisson distribution (c.f. Eq. (2.40)), with the mean number $\langle N_g \rangle$ given by the integral of the gluon emission spectrum

$$\langle N_g \rangle = \int_0^1 dx_E \frac{dN_g^{n=1}}{dx_E}(x_E) \ . \tag{3.21}$$

The gluon radiation can be thought of as a stochastic event, and it makes sense to speak of a probability distribution $P_{rad}(\epsilon)$ of radiating a certain amount of energy $\epsilon \equiv \Delta E_{rad}/E_0$:

$$P_{rad}(\epsilon) = P_r^{null}\delta(\epsilon) + P_r(\epsilon) + P_r^{full}\delta(\epsilon - \epsilon_{max}) \ , \tag{3.22}$$

[9]The exact probability distribution for multiple gluon emissions is an open question. For instance, Landau used steepest descent method when studying energy loss fluctuations in ordinary matter. The approximate form been derived as a solution is known as the Gumbel distribution, c.f. e.g. https://en.wikipedia.org/wiki/Gumbel_distribution.

where the maximum energy loss ratio $\epsilon_{max} = 1 - M/E_0$[10]. For simplicity, from now on the $n = 1$ superscript of $N_g^{n=1}$ and E subscript of x_E will be suppressed. The probability distribution Eq. (3.22) is split into three components:

The first term corresponds to the probability of zero radiation, $P_r^{null} = \mathrm{e}^{-\langle N_g \rangle}$.

The second term is given by

$$P_r(\epsilon) = \sum_{n=1}^{\infty} P_n(\epsilon) \ , \tag{3.23}$$

with

$$P_0(\epsilon) = P_r^{null}(\epsilon) = \mathrm{e}^{-\langle N_g \rangle} \ , \ P_1(\epsilon) = P_0 \frac{dN_g}{dx}(x = \epsilon) \ , \tag{3.24}$$

and

$$P_{n+1}(\epsilon) = \frac{1}{n+1} \int_0^1 dx_n P_n(\epsilon - x_n) \frac{dN_g}{dx}(x = x_n) \ . \tag{3.25}$$

Fast Fourier transform techniques are used to solve this equation numerically. Let $\tilde{P}_i(k)$ and $P_i(\epsilon)$, $\frac{d\tilde{N}_g}{dk}(k)$ and $\frac{dN_g}{dx}(x)$ be Fourier integral pairs, i.e.

$$\tilde{P}_i(k) = \int d\epsilon \ \mathrm{e}^{\mathrm{i}k\epsilon} \ P_i(\epsilon) \ , \ \frac{d\tilde{N}_g}{dk}(k) = \int dx \ \mathrm{e}^{\mathrm{i}kx} \ \frac{dN_g}{dx}(x) \ . \tag{3.26}$$

One immediately gets from Eq. (3.23) (3.25) that

$$\tilde{P}_r(k) = \sum_{n=1}^{\infty} \tilde{P}_n(k) \ , \tag{3.27}$$

and

$$\tilde{P}_n(k) = \frac{1}{n!} \left(\frac{d\tilde{N}_g}{dk}(k) \right)^n P_0 \ . \tag{3.28}$$

[10] E_0 is the initial energy of the incoming jet, and M is the parton mass.

Plug Eq. (3.28) into Eq. (3.27), one gets

$$\tilde{P}_r(k) = P_0 \left(\exp\left(\frac{d\tilde{N}_g}{dk}(k) \right) - 1 \right) \quad . \tag{3.29}$$

Fourier transform back, one has

$$P_r(\epsilon) = \frac{\mathrm{e}^{-\langle N_g \rangle}}{2\pi} \int dk\ \mathrm{e}^{-\mathrm{i}k\epsilon} \left(\exp\left(\int dx\ \mathrm{e}^{\mathrm{i}kx}\ \frac{dN_g}{dx}(x) \right) - 1 \right) \quad . \tag{3.30}$$

Practically, the numerical evaluation of Eq. (3.30) uses finite discrete k_i and x_j series, for example, $k_i = -1000 + i$ $(i = 0, 1, \cdots, 2000)$ and $x_j = j\sigma$ $(j = 0, 1, \cdots, \sigma^{-1}; \sigma = 0.0025)$, meaning the Fourier transform in the exp(...) of Eq. (3.30) is in fact

$$\int dx\ \mathrm{e}^{\mathrm{i}kx}\ \frac{dN_g}{dx}(x) \to \sum_j \mathrm{e}^{\mathrm{i}k_i x_j}\ \frac{dN_g}{dx}(x_j)\ \sigma \quad . \tag{3.31}$$

The $\frac{dN_g}{dx}(x)$ itself is fluctuating because of limited computing power to implement Monte-Carlo iterations. At large $|k_i|$, this fluctuation is worsened with the highly oscillating $\mathrm{e}^{\mathrm{i}k_i x_j}$, and will generate unphysical variations in $P_r(\epsilon)$. However, if take the $\int dk\ \mathrm{e}^{-\mathrm{i}k\epsilon}$ in Eq. (3.30) into account, one sees components with larger $|k|$ will have less weight in the evaluation of $P_r(\epsilon)$. Therefore, the exp(...) in Eq. (3.30) smoothfied by a Gaussian with proper width, put more weight on small k Fourier components, and modify Eq. (3.30) to

$$P_r(\epsilon) = \frac{\mathrm{e}^{-\overline{N}_g}}{2\pi} \int dk\ \mathrm{e}^{-\mathrm{i}k\epsilon} \left[\exp\left\{ \sum_j \mathrm{e}^{\mathrm{i}kx_j}\ \frac{dN_g}{dx}(x_j)\ \sigma\ \mathrm{e}^{-\frac{k^2\sigma^2}{2}} \right\} - 1 \right] \quad . \tag{3.32}$$

with $x_j = j\sigma$ $(j = 0, 1, \cdots, \sigma^{-1})$. In CUJET, $P_r(0) = 0$, one uses Eq. (3.32) to calculate $P_r(\epsilon)$ in the range of $0 < \epsilon \leq \epsilon_{max}$, as well as in the range of $\epsilon_{max} < \epsilon \leq \epsilon_{leak} = 1.75$ for numerical purposes.

The third and last term in Eq. (3.22) represents instead the probability of total quench-

ing. Under soft approximation, the radiated energy ω is assumed to be much smaller than the initial jet energy E, and $x \ll 1$. Consequently, the energy of the outgoing parton E' is approximately equal to E. When the $\{x_n\}$ are integrated up to the kinematic limit $x_n = 1$, a "leakage" error into the unphysical region $P_r(\epsilon > \epsilon_{max}) \neq 0$ occurs, and this error is calculated in $P_r^{full} = \int_{\epsilon_{max}}^{\infty} d\epsilon\ P_r(\epsilon)$[11].

For the normalization of $P_{rad}(\epsilon)$, the weight of the physical zero quenching probability P_{null} is unchanged, and the probability distribution is rescaled as follows: firstly, the norm $\mathcal{N}_{rad}$ is calculated from $\mathcal{N}_{rad} = \int_0^{\epsilon_{max}} P_{rad}(\epsilon)$. When doing this integral, the Delta functions at both boundaries are included. Secondly, the complete $P_{rad}(\epsilon)$ is rescaled according to $P_{rad}(\epsilon) \to \frac{1-\mathrm{e}^{-\langle N_g \rangle}}{\mathcal{N}_{rad}} P_{rad}(\epsilon)$. Finally the coefficient of $\delta(\epsilon)$ in $P_{rad}(\epsilon)$ is replace with zero radiation probability, i.e. $\frac{1-\mathrm{e}^{-\langle N_g \rangle}}{\mathcal{N}_{rad}} P^{null} \to \mathrm{e}^{-\langle N_g \rangle}$. Through this procedure $\int_0^{\epsilon_{max}} P_{rad}(\epsilon) = 1$ is maintained, and the $\delta(\epsilon)$ at the $\epsilon = 0$ boundary has weight $\mathrm{e}^{-\langle N_g \rangle}$. If $\langle N_g \rangle = 0$, $P_{rad}(\epsilon) = \delta(\epsilon)$.

Note $P_{rad}(\epsilon)$ inherits the dependence of jet production coordinates, parton mass and energy, and model parameter from $\frac{dN_g}{dx}$. Thus in CUJET2.0, if written down all dependencies explicitly, then:

$$P_{rad}(\epsilon) = P_{rad}(\epsilon = \Delta E_{rad}/E_0; \mathbf{x}_{0\perp}, \phi; M, E_0; \alpha_{max}, f_E, f_M) \ . \tag{3.33}$$

Fluctuations: collisional energy loss

In the collisional energy loss sector, fluctuations of the elastic scatterings around the mean were addressed in [212] and [158]. Using a framework generally applied to diffusive processes that are characterized by a large number of soft collisions, the probability distri-

[11] In the numerical evaluation, the upper bound is $\epsilon_{\rm leak} = 1.75$ instead of infinity. How sensitive is the total energy loss probability distribution to this particular choice $\epsilon_{\rm leak} = 1.75$ is subject to future studies. As a rough estimate, from analyzing the tail of total $P(\epsilon)$ in the right panel of Fig. 2.4, to have $P(\epsilon_{\rm leak}) < 0.1P(\epsilon_{\rm max})$, $\epsilon_{\rm leak} = 1.75$ would be necessary.

bution to loose the collisional energy $\epsilon \equiv \Delta E_{el}/E_0$ is represented by a Gaussian centered around the average $\langle \Delta E_{el} \rangle$, with variance $\sigma^2 = 2 \langle T \rangle \langle \epsilon \rangle / E_0$. Here $\langle \epsilon \rangle \equiv \langle \Delta E_{el} \rangle / E_0$, and the average elastic energy loss $\langle \Delta E_{el} \rangle$ is calculated according to Eq. (3.14),

$$\langle \Delta E_{el} \rangle = E(\tau; \mathbf{x}_0, \phi; M, E_0; \alpha_{max})|_{\tau=0}^{\tau=\tau_{max}} = \int_0^{\tau_{max}} d\tau \frac{dE(\mathbf{z})}{d\tau} \quad , \tag{3.34}$$

with $T(\mathbf{z})|_{\tau=\tau_{max}} = T_f$, and $E(\mathbf{z})$ is solved recursively from Eq. (3.14) given $E(\mathbf{z})|_{\tau=0} = E_0$. The average temperature along the jet path is[12]

$$\langle T \rangle = \frac{1}{\tau_{max}} \int_0^{\tau_{max}} d\tau \, T(\mathbf{z}) \quad . \tag{3.35}$$

The collisional energy loss probability distribution is

$$P_{el}(\epsilon) = e^{-\langle N_c \rangle} \delta(\epsilon) + \frac{\mathcal{N}}{\sqrt{2\pi\sigma^2}} e^{-\frac{(\epsilon - \langle \epsilon \rangle)^2}{2\sigma^2}} \quad . \tag{3.36}$$

The first term represents the probability of no collisions, with the average number of collisions $\overline{N}_c$ calculated according to Eq. (3.15). The second term is the normalized Gaussian distribution centered around $\langle \epsilon \rangle$, with $\mathcal{N} = 1 - e^{-\langle N_c \rangle}$. The Gaussian distribution reaches unphysical regions $\epsilon < 0$ and $\epsilon > \epsilon_{max}$, those "leaks" are absorbed into Delta functions at respective boundaries, and $P_{el}(\epsilon)$ is rewritten as

$$P_{el}(\epsilon) = P_e^{null} \delta(\epsilon) + P_e(\epsilon) + P_e^{full} \delta(\epsilon - \epsilon_{max}) \quad . \tag{3.37}$$

[12] Assuming event-averaged, smooth QGP evolution profiles are embedded.

This equation resembles the definition of $P_{rad}(\epsilon)$ in Eq. (3.22). Here

$$\begin{aligned} P_e^{null} &= e^{-\langle N_c \rangle} + \int_{-\infty}^{0} d\epsilon \frac{\mathcal{N}}{\sqrt{2\pi\sigma^2}} e^{-\frac{(\epsilon-\langle\epsilon\rangle)^2}{2\sigma^2}} \quad , \\ P_e^{full} &= \int_{\epsilon_{max}}^{\infty} d\epsilon \frac{\mathcal{N}}{\sqrt{2\pi\sigma^2}} e^{-\frac{(\epsilon-\langle\epsilon\rangle)^2}{2\sigma^2}} \quad , \end{aligned} \tag{3.38}$$

and

$$P_e(\epsilon) = \frac{\mathcal{N}}{\sqrt{2\pi\sigma^2}} e^{-\frac{(\epsilon-\langle\epsilon\rangle)^2}{2\sigma^2}} \quad , \tag{3.39}$$

here $0 \leq \epsilon \leq \epsilon_{max}$. For numerical purposes $P_e(\epsilon)$ is calculated in the range of $\epsilon_{max} \leq \epsilon \leq \epsilon_{leak} = 1.75$ according to Eq. (3.39). Note that integrating $P_{el}(\epsilon)$ over $0 \leq \epsilon \leq \epsilon_{max}$ automatically gives unity. The rearrangement of Eq. (3.37) provides great conveniences for the convolution of radiative and elastic energy loss probability distributions.

Similar to the radiative sector, the elastic energy loss probability distribution also inherits the dependence on the jet production coordinates, parton mass and energy, and model parameter from $\langle \Delta E_{el} \rangle$ and $\langle N_c \rangle$. The explicit dependencies for $P_{el}(\epsilon)$ has the form:

$$P_{el}(\epsilon) = P_{el}(\epsilon = \Delta E_{el}/E_0; \mathbf{x}_{0\perp}, \phi; M, E_0; \alpha_{max}) \quad . \tag{3.40}$$

Convolutions: radiative energy loss $\otimes$ collisional energy loss

In the CUJET framework, after calculating the radiative energy loss probability distribution $P_{rad}(\epsilon)$ from Eq. (3.22) and elastic energy loss probability distribution $P_{rad}(\epsilon)$ from Eq. (3.37), their contributions are convoluted to get the total energy loss probability distribution $P_{tot}(\epsilon)$. Symbolically,

$$P_{tot}(\epsilon) = \int_0^{\epsilon} dx \; P_{rad}(x) P_{el}(\epsilon - x) \quad . \tag{3.41}$$

In the CUJET framework, when computing Eq. (3.41), while keeping the δ function at 0 in each sector fixed, $P_r(\epsilon)$ and $P_e(\epsilon)$ are spread over $0 \leq \epsilon \leq \epsilon_{leak} = 1.75$, and the

convoluted leak is then absorbed to the δ function at ϵ_{max}. In this way, rewrite $P_{rad}(\epsilon)$ and $P_{el}(\epsilon)$ as

$$P_{rad}(\epsilon) = e^{-\overline{N}_g}\delta(\epsilon) + P_r(\epsilon) \ , \ P_{el}(\epsilon) = e^{-\overline{N}_c}\delta(\epsilon) + P_e(\epsilon) \ . \tag{3.42}$$

$P_r(\epsilon)$ and $P_e(\epsilon)$ are calculated over $0 \leq \epsilon \leq \epsilon_{leak} = 1.75$. Plug them into Eq. (3.41),

$$\begin{aligned} P_{tot}(\epsilon) &= \int_0^\epsilon dx \ \left(e^{-\overline{N}_g}\delta(x) + P_r(x)\right)\left(e^{-\overline{N}_c}\delta(\epsilon - x) + P_e(\epsilon - x)\right) \\ &= e^{-(\overline{N}_g+\overline{N}_c)}\delta(\epsilon) + e^{-\overline{N}_g}P_e(\epsilon) + e^{-\overline{N}_c}P_r(\epsilon) + \int_0^\epsilon dx \ P_r(x)P_e(\epsilon - x) \ . \end{aligned} \tag{3.43}$$

One may define

$$\begin{aligned} P_t^{null} &\equiv e^{-(\overline{N}_g+\overline{N}_c)} \ , \\ P_t^{full} &\equiv \int_{\epsilon_{max}}^{\epsilon_{leak}} d\epsilon \ \int_0^\epsilon dx \ P_r(x)P_e(\epsilon - x) \ , \\ P_t(\epsilon) &\equiv e^{-\overline{N}_g}P_e(\epsilon) + e^{-\overline{N}_c}P_r(\epsilon) + \int_0^\epsilon dx P_r(x)P_e(\epsilon - x) \ , \end{aligned} \tag{3.44}$$

and $P_{tot}(\epsilon)$ can be rewritten as

$$P_{tot}(\epsilon) = P_t^{null}\delta(\epsilon) + P_t(\epsilon) + P_t^{full}\delta(\epsilon - \epsilon_{max}) \ , \tag{3.45}$$

where $0 \leq \epsilon \leq \epsilon_{max}$. $P_{tot}(\epsilon)$ is normalized in the usual way, i.e. $\int_0^{\epsilon_{max}} d\epsilon \ P_{tot}(\epsilon) = 1$.

Strictly speaking, $P_{tot}(\epsilon)$ depends on other parameters that are inherited from $P_{rad}(\epsilon)$ and $P_{el}(\epsilon)$, and explicitly,

$$P_{tot}(\epsilon) = P_{tot}(\epsilon = \Delta E_{tot}/E_0; \mathbf{x}_{0\perp}, \phi; M, E_0; \alpha_{max}, f_E, f_M) \ . \tag{3.46}$$

For simplicity, throughout rest of this thesis the "tot" subscript will be suppressed unless otherwise reinstated.

Convolutions: binary distribution ⊗ unquenched spectrum ⊗ energy loss

To get the quenched partonic spectra in AA collisions within CUJET, the pQCD (unquenched) partonic spectra in pp collisions is first convoluted with the total energy loss probability distribution $P(\epsilon)$, then convoluted with the Glauber binary distribution in AA collisions (c.f. Appendix B). The unquenched partonic spectra in CUJET are generated from pQCD calculations. In the light sector, the parton production spectrum is based on a leading order (LO) calculation scaled by a simple K-factor and computed from the LO pQCD CTEQ5 code of X.N. Wang [249]. In the heavy sector, both next-to-leading order [250] and fixed-order plus next-to-leading-log (FONLL) [251, 252] computations are used. In addition to including the full NLO result [253–255], the FONLL calculation re-sums large perturbative terms with next-to-leading logarithmic accuracy [256]. More details about the partonic spectra used in CUJET can be found in [231].

Here is a summary of how CUJET computes the quenched partonic spectra in AA:

1. The algorithm starts from a jet created at $\mathbf{x}_{0\perp}$ in the azimuthal plane (with respect to the beam axis) with azimuthal angle ϕ and mass M. The distribution of jet productions in the transverse plane in the AA collision is given by ρ_{binary} (cf. Section B). The initial transverse momentum probability distribution $P_0(p_i)$[13] of the partons is proportional to the production cross section:

$$P_0(p_i) \propto \frac{d\sigma^{pp\to q}}{dp_i}(p_i) \ , \tag{3.47}$$

   Here $d\sigma^{pp\to q}/dp_i$ represents a generic p+p partonic production spectrum. A range of discrete transverse momenta $[p_i^{min}, p_i^{max}]$ needs to be defined for the numerical computation.

[13] Note that $p_i \equiv (p_T)_i$. The "T" (transverse) subscript will be suppressed in this subsection, hence all p_i's and p_f's should be interpreted as transverse momenta.

2. For each initial transverse momentum p_i in the range $[p_i^{min}, p_i^{max}]$, CUJET computes the energy loss according to Eq. (3.8)(3.14). This is the most resource- and time-consuming process, where the full jet path Monte Carlo integral is evaluated over the expanding plasma and the medium-induced gluon radiation spectrum as well as elastic collisional energy loss are computed. All the dynamical properties of the plasma can be specified and their contributions to the energy loss – radiative and/or elastic – should be considered. Once fluctuations effects are taken into account – Eq. (3.22),(3.37) – the output takes the form of a distribution function which represents the probability for a parton with initial transverse momentum p_i ($p_i = \sqrt{E_i^2 - M^2}$) to lose an energy faction ϵ ($\epsilon = 1 - E_f/E_i, E_{i,f}^2 = p_{i,f}^2 + M^2$) (cf. Eq. (3.45)):

$$P(\epsilon; p_i; \mathbf{x}_0, \phi) = P_t^{null}(p_i)\delta(\epsilon) + P_t(\epsilon; p_i) + P_t^{full}(p_i)\delta(\epsilon - \epsilon_{max}) \ , \tag{3.48}$$

and $\epsilon_{max} = 1 - M/\sqrt{p_i^2 + M^2}$.

3. Once all the $\{p_i\}$ in the range specified have been computed, the $\{P(\epsilon; p_i)\}$ are converted into a two-dimensional distribution map that represents the probability of a jet with initial transverse momentum p_i to leave the plasma with final transverse momentum p_f:

$$\begin{aligned} P(p_f, p_i) &= P(\epsilon; p_i)\frac{d\epsilon}{dp_f} \\ &= P_t^{null}(p_i)\delta(p_f - p_i) + P_t(\epsilon(p_f, p_i); p_i)\frac{p_f}{E_f E_i} + P_t^{full}(p_i)\delta(p_f) \ , \end{aligned} \tag{3.49}$$

with

$$\epsilon(p_f, p_i) = 1 - \frac{E_f}{E_i} \ , \quad E_f = \sqrt{p_f^2 + M^2} \ , \quad E_i = \sqrt{p_i^2 + M^2} \ . \tag{3.50}$$

The normalization is such that

$$\int_0^{p_i} dp_f \; P(p_f, p_i) = 1 \quad , \tag{3.51}$$

which is automatically ensured by $\int_0^{\epsilon_{max}} d\epsilon P(\epsilon; p_i) = 1$. In Eq. (3.49) the explicit dependence on the jet coordinates $\mathbf{x}_{0\perp}$ and ϕ is dropped.

4. CUJET then integrates over the production spectrum, Eq. (3.47), to obtain the "quenched" partonic p+p spectra $\frac{d\sigma'^{pp\to q}}{dp_f d\phi}$:

$$\frac{d\sigma'^{pp\to q}}{dp_f d\phi}(p_f; \mathbf{x}_{0\perp}, \phi) = \int_{p_i^{min}}^{p_i^{max}} dp_i \; P(p_f, p_i; \mathbf{x}_{0\perp}, \phi) \frac{d\sigma^{pp\to q}}{dp_i}(p_i) \quad . \tag{3.52}$$

5. Lastly, the quenched partonic spectra in AA collisions as a function of the observed transverse momentum $p_f (\equiv p_T)$ and azimuthal angle ϕ are obtained by integrating over the jet transverse distribution (binary distribution):

$$\frac{d\sigma^{AA\to q}}{dp_f d\phi}(p_f; \phi) = \int d\mathbf{x}_{0\perp} \; \rho_{binary}(\mathbf{x}_{0\perp}) \; \frac{d\sigma'^{pp\to q}}{dp_f d\phi}(p_f; \mathbf{x}_{0\perp}, \phi) \quad . \tag{3.53}$$

Convolutions: quenched partonic spectrum $\otimes$ fragmentation function

The quenched partonic spectra in AA collisions can provide useful information about the jet quenching mechanism, nevertheless, comparisons with data can only be carried out at the hadronic level. Therefore, quenched partonic spectra in Eq. (3.53) must be convoluted with a set of fragmentation functions (FFs).

The process that leads to the fragmentation of partons in the medium is not theoretically well understood, especially for heavy quarks: dissociation and recombination theories [257, 258] assume that heavy D and B mesons can be formed within the plasma and lose additional energy through collisional dissociation, in a similar fashion to what

has been suggested for heavy quarkonium states [259]. This, however, seems to contradict more recent lattice results [260], which indicate the complete melting of open heavy flavors occurs at temperature $T \gtrsim 220$ MeV.

Since high p_T hadrons are of primary interests, contributions from recombination will not be treated in this analysis. Rather, hadronizations via fragmentations are considered. This fragmentation will be assumed to take place in vacuum, on a hypersurface parametrized by $\mu(\vec{x}, \tau_f) = \Lambda_{QCD}$.

The convolution of the quenched partonic spectra over appropriate FFs takes the form

$$\begin{aligned} \frac{d\sigma^h}{dp}(p) &= \sum_i \int_{p/p_{max}}^1 dx \; \frac{d\sigma^i}{dp}(\frac{p}{x}) \; D_i^h(x, \left(\frac{p}{x}\right)^2) \\ &= \sum_i \int_{p/p_{max}}^1 dx \; \frac{1}{x}\frac{d\sigma^i}{d\frac{p}{x}}(\frac{p}{x}) \; D_i^h(x; \left(\frac{p}{x}\right)^2) \quad . \end{aligned} \tag{3.54}$$

Here $D^{i\to h}(z, Q^2)$ represents the probability that a parton i fragments into a hadron h which carries a fraction z of the parton energy. Q is the scale at which the FF is evaluated, here it is given by the energy of the parton. Eq. (3.54) is summed over all species i that fragment into h.

For light quarks and gluons fragmented into pions, leading order KKP functions are used [130]. For heavy quarks fragmented into D and B mesons ($c \to D$ and $b \to B$), the Peterson [261] function with $\epsilon_c = 0.06$ and $\epsilon_b = 0.006$ is used respectively, as done also in [262]. While the Peterson FF does not couple well with the FONLL production cross section [263], it was shown in [262] that similar results are produced anyway even using a more accurate fragmentation description. Finally for the decay of the heavy mesons into non-photonic electrons ($c \to D \to e$ and $b \to B \to e$), the same functions as in [263] is used. The secondary decay $D \to B \to e$ is also accounted for.

3.2 Heavy-ion phenomenology

While the multiple ingredients built into CUJET2.0 all have physical origins, this section will focus on discussing two of the most important ones – they are two critical phenomenological puzzles in heavy-ion collisions at RHIC and LHC energies – (1) the "heavy quark energy loss puzzle", which is an observation that the heavy flavor decay electrons measured at RHIC experience an anomalously high suppression, and this stimulates more realistic modeling of the medium properties as well as geometric fluctuations; and (2) the "surprising transparency of the QGP" at the LHC, which is a statement the that extrapolation of pQCD energy loss models from RHIC to the LHC over-predicts the suppression of light hadrons at the LHC if the QGP opacity scales linearly with the jet path length, and this is a direct outcome of QCD asymptotic freedom.

3.2.1 Heavy quark energy loss puzzle

To begin, recall the nuclear modification factor R_{AA} that was defined in Section 1.2.6 Eq. (1.48) and Eq. (1.49). R_{AA} is a key observable at RHIC and the LHC, it quantifies the magnitude of jet quenching in the QGP. It is defined as the ratio of the quenched hadronic A+A spectrum to the unquenched p+p spectrum scaled according to the number of binary collisions N_{bin}:

$$R_{AA}^{h}(p_T) = \frac{\dfrac{d\sigma^{AA\to h}}{2\pi p_T dp_T}(p_T)}{N_{bin}\,\dfrac{d\sigma^{pp\to h}}{2\pi p_T dp_T}(p_T)} \quad . \tag{3.55}$$

Here the explicit dependence on the rapidity y and the center of mass energy $\sqrt{s}$ are suppressed. In Eq. (3.55) the azimuthal angle ϕ in the AA/pp spectrum is integrated out, the expression is thus azimuthally averaged.

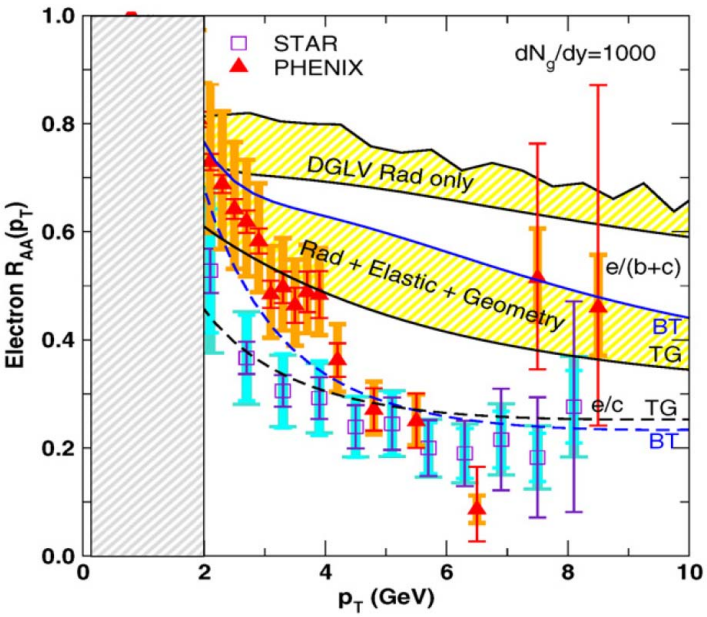

Figure 3.4: *The heavy quark energy loss puzzle at RHIC. The suppression factor, $R_{AA}(p_T)$, of non-photonic electrons from decay of quenched heavy quark (c + b) jets within the WHDG/DGLV model (yellow bands; the lower one includes both radiative and elastic energy loss, as well as geometric fluctuations) is compared to PHENIX and STAR measurements in central Au+Au reactions at 200 AGeV. Taking into account both c and b decay, theoretical results are significantly above the data, suggesting a large underestimate of the b quark energy loss. (Taken from [212].)*

The "heavy quark energy loss puzzle" is demonstrated in Fig. 3.4, where predictions of high p_T non-photonic electrons at mid-rapidity in Au+Au $\sqrt{s_{NN}} = 200$ GeV central collisions from the WHDG/DGLV model are compared with measurements by the PHENIX and STAR at RHIC [212]. Observations one can make about this figure include: in the WHDG/DGLV model, while electrons from the decay of c jets have a suppression factor that is compatible with what is measured at RHIC, after taking into account both c and b jets, the R_{AA} results are significantly above data, despite the inclusion of collisional energy losses as well as path length fluctuations.

The above suggest that the b quark energy loss in the QGP is significantly underes-

timated in the pQCD/DGLV energy loss framework. In Fig. 2.5 and Fig. 2.6, one sees that the dead cone effect is strong for b quark jets. In a simple fashion, this suppression comes from the fact the it is harder to kick a heavy quark off-shell thus a reduction will occur in the radiated gluon spectrum compared with a light quark. Therefore, collisional energy loss becomes important for heavy flavors.

One sees from Fig. 2.6 that the averaged path length is comparable for u and c quarks, while both are shorter than that for the b quark. Meanwhile, one sees from Fig. 2.9 and 2.10 that the light to heavy quark energy loss ratio $\Delta E_l/\Delta E_h$ increases as the length of a brick medium increases. All these figures indicate the strong influences of jet path length estimations on the resulting heavy quark energy loss. Bearing this in mind, and inspecting the WHDG setup for geometric fluctuations, Eq. (2.47), one immediately sees that because the proper time is integrated to infinity, a overestimation of the path length may occur in the presence of density fluctuations and transverse expansions, and both of them are indeed present in the QGP evolution profiles generated from 2+1D viscous hydrodynamical simulations.

Thus, a first improvement that the CUJET model made over its predecessor WHDG is that, for the full jet path integration carried out in the radiative Eq. (3.8) and elastic Eq. (3.14), the proper time τ is evolved to a cutoff τ_{max} that is related to a fixed fragmentation temperature T_f via $T(\mathbf{z})|_{\tau=\tau_{max}} = T_f$,[14] and the value of T_f is chosen such that an agreement with hydro simulations can be reached. Embedded in CUJET2.0 are the VISH2+1 [244, 246, 248] event-averaged smooth profiles with MC-Glauber initial conditions, $\tau_0 = 0.6$ fm/c, s95p-v0-PCE Equation of State (EOS) with $T_c = 160$ MeV, $\eta/s = 0.08$, and Cooper-Frye freeze-out temperature 120 MeV [238, 264–268]. The path integrations $\int d\tau$ for jets initially produced at transverse coordinates $(\mathbf{x}_{0\perp}, \phi)$ are hence

[14] Technically, in the CUJET code, τ_{max} satisfies $\forall\ 0 < \delta < 5$ fm, $T(\mathbf{z}(\tau_{max} + \delta; \mathbf{x}_{0\perp})) < T_f$. Both τ_{max} and δ are in the lab frame.

cut off at dynamical $T(\mathbf{z}(\mathbf{x}_{0\perp},\phi,\tau))|_{\tau_{max}} = T_f = 160$ MeV hypersurfaces.

The second improvement to solve the heavy quark puzzle is related to the dynamical QCD medium effects that have been extensive discussed in Section 2.3.4. Here is a brief summary of the physical picture: static color-screened scattering centers are implemented in the original DGLV theory, in this setup, the elastic energy loss averages to zero, yet for heavy quark suppression, because contributions from the collisional sector is comparable to the dead cone reduced radiative, a medium consists of dynamical quarks and gluons must be considered using the finite temperature HTL approach [200–205], and the result is a replacement in the mean free path and in the interaction potential [219]. One can tell from Eq. (3.8) that a hybrid interaction potential is introduced

$$|\bar{v}(\mathbf{q}_\perp)|^2 = \frac{1}{\pi}\frac{\mu_E^2}{(\mathbf{q}_\perp^2+\mu_E^2)(\mathbf{q}_\perp^2+\mu_M^2)} \quad , \tag{3.56}$$

such that smooth interpolations between pure HTL dynamical and pure static limit can be realized.

CUJET2.0 has been applied to study the suppression pattern of D mesons, B mesons and non-photonic electrons at RHIC and the LHC. The open heavy flavor and heavy flavor lepton nuclear modification factors calculated from CUJET2.0 $(\alpha_{max}, f_E, f_M) = (0.26, 1, 0)$ HTL model are shown in Fig. 3.5. Notice that the $(f_E, f_M) = (1, 0)$ is the pure HTL dynamical limit. Here inclusive non-photonic electrons R_{AA}'s in central and semi-peripheral A+A collisions are compared with experimental data from PHENIX [269] and STAR [270], and D meson R_{AA}'s are compared with measurements from ALICE [271].

The quenching pattern of heavy flavor decay electrons at Au+Au 200AGeV collisions calculated from CUJET2.0 (panel (a) and (b) of Fig. 3.5) is in agreements with RHIC data in central and semi-peripheral centralities. This clearly indicates the solution to the "heavy quark puzzle" is built intrinsically in the structure of CUJET energy loss

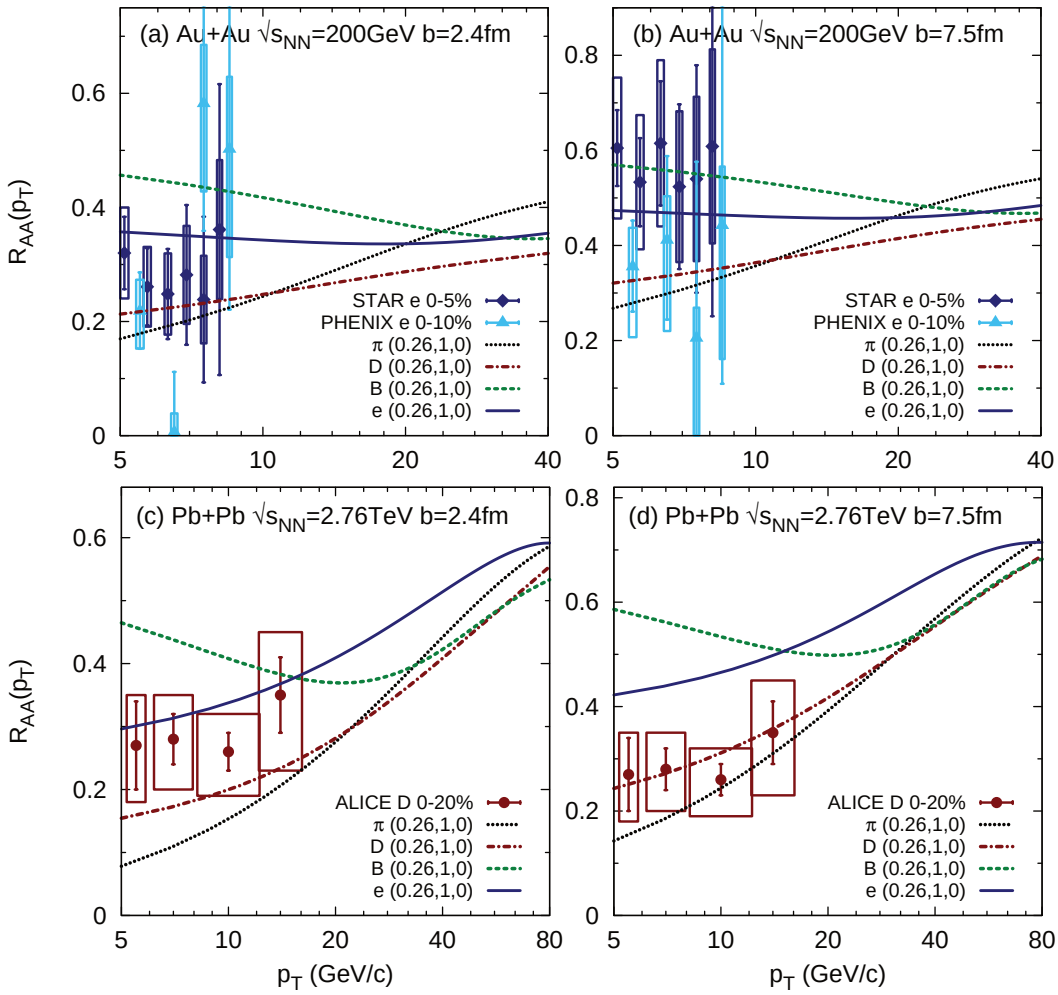

Figure 3.5: *CUJET2.0 explains the strong suppression of heavy flavor decay electrons at RHIC thus solves the heavy quark energy loss puzzle. Besides, it predicts a unique hierarchy for the QGP suppressions of jet fragments at RHIC and the LHC, i.e.* $R_{AA}(p_T)$*'s* $B > e > D \gtrsim h^{\pm}/\pi^0$ *ordering at* $p_T < 10$ *GeV evolves into* $h^{\pm}/\pi^0 > B \sim D$ *at high* p_T*. (Taken from [216].)*

framework. The underlying physics is that the combination of the dynamical medium effect and elastic energy loss significantly brings down the light to heavy quark energy loss ratio, and the more realistic modeling of path length fluctuations further reduces this ratio.

Besides solving the heavy quark energy loss puzzle, CUJET2.0 predicts a novel crossing pattern of p_T dependent π, D, B, e^- nuclear suppression factors. Compare the left panels of Fig. 3.5 to Fig. 1 in [221], one finds that despite the inclusion of multi-scale running couplings and dynamical viscous hydro fields in CUJET2.0, and the crossings of π, D, B, e^- R_{AA}'s in CUJET2.0 occur at about same p_T as in CUJET1.0[15]. For example, at RHIC Au+Au $\sqrt{s_{NN}}$ =200GeV central collisions, pion R_{AA} intersects D meson, non-photonic electron, B meson at $p_T \approx 9, 19, 24$ GeV, and at the LHC Pb+Pb $\sqrt{s_{NN}}$ =2.76TeV central collisions, pion R_{AA} intersects D meson, B meson at $p_T \approx 23, 33$ GeV. Note all these p_T's are within the range of $p_T < 40$ GeV where running coupling effects contribute significantly to a steeper rising R_{AA}. The running coupling induced change of slope emerges from pion, D meson and B meson R_{AA} in a similar manner, this is as expected, because when considering the gluon radiation vertex for running coupling, the mass scale is small comparing to kinetic terms hence being dropped, cf. Eq. (2.50) and (2.51). The robust R_{AA} crossings in CUJET also suggests that the mass ordering of π, D, B, e^- suppression pattern comes intrinsically from the DGLV gluon radiation spectrum and TG elastic energy loss formula, and the bulk evolution profile has limited effects on this mass hierarchy.

Generally speaking, the quenched hadron (h) spectrum in an AA collision is calculated with

$$\frac{Ed\bar{\sigma}^{AA\to h}}{d^3p} \equiv \frac{1}{N_{bin}}\frac{Ed\sigma^{AA\to h}}{d^3p} = \frac{E_i d\sigma^{pp\to q}}{d^3p_i} \otimes P(E_i(p_i) \to E_f(p_f)) \otimes D(q \to h) \quad , \quad (3.57)$$

where $E_i d\sigma^{pp\to q}/d^3p_i$ is the unquenched partonic pp spectrum, P is the energy loss probability distribution which is linked to $\Delta E/E(E)$, and D is the fragmentation function from parton q to hadron h. It is of great importance to study which one of the three factors

[15]Note that the CUJET1.0 results in [221] does not show predictions for e^-.

plays the most critical role in maintaining the robust level crossing pattern for pion and B meson. In [216] one sees that fragmentation functions do not alter the p_T dependent quenching pattern of light and bottom quark significantly, i.e. $R_{AA}^{\rm light}(p_T) \sim R_{AA}^{\rm pion}(p_T)$ and $R_{AA}^{\rm bottom}(p_T) \sim R_{AA}^{\rm B}(p_T)$, and at the partonic level the crossing between light and bottom $R_{AA}(p_T)$ already occurred at $p_T \simeq 25$GeV for RHIC and $p_T \simeq 35$GeV for the LHC, this fact suggests the near-negligible contribution of fragmentation functions to the intersection of $R_{AA}^{\pi}(p_T)$ and $R_{AA}^{B}(p_T)$. Furthermore, one also notices in [216] that at fixed L the $\Delta E/E(E)$ for light and bottom do not intersect each other until $p_T = 50$GeV/c, meaning the influence of partonic energy loss on the crossing pattern is less decisive than initial pp spectra. Indeed, one observes similar slopes of $d\sigma/dp_T(p_T)$ for light and bottom quark in the p_T range of $10 - 15$ GeV at RHIC and $20 - 30$ GeV at the LHC. It indicates the combined effect of partonic energy loss and initial spectra results in the crossing of $R_{AA}^{\pi}(p_T)$ and $R_{AA}^{B}(p_T)$, and among these two factors the latter is apparently more critical.

We can make several other observations about the flavor dependent quenching patterns in Fig. 3.5: firstly, R_{AA} for inclusive D meson and pion becomes similar at lower p_T at both RHIC and the LHC. One notices in [216] that the radiative energy loss probability distribution for charm and light quark almost overlap when jet has reasonably low initial energy, the similar suppression pattern of D meson and pion in this region would suggest comparable elastic energy loss probability distribution for them, and the D meson A+A production spectrum is expected to have a steeper slope at lower p_T.

Additionally, CUJET2.0 predicts in Fig. 3.5 that in lower p_T region the inclusive leading B meson is significantly less quenched than pion and D meson, whose R_{AA} tangles together. This prediction indicates measurements of open beauty spectra in the soft regime are decisive constraints on a wide range of pQCD energy loss models. Finally, at the LHC, the R_{AA}'s $B > e > D$ mass ordering at lower p_T evolves into $e > B > D$ at $p_T \approx 23$ GeV, and RHIC seems to have the same inversion at slightly larger p_T but less

discernible than the LHC. This mass ordering comes from a complex interplay between total energy loss probability distribution, and initial production spectra for charm and bottom jets, and fragmentation functions in the hadronization processes. Since non-photonic electron spectrum is the combination of $B \to e$, $D \to e$, and $B \to D \to e$ channels, the change in mass hierarchy can partially be attributed to a significant enhancement in the $B \to D \to e$ channel in certain p_T range, this range occurs at lower p_T at the LHC which has a larger multiplicity density and higher temperature than RHIC, and a semi-exclusive measurement of non-photonic electron productions in AA can thus be a critical benchmark.

3.2.2 The surprising transparency of QGP

As a representative fixed coupling pQCD energy loss model, WHDG [212] encountered dramatic challenges in the extrapolation to higher energy regimes probed by the LHC. First noted in [224], there is a generic "surprising transparency of QGP" phenomenon for pQCD energy model predictions at LHC, as shown in Fig. 3.6, that after a energy loss framework's physical parameters have been constrained using RHIC data, though its predictions in the LHC low multiplicity events are compatible with data, for the LHC high multiplicity events they render over-quenched results, and this discrepancy is significant. Quoting [224]: "The discrepancy challenges the two most basic jet tomographic assumptions: (1) that the energy loss scales linearly with the initial local comoving QGP density, ρ_0, and (2) that $\rho_0 \propto dN_{ch}(\sqrt{s}, \mathcal{C})/dy$ is proportional to the observed global charged particle multiplicity per unit rapidity as a function of $\sqrt{s}$ and centrality class, $\mathcal{C}$."

The scaling between the medium density and event multiplicity is required by the fundamental law of particle number conservation. Therefore, the "surprising transparency" can be translated into: the jet opacity scales weaker than linearly with the medium den-

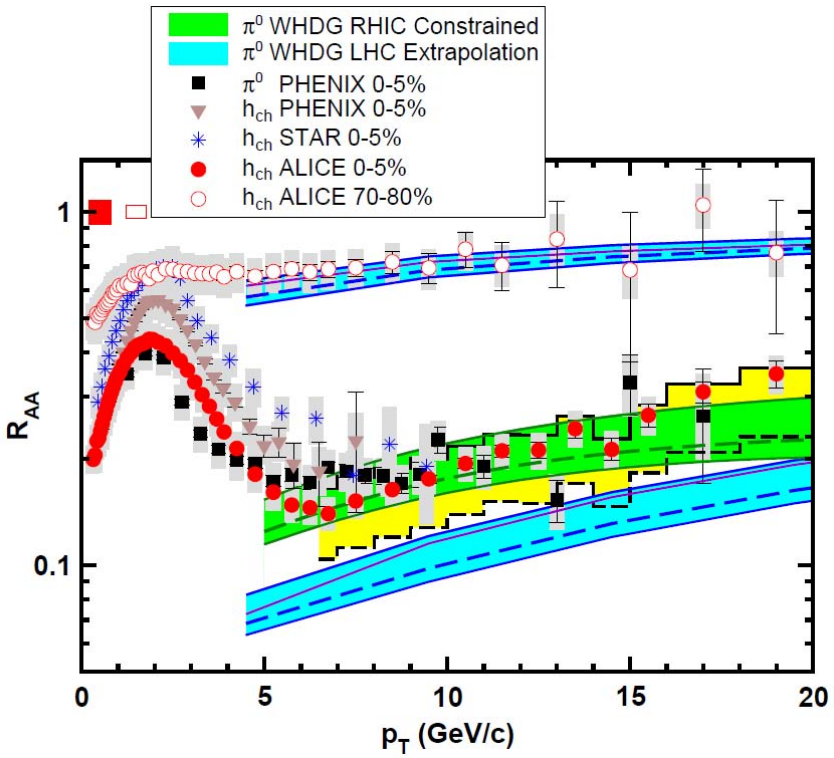

Figure 3.6: *The WHDG result of the nuclear modification factor R_{AA} at RHIC and the LHC. After its coupling strength parameter has been constrained at RHIC, the WHDG's extrapolation to the LHC underpredicts the experimental R_{AA}. This suggests a necessity for introducing running coupling effects into energy loss computations. (Taken from [224].)*

sity.

Since the jet opacity $\bar{n} = L/\lambda \sim L\rho\sigma \sim L\rho\alpha_s^2$, and harder momentum transfers between the jet parton and the hot deconfined plasma are expected in the LHC high multiplicity events, a natural way to solve the puzzle of the "surprising transparency" is to include running coupling effects into the energy loss theory. This effect has been extensive discussed in Section 2.3.5. And CUJET2.0 Eq. (3.8) has already implemented such a weakening of the coupling strength at short distances.

Fig. 3.7 shows the comparison between the CUJET2.0 results of the $R_{AA}(p_T)$ of inclusive π^0 at Au+Au 200AGeV and $h^{\pm}$ at Pb+Pb 2.76ATeV and corresponding RHIC and

the LHC measurements.

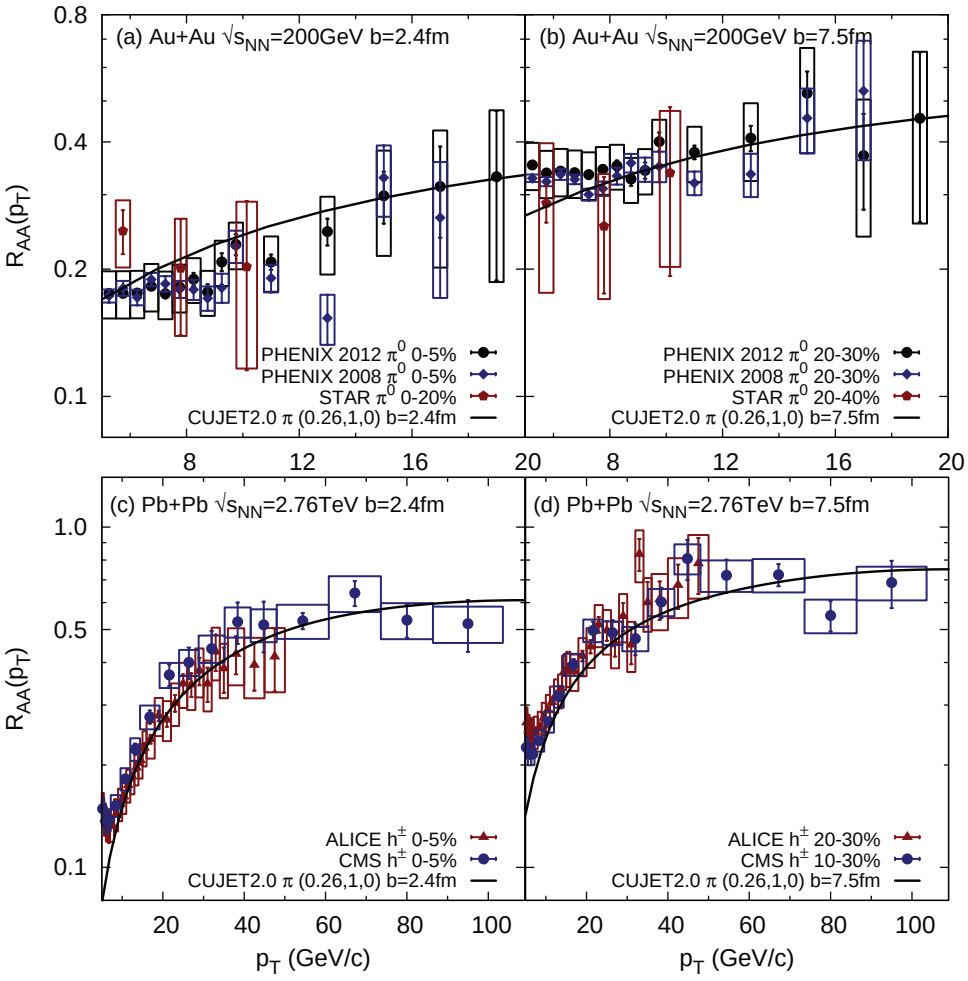

Figure 3.7: *Running coupling CUJET2.0 explains the "surprising transparency": the $\pi^0/h^{\pm}$ nuclear modification factors $R_{AA}(p_T)$ at RHIC and the LHC central and semi-peripheral collisions are consistent with data. (Taken from [216].)*

After adjusting $\alpha_{max} = 0.26$ to match the calculated pion nuclear modification factor from CUJET2.0 with the $p_T = 15$GeV/c reference point of experimentally measured inclusive neutral pion suppression factor from PHENIX 2012 [272] Au+Au 200AGeV central collisions, the rest of the R_{AA} curve in the range of $p_T = 5 \sim 20$GeV/c shows reasonable compatibility with both PHENIX 2008 and 2012 data. More importantly, when

moving on to simulate RHIC 20-30% centrality collisions by changing solely the impact parameter to $b = 7.5$ fm and fixing all other parameters in CUJET2.0, the theoretical R_{AA} result demonstrates even better agreement with experimental data.

Switching to the LHC data after constraining all CUJET model parameters with RHIC data, it was known fixed coupling CUJET1.0 encountered difficulties explaining the surprising transparency of the QGP in the LHC high p_T region [221], though this problem is eased by running coupling CUJET1.0 which has effectively reduced coupling strength at high energies, the pion R_{AA}'s steep rising and successive flattening pattern at the LHC remains only partially explained [223]. This issue is fully solved in running coupling CUJET2.0. As shown in Fig. 3.7(c)(d), at both ALICE and CMS, both central and semi-peripheral collisions, the CUJET2.0 inclusive pion R_{AA} curves seamlessly explained both the lower p_T steep rising and the high p_T saturating behavior of π^0 or $h^{\pm}$ nuclear suppression factor[16].

To get a mathematically more rigorous best fit α_{max} in CUJET2.0, the variance per degree of freedom $\chi^2/d.o.f.$ must be calculated. As shown in Fig. 3.8, α_{max} in CUJET2.0 is varied from 0.20 to 0.35 with 0.01 steps, while the dynamical HTL scenario is maintained by fixing $f_E = 1, f_M = 0$, in such a way the most compatible CUJET2.0 one parameter (α_{max}) fit at RHIC and the LHC can be studied, and the consistency of the model at different $\sqrt{s_{NN}}$'s can be tested. Fig. 3.8 shows the pion R_{AA} curves with those different α_{max} values at RHIC Au+Au 200AGeV and the LHC Pb+Pb 2.76ATeV central ($b = 2.4$ fm) and semi-peripheral ($b = 7.5$ fm) collisions. The experimental data being compared with are PHENIX 2008 [149], 2012 [272] and STAR [273] π^0 R_{AA} at RHIC; and ALICE [274] and CMS [152] $h^{\pm}$ R_{AA} at the LHC.

In all four panels of Fig. 3.8, focusing on $p_T < 40$ GeV region, when increasing max-

[16]There are more notable features about the CUJET2.0 results of light hadrons what have been included here. Extensive discussions about them can be found in [216].

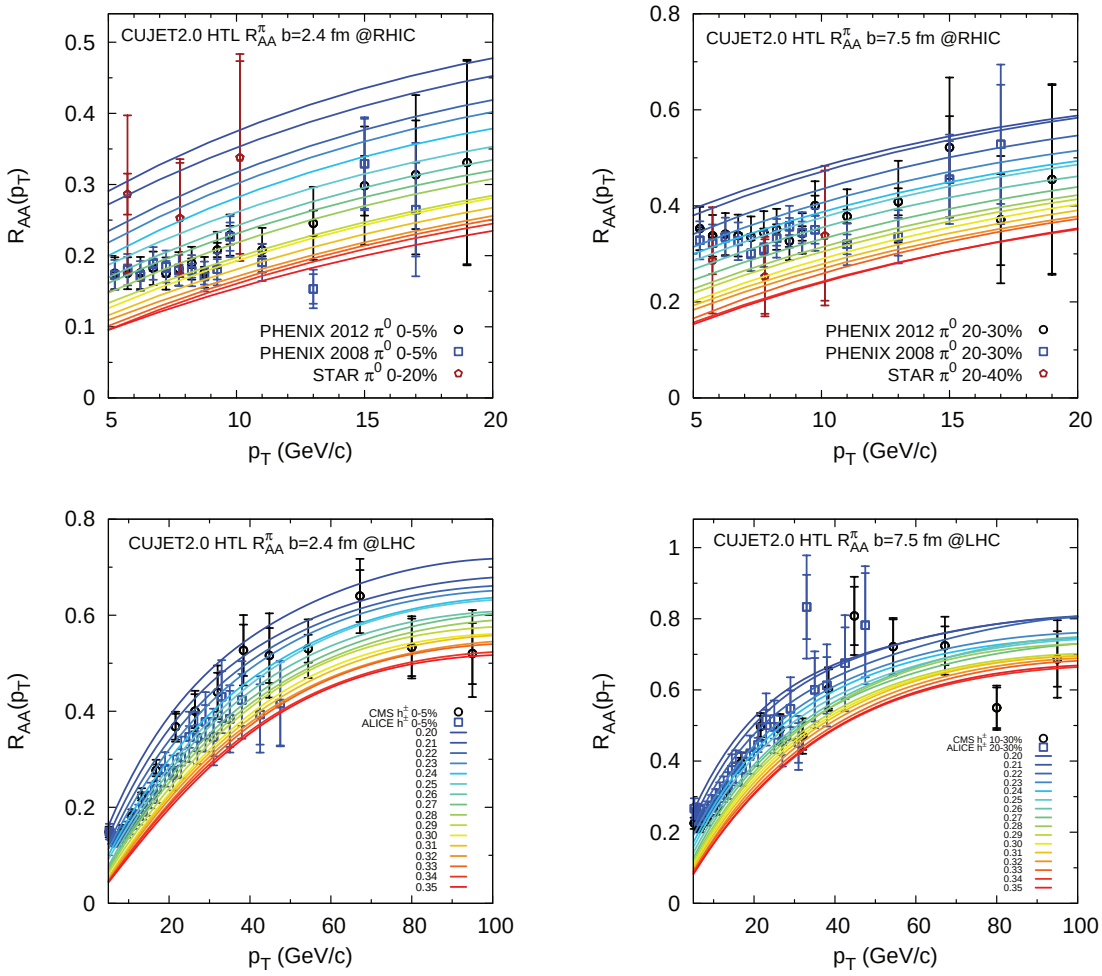

Figure 3.8: *CUJET2.0 results for π^0 $R_{AA}(p_T)$, with maximum coupling strength $\alpha_{max} = 0.20 \sim 0.35$ in the dynamical HTL scenario, at RHIC Au+Au 200AGeV (top panels) and the LHC Pb+Pb 2.76ATeV (bottom panels), central (b=2.4fm, left panels) and semi-peripheral (b=7.5fm, right panels) collisions. Despite the existence of multi-scale running coupling, the magnitude of jet quenching monotonically enhances with increasing α_{max} in both central and semi-peripheral collisions at both RHIC and the LHC. (Taken from [216].)*

imum coupling α_{max}, there is a monotonic decrease in R_{AA}[17]. Note that the saturation scale Q_{min} for the running coupling depends solely on the maximum coupling constant

[17]Very roughly, by eyeball, the magnitude of inclusive hadron suppression has near uniform increment with an uniformly increasing maximum coupling α_{max}, with exceptions at relatively large α_{max}'s where the spacing between R_{AA} curves becomes smaller.

α_{max}, i.e., $Q_{min} = \Lambda_{QCD}\text{Exp}\{2\pi/9\alpha_{\max}\}$. Take $\alpha_{max} = 0.20, 0.25, 0.30$ and 0.35 for example, the saturation scale $Q_{min} = 6.56, 3.26, 2.05$ and 1.47GeV respectively. At relatively low α_{max}, because of the large saturation scale, the strong coupling recovers asymptotically the fixed coupling scenario up to a relatively high energy, this explains the near uniform increment in the panels. The influence of running coupling is substantial at relative high α_{max} where the minimum running scale is low, in that situation the logarithmic decay of coupling strength resulted from vacuum running shrinks the spacing of R_{AA}'s more effectively.

A significant phenomenon shows up in the bottom panels of Fig. 3.8 – the flattening pattern (slope) of R_{AA} in high p_T ($p_T > 50$ GeV) region at the LHC is almost independent of the choice of α_{max}, this implies the relative insensitivity of R_{AA} saturation to the running coupling effect, and therefore to a certain extent the influence of running on the saturation of R_{AA} for ultra-high energy jets can be excluded. Note in [223], the previous calculation of multi-scale running coupling combined CUJET1.0, whose medium assumes static Glauber transverse profile plus 1+1D Bjorken longitudinal expansion, did not exhibit a clear signature of R_{AA} flattening. Therefore, evident R_{AA} saturation comes largely from the kinematics in a medium with both transverse and longitudinal expansion, which feature distinguishes CUJET2.0 from running coupling CUJET1.0. A dynamically transverse expanding medium, for instance a 2+1D viscous hydro fluid, plays a very important role in the R_{AA} flattening of high p_T jet in ultra-relativistic heavy ion collisions, and shall receive more attention in predicting jet quenching observables in A+A collisions from pQCD energy loss models.

The eikonal and soft approximation in the dynamical DGLV opacity expansion may break down in the low p_T region, hence for the purpose of calculating $\chi^2/d.o.f.$, experimental results in the range of $p_T > 8$ GeV are used to compare with CUJET2.0 R_{AA} curves. Note $\chi^2/d.o.f.(\alpha_{max}) < 2$ is an indicative signature of model consistency, and the con-

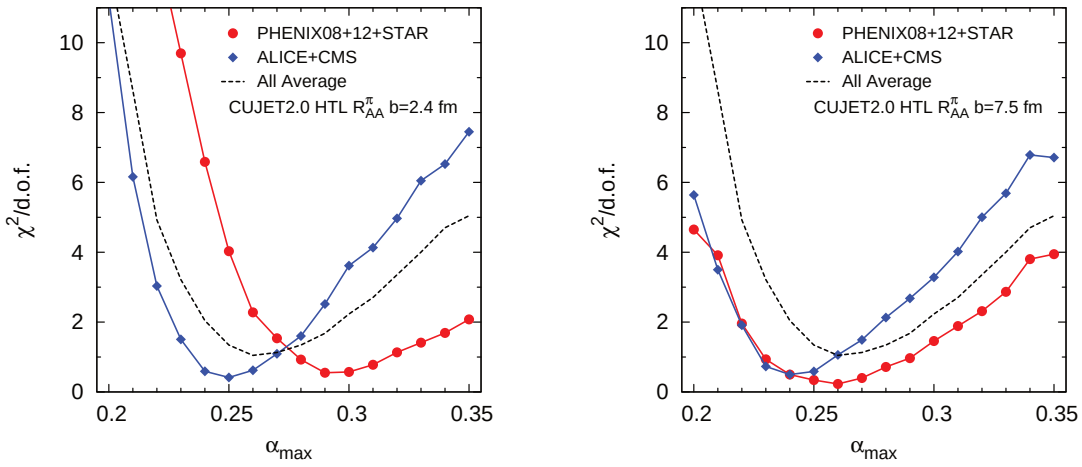

Figure 3.9: *$\chi^2/d.o.f.$ versus α_{max} calculated from Fig. 3.8 at RHIC and the LHC central and semi-peripheral collisions. Data from $p_T > 8$ GeV is used for safer preservation of DGLV's basic eikonal and soft approximations. The α_{max} ranges for $\tilde{\chi}^2 < 1$ and $\tilde{\chi}^2 < 2$ ($\tilde{\chi}^2 \equiv \chi^2/d.o.f.$) at RHIC and the LHC are shown in Table 3.1. If allowing 1.5 standard deviations per d.o.f., interpreting from the average curve, the most consistent CUJET2.0 HTL model at both RHIC and the LHC has $\alpha_{max} = 0.25 - 0.27$. If let average $\chi^2/d.o.f. < 2$, then $\alpha_{max} = 0.23 - 0.30$. (Taken from [216].)*

strained α_{max} range should be independent of whether $p_T > 5$ GeV or $p_T > 8$ GeV is chosen as long as the minimum p_T is sufficient for preserving basic assumptions of the CUJET2.0 model and number of points being selected at high p_T is large enough. Hence for safer comparisons $p_T > 8$ GeV is chosen, and Fig. 3.9 shows $\chi^2/d.o.f.$ vs α_{max} at RHIC (PHENIX08+12+STAR [149, 272, 273]) and the LHC (ALICE+CMS [152, 274]), in both central ($b = 2.4$ fm) and semi-peripheral ($b = 7.5$ fm) collisions[18]. And for better analyzing $\chi^2/d.o.f.$ curves in Fig. 3.9, detailed α_{max} ranges with $\tilde{\chi}^2 < 1$ and $\tilde{\chi}^2 < 2$ ($\tilde{\chi}^2 \equiv \chi^2/d.o.f.$) at RHIC and the LHC are listed in Table 3.1.

[18]Note that in statistical analyses most often χ^2 is studied rather than χ^2/dof. The σ error is given by the location of the parameter values where χ^2 increases above the minimum value by n^2, i.e., n σ error at $\chi^2 = \chi^2_{\rm min} + n^2$. In CUJET2.0 analyses, experimental systematic and statistical errors must be included, therefore χ^2/dof is computed.

α_{max}	RHIC $\tilde{\chi}^2 < 1$	LHC $\tilde{\chi}^2 < 1$	RHIC $\tilde{\chi}^2 < 2$	LHC $\tilde{\chi}^2 < 2$
$b = 2.4$ fm	0.28-0.32	0.24-0.27	0.26-0.35	0.23-0.28
$b = 7.5$ fm	0.23-0.29	0.23-0.25	0.22-0.31	0.22-0.27

Table 3.1: *Compilation of α_{max} values at RHIC and the LHC for two different centralities. (Taken from [216].)*

The combination of Fig. 3.9 and Table 3.1 provides quantitative information about the consistency of CUJET2.0 HTL model in various A+A collision configurations. One sees that if $\tilde{\chi}^2$ is strictly constrained to be less than 1,[19] for $b = 2.4$ fm central collisions, CUJET2.0 results at RHIC and the LHC have 0.01 offset in α_{max}, and for $b = 7.5$ fm semi-peripheral collisions, the results are in perfect agreements with RHIC and the LHC at $\alpha_{max} = 0.23 - 0.25$ range. One also notices that the averaged best fit α_{max} value at RHIC and the LHC in semi-peripheral collisions is around 0.03 lower than central collisions, and at either centrality the best fit the LHC α_{max} is approximately 0.03 lower than RHIC. These observations will trigger useful analysis in Section 3.4.

At current stage, in the CUJET2.0 HTL scenario, if restrict separate maximum $\tilde{\chi}^2$ to be 2, one finds that the intersecting α_{max} range for all four collisions at RHIC and the LHC, i.e. Au+Au 200AGeV and Pb+Pb 2.76ATeV mix with $b = 2.4$ fm and $b = 7.5$ fm, is $\alpha_{max} = 0.26 - 0.27$. This range of α_{max} $(0.26 - 0.27)$ coincides almost ideally with the range interpreted from $\tilde{\chi}^2 < 1.5$ for the average curve in Fig. 3.9 ($\alpha_{max} = 0.25 - 0.27$), indicating the CUJET2.0 model's rigorous consistency at varied A+A collisions, spanning a broad range of $\sqrt{s}$ and b[20].

Based on all the above discussions, one can conclude that from testing CUJET2.0 HTL scenario's agreement with centrality dependent neutral pion and charged hadron

[19] The expectation value of $\chi^2/d.o.f.$is 1 for a good fit, but with fluctuations about 1 of order $\sqrt{2/d.o.f.}$. Therefore in principle, determining the statistical significance of the parameters requires knowledge of both χ^2 and $d.o.f.$.

[20] Note that the similar curvature of the RHIC and the LHC $\chi^2/d.o.f.(\alpha_{max})$ parabolas at both centralities may play the role of a circumstantial evidence of the consistency of CUJET2.0, but this requires that the $d.o.f.$ at RHIC and the LHC are about the same.

suppression factors at RHIC and the LHC in the mid-rapidity region, the maximum coupling constant in the model is constrained to $\alpha_{max} = 0.25 - 0.27$[21], in which range the averaged $\chi^2/d.o.f.$ is strictly less than 1.5; if allow average $\chi^2/d.o.f. < 2$, then $\alpha_{max} = 0.23 - 0.30$.

3.3 Jet transport coefficient

The suppression of hadrons at large p_T results from scatterings of the leading parton with color charges in the thermal medium. This process can be characterized by the jet transport coefficient $\hat{q}$, defined as the average transverse momentum exchange squared per unit path length. CUJET2.0 treats thermal excitations in the homogeneous QCD medium as partonic quasi-particles, and the quark jet transport parameter $\hat{q}$ in CUJET2.0 is related to the (partonic) effective differential scattering cross section via

$$\hat{q}(E,T;\alpha_{max},f_E,f_M) = \int_0^{6ET} d\mathbf{q}_\perp^2 \mathbf{q}_\perp^2 \frac{d\sigma_{\rm eff}}{d\mathbf{q}_\perp^2}\rho_{\rm eff}(T) \ , \tag{3.58}$$

where the energy E and temperature T dependence comes in naturally from the partonic kinematics and the plasma density. In CUJET2.0, $\hat{q}$ depends also on the maximum strong coupling constant α_{max}, as well as chromo-electric and chromo-magnetic HTL screening mass deformation parameters (f_E, f_M), all of which originate from the effective cross section of the jet-medium scattering process,

$$\frac{d\sigma_{\rm eff}}{d\mathbf{q}_\perp^2} = \frac{2\pi f_E^2 \alpha_{\rm s}^2(\mathbf{q}_\perp^2)}{(\mathbf{q}_\perp^2+f_E^2\mu^2(T))(\mathbf{q}_\perp^2+f_M^2\mu^2(T))} \ , \tag{3.59}$$

[21] Note that the small α_{max} value originates partially from the fact that $\mu_E^{\rm HTL} \sim gT$ and $\mu_M = 0$ are less than the lattice QCD results (cf. e.g. [275]) which have $\mu_E \sim 2\mu_E^{\rm HTL}$ and $\mu_M \sim \mu_E/2$.

where the Debye mass $\mu(T) = T\sqrt{4\pi\alpha_s(9T^2)(1+N_f/6)}$. Note that from the derivation in Appendix A, in the Stefan-Boltzmann limit, the quasi-particle number density $n = \frac{\zeta(3)}{\pi^2}(16+9N_f)T^3$, and in a uniform thermal equilibrated medium, $\rho_{\rm eff} = n\frac{9N_fC_F/C_A+16}{16+9N_f}$ for a quark jet, and if gluons dominate, $\rho_{\rm eff} \approx 2T^3$.

Following the above the CUJET2.0 jet transport coefficient $\hat{q}$ (for a fundamental light quark jet) is calculated with $\alpha_{max} = 0.25 \sim 0.27$[22] in the dynamical HTL $f_E = 1, f_M = 0$ limit. The variations of the dimensionless jet transport parameter $\hat{q}/T^3$ with energy E and temperature T are illustrated in Fig. 3.10.

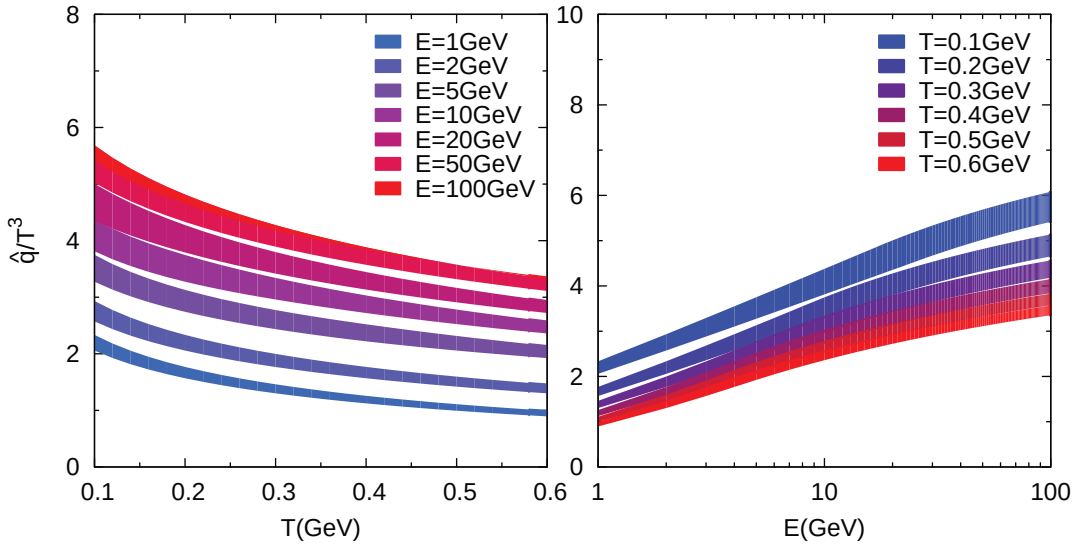

Figure 3.10: *The dimensionless jet transport coefficient $\hat{q}/T^3$ calculated in CUJET2.0 according to Eq. (3.58)(3.59) with parameters $\alpha_{max} = 0.25 - 0.27, f_E = 1, f_M = 0$ When E is fixed, the decrease of $\hat{q}/T^3$ with the rising T follows approximately a logarithmic law. When T is fixed, the logarithmic E dependence of $\hat{q}/T^3$ at high energy region comes naturally from the kinematic limit of the exchanged transverse momentum. (Taken from [216].)*

As shown in the right panel of Fig. 3.10, for an idealized static equilibrium QGP with

[22]These parameters are derived in the previous section through rigorous $\chi^2/d.o.f.$ consistency tests at various A+A collision configurations.

fixed temperature T, the average transverse momentum transfer squared per unit length between the quark jet and dynamical scattering centers shows a logarithmic dependence on initial jet energy, if the T^3 contribution from the medium density is factored out. This is expected from the kinematic limit of transverse momentum exchange, i.e. $(\mathbf{q}_\perp^2)_{max} = 6ET$ in Eq. (3.58). As one can tell, if Eq. (3.59) substituted into Eq. (3.59) and evaluated with $f_E = 1, f_M = 0$, then $\hat{q} \propto T^3 \log(1 + \frac{6ET}{\mu^2})$.

On the other end, as shown in the right panel of Fig. 3.10, for a light quark jet with fixed initial energy E, the dimensionless jet transport coefficient $\hat{q}/T^3$ drops logarithmically at an reducing rate as the temperature rises and reaches the high T region. This behavior first indicates that in CUJET2.0, as T increases, the absolute $\hat{q}$ itself increases since $d(T^3/\log T)/dT > 0$, but it gains slightly slower than medium density ($\rho \propto T^3$). One immediately sees that this characteristic is exactly consistent with the observed "surprising transparency" of the QGP that has been extensively discussed in the Section 3.2.2. The flattening of $\hat{q}/T^3$ versus T is expected from the Debye mass μ's temperature dependence, i.e. $\mu(T) = T\sqrt{4\pi\alpha_s(4T^2)(1 + N_f/6)}$. The thermal running effect has negligible contributions to the T dependence of $\hat{q}/T^3$ until T is high, at such high T the logarithmic reduction of the coupling strength will weaken the linear increase of the Debye mass with the increasing temperature.

It is also shown in the left panel of Fig. 3.10 that, for an initial quark jet with energy $E = 10$ GeV, in the typical temperature range reached by RHIC for most central Au+Au collisions, i.e. $180 \sim 370$ MeV, CUJET2.0 has $\hat{q}/T^3 \approx 3.8$; in the typical temperature range reached by the LHC for most central Pb+Pb collisions, i.e. $300 \sim 470$ MeV, CUJET2.0 has $\hat{q}/T^3 \approx 3.5$. Both values are consistent with not only LO pQCD estimates, but also the jet transport parameters extracted from other models such as HT-BW, HT-M, MARTINI and McGill-AMY in the JET collaboration [228] fitting to the same set of experimental hadron suppression factors at RHIC and the LHC A+A central collisions

[276]. This is demonstrated in Fig. 3.11 [276].

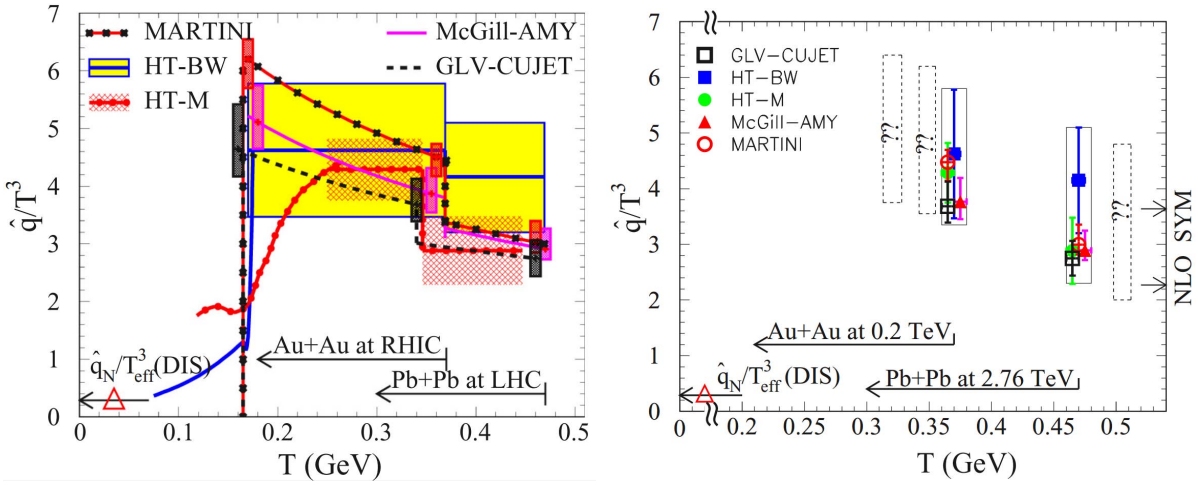

Figure 3.11: *Results of the jet transport coefficient $\hat{q}$ from the JET collaboration. The temperature dependence of the scaled $\hat{q}/T^3$ in different jet quenching models for an initial quark jet with energy $E = 10$ GeV is plotted. Besides the $\hat{q}/T^3$ computed from pQCD energy loss models in the JET collaboration, the arrows indicate the range of temperatures at the center of the most central A+A collisions, the dashed boxes indicate expected values in A+A collisions at $\sqrt{s_{NN}} = 0.063, 0.130, 5.5$ A · TeV, the triangle indicates the value of $\hat{q}_N/T^3_{\rm eff}$ in cold nuclei from deep inelastic scattering (DIS) experiments, the two arrows on the right axis in the right panel indicate values of $\hat{q}^{\rm NLO}_{\rm SYM}/T^3$ from next-to-leading order (NLO) supersymmetric Yang-Mills (SYM) theory. (Taken from [276].)*

In this figure, values of $\hat{q}$ at the center of the most central A+A collisions at an initial time $\tau_0 = 0.6$ fm/c in HT-BW and HT-M models are extracted from fitting to experimental data on hadron suppression factor R_{AA} at both RHIC and the LHC. In GLV-CUJET, MARTINI, and McGill-AMY models, it is calculated within the corresponding model with parameters constrained by experimental data at RHIC and the LHC.

Combining all 5 models and treating their variations as theoretical uncertainties, one can extract the range of $\hat{q}$ values constrained by the measured $R_{AA}(p_T)$'s of single hadrons

at RHIC and the LHC as

$$\frac{\hat{q}}{T^3} \approx \begin{cases} 4.6 \pm 1.2 & \text{at RHIC} , \\ 3.7 \pm 1.4 & \text{at LHC} . \end{cases} \tag{3.60}$$

At the highest temperatures reached in most central Au+Au 200 AGeV collisions at RHIC and Pb+Pb 2.76 ATeV collisions at the LHC. The corresponding absolute $\hat{q}$ is

$$\hat{q} \approx \begin{cases} 1.2 \pm 0.3 \\ 1.9 \pm 0.7 \end{cases} \text{GeV}^2/\text{fm at} \begin{cases} \text{T} = 370 \text{ MeV} , \\ \text{T} = 470 \text{ MeV} . \end{cases} \tag{3.61}$$

Note these values are for 10 GeV quarks jet at initial time $\tau_0 = 0.6$ fm/c,[23] they are very close to BDMPS-Z estimate [175] and are consistent with leading order (LO) pQCD estimates. CUJET, MARTINI and MCGILL-AMY models all show logarithmic temperature dependences. As a comparison, the value of $\hat{q}_N$ in cold nuclei extracted from jet quenching in DIS is 0.02-0.06 GeV^2/fm [277]. It is an order of magnitude smaller than the $\hat{q}/T^3$ Eq. (3.60) in A+A collisions at RHIC and the LHC.

There are attempts in lattice gauge theories to calculate $\hat{q}$ as well. In [278–280], it is found that nonperturbative contributions from soft modes in the collision kernel double the value of the NLO pQCD result for the jet quenching parameter[24]. Besides lattice QCD, there are other nonperturbative estimates with which one can compare the extracted values of $\hat{q}$ with. From the Anti-de Sitter/Conformal Field Theory (AdS/CFT) correspondence, the $\hat{q}$ in an $\mathcal{N} = 4$ SYM plasma at the strong coupling limit ('t Hooft coupling $\lambda = g^2_{\text{SYM}} N_c \to \infty$) has been calculated at LO (neglecting corrections of $\mathcal{O}(1/N_c)$

[23] Note that $\hat{q} \sim \alpha_s^2 T^3$, as a rough estimate, $\frac{(\hat{q}/T^3)_{\text{RHIC}}}{(\hat{q}/T^3)_{\text{LHC}}} \sim \frac{\alpha_s^2((3\times0.37)^2)}{\alpha_s^2((3\times0.47)^2)} = \frac{\log^2(3\times0.47/0.2)}{\log^2(3\times0.37/0.2)} \approx 1.4$, and $\hat{q}_{\text{RHIC}}/\hat{q}_{\text{LHC}} \approx 1.4 \times (0.37/0.47)^3 \approx 0.7$.

[24] In CUJET, N$^{\text{n}}$LO effects can be included by replacing the screened potential for parton scatterings with parameterized collision kernels that include both perturbative and nonperturbative contributions. This will be discussed in Chapter 5.

and $\mathcal{O}(1/\sqrt{\lambda})$) in [281]:

$$\hat{q}^{\rm LO}_{\rm SYM} = \frac{\pi^{3/2}\Gamma(3/4)}{\Gamma(5/4)}\sqrt{\lambda}T^3_{\rm SYM} \quad . \tag{3.62}$$

Taken into different degrees of freedom in three-flavor QCD and $N_c = 3$ SYM, through matching the local entropy density, one can get $T^3 \approx 3T^3_{\rm SYM}$. Thus $\hat{q}^{\rm LO}_{\rm SYM}/T^3 \sim 7.2 - 8.6$, it is significantly above the extracted $\hat{q}/T^3$ from pQCD models[25]. More on this will be discussed in Chapter 5.

The values of $\hat{q}$ have other implications[26]. As one already known, the QGP produced in heavy-ion collisions is a strongly interacting matter [94] whose collective flow is known to be well described by relativistic hydrodynamics with a negligible shear viscosity, and perturbation theory may not be applicable to study interactions in such a medium which is not dominated by quasi-particles. In [282], the authors derived a general expression relating the jet quenching parameter $\hat{q}$ with the shear viscosity η of a weakly coupled QGP, and the deviation from this relation is conjectured to be a more broadly valid measure of "strong coupling" of the medium than considering solely the shear viscosity divide by entropy density η/s. The relation is expressed as follows:

$$\frac{\eta}{s} \begin{cases} \approx 1.25T^3/\hat{q} & \text{for weak coupling ,} \\ \gg 1.25T^3/\hat{q} & \text{for strong coupling .} \end{cases} \tag{3.63}$$

In high energy region where the QCD coupling is supposed to be weak, the simplified CUJET2.0 $\hat{q}$ calculation from Eq. (3.58) and (3.58) shows $\hat{q}/T^3 \approx 3.7$ for typical temperatures reached by RHIC and the LHC, and $1.25T^3/\hat{q} \approx 4.2/4\pi$. This value is larger than

[25] NLO calculations of $\hat{q}$ however are $\sim 50\%$ lower compared with LO results, cf. e.g. [276].

[26] Note from Fig. 2.5 that $\hat{q}_{\rm ASW} \approx \hat{q}_{\rm GLV}/2$ by missing the first order in opacity. This means to fit RHIC and LHC data, $\hat{q}_{\rm ASW}$ must be artificially increased. It also suggests that high-p_T jets are sensitive to the mesoscopic finite opacity and the semi-hard $n = 1$ power law tail of the gluon radiation spectrum $dN_g/dxdk_\perp$.

the KSS quantum limit $\eta/s = 1/4\pi$ [114][27].

NLO pQCD may be one way to remove this discrepancy, however recent calculations show only a 50% increase in $\hat{q}$ at NLO [283–287]. On the other hand, even if the weak-strong coupling consistency in Eq. (3.63) can be reached through (N^n)LO calculations, since (N^n)LO corrections apply to all temperature range, overestimates of jet energy loss in heavy-ion collisions at RHIC and the LHC are guaranteed. One can thus see that this discrepancy implies deeper physics among non-perturbative aspects of QCD, and this is one of the key motivators for studies in Chapter 5.

3.4 The high p_T v_2 puzzle

Previous discussions in this chapter haven been focused on the overall suppression magnitude of jets in the hot deconfined medium formed in high energy A+A collisions, i.e. the nuclear modification factor R_{AA} (defined in Eq. (3.55)). The azimuthal angle dependence of the parton energy loss is however averaged out in this case. To quantify the anisotropy of the radiated gluon spectra, azimuthal harmonic coefficients defined in Eq. (1.38) must be taken into account. Specifically, the second Fourier coefficient – the azimuthal elliptic asymmetry v_2, that characterizes the energy loss difference between jets traveling along in reaction plane directions and out-of reaction plane directions, is of particular interests.

In the light quark sector, Fig. 3.12 shows the data of v_2 versus R_{AA} for charged hadrons or neutral pions with specific p_T's at different centralities in Au+Au $\sqrt{s_{NN}} = 200$ GeV collisions at RHIC [288]. The Geometric Radiative Energy Loss (GREL) model and the Molnar Parton Cascade (MPC) model results with varying effective coupling strengths are plotted as the red solid curve and the blue dashed curve. Neither curve goes through

[27]Note that $\eta/s \gg 1.25T^3/\hat{q}$ does not show up in this case, which is as expected since in computing the $\hat{q}$ in CUJET2.0, a weak coupling HTL QGP is assumed such that pQCD is applicable. On a separate note, the VISH2+1 with MC-Glauber has $\eta/s = 0.08 \approx 1/4\pi$, which value is extracted from fitting to hadron spectra and harmonics at low p_T.

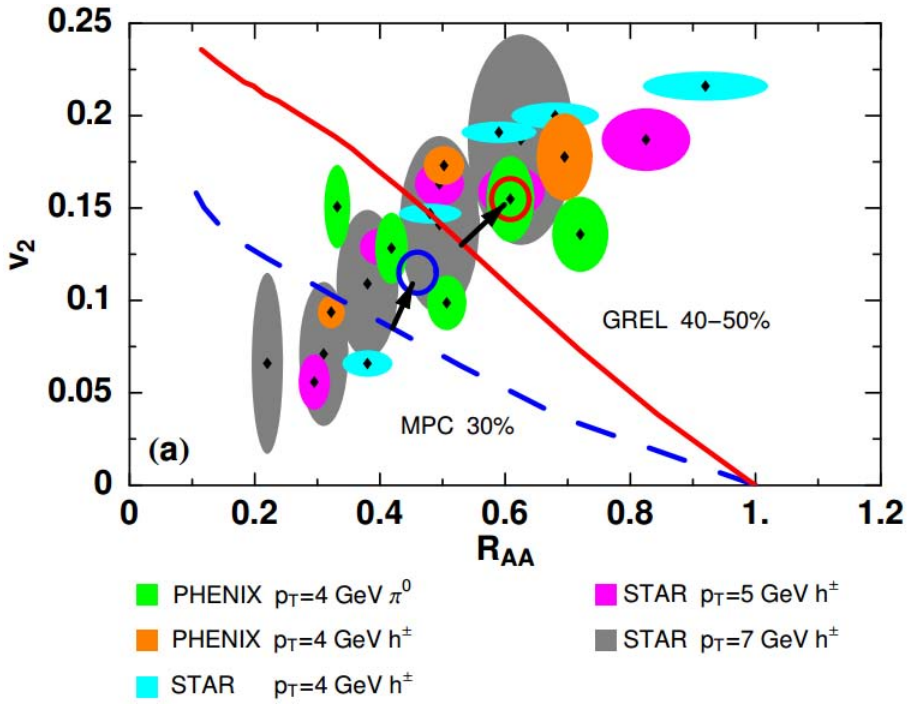

Figure 3.12: *Both the Geometric Radiative Energy Loss (GREL) model and the Molnar Parton Cascade (MPC) model are not able to simultaneously describe the R_{AA} and v_2 data from PHENIX/STAR (Au+Au $\sqrt{s_{NN}} = 200$ GeV) no matter how one tunes the effective coupling strength (along the red solid and blue dashed curve respectively) [288].*

the data points (both curves are below data). This implies for high p_T light hadrons, while most energy loss models may be able to explain their R_{AA}'s, they generally underestimated their v_2's.

In the heavy flavor sector, Fig. 3.13 shows a data-model comparison for D meson R_{AA} and v_2 simultaneously. One can immediately see from the comparison for R_{AA} and v_2 that it is challenging to simultaneously describe the large suppression of D mesons in central collisions and their anisotropy in non-central collisions. In general, models that are best in describing R_{AA} tend to underestimate v_2 and the models that describe v_2 tend to underestimate the measured R_{AA} at high p_T.

Combining the above results, one sees that the dilemma of simultaneously describing

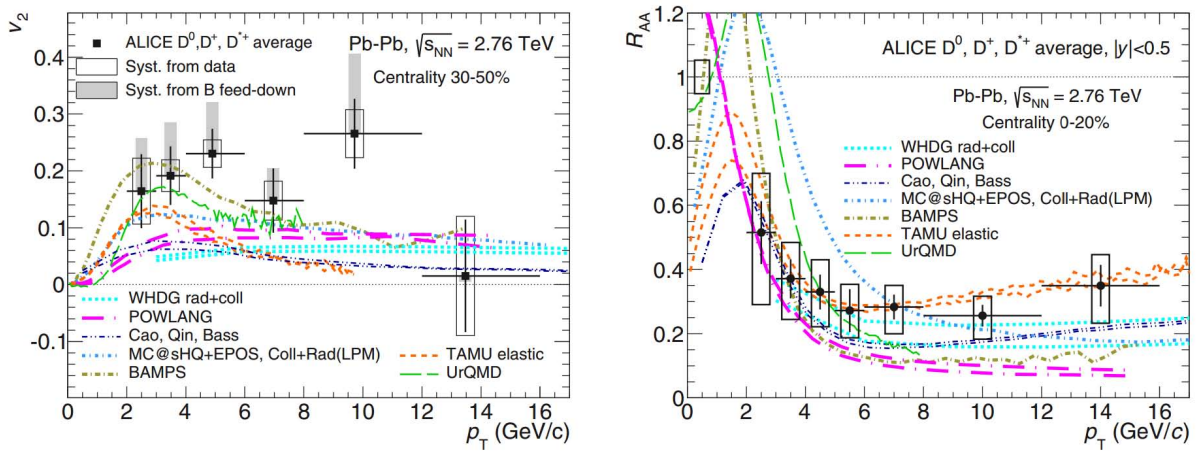

Figure 3.13: *Comparisons between recent ALICE measurements and pQCD/transport models for average D-meson v_2 in 30%-50% centrality and R_{AA} in 0-20% centrality Pb+Pb $\sqrt{s_{NN}}$ =2.76 TeV collisions. (Taken from [289].)*

high p_T hadrons' R_{AA} and v_2 at RHIC and the LHC is present in both the light hadron and heavy flavor sector. Since R_{AA}'s in central collisions are normally chosen as the reference for constraining parameters of energy loss models, the consequent near-universal $\sim 50\%$ underestimation of v_2 at large transverse momentum in peripheral collisions among these pQCD models is referred to as the "high p_T v_2 puzzle".

This is the topic that will be extensively discussed in this section. One will see that the solution to this puzzle requires a jet-medium coupling with non-trivial temperature dependence, and this is a hint for the dramatic role that non-perturbative aspects of QCD play on the "as if purely perturbative" jet quenching.

3.4.1 Azimuthal elliptic anisotropy

The v_n's defined in Chapter 1 Section 1.2.3 Eq. (1.38) concentrated on the "soft" aspects of the azimuthal harmonics, i.e. the low p_T particle anisotropic collective flows that are key observables related to the formation of QGPs in relativistic heavy-ion collisions. It is intuitive to imagine that with a large impact parameter for an A+A event, the region

of interest gains an increasingly asymmetric shape, and in a strongly coupled medium, the pressure gradients due to this initial azimuthal anisotropy effectively transfer into the collective flow of its components. On the other end, from the principle of jet tomography, these collective behaviors will be "seen" by the hard eikonal partons, therefore the "hard" aspects of these anisotropies, i.e. v_n components at high p_T, in fact characterize the asymmetries of jet energy loss in the medium. For this reason they are referred to as "azimuthal anisotropies", such that being distinctive from low p_T azimuthal collective flows.

The different types of azimuthal anisotropies are quantified in terms of Fourier components of the azimuthal angle distribution [290] (which is equivalent to Eq. (1.38)):

$$\frac{dN_h}{dyp_Tdp_Td\phi}(\sqrt{s},b)=\frac{1}{2\pi}\frac{dN_h}{dyp_Tdp_T}(\sqrt{s},b)\left(1+2\sum_{n=1}^{\infty}v_n(y,p_T;\sqrt{s},b;h)\cos\left(n(\phi-\Psi_n^h)\right)\right) . \tag{3.64}$$

Here $dN_h/dyp_Tdp_Td\phi$ represents the number of hadrons of species h observed at rapidity y, with transverse momentum p_T and azimuthal angle ϕ. Both $\frac{dN_h}{dydp_T}$ and the Fourier coefficients v_n depend on the initial rapidity density dN_i/dy. And dN_i/dy is a function of the energy $\sqrt{s}$ and centrality b of the collision.

Generally speaking, in the transverse plane with respect to the beam axis, the anisotropies generated from non-central A+A collisions is centrosymmetric if there are no fluctuations, and odd number Fourier components hence drop out. Among all harmonics, the azimuthal elliptic anisotropy v_2 is the most important one, and it is also the one that is least sensitive to fluctuations. Therefore, a systematic study of single particle v_2 can provide critical information about the jet-medium interaction mechanism as well as properties of the QGP.

3.4.2 The a-b-c model

To explore the solution to the high p_T v_2 puzzle, the phenomenological a-b-c model [224, 225, 291] introduced in Section 2.3.5 is an appropriate starting point. This model, albeit a simplified power law representation of the parton energy loss, can provide quantitative information about the interaction between the jet and the hot deconfined medium. Recall that in the a-b-c model, the energy loss is parameterized as (cf. Eq. 2.54)

$$\frac{dE}{dL} = -\kappa E^a L^b T^{2-a+b} \quad . \tag{3.65}$$

As noted in [224, 225, 291], approximately speaking, $a = 0$ is the elastic limit, $a = 1$ is the pQCD radiative limit, and $a = 2$ is the strong coupling AdS/CFT limit. In [291], the $a = 1$ "pQCD" energy loss model with κ constrained by RHIC and the LHC R_{AA} is utilized to study the high p_T v_2 and results are shown in Fig. 3.14.

One can see that the $\sim 50\%$ underestimation of high transverse momentum v_2 in the heavy flavor sector again appears in the light sector, and energy loss fluctuations influence only minimally the azimuthal elliptic anisotropy. Since the a-b-c model characterization of different energy loss mechanisms is almost generic, one thus expect the high p_T v_2 puzzle to be a universal problem for all pQCD based jet energy loss models in computing the flavor dependent azimuthally anisotropic gluon radiation spectra.

3.4.3 Path-dependent coupling

To visualize more clearly the simultaneous fit to high p_T particle suppression patterns and azimuthal elliptic asymmetries, one can calculate the R_{AA} with two distinctive azimuthal directions. The typical choice of the azimuthal angle set is the in reaction plane $\phi = 0$ and the out of reaction plane $\phi = \pi/2$. The corresponding angle-wise nuclear suppression

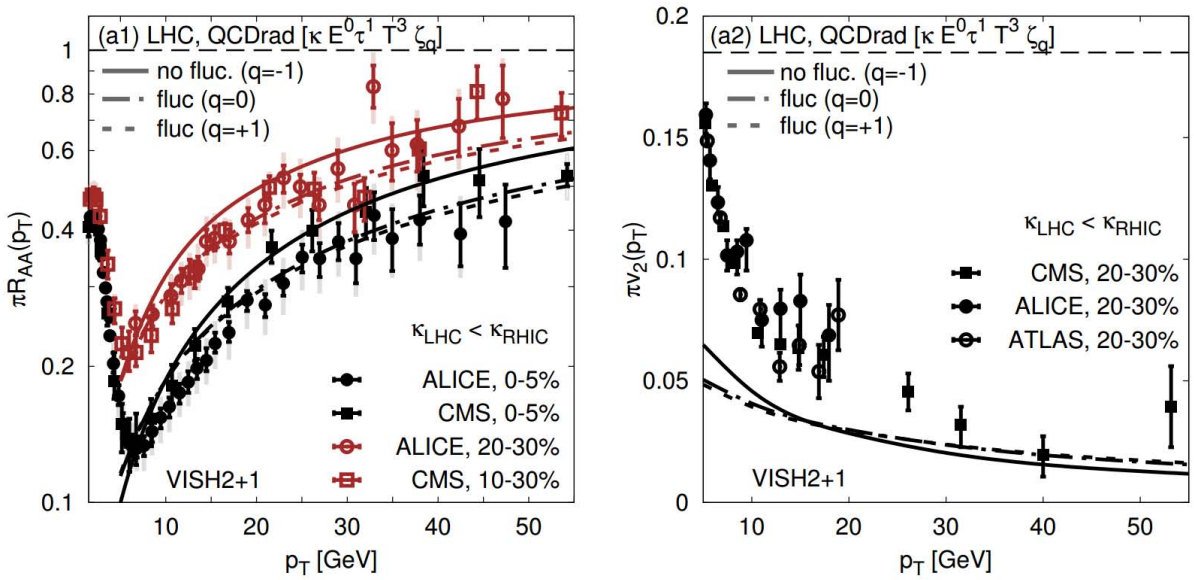

Figure 3.14: *The a-b-c model study of high p_T R_{AA} and v_2 for light hadrons at the LHC with parameter $a = 1$ simulating the pQCD radiative energy loss limit. The bulk QGP flow fields are from $\eta/s = 0.08$ VISH2+1 viscous hydro simulations. After parameters are constrained using reference R_{AA}, the model underestimates the high p_T v_2 by $\sim 50\%$. (Take from [291].)*

factors R^{in}_{AA} and R^{out}_{AA} are defined as:

$$\begin{cases} R^{in}_{AA}(y,p_T) = \dfrac{\frac{dN_h^{AA}}{dydp_Td\phi}|_{\phi=0}}{N_{binary}\frac{dN_h^{pp}}{dydp_Td\phi}|_{\phi=0}} = \dfrac{\frac{dN_h^{AA}}{dydp_T}\frac{1}{2\pi}(1+2v_1+2v_2+\cdots)}{N_{binary}\frac{dN_h^{pp}}{dydp_Td\phi}|_{\phi=0}} \\ R^{out}_{AA}(y,p_T) = \dfrac{\frac{dN_h^{AA}}{dydp_Td\phi}|_{\phi=\frac{\pi}{2}}}{N_{binary}\frac{dN_h^{pp}}{dydp_Td\phi}|_{\phi=\frac{\pi}{2}}} = \dfrac{\frac{dN_h^{AA}}{dydp_T}\frac{1}{2\pi}(1-2v_2-\cdots)}{N_{binary}\frac{dN_h^{pp}}{dydp_Td\phi}|_{\phi=\frac{\pi}{2}}} \end{cases} , \quad (3.66)$$

The AA, pp superscript and N_{binary} has the same meaning as in Eq. (3.55). Since the p+p collision is presumably central, and generally no azimuthal anisotropy is expected, one has $\frac{dN_h^{pp}}{dydp_Td\phi}|_{\phi=0} = \frac{dN_h^{pp}}{dydp_Td\phi}|_{\phi=\frac{\pi}{2}}$, and $\frac{dN_h^{pp}}{dydp_T} \equiv \int_0^{2\pi} d\phi \frac{dN_h^{pp}}{dydp_Td\phi} = 2\pi \frac{dN_h^{pp}}{dydp_Td\phi}|_{\phi=\phi_0}$, where ϕ_0 is an arbitrary azimuthal angle. In terms of rapidity y, the region of interests has $y \approx 0$, hence one short-writes $\frac{dN_h^{pp}}{dydp_T}|_{y=0}$ as $\frac{dN_h^{pp}}{dp_T}$. Neglecting fluctuations by setting odd number

harmonics to zero, in the mid-rapidity region, one gets

$$\begin{cases} R_{AA}^{in}(p_T) \approx \dfrac{\frac{dN_h^{AA}}{dydp_T}\left(1+2v_2+2v_4\cdots\right)}{N_{binary}\frac{dN_h^{pp}}{dydp_T}} = R_{AA}^{h}\left(1+2v_2+2v_4\cdots\right) \quad , \\ R_{AA}^{out}(p_T) = \dfrac{\frac{dN_h^{AA}}{dydp_T}\left(1-2v_2-2v_4\cdots\right)}{N_{binary}\frac{dN_h^{pp}}{dydp_T}} = R_{AA}^{h}\left(1-2v_2-2v_4\cdots\right) \quad . \end{cases} \tag{3.67}$$

In CUJET2.0, the pion's R_{AA}^{in} and R_{AA}^{out} in the mid-rapidity region for p_T up to 18 GeV/c is calculated for Au+Au 200AGeV central and semi-peripheral collisions, and compared with corresponding PHENIX [272] data[28]. The results are shown in Fig. 3.15.

In Section 3.3, the maximum coupling constant α_{max} in the CUJET2.0 HTL scenario has been constrained to be $0.25-0.27$, this range of α_{max} renders the most consistent pion R_{AA} at RHIC Au+Au $\sqrt{s_{NN}}=200$GeV and the LHC Pb+Pb $\sqrt{s_{NN}}=2.76$TeV central and semi-peripheral collisions through stringent $\chi^2/d.o.f.$ calculations. However, the R_{AA}^{in} and R_{AA}^{out} for $\alpha_{max}=0.26$ in both panels of Fig. 3.15 have smaller gaps than the PHENIX measurements, indicating over-isotropized high p_T single inclusive pion spectra in the model, despite mean values that are in agreement with data.

Nevertheless, one notes in Section 3.3 that, Fig. 3.9 and Table 3.1 suggest, when χ^2/d.o.f. < 1[29], α_{max} has a non-negligible range which varies for different collisions. Taking advantage of this flexibility, CUJET2.0 may create reaction plane dependent pion quenching patterns which are compatible with experiment measurements[30]. To be rigor-

[28] In principle, better comparison with experiments can be achieved by integrating over the same $\Delta\phi$ window of measurements of R_{AA} with respective to reaction planes. However, due to limited computing power, we have to stay with the faster way of computing R_{AA} in-plane/out-plane, i.e. evaluating the spectra at $\phi=0,\pi/2$. The effect of window size will be explored in future works, on an event-by-event basis, it may contribute non-trivially.

[29] Note that when computing χ^2/d.o.f., the experimental errors taken into account are the statistical and systematic errors combined in quadrature. And strictly speaking, the systematic errors should be separated into the part that varies in common for all points and the part that varies point-to-point.

[30] Allow at most 10% variations in α_{max} and choose $\alpha_{max}=0.26$ R_{AA}^{in} and $\alpha_{max}=0.29$ R_{AA}^{out} for $b=2.4$ fm, $\alpha_{max}=0.23$ R_{AA}^{in} and $\alpha_{max}=0.26$ R_{AA}^{out} for $b=7.5$ fm can generate a compatible reaction plane dependent suppression pattern for pion, and all these α_{max} values fall within respective $\chi^2/d.o.f.<1$ and $\chi^2/d.o.f.<2$ entries in Table 3.1.

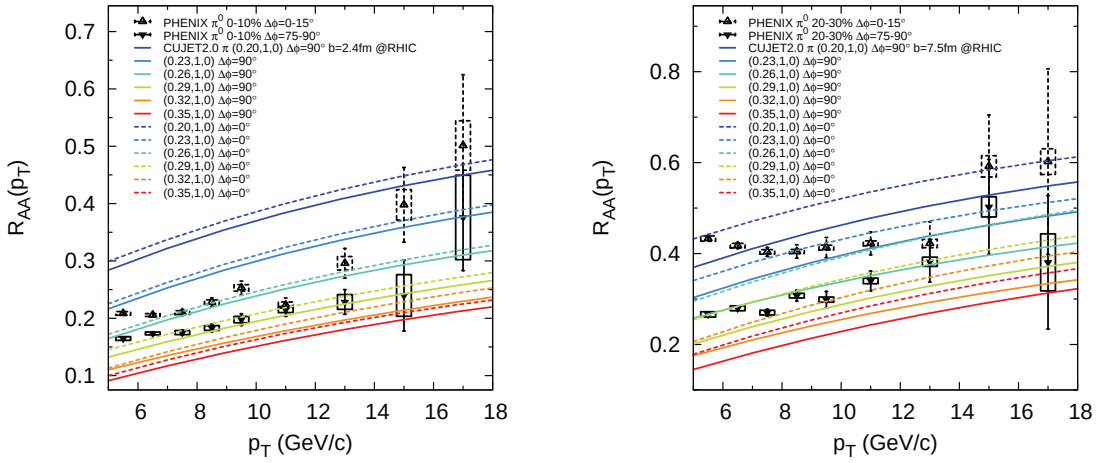

Figure 3.15: *CUJET2.0 pion R_{AA}^{in} ($\Delta\phi = 0°$, dashed curves) and R_{AA}^{out} ($\Delta\phi = 90°$, solid curves) versus p_T for Au+Au 200AGeV $b = 2.4$ fm (left panel) and $b = 7.5$ fm (right panel) calculated in the HTL $(f_E, f_M) = (1, 0)$ scenario with maximum coupling constant α_{max} varies from 0.20 to 0.35 in 0.03 steps. Theoretical results are compared with PHENIX [272] $\pi^0 R_{AA}$ in Au+Au collisions at $\sqrt{s_{NN}} = 200$ GeV with centrality 0-10% and reaction plane $\Delta\phi = 0 - 15°$ (left panel, dashed black), 0-10% and $\Delta\phi = 75 - 90°$ (left panel, solid black), 20-30% and $\Delta\phi = 0 - 15°$ (right panel, dashed black), 20-30% and $\Delta\phi = 75 - 90°$ (right panel, solid black). (Taken from [216].)*

ous, one should first plot the $\chi^2/d.o.f.$ vs α_{max} for the R_{AA}^{in} and R_{AA}^{out} in Figure 3.15 using $p_T > 8$ GeV, which p_T range matches the choice in Section 3.3, the results are shown in Figure 3.16.

One finds that in the left panel of Figure 3.16, for $b = 2.4$ fm central collisions at RHIC, in the CUJET 2.0 HTL scenario R_{AA}^{in} is best fitted by $\alpha_{max} = 0.26 - 0.27$, while R_{AA}^{out} is best fitted by $\alpha_{max} = 0.28 - 0.30$. In the right panel of Figure 3.16, for $b = 7.5$ fm semi-peripheral collisions at RHIC, R_{AA}^{in} is best fitted by $\alpha_{max} = 0.23 - 0.25$, while R_{AA}^{out} is best fitted by $\alpha_{max} = 0.26 - 0.27$.

If one chooses $\alpha_{max} = 0.26$ R_{AA}^{in} and $\alpha_{max} = 0.29$ R_{AA}^{out} for $b = 2.4$ fm, $\alpha_{max} = 0.23$ R_{AA}^{in} and $\alpha_{max} = 0.26$ R_{AA}^{out} for $b = 7.5$ fm, the CUJET2.0 results are able to reach perfect

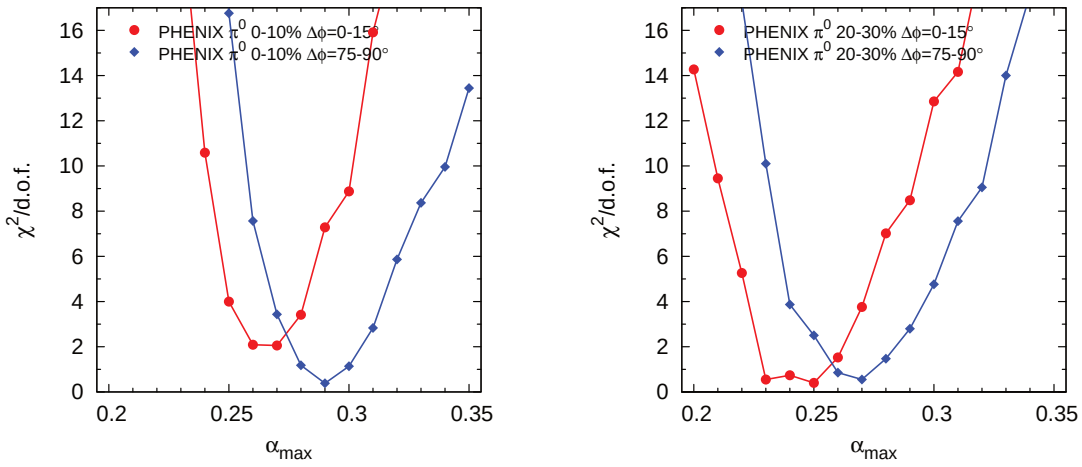

Figure 3.16: *$\chi^2/d.o.f.$ versus α_{max} calculated from Fig. 3.15 at RHIC Au+Au $\sqrt{s_{NN}} = 200 GeV$ central $b = 2.4$ fm (left panel) and semi-peripheral $b = 7.5$ fm (right panel) collisions. PHENIX [272] $\pi^0 R_{AA}$ with reaction plane $\Delta\phi = 0-15°$ (red) and $\Delta\phi = 75-90°$ (blue), and centrality 0-10% (left) and 20-30% (right) are the experimental references. (Taken from [216].)*

agreements with RHIC R_{AA}^{in} and R_{AA}^{out} date. Since $R_{AA} = (R_{AA}^{in} + R_{AA}^{out})/2$, this set of α_{max}'s effectively generates R_{AA} with $\alpha_{max} = 0.275$ at $b = 2.4$ fm and $\alpha_{max} = 0.245$ at $b = 7.5$ fm. Based on Figure 3.9 and Table 3.1, one sees that the $\chi^2/d.o.f.$ for the average R_{AA} resulting from this α_{max} sequence is: RHIC $b = 2.4$ fm, $\chi^2/d.o.f. < 1.5$; RHIC $b = 7.5$ fm, $\chi^2/d.o.f. < 1$[31]; LHC $b = 2.4$ fm, $\chi^2/d.o.f. < 1.5$; LHC $b = 7.5$ fm, $\chi^2/d.o.f. < 1$ – the $\chi^2/d.o.f.$ for average R_{AA} with these α_{max}'s in the CUJET2.0 HTL scenario is strictly less than 1.5 in all four collisions. That means this modest variation in α_{max} is intrinsically allowed by the CUJET2.0 model without jeopardizing its consistency with averaged hadron R_{AA}'s in various collision configurations.

Notice among this set of α_{max} parameters, for both $b = 2.4$ fm and $b = 7.5$ fm, the difference in α_{max} for R_{AA}^{in} and R_{AA}^{out} is 0.03. And for either R_{AA}^{in} or R_{AA}^{out}, the variance

[31] In fact if one has χ^2/d.o.f. consistently less than 1 one may overestimate the experimental errors in the data if a systematic error common to all points is treated as a point-to-point error).

in α_{max} for $b = 2.4$ fm and $b = 7.5$ fm is 0.03 (which surprisingly coincides with the RHIC and the LHC averaged α_{max} gap discussed in Section 3.3). The maximumly 10% α_{max} deviations in R_{AA}^{in} and R_{AA}^{out}, $b = 2.4$ fm and $b = 7.5$ fm imply that the anisotropic path averaged effective coupling strengths can be originated from local effects.

In addition, the ordering of α_{max} in terms of averaged path length is noteworthy: at τ_0, the length of the medium in $b = 2.4$ fm and $b = 7.5$ fm collisions along $\phi = 0°$ and $\phi = 90°$ direction can be approximately ordered as 7.5fm+0° < 7.5fm+90° ≈ 2.4fm+0° < 2.4fm+90°, and the best fit α_{max} in corresponding situations is $0.23 < 0.26 = 0.26 < 0.29$. It means that within CUJET2.0, longer path length requires stronger coupling in order to predict the correct high p_T single particle v_2.

After constrained the azimuthal anisotropy in CUJET2.0 at RHIC, the natural next step is to test the model consistency with R_{AA}^{in} and R_{AA}^{out} for the LHC Pb+Pb 2.76 ATeV central and semi-peripheral collisions.

Assuming no fluctuations in the azimuthal plane, recall that Eq. (3.67) suggests R_{AA}^{in} and R_{AA}^{out} depend solely on even harmonics. If one further assumes higher order components have much smaller magnitude compared to v_2 and hence can be dropped, one gets

$$\begin{cases} R_{AA}^{in}(p_T) \approx R_{AA}^{h}\,(1 + 2v_2) \quad , \\ R_{AA}^{out}(p_T) \approx R_{AA}^{h}\,(1 - 2v_2) \quad , \end{cases} \tag{3.68}$$

in this limit. And the elliptic asymmetry v_2 follows from R_{AA}^{in} and R_{AA}^{out} via

$$v_2(p_T) = \frac{1}{2}\frac{R_{AA}^{in}(p_T) - R_{AA}^{out}(p_T)}{R_{AA}^{in}(p_T) + R_{AA}^{out}(p_T)} \quad . \tag{3.69}$$

In CUJET2.0, results of pion v_2's using Eq. (3.69) for RHIC Au+Au $\sqrt{s_{NN}} = 200$GeV and the LHC Pb+Pb $\sqrt{s_{NN}} = 2.76$TeV, central $b = 2.4$ fm and semi-peripheral $b = 7.5$

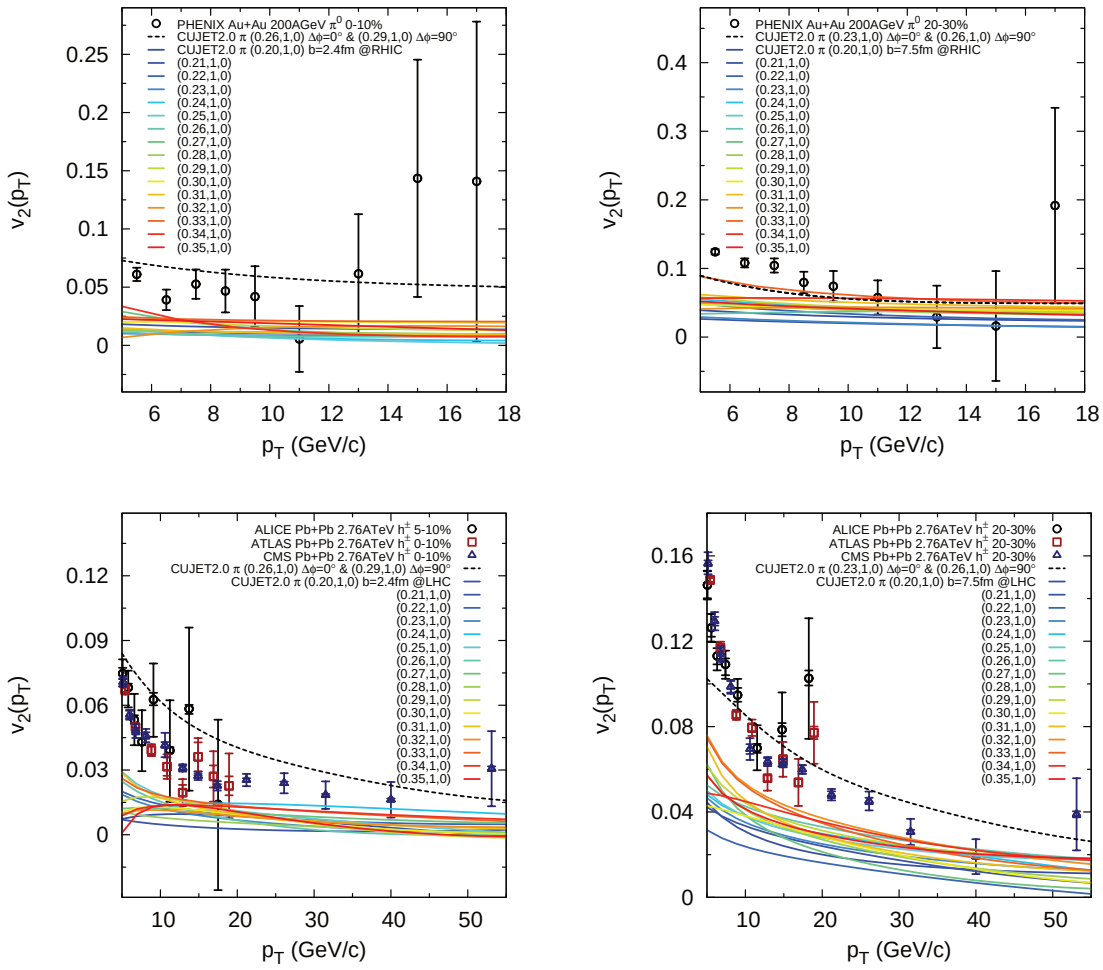

Figure 3.17: *CUJET2.0 pion single particle anisotropy $v_2(p_T)$in Au+Au $\sqrt{s_{NN}} = 200\,GeV$ (top panels) and Pb+Pb $\sqrt{s_{NN}} = 2.76\,TeV$ (bottom panels), central ($b = 2.4$ fm, left panels) and semi-peripheral ($b = 7.5$ fm, left panels) collisions at mid-rapidity are compared with corresponding PHENIX [294], ALICE [292], ATLAS [293] and CMS [107] measurements. The maximum coupling constant α_{max} is varied from 0.20 to 0.35 with 0.01 steps in the CUJET2.0 HTL scenario. After allowing 10% variations of α_{max} along different jet paths, CUJET2.0's v_2's (dashed black) arrive at an excellent consistency with the LHC measurements in both central and semi-peripheral collisions.*

fm collisions are shown in Fig. 3.17, and corresponding ALICE [292], ATLAS [293], CMS [107], and PHENIX [294] data are compared.

$\chi^2/d.o.f.$ ($b = 7.5$ fm)	v_2, RHIC	v_2, LHC	R_{AA}, RHIC	R_{AA}, LHC
$\alpha^{in}_{max} = 0.23$, $\alpha^{out}_{max} = 0.23$	3.72	43.03	0.93	0.73
$\alpha^{in}_{max} = 0.26$, $\alpha^{out}_{max} = 0.26$	2.06	24.89	0.23	1.06
$\alpha^{in}_{max} = 0.23$, $\alpha^{out}_{max} = 0.26$	0.50	4.92	0.42	0.54

Table 3.2: *$\chi^2/d.o.f.$ for v_2 and azimuthally averaged R_{AA} in semi-peripheral $b = 7.5$ fm collisions at RHIC Au+Au $\sqrt{s_{NN}} = 200\,GeV$ and the LHC Pb+Pb $\sqrt{s_{NN}} = 2.76\,TeV$, with different choices of α_{max} values for R^{in}_{AA} (α^{in}_{max}) and R^{out}_{AA} (α^{out}_{max}) in the CUJET2.0 HTL scenario. Reference curves are shown in Fig. 3.8, Fig. 3.15, and Fig. 3.17.*

Fig. 3.17 shows that if varying solely the maximum coupling constant α_{max} from 0.20 to 0.35 with 0.01 steps in the CUJET2.0 HTL scenario, none of the theoretical curves matches the single pion v_2 at both Au+Au 200AGeV and Pb+Pb 2.76ATeV, central and semi-peripheral collisions. Nevertheless, due to the non-negligible influence that anisotropy and heterogeneity/inhomogeneity have on the jet-medium interaction, local effects can alter the CUJET2.0 framework significantly.

By choosing $\alpha_{max} = 0.26$ R^{in}_{AA} and $\alpha_{max} = 0.29$ R^{out}_{AA} for $b = 2.4$ fm, $\alpha_{max} = 0.23$ R^{in}_{AA} and $\alpha_{max} = 0.26$ R^{out}_{AA} for $b = 7.5$ fm in the HTL scenario, one has effectively constrained the CUJET2.0 model at RHIC with assumed azimuthal α_{max} anisotropy caused by possible local temperature field effects. The top panels of Fig. 3.17 show the consequential single pion v_2's at RHIC central and semi-peripheral collisions are compatible with respective experimental measurements, as expected. More importantly, one extrapolates the same CUJET2.0 framework (with azimuthal dependence of α_{max}) to the LHC and calculate the single particle v_2 using the same α_{max} parameter set, theoretical results demonstrate an even better agreement with ALICE, ATLAS and CMS data, in both central and semi-peripheral collisions (particularly the latter, cf. Table 3.2). Note that the choice of $\alpha^{in}_{max} = 0.23$, $\alpha^{out}_{max} = 0.26$ significantly reduces the $\chi^2/d.o.f.$ for v_2 at both RHIC and the LHC, especially the latter one. Meanwhile, this set of α_{max} parameters maintains almost perfect agreements with both RHIC and the LHC for azimuthally averaged R_{AA}.

The consistency, of the open heavy flavor and heavy flavor lepton's single particle azimuthal anisotropy calculated in the same CUJET2.0 framework (with azimuthal variations), with experimental measurements can shed light on the underlying physics for this azimuthal variation of path averaged coupling strength [32].

A mini-summary of Section 3.4.3: in the CUJET2.0 framework, by allowing the path averaged maximum coupling constant α_{max} to increase by 10% from in reaction plane to out-of reaction plane paths one can get a 100% boost in the high p_T particle azimuthal anisotropy, and bring theoretical results to be compatible with data. This suggest a non-trivial temperature dependence of the jet-medium coupling, especially in the near-T_c regime. This suggests the importance of considering non-perturbative aspects of QCD in the seemingly "purely perturbative" jet quenching problem.

3.4.4 Near T_c enhancement

The path dependent coupling found in the previous section to account for the anomalously large high p_T v_2 in non-central heavy-ion collisions indicates a surprising sensitivity of the jet-medium coupling to the local QGP temperature. In reality, quenching is not proportional to the matter density, but a non-trivial function of it. In the study of [295], the authors show that there is a geometric limit for v_2: the observed asymmetry should be less than some value $v_2(\text{large } \mathrm{p_T}, b) < v_2^{\max}(b)$ provided by the geometry of the overlapping region of two colliding nuclei (shown in the right panel of Fig. 3.18). They further show a layer-wise geometric limit for v_2, that is, if one slices the (expanding) fireball into shells

[32] Note that by allowing azimuthal variations of the coupling strength (the origin of the azimuthal variation of the coupling strength will be discussed in following chapters), the prediction power of CUJET2.0 model is not jeopardized. It has been shown that by fixing α_{max} for in-plane/out-of-plane at RHIC, the extrapolation of $R_{AA}^{in/out}(p_T)$ to the LHC is in agreement with data. That means one can use CUJET2.0 to fit RHIC at a particular centrality, then extrapolate it to predict the LHC, or vice versa. Moreover, provided the built-in mass hierarchy in the CUJET2.0 model, one can extrapolate $v_2^{\pi}(p_T)$ to predict $v_2^{D,B,e^-}(p_T)$ at various centralities at both RHIC and the LHC.

with a certain entropy density range, the anisotropy has an upper bound in each section, and results are shown in the left panel of Fig. 3.18.

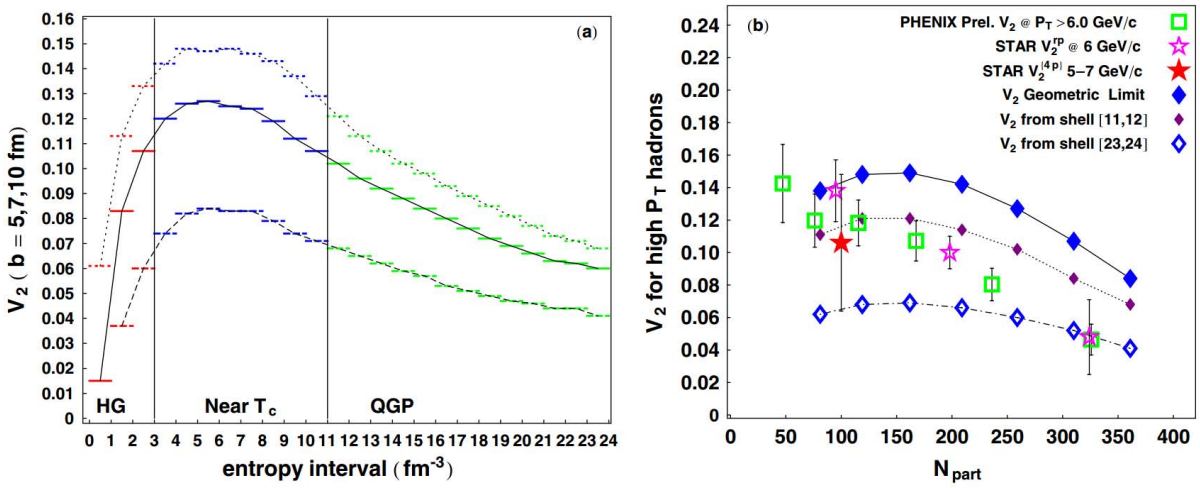

Figure 3.18: *Left: The v_2 obtained for each entropy shell at different centralities. Right: $v_2^{\max}$ for high p_T hadrons calculated at different $N_{\rm part}$ compared with available RHIC data. (Taken from [295].)*

One can tell that different entropy density (or temperature) shells possess different azimuthal anisotropies as the QGP evolves, among them, the near T_c shells are most significant. They will contribute differently to the final observed high p_T v_2. The right panel of Fig. 3.18 shows the hard hadrons' v_2 computed from assuming all jet quenching would be due to two different single entropy shells: one near T_c and one at high T. The authors of [295] found that the former results in a larger v_2 than the latter. This layer-wise study suggests that the large high p_T v_2 indicates the observed jet energy loss should weigh more on the near T_c regime compared to the high T regime, and it is possible when the jet-medium coupling sees a strong enhancement when the temperature gets close to T_c.

Fig. 3.19 shows the simple jet quenching study from [295] that if one assumes near s_c (equivalent to T_c) enhanced parton-medium coupling strengths as in the left panels,

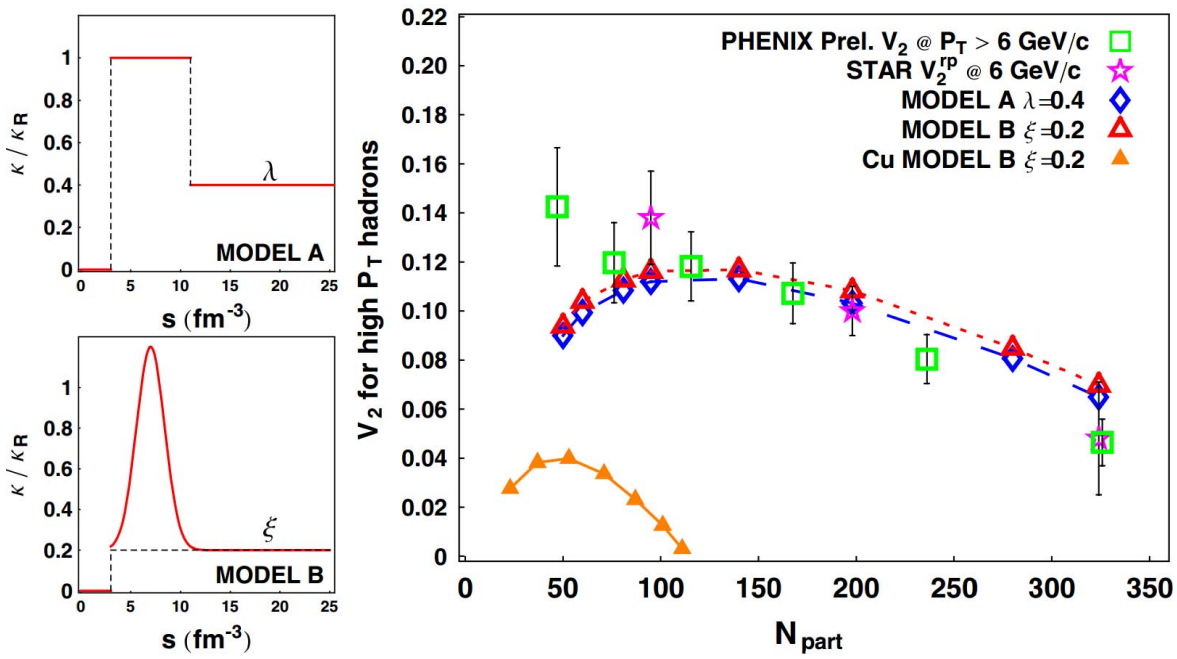

Figure 3.19: *The two schemes for coupling strengths with near T_c enhancements on the left can both explain the high p_T hadrons v_2 in simplified jet quenching model. (Taken from [295].)*

one can boost the v_2 for high p_T hadrons to be in line with data. This near T_c enhanced coupling has been applied to a recent jet quenching study with the a-b-c model, and it is shown in Fig. 3.20 that the pQCD limit $a = 1$ can explain the high p_T light hadrons v_2 quantitatively if a near T_c enhanced coupling κ is utilized.

A natural question to ask is where is exactly the origin of this near T_c enhancement in the jet-medium coupling. One notices that in the vicinity to T_c, complicated QCD phenomena like the confinement/deconfinement transition and chiral symmetry breaking/restoration that are related to non-perturbative asepcts of QCD will happen. What may contribute to a strongly enhanced jet-medium scattering amplitude in the near critical QGP will be the topic for next chapter.

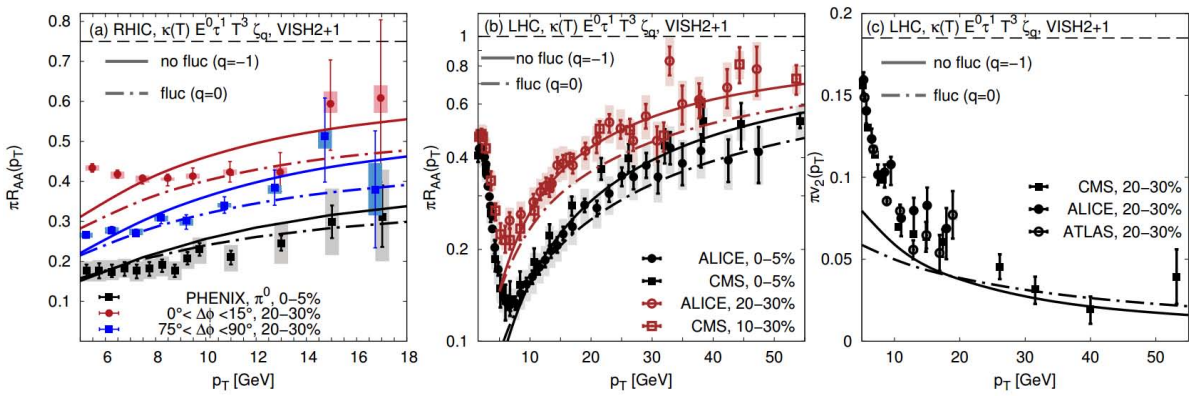

Figure 3.20: *Azimuthal jet tomography at RHIC and the LHC assuming a pQCD-like jet-energy loss in the a-b-c model Eq. (3.65) and a jet-medium coupling $\kappa(T)$ showing an exponential temperature-dependence with ($q = 0$) and without ($q = 1$) additional jet-energy loss fluctuations considering the bulk QGP flow fields from VISH2+1. Panel (a) shows the R_{AA} for most central collisions as well as their in- and out-of-plane contributions at RHIC, panel (b) shows the $R_{AA}(p_T)$ at the LHC, and panel (c) shows the high-p_T v_2 at the LHC. (Taken from [291].)*

3.5 Conclusions

Here is a brief summary of this Chapter: the pQCD based azimuthal jet flavor tomography model, CUJET2.0, that features dynamical running coupling DGLV opacity series coupled with 2+1D viscous hydrodynamical backgrounds is introduced. Within the CUJET2.0 framework, one finds that:

1. Solutions to the "heavy quark energy loss puzzle", i.e. the anomalously strong suppression of heavy flavor decay electrons measured in central A+A collisions at RHIC, are intrinsically integrated in the framework of CUJET, through the inclusion of dynamical QCD medium effect, realistic geometry fluctuation, elastic energy loss, and energy loss fluctuations.

2. CUJET2.0 explains the "surprising transparency of the QGP" at the LHC, i.e. the jet opacity scales weaker than linearly with the medium density, through the

inclusion of multi-scale running strong coupling in the DGLV opacity expansion theory.

3. The scaled jet transport coefficient $\hat{q}/T^3$ calculated from CUJET2.0 along with extracted $\hat{q}/T^3$'s from HT-BW, HT-M, MARTINI and McGill-AMY models fitting to the same set of experimental hadron suppression factors at RHIC and the LHC A+A central collisions constrained the value of this crucial transport parameter to a small window [276].

4. The ordering of π, D, B, e^- R_{AA}'s at the same p_T is rigorously encoded in the flavor dependent jet quenching structure of the DGLV opacity expansion combined with TG elastic energy loss, and a transverse expanding medium has minor effects on this mass hierarchy.

5. CUJET2.0 predicts a less quenched B meson R_{AA} which is well above D meson and pion at 5 GeV $< p_T <$ 15 GeV, as well as a transition of R_{AA}'s mass ordering from $B > e^- > D$ at $p_T <$ 15 GeV to $e^- > B > D$ at $p_T \gtrsim 25$ GeV.

6. A "high p_T v_2" problem exists universally in pQCD based jet quenching models, i.e. in both the light and heavy flavor sector, after one has constrained the energy loss model parameters with R_{AA} data, the high p_T hadrons v_2 will be underestimated by $\sim 50\%$. In CUJET2.0, it is found that if one allows the path averaged coupling strength to be enhanced by 10% from in reaction plane to out-of reaction plane paths in non-central A+A collisions, one can get a 100% boost in the high p_T particle v_2, and bring theoretical results to be in line with data. This extreme sensitivity of the azimuthal anisotropy on path averaged couplings suggests that the jet-medium interaction has a non-trivial dependence on the local temperature of the QGP, especially in the near-T_c strong-coupling regime. And it further suggests the

importance of taking into account non-perturbative aspects of QCD in the "seemly perturbative" jet quenching studies.

Chapter 4

Beyond perturbative QGP

As we have seen in the previous chapter, to solve the high p_T v_2 puzzle in perturbative QCD based energy loss models, a path dependent coupling that is extremely sensitive to local temperature of the QGP is required. This sensitivity suggests that the jet-medium interaction behaves non-trivially in the QCD phase transition regime near the critical temperature T_c. There the QGP is strongly coupled and is govern by non-perturbative components of QCD. These point to the necessity of more careful considerations of QGPs in the confinement/deconfinement transition region near T_c in the "as if purely perturbative" jet quenching studies.

Meanwhile, we have also seen from the simplified phenomenological study of the high p_T hadrons v_2 in [295] that the large azimuthal anisotropy data imply an enhanced parton-medium interaction near T_c. The natural question is what is the microscopic origin of this near T_c enhancement. A promising candidate is the emergent chromo-magnetic monopoles within the magnetic scenario for strongly-coupled quark-gluon plasmas (sQGP) [296]. The main goal of this chapter is to introduce this view of finite temperature-density QCD that is based on a competition between electrically charged quasi-particles (EQPs) and magnetically charged quasi-particles (MQPs).

This scenario will be one of the key ingredients in building up the perturbative-nonperturbative hybrid CUJET3.0 jet energy loss framework in Chapter 5, where we will see a robust solution to the high p_T v_2 puzzle and more importantly a quantitative reconciliation of the perturbatively inconsistent soft and hard transport properties in the QGP.

4.1 Magnetic Scenario for sQGP

In the electro-magnetic (E-M) seesaw scenario [297] as shown in Fig. 4.1, the QGP has both an electric component and a magnetic component, the two components have their own constituent masses, coupling, and densities, these properties change with the temperature T and the baryon chemical potential μ, and they dominate in different regimes of the QCD phase diagram. In the sQGP regime, the magnetic components are dominant and are correlated. This is called the magnetic scenario for sQGP.

This E-M seesaw scenario is different from traditional approaches that centered around confinement/deconfinement phenomenon and dividing the temperature regimes into confined or hadronic phase at $T < T_c$ and deconfined or QGP phase at $T > T_c$. It focuses on the competition between EQPs and MQPs and divide the QCD phase digram into the "magnetically dominated" regime for $T < T_{E=M}$ and "electrically dominated" regime $T > T_{E=M}$, assuming the key aspect of the physics involved is the coupling strength of both electric and magnetic interactions. Therefore on the $T - \mu$ plane, the divider for these regimes is the E-M equilibrium line. One notices that the condition

$$e \cdot g = 1 \rightarrow e = g = 1 \tag{4.1}$$

is a line indicating equal magnetic and electrical coupling which also satisfies the Dirac

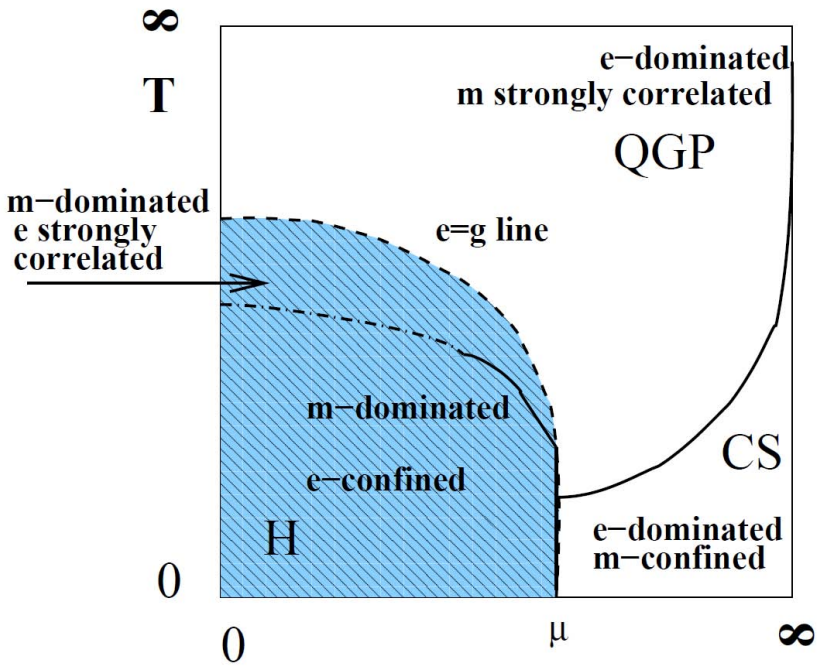

Figure 4.1: *A schematic phase diagram on a plane of temperature T and baryonic chemical potential μ. The (blue) shaded region shows the "magnetically dominated" region $g < e$, which includes the electrically confined hadronic phase as well as postconfined part of the QGP domain. The light region includes the "electrically dominated" part of QGP as well as the color superconductivity (CS) region, which has electrically charged diquark condensates and therefore magnetically confined. The dashed line called "e=g line" is the line of electric-magnetic equilibrium. The solid lines indicate true phase transitions, while the dot-dashed line is a deconfinement cross-over transition line. (Taken from [297].)*

quantizaiton condition [298]. In this equilibrium regime, both electric and magnetic quasi-particles have comparable densities and masses, however the E-M duality is not exact because EQPs are quarks or gluons and with spin 1/2 or 1 while MQPs are spherically symmetric "hedgehogs" without any spin [299].

The "magnetic-dominated" low-T and low-μ region can be subdivided into the confining part at $T < T_c$ where electric fields are confined into quantized flux tubes surrounded by condensates of MQPs forming 't Hooft-Mandelstam "dual superconductor" [300, 301],

and a new "post-confinement" region at $T_c < T < T_{E=M}$ where EQPs are still strongly coupled, correlated, and connected by electric flux tubes. In this picture QCD string-related physics is not terminated at $T = T_c$, it is at its prime there instead. If one increases T and/or μ and thus leaves this "magnetic-dominated" region and passes through the E-M equilibrium line, one either enters the high-T "electric-dominated" QGP or a color-electric superconductor at high-μ replacing the dual superconductor where diquark condensates replace monopole condensates. The new phase diagram based on this viewpoint is illustrated in Fig. 4.1. In the following sections the underlying physical picture will be discussed in more details.

4.2 Electric-magnetic dualities

The E-M seesaw scenario is stimulated by the electric-magnetic dualities in supersymmetric (SUSY) theories. The original motivation for studying the SUSY QFT was to remove the perturbative divergence and solve the hierarchy problem. A wide range of of nonperturbative phenomena have been discovered in this context, however their relevance to QCD-like theories is neither understood nor explored in a deep fashion. Studies of instantons in these theories provide one with tools like the exact beta function, and these have allowed Seiberg to derive the complete phase structure of supersymmetric QCD in [302]. Following up on this, in the context of $\mathcal{N} = 2$ SUSY gauge theories, Seiberg and Witten [303, 304] were able to show how the physical content of the theory changes as a function of the Higgs vacuum expectation values (VEVs) in a moduli space of possible vacua. Singularities in moduli space were identified as phase transitions where one of the MQPs will become massless. Seiberg and Witten found a set of dualities, explaining where and how a transition from one language to another, e.g. from "electric" to "magnetic" to "dyonic", can explain in a simple and natural way what is happening at respective

regions of the moduli space.

One of the most important lessons one can learn from these results is what happens with the strength of electric coupling e and magnetic coupling g near the phase transition. As T decreases, monopoles become light and even massless at some point, the "Landau zero charge" in the infrared (IR) is enforced by the $U(1)$ beta function of the magnetic QED, and it makes monopoles weakly coupled in the IR, i.e. $g \ll 1$. The Dirac quantization therefore enforces the electric coupling e being large in this region, i.e. $e \gg 1$, forming the "strongly coupled" electric sector.

Because the two foundations of this picture, i.e. the $U(1)$ beta function and Dirac quantization, do not depend on the supersymmetry or any other details of the Seiberg-Witten (SW) theory, one can therefore speculate it to be a generic phenomenon. Consequently, it is conjectured that this picture is applicable to the region near the QCD confinement/deconfinement transition $T \approx T_c$ hence explains the strongly coupled electric degrees of freedom (DOFs) there phenomenologically. On the other end, the high temperature limit is similar to the large VEV domain of the moduli space, there the $SU(N_c)$ ultraviolet (UV) asymptotic freedom and screening effects make the electric coupling small. As a consequence, MQPs will be heavy and strongly coupled in that regime.

4.3 Lattice QCD on magnetically charged quasiparticles in sQGP

4.3.1 Static $q\bar{q}$ potential

One of the reasons for redividing the QCD phase diagram can be explained using lattice data on the temperature dependence of the static quark-antiquark potential $V(r)$. Regarding this potential, in lattice QCD computations (c.f. Section 1.1.4), since the Wilson

loop $\langle W(\mathcal{C})\rangle$ is proportional to $\exp(-V(r)\tau)$, where the area enclosed by the loop $\mathcal{C}$ is $A = r \times \tau$, $V(r, \tau = 1/T)$ is hence extracted via

$$V(r, \tau = 1/T) = -\frac{1}{\tau} \log\langle W(\mathcal{C})\rangle \quad . \tag{4.2}$$

As an example, shown in the left panel of Fig. 4.2, lattice QCD results at $T = 0$ are plotted together with an empirical linear plus Coulomb potential (Cornell potential), one sees that the attractive short-distance potential becomes linearly confining at long distances. Note that here β corresponds to the gauge coupling $10/g^2$. From the form of Eq. (4.2) one can infer that V characterizes the free energy of a static $q\bar{q}$ pair. The right panel of Fig. 4.2

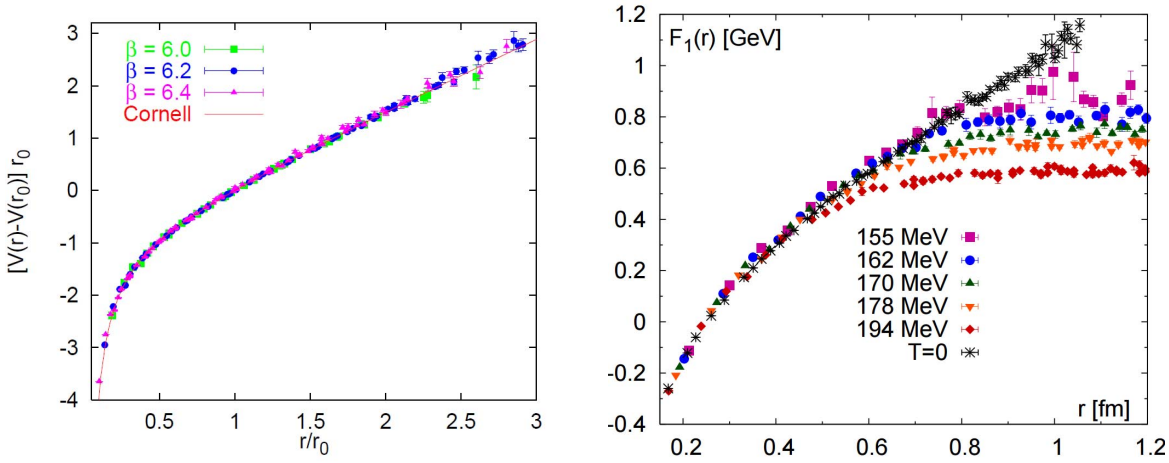

Figure 4.2: *Left: The quenched Wilson action $SU(3)$ potential normalized to $V(r_0) = 0$. (Note that $r_0 \approx 0.5$ fm, taken from [305].) Right: The singlet free energy as function of distance r for different temperatures $T < 200$ MeV calculated in Coulomb gauge. (Taken from [306].)*

shows the singlet free energy from [306].

The traditional reasoning points to the free energy $F(r, T)$ associated with static quark pair separated by a distance r, and defines the deconfinement as the disappearance of a linearly growing string term in it, so that at $T > T_c$ there is a finite limit of the free

energy at large distances, $F(\infty, T)$. This phenomenon is referred to as the melting of the confining string at T_c.

However, as pointed out by Polyakov [307], the string should not disappear at T_c: at this point the energy of the string gets compensated by the entropy term so that the free energy $F = U - TS$ vanishes. Fig. 4.3 shows that lattice studies suggest the internal

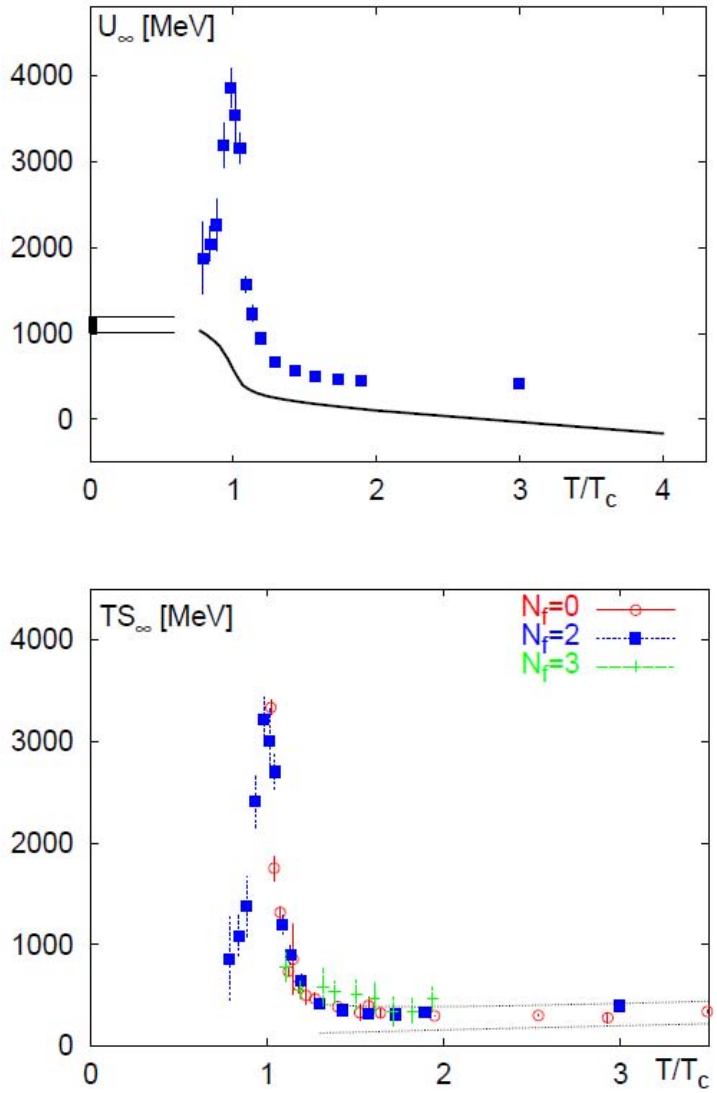

Figure 4.3: *The energy (upper panel) and entropy (lower panel) (as $TS_\infty(T)$) derived from the free energy of two static quarks separated by large distance, in $N_f = 2$ QCD. (Taken from [308].)*

energy and entropy associated with a static $q\bar{q}$ pair are strongly peaked exactly at T_c. The huge mangitude of them can not be explained on the basis of a Debye-screened weakly-coupled gas of EQPs. The explanation of such large energy and huge number of occupied states may be that several correlated quasi-particles are bound to heavy charges in the form of gluonic chains or polymers [309].

Therefore, the deconfinement seen in the disappearing linear term in the free energy is restricted to static or adiabatically slowly moving color charges. Assuming that there is some chain-like structure surrounding static quarks that creates the large entropy, and that this structure can not survive for fast-moving quarks, then for fast-moving light or even charmed quarks, one should still find mesonic bound states even in the deconfined phase [310].

Studies of light quark and charmonium states from lattice QCD [311, 312] found that they persist until $2T_c$. This was further supported by the experimental discovery that the J/ψ suppression at RHIC is smaller than expected, which is consistent with the new view that J/ψ not melting at RHIC where $T < 2T_c$.

In fact there are even more studies supporting the MQPs dominated "post-confinement" phase at $T_c < T < T_{E=M}$. For example, [313] discussed a set of lattice calculations and showed that a "dual superconductor" picture is consistent with what is observed on the lattice, and the shape and field distribution inside the confining strings is in agreement with that in the Abrikosov flux tube of a superconductor. On the other hand, [314] showed that one can define on some way monopoles and their paths, and those are in average consistent with dual Maxwell equations.

However as reviewed in [315], the previous studies were mostly rather concentrated in the vacuum $T = 0$ than considering the temperature range of deconfined plasma at $T > T_c$. Nevertheless, there are general reasons to think that MQPs play an important role in the "post-confinement" phase. Among them the most important one is the persistence

of static magnetic screening up to infinitely high temperature. This topic will be discussed in the next section.

4.3.2 E-M screening mass

Following up with the discussions in the previous section, although static magnetic screening was shown to be absent in perturbative diagrams [316], it has been proposed by Polyakov [307] that it does appear nonperturbatively at the "magnetic scale" $\Lambda_M = e^2T$ at high T. Consequently, the magnetic screening mass is $\mu_M = c_M\Lambda_M$ and the monopole density is $\rho_M = c_n\Lambda_M^3$, where c_M and c_n are some proportionality constants.

There is a recent lattice calculation in [275] of the temperature dependence of the electric screening mass and magnetic screening mass that is shown in Fig. 4.4. Note

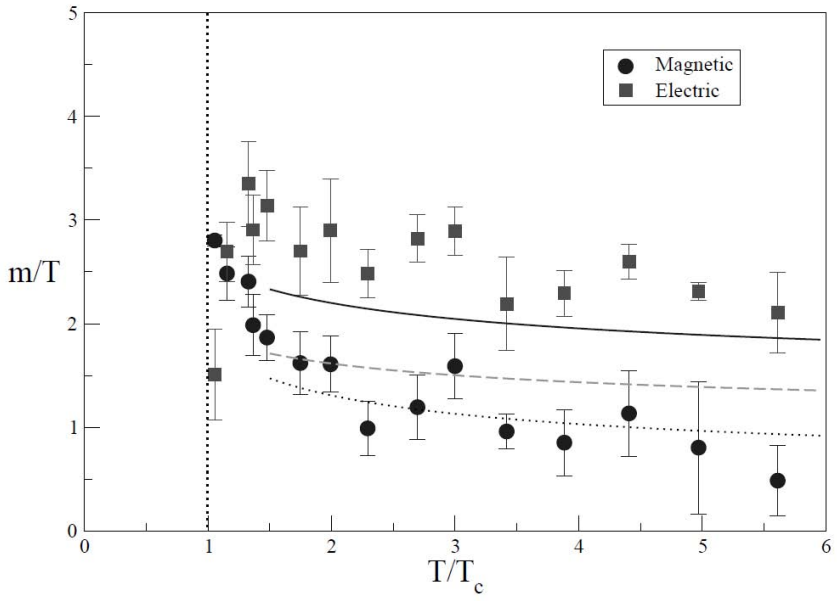

Figure 4.4: *Temperature dependence of electric and magnetic screening masses according to Nakamura et al [275]. The dotted line is fitted by the assumption that magnetic screening mass $\mu_M \sim e^2T$. For the electric mass, the dashed and solid line represents the leading-order perturbation and the hard thermal loop resummation results, respectively. (Taken from [297].)*

that the electric screening mass μ_E is larger than μ_M at high T, but vanishes at T_c because electrically charged objects become too heavy at T_c and effectively disappear. The magnetic screening mass μ_M however increases as T cools down toward T_c. This is consistent with the scaling estimate that $\mu_M^2 \sim e(T)^4 T^2$.[1]

If one uses the screening masses to get an estimate about density of electric and magnetic objects, one finds that the point at which μ_E and μ_M are equal should be close to the E-M equilibrium point. This places the equilibrium temperature in the range of $T_{E=M} \approx (1.2 - 1.5)T_c = 250 - 300$ MeV [317].

4.3.3 High temperature monopoles

Other lattice "observables" related to MQPs above T_c include the total pressure for the magnetic sector of QCD and the spatial string tension. Details about them can be found in the review by Korthals-Altes [318], there Korthals-Altes made two important points: (1) MQPs must be in the adjoint color representation in order to explain the lattice data of k-strings and magnetic pressure; (2) there seems to be a nontrivial small "diluteness" parameter of the MQPs ensemble $\delta = \sigma_1/\mu_M^2 \sim 1/20$ where σ_1 is the string tension.

The fact that screening near T_c takes place at distances smaller than the average distance between MQPs is a clear indication that screening near T_c is not a Debye-type weak coupling one, but on the contrary, a strongly coupled/correlated screening.

4.3.4 Dyons

A special sector of MQPs is the particle with both E and M charges – dyons. Because they produce parallel electric and magnetic fields, they have nonzero topological charge ($\mathbf{E} \cdot \mathbf{B} \neq 0$). As shown by Kraan et al [319], finite temperature instantons can be viewed

[1] Another estimate of the magnetic screening can be done in the dual language as $\mu_M^2 \sim g^2 \rho_M/T \sim g^2(e^2T)^3/T \sim (e^2T)^2$ this is a perturbative loop with small magnetic coupling g.

as being made of N_c self-dual dyons, and in [320] there is an AdS/CFT "brane-based" construction leading to the same conclusion.

Topology is in turn associated with the Dirac zero eigenvalues for fermions, which can be located and counted on the lattice very accurately. Furthermore, a visualization of dyons inside lattice gauge field configurations using variable non-trivial holonomy has been developed in [321], and one can use this tool to reveal multi-dyon configurations and their dynamics. One can find that they make a dilute but highly correlated systems, where closed chains of up to 6 dyons of alternating charges have been seen. The self-dual dyon density and other properties, as well as their relation to instantons and confinement are summarized in [322]. It is enough to mention only that self-dual dyons, like instantons, are electrically screened [323] and thus rapidly disappear in the QGP phase at $T > T_c$. Around Tc their density can be related to the instanton density $n_{\rm dyon} \sim N_c n_{\rm instanton}/T \sim 3$ fm^{-3}, and their mass can be related to the instanton action $m_{\rm dyon} = T \cdot n_{\rm instanton}/N_c \sim (3-4)T$. They are of the order of the density and the mass of electric quasi-particles at $1.5T_c$. This confirms the suggested E-M equilibrium in this region.

Regarding the relation between particle-monopoles and instanton-dyons, there is a useful quote from Shuryak [324]: "Traditional explanation of the confinement is often given in terms of particle-monopoles and dual superconductor model of 't Hooft and Mandelstam: so one may ask about any relation between particle-monopoles and instanton-dyons. In $\mathcal{N} = 2$ SYM (Seiberg-Witten theory) both are under theoretical control, so one can calculate how each of them contribute to partition function. Remarkably one finds that the results are equal [325]. One can see that particle-monopoles provide better behaved sum at low-T, while the instanton-dyons better converge at the high-T end, but both describe the same physics. Unfortunately, in non-supersymmetric theories, without such explicit expressions available, the relation between the two remains unclear."

4.4 Polyakov loop

The magnetic scenario of sQGP has been concentrated on the chromo-magnetic components of the nonperturbative QCD matter in the confinement/deconfinement transition regime, however it does not provide quantitative information about the chromo-magnetic components near T_c. Therefore, more careful considerations about both composites in the critical transition regime should be carried out.

In the case of confinement/deconfinement transition, one can consider the Polyakov loop as the order parameter:

$$L(\vec{x}) = \frac{1}{N_c}\mathrm{Tr}\left[\mathcal{P}\exp\left(ig\int_0^\beta A_0 d\tau\right)\right], \tag{4.3}$$

where the gauge fields are periodic in imaginary time τ with period $\beta = 1/T$, as in thermal field theory[2].

To see the reason why the Polyakov loop is useful in characterizing confinement or deconfinement transition, one can consider an "aperiodic" gauge transformation of the form $V(\tau+\beta,\vec{x}) = z_n V(\tau,\vec{x})$, where $z_n \in Z_{N_c} = \left\{\mathbb{1}e^{2\pi i n/N_c} | n = 0, ..., N_c - 1\right\}$ is the center of the gauge group $SU(N_c)$. Under this center symmetry, gauge fields A_μ's are invariant, but quarks transform as $q \to -z_n q$.

For a pure gauge theory (or assuming quarks have infinite masses) in the confined phase, N_c external test quarks that form a "test baryon" are together invariant since $z_n^{N_c} = 1$. Therefore, the center symmetry is a symmetry of the confined phase. However, the Polyakov loop is not invariant under this symmetry: $L \to z_n L$, which means that $\langle L\rangle$

[2]In thermal field theory, the Boltzmann operator $e^{-\beta\hat{H}}$ (where $\hat{H}$ is the Hamiltonian) can be interpreted as a quantum evolution operator in imaginary time. Consequently, one can express the partition function as a path integral in Euclidean space. The bosonic/fermionic fields that subject to periodic/anti-periodic boundary conditions in imaginary time τ can be integrated over. Through this, one can find the partition function in terms of the path integral, then compute various thermodynamic quantities and averages of operators over thermal ensembles.

must vanish in the confined phase. On the other hand, in the deconfined phase, the center symmetry is broken and $\langle L \rangle$ is not vanishing anymore. The Polyakov loop is therefore an order parameter for this symmetry. To summarize,

$$\langle L \rangle \begin{cases} = 0, & \text{confined } (T < T_c) \\ \neq 0, & \text{deconfined } (T > T_c)\,. \end{cases} \tag{4.4}$$

Physically speaking, similar to the case of Wilson lines, the expectation value of the Polyakov loop is related to the free energy of a single (heavy) quark, $\langle L \rangle \propto e^{-F_Q/T}$. Therefore, in the confined phase, since there are no free isolated quarks, the free energy should be infinite and $\langle L \rangle \to 0$. On the other hand, in the deconfined phase, the free energy is finite and hence $\langle L \rangle \neq 0$.

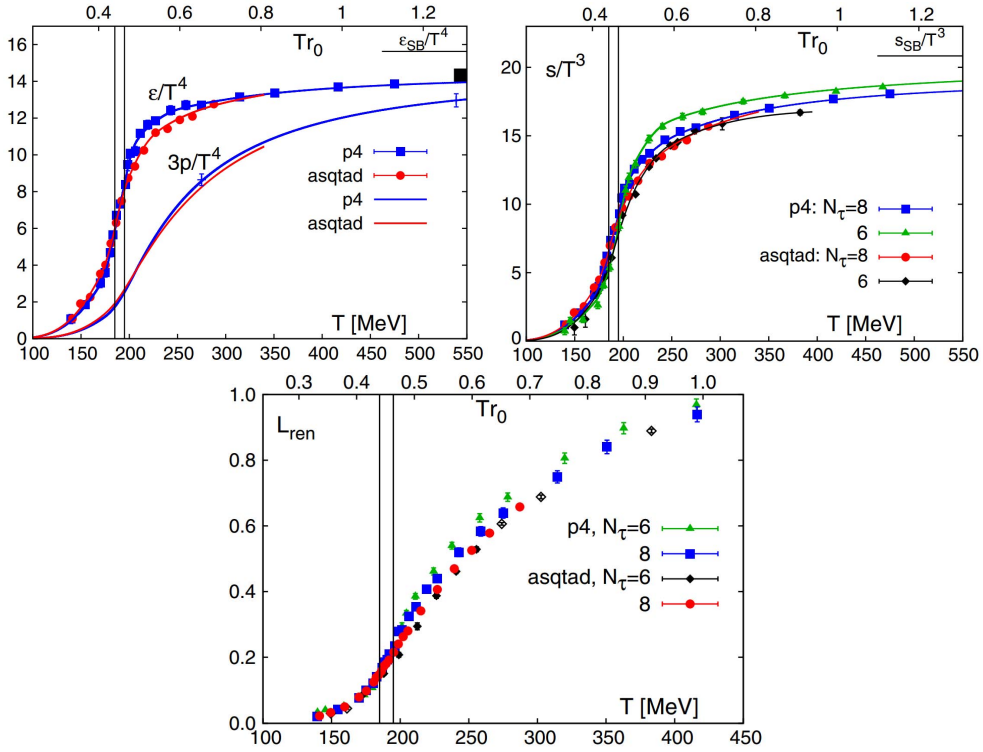

Figure 4.5: *The lattice 2+1 flavor QCD calculation of the energy density (left), pressure (left), entropy density (middle), and Polyakov loop (right). Taken from [103].*

Fig. 4.5 shows the lattice 2+1 flavor QCD calculation of the energy density, pressure, entropy density, and Polyakov loop from [103]. One can clearly see that in the near T_c regime, the thermodynamic quantities rises faster than the Polyakov loop. In the "semi-QGP" model proposed by Pisarski et al that will be discussed in detail in the next chapter, a non-zero Polyakov loop in the presence of non-trivial holonomy suggests a power law suppression of color electric charges [326–329]. The phenomenon observed in Fig. 4.5 hence suggests the thermal degrees of freedom rises faster than the color degrees of freedom in the near T_c regime, and it points to a "missing" degrees of freedom for the sQGP. Within the magnetic scenario introduced in this chapter, the "missing" part can be naturally accounted for by chromo-magnetic monopoles. And this will stimulate our development of the CUJET3.0 model in the next chapter.

Chapter 5

Jet quenching in near-critical QGP

One has seen in Chapter 3 and 4 that there are two main problems associated with perturbative QCD (pQCD) based jet quenching frameworks: (1) These models have been found to fail to describe *simultaneously* the high p_T light hadrons' and open heavy flavors' R_{AA} and v_2 data at RHIC and the LHC [225, 291, 330–332], c.f. e.g. Fig. 3.13, and this is often referred to as a "high p_T v_2 puzzle" for pQCD energy loss models (c.f. Section 3.4). (2) The leading order (LO) pQCD estimates of the shear viscosity to entropy density ratio (η/s) based on the conventional picture of HTL quasiparticle degrees of freedom in the QGP has [112, 333–335] $\eta/s \approx 0.071[\alpha_s^2 \log(1/\alpha_s)]^{-1}$. This gives the value of η/s being of the order 1, which is an order of magnitude larger than the unitarity $\eta/s = 1/4\pi \approx 0.08$ lower bound [334, 336] that was found to be required to explain the "perfect fluidity"property of QGP produced in high energy nuclear collisions [94, 115, 239, 331, 337, 338].

While the factor of ~ 5 quenching of hard jets observed in central collisions with $R_{AA} \sim 0.2$, was well predicted [144] even with pQCD jet medium coupling, the collective bulk azimuthal flow moments observed at RHIC and the LHC appear to require much stronger interactions such as those assumed, e.g., in AdS/CFT black hole modeling of the

sQGP to account for perfect fluidity [331, 336]. The long-standing "jet" $R_{AA}(p_T > 5$ GeV) vs "bulk" $v_2(p_T < 2$ GeV) [330, 331] as well as the "jet" azimuthal $v_2(p_T > 10$ GeV) puzzles [216, 225, 291, 339] continue to raise critical questions about one's understanding of the dynamics and composition of the QGP medium produced in high energy nuclear collisions and especially the consistency of information derived from high $p_T > 10$ GeV jet quenching observables and low $p_T < 2$ GeV bulk collective flow observables at RHIC and the LHC.

How do the effective degrees of freedom of nonperturbative QCD origin interpolate between the confined Hadron Resonance Gas (HRG) world at low energy energy density into an asymptotically free quark gluon plasma at extreme densities? Are there effective quasi-particles in the highly non-perturbative non-conformal temperature range near the deconfinement transition temperature $T_c \sim 160$ MeV? How do those "emergent" degrees of freedom near T_c affect high $p_T > 10$ GeV jet flavor observables? Can an effective quasi-particle description be constructed that is consistent with lattice QCD thermodynamic data and simultaneously could reconcile the apparent inconsistency between the bulk "perfect fluid", minimally viscous hydrodynamics and the success (modulo v_2) of pQCD based jet quenching phenomenology? Can the combined set of soft plus hard observables be used to elucidate the mechanism of color confinement?

The goal of this chapter is to demonstrate in detail the existence of at least one possible model that involves partially suppressed chromo-electric-charges (CEC) together with emergent chromo-magnetic-monopole (CMM) effective degrees of freedom (the semi-Quark-Gluon-Monopole-Plasma model) that via the CUJET3.0 numerical framework allows us to constrain the $\hat{q}(E,T)$ and $\eta/s(T)$ fields over a much wider range than previously possible.

We will present in this chapter the theoretical details of the CUJET3.0 framework and concentrate on the robustness and consistency of its components as well on its phenomeno-

logical applications that successfully account for a large set of leading hadron inclusive jet energy loss data. We address a number of key questions concerning the theoretical robustness of the underlying sQGMP microscopic scenario and report new results that help in estimating theoretical uncertainties in our present understanding of jet energy loss phenomena via the sQGMP model. Such questions include: (1) Can an effective quasi-particle chromodynamic model be formulated with sufficient ab-initio lattice QCD and experimental data constraints to explain simultaneously both long and short wavelength observables in high energy A+A reactions? (2) How do theoretical uncertainties on Quark and Glue CEC quasi-particle number densities $\rho_Q(T)$ and $\rho_G(T)$ and chromo Magnetic monopole CMM density $\rho_M(T)$ of the sQGMP propagate to the observables? (3) How do uncertainties in the chromo electric and magnetic screening masses $\mu_{E,M}(T)$ near T_c effect the observables? (4) Can we constrain in the sQGMP model the temperature dependence of the jet quenching parameter $\hat{q}(E,T)$ well enough to predict the shear viscosity to entropy ratio $\eta/s(T)$ by extrapolating down to $E \sim 3T$ thermal scales? (5) How does the effective path length dependence of light and heavy quark energy loss depend on the detailed CEC and CMM composition of sQGMP matter, and how do these compare to perturbative QCD HTL path length dependences?

5.1 The CUJET3.0 model

The CUJET3.0 jet quenching framework generalizes the CUJET2.0 perturbative non-Abelian gluon bremsstrahlung kernel of the DGLV opacity expansion theory (c.f. Section 3.1) of radiative jet energy loss to incorporate lattice QCD constraints on the nonperturbative semi-QGP suppression of color DOFs, and emergent nonperturbative chromomagnetic monopole DOF near the crossover QCD temperature regime $T \sim T_c$ regime . CUJET3.0 incorporates lattice QCD data on the QCD pressure equation of state (EOS)

$P(T)$, nonperturbative chromo electric and magnetic screening masses, $m_E(T), m_M(T)$, and the Polyakov loop $L(T)$. To begin, let us first have a quick overview of the physical pictures behind the CUJET3.0 framework.

5.1.1 Motivations of CUJET3.0

Recall that a possible mechanism of color confinement based on a "dual superconductor" picture was proposed by Mandelstam, Nambu, Polyakov, 't Hooft [31, 300, 301, 340] — It is understood that in type II superconductors the condensate of Cooper pairs generates a "Meissner Effect" that repels magnetic field lines and squeezes monopole pair fields into flux tubes. In models possessing electric-magnetic duality, e.g. the Seiberg-Witten solution of the $\mathcal{N} = 2$ supersymmetric gauge theory [303, 304], a "dual superconductor" phase does emerge in the strong coupling regime. Stable magnetic monopoles condensates can be generated leading to "Dual Meissner Effect" that forces the chromo-electric fields sourced by CEC pairs to form flux tubes that gives rise to linearly rising potential and confines quark-antiquark pairs.

Partially motivated by the "dual superconductivity" picture of color confinement, a magnetic scenario for the near T_c QCD plasma was proposed in [295–297, 317, 341, 342]. This scenario emphasizes the change in chromo degrees of freedom with the gauge coupling, and recasts the QCD phase diagram into electrically and magnetically dominated regimes. For example, focusing on increasing temperature (at zero baryonic density), a particular temperature $T_{E=M}$ may be identified as a new phase boundary where the coupling strength of electric (E) and magnetic (M) interactions are equal and satisfy the Dirac quantization condition [298]. Interestingly, a novel post-confinement non-conformal non-perturbative region emerges at $T_c < T < T_{E=M} \sim 1.4T_c$ where chromo magnetic monopoles (CMM) are the lightest degrees of freedom (DOFs) in the system while chromo

electrically charged (CEC) quasi-particles are strongly correlated and connected by flux tubes. Phenomenologically it has been qualitatively demonstrated that with the inclusion of such emergent monopoles near T_c, the scatterings in both the soft and hard sectors are strongly enhanced and thus help explaining the small η/s of the bulk sQGP as well as leading to significant v_2 of high p_T hadrons [295, 297, 343–346].

However, a quantitative and phenomenologically robust modeling framework for the QCD matter in the near T_c regime has not been built previously. Such a framework has to couple the hard jet probes with the state-of-the-art bulk constrained viscous hydrodynamic $(T(x,t), u^\mu(x,t))$ fields. It also needs to have a sophisticated implementation of the microscopic nonperturbative physics for both the CEC and CMM degrees of freedom. For that, we need to constrain how the E and M quasi-particles DOF vary with temperature in a way that is consistent with available lattice QCD data [44, 103, 275, 347–350] on thermodynamic pressure, entropy density, energy density as well as the Polyakov loop and quark susceptibilities. Specifically for the nonperturbative dynamics of the CEC near T_c, the "semi-QGP" model [326–329, 351, 352] was previously proposed to build in the color suppression effect in the deconfinement transition region. In that model the Polyakov loop is the relevant parameter that controls confinement/deconfinement of color electric charge DOFs. When temperature drops towards T_c, the excitation of CEC quarks and gluons are quenched by powers of the loop, resulting in a number of novel phenomenological effects. For example it was found in the semi-QGP that there is a mild enhancement for the production of thermal dileptons and a strong suppression for the production hard photons [353, 354].

The above considerations of the nonperturbative medium near T_c have motivated us to propose and study a nonperturbative semi-Quark-Gluon-Monopole-Plasma (sQGMP) model for the "perfect chromo fluid" near the deconfinement transition range. The CUJET3.0 framework [232, 233] is an extension of the CUJET2.0 model [216, 231] discussed

in Chapter 3) which integrates local jet energy loss over (2+1)D viscous hydrodynamic flows. It models jet medium interactions via the sQGMP quasi-particle model picture of the chromo structure of the fluid that include specific non-pertubative features related to confinement in the vicinity of T_c. In CUJET3.0 all thermodynamic properties are constrained by lattice QCD data. At very high temperature $T \gg T_c$ the model by construction would smoothly reduce to CUJET2.0 corresponding to a perturbative Hard Thermal Loop (HTL) picture of the QGP. As T approaches T_c, the chromo-electric charge (CEC) degrees of freedom are suppressed as powers of the Polyakov loop as in the semi-QGP framework while chromo-magnetic monopoles emerge to account for the total lattice QCD pressure or the total entropy density.

Having grasped the physical pictures behind the CUJET3.0 model, let us move on to look at the details of its ingredients. The perturbative component of this model is the dynamical running coupling DGLV opacity expansion theory that have been extensively discussed in Chapter 3. Therefore, in the following subsections, we will present comprehensive discussions of the details of its non-perturbative ingredients.

5.1.2 Semi-quark-gluon plasmas

In the vicinity of the QCD deconfinement transition temperature $T_c \sim \Lambda_{QCD}$, the strength of the chromo-electric coupling becomes very strong. Novel nonperturbative effects should enter and modify the properties of the QGP in this regime. Based on first-principle lattice QCD calculations and reasonable theoretical assumptions, in the CUJET3.0 framework, we model the near T_c QCD matter as a semi-Quark-Gluon-Monopole-Plasma (sQGMP) that includes two ingredients with nonperturbative origins – the semi-QGP suppression of color electric DOFs and the emergent chromo magnetic monopoles.

The semi-QGP model was developed and discussed in detail in [326–329, 351–354]. It

is constructed to describe QCD as temperature $T \to T_c^+$, where both the naive perturbative methods and the hadronic models are not applicable. A main emphasis is on the "mismatch" seen from lattice data between the liberation of thermal excitations (as indicated by e.g. rapid increase of entropy density around T_c) and the liberation of "color" (as indicated by the rather slow increase of Polyakov loop toward fully deconfined limit). This observation indicates at a region above T_c where significant nonperturbative suppression of color charge is still present. In the semi-QGP, how color is suppressed is quantified by the decrease of the expectation value of the Polyakov loop $\langle \ell \rangle$, which is the trace of a straight Wilson line in imaginary time. Properly normalized $\langle \ell \rangle$ is near unity in the perturbative QGP, but in the near T_c regime, it is smaller than 1 (from lattice, $\langle \ell \rangle \sim 0.1$ at T_c). This implies a non-trivial distribution for the eigenvalues of the Wilson line and a non-trivial background field for the time-like component of the gauge field A_0. In the presence of a nonzero A_0, as $T \to T_c^+$, the colored excitations are suppressed by powers of the Polyakov loop.

Let us briefly review how this suppression works in the semi-QGP following [328, 329]. Adopting the double line basis for color factors, fundamental quarks carry a single index in the fundamental representation, $a = 1, \cdots, N_c$, and adjoint gluons carry a pair of fundamental indices, ab. In an $SU(N_c)$ gauge theory, under mean field approximation, we take the temporal component of the gluon field to be a constant, diagonal, traceless matrix [327]

$$(A_0^{cl})^{ab} = \delta^{ab} Q^a / g \tag{5.1}$$

where g is the coupling constant for the $SU(N_c)$ gauge theory. For the spatial components of the gluon vector potential, A_i, there is no background field. In the Euclidean spacetime,

the Wilson line in the temporal direction is

$$L(\vec{x}) \equiv \mathcal{P} \exp\left(ig \int_0^{1/T} d\tau A_0(\tau, \vec{x}) \right). \tag{5.2}$$

We neglect fluctuations in A_0 to leading order in the coupling constant under mean field approximation. Gauge invariant Polyakov loops are traces of powers of the Wilson line:

$$\ell_n(Q) \equiv \langle trL^n \rangle / N_c = \sum_{a=1}^{N_c} e^{inQ^a/T}/N_c. \tag{5.3}$$

We define ℓ as the first Polyakov loop $\ell \equiv \ell_1$. Physically, one can think of the Polyakov loop as measuring the extra free energy F which arises from adding a colored heavy quark to a thermal bath, $\langle \ell \rangle \sim \exp(-F/T)$. In the perturbative QGP, all Q^a's vanish and $\ell_n = 1$. In the confined phase of a pure gauge theory, eigenvalues of Q are uniformly distributed on a circle of radius T, and $\ell_n = 0$ if $n \neq [N_c/2]N_c$. Dynamical quarks act as a background $Z(N)$ field, if they are present, there is no rigorous definition of a confined phase, and all Polyakov loops are nonzero at nonzero temperatures [328]. Lattice simulations find that ℓ is small ($\langle \ell \rangle \sim 0.1$) in the phase transition regime for $N_c = 3$ and $N_f = 3$ [329].

In the imaginary time formalism, the Euclidean four momentum is $P_\mu = (p_0, \mathbf{p})$, where p_0 is an even/odd multiple of πT for bosons/fermions. Expanding around the background field in Eq. (5.1), the 4-momentum of a quark becomes $P_\mu^a = (p_0 + Q^a, \mathbf{p})$, and the 4-momentum of a gluon becomes $P_\mu^{ab} = (p_0 + Q^{ab}, \mathbf{p})$ ($Q^{ab} \equiv Q^a - Q^b$). Each Q^a is typically a non-integral multiple of $2\pi T$, in the space of diagonal generators, it is like an imaginary chemical potential for color charges. To analytically continue from Euclidean to Minkowski spacetime, one continues the entire Euclidean energy to $-iE$, where E is a continuous energy variable. For quarks, the usual Fermi-Dirac statistical distribution

function $\widetilde{n}(E)$ becomes

$$\widetilde{n}_a(E) = \frac{1}{e^{(E-iQ^a)/T}+1} = \sum_{j=1}^{\infty}(-1)^{j+1}e^{-j(E-iQ^a)/T} \ . \tag{5.4}$$

The first term represents the Boltzmann approximation to the quantum distribution function, and is accompanied by $\exp(iQ^a/T)$. Consider the trace of the quark propagator which enters e.g. in the calculation of the pressure at leading order. The sum is

$$\frac{1}{N_c}\sum_a \widetilde{n}_a(E) = \sum_{j=1}^{\infty}(-1)^{j+1}e^{-jE/T}\frac{1}{N_c}trL^j \ . \tag{5.5}$$

Denote $\langle\cdots\rangle_Q$ as the average over the Q distribution and an integration over the particles three momenta. At $T \to T_c^+$ where ℓ is nonzero but small,

$$\langle\sum_a \widetilde{n}_a\rangle_Q \sim N_c T^3 \ell \ . \tag{5.6}$$

This means the distribution function for a quark field vanishes as a single power of the loop, i.e. $n_q \sim \ell$. For gluons, the usual Bose-Einstein statistical distribution function $n(E)$ becomes

$$n_{ab}(E) = \frac{1}{e^{(E-i(Q^a-Q^b))/T}-1} = \sum_{j=1}^{\infty} e^{-j(E-i(Q^a-Q^b))/T} \ . \tag{5.7}$$

Consider summing over the color indices of the gluon propagator, to avoid taking the trace which is part of the $1/N_c$ correction, one sums separately over a and b. Since $\sum_a e^{iQ^a/T}\sum_b e^{-iQ^b/T} \ = \ trL\ trL^\dagger$, we have

$$\langle\sum_{ab} n_{ab}\rangle_Q \sim N_c^2 T^3 \ell^2 \ . \tag{5.8}$$

This means in the near T_c regime, the density of gluons vanishes as the square of the loop, i.e. $n_g \sim \ell^2$. In the perturbative regime, the density of massless fields is necessarily a pure number times T^3 therefore such a suppression is not present. Note that we always perform a global color rotation to enforce that the expectation value of the Polyakov loop ℓ is real.

5.1.3 Magnetic scenario for near T_c QCD plasmas

The magnetic scenario for the near T_c QCD matter was proposed and discussed in [295–297, 317, 341, 342], and there have since been extensive studies of the magnetic component of the plasma using different approaches [343, 355–357]. In this scenario, the QGP not too far above T_c contains not only electrically charged quasi-particles (CEC), quarks and gluons, but also magnetically charged quasiparticles (CMM), monopoles and dyons.

This approach is different from many traditional discussions, which focus on the thermodynamic transition and divide the temperature regimes into the hadronic phase at $T < T_c$ and the QGP phase at $T > T_c$. Rather, the emphasis is on the competition between EQPs and MQPs, based on which one may divide the phases of QCD matter into the magnetically dominated region at $T < T_{E=M} \sim 1.4T_c$ and the electrically dominated region at $T > T_{E=M}$. This picture is largely motivated by analogy with electric-magnetic duality in supersymmetric Yang-Mills theories. The key aspect of the physics involved is the coupling strength of the electric (e) and magnetic (g) interaction, which can lead to different dominance of dynamical degrees of freedom in different regimes. Under Dirac quantization condition [298], $e \cdot g = n/2$, and magnetic objects are in the adjoint color representation if $n = 2$ [297]. In a so-called E/M-equilibrium region, the couplings are equal, i.e. $e = g$, densities as well as masses of both EQPs and MQPs are comparable. Then depending on the change of these couplings in different physical regimes, the "bal-

ance" between E and M sectors would shift one way or the other, giving rise to distinctive phases.

Let us start with the QGP at very high temperature $T \gg T_c$ where the electric coupling is weak. This regime is well described by perturbative EQPs with small quark and gluon effective masses. The monopoles in this case are heavy, dilute and strongly coupled, but they play a minor role and contribute little to the overall bulk properties. They do manifest themselves through nonperturbative contributions to certain observables at the soft magnetic scale.

On the other hand, as T goes down and approaches the confinement transition $T \to T_c$, the converse is expected to happen: the electric coupling becomes very strong and the EQPs, i.e. quarks and gluons, are getting heavier and gradually suppressed dynamically. The emergent MQPs gradually become light, abundant, and dominate the system at $T < T_{E=M}$. With further decrease of temperature toward T_c the thermal monopoles will eventually reach the Bose-Einstein condensation, forming a 't Hooft-Mandelstam "dual superconductor" [300, 301] that enforces color confinement. In the post-confinement region at $T_c < T < T_{E=M}$ EQPs are still strongly correlated and connected by the electric flux tubes, but MQPs are the dominant DOFs and they serve as an effective description of the strong nonperturbative gauge dynamics. In [296], the authors showed that gauge theory monopoles in a deconfined phase behave as magnetic charges in a Coulomb plasmas. At $T \approx 1.3T_c$ where lattice potentials indicate flux tubes dissolve, an estimate of total density of magnetic quasi-particles is $n_{CMM} \approx 4.4 - 6.6$ fm^3 [317].From an analysis of the lattice monopole-(anti)monopole correlators, they showed that the temperature dependence of the magnetic couplings in gauge theories is indeed the inverse of the electric one as per the electric-magnetic duality arguments. More specifically, the magnetic part of the QGP at $T \sim 1 - 3T_c$ possesses an effective plasma parameter in the "good liquid" domain, thus in consistency with the "nearly perfect liquid" property

observed at RHIC and the LHC.

5.1.4 Jet suppression in semi-quark-gluon-monopole plasmas

Having discussed the foundations of the sQGMP, let us integrate it into the jet energy loss kernel of CUJET2.0. The critical component in Eq. (3.8) is the 1-HTL dynamical scattering potential,

$$x\frac{dN}{dx} \propto ... \int d^2q \left[\frac{\rho\, \alpha_s^2(\mathbf{q}_\perp^2)\, f_E^2}{\mathbf{q}_\perp^2(\mathbf{q}_\perp^2 + f_E^2\mu^2)}\right] ... \ . \tag{5.9}$$

Since the sQGMP contains both chromo electrically charged quasi-particles (CEC) and chromo magnetically charged quasiparticles (CMM), when jets propagate through the medium near T_c, scattering channels of $E+E$ and $E+M$ exist simultaneously. One way to generalize Eq. (5.9) is to symmetrize it with respect to the E and M components of the kernel based on demanding electric-magnetic duality as illustrated in e.g. the celebrated Seiberg-Witten solution of the $\mathcal{N}=2$ super-Yang-Mills theory. This leads to the following modified form of the kernel:

$$x\frac{dN}{dx} \propto ... \int d^2q \left[\frac{\rho_E\, (\alpha_s(\mathbf{q}_\perp^2)\alpha_s(\mathbf{q}_\perp^2))\, f_E^2}{\mathbf{q}_\perp^2(\mathbf{q}_\perp^2 + f_E^2\mu^2)} + \frac{\rho_M\, (\alpha_E(\mathbf{q}_\perp^2)\alpha_M(\mathbf{q}_\perp^2))\, f_M^2}{\mathbf{q}_\perp^2(\mathbf{q}_\perp^2 + f_M^2\mu^2)}\right] ... \ . \tag{5.10}$$

Where $\alpha_s \equiv \alpha_E$, and $\alpha_E \cdot \alpha_M = 1$ at any scale by Dirac quantization condition [296, 298]. The total quasi-particle number density ρ is divided into EQPs with fraction $\chi_T = \rho_E/\rho$ and MQPs with fraction $1-\chi_T = \rho_M/\rho$. The parameter f_E and f_M is defined via $f_E \equiv \mu_E/\mu$ and $f_M \equiv \mu_M/\mu$, with μ_E and μ_M being the electric and magnetic screening mass respectively. We emphasize that Eq.(5.10) is a nonperturbative sQGMP model ansatz that differs substantially from other generalization of HTL, see e.g. [219, 358].

To determine χ_T, one notices that: (1) when temperature is high, χ_T should reach unity, i.e. $\chi_T(T \gg T_c) \to 1$; (2) in the vicinity of the regime $T \sim (1-3)T_c$, the

renormalized expectation value of the Polyakov loop L[1] deviates significantly from unity, implying the suppression $\sim L$ for quarks and $\sim L^2$ for gluons in the semi-QGP model [327, 329, 352, 359]. In the regime the quark and gluon density drop much faster than the thermodynamic quantities. This points to "missing" DOFs, in the magnetic scenario [296, 297], they are identified as chromo-magnetic monopoles who emerge in gauge theories at strong coupling and are thermal excitations of the vacuum magnetic condensate as in the "dual superconductivity" picture of color confinement [305, 360, 361]. For the CEC component fraction, we use the semi-QGP ansatz:

$$\chi_T(T) = c_q\, L(T) + c_g\, L^2(T)\ . \tag{5.11}$$

For the respective fraction of quarks and gluons, we take the Stefan-Boltzmann (SB) fraction coefficients, $c_q = (10.5N_f)/(10.5N_f + 16)$ and $c_g = 16/(10.5N_f + 16)$. To be consistent with lattice data, we fit the temperature dependent Polyakov loop $L(T)$ (T in GeV) with

$$L(T) = \left[\frac{1}{2} + \frac{1}{2}\mathrm{Tanh}[7.69(T - 0.0726)]\right]^{10}\ . \tag{5.12}$$

Eq. (5.12) adequately fits both the HotQCD [103] and Wuppertal-Budapest [348] Collaboration results, c.f. Fig. 5.1(a). With χ_T and $(1 - \chi_T)$, ρ_E/ρ and ρ_M/ρ are completely fixed.

To specify the electric and magnetic screening mass ($\mu_{E,M} = f_{E,M}\,\mu$), we recall that at very high temperature, one expects (1) $f_E \to 1$, i.e. $\mu_E \sim gT$ from HTL results and (2) $f_M \sim g$, i.e. $\mu_M \sim g^2T$, from magnetic scaling in dimensional reduction. Assuming

[1] Let us redefine $L \equiv \ell = \langle tr\mathcal{P}\exp\{ig\int_0^{1/T} d\tau A_0\}\rangle/N_c$.

E-M duality, the screening masses are expected to scale as

$$\mu_{E,M}^2 \sim \alpha_{E,M}\, \rho_{E,M}/T\ . \tag{5.13}$$

The extrapolation to lower temperature thus gives

$$\mu_E^2 \sim \alpha_E\, (\chi_T \rho)/T \sim \chi_T \mu^2\ , \tag{5.14}$$

and we expect the electric screening mass to be suppressed as $\sqrt{\chi_T(T)}$ in the near T_c regime but approach the HTL $\mu(T)$ at high T limit. Regarding the magnetic screening mass, since we have $n_M \sim (\alpha_E T)^3$ following the magnetic scaling, then

$$\mu_M^2 \sim \alpha_M\, (\alpha_E T)^3/T \sim \alpha_E^2 T^2 \sim g^2\, g^2 T^2 \sim g^2 \mu^2\ . \tag{5.15}$$

This prescription is supported by lattice data [275]. Therefore, we assume the following local temperature dependent screening masses in the CUJET3.0 model:

$$f_E(T(\mathbf{z})) = \sqrt{\chi_T(T(\mathbf{z}))} \quad , \quad f_M(T(\mathbf{z})) = c_m\, g(T(\mathbf{z}))\,. \tag{5.16}$$

To be consistent with previous treatments in Eq. (3.8) and (3.5), the local electric "coupling" $g(T(\mathbf{z}))$ is defined via

$$g(T(\mathbf{z})) = \sqrt{4\pi\alpha_s(\mu^2(T(\mathbf{z})))} = \frac{\mu(T(\mathbf{z}))}{T(\mathbf{z})\sqrt{1+N_f/6}}. \tag{5.17}$$

Note that c_m is a constant parameter that can be constrained by lattice data on the magnetic screening. Fig. 5.1(b) illustrates the agreement between this prescription of $\mu_{E,M}$ and lattice extracted values [275].

Finally, in the CUJET3.0 framework, the energy loss kernel Eq. (3.8) is generalized to

$$\begin{aligned} x_E\frac{dN_g^{n=1}}{dx_E} &= \frac{18C_R}{\pi^2}\frac{4+N_f}{16+9N_f}\int d\tau\ \rho(\mathbf{z})\Gamma(\mathbf{z})\ \int d^2k_\perp\alpha_s(\frac{\mathbf{k}_\perp^2}{x_+(1-x_+)}) \\ &\times \int d^2q\frac{\alpha_s^2(\mathbf{q}_\perp^2)\left(f_E^2+\frac{f_E^2f_M^2\mu^2(\mathbf{z})}{\mathbf{q}_\perp^2}\right)\chi_T+\left(f_M^2+\frac{f_E^2f_M^2\mu^2(\mathbf{z})}{\mathbf{q}_\perp^2}\right)(1-\chi_T)}{(\mathbf{q}_\perp^2+f_E^2\mu^2(\mathbf{z}))(\mathbf{q}_\perp^2+f_M^2\mu^2(\mathbf{z}))} \\ &\times \frac{-2(\mathbf{k}_\perp-\mathbf{q}_\perp)}{(\mathbf{k}_\perp-\mathbf{q}_\perp)^2+\chi^2(\mathbf{z})}\left[\frac{\mathbf{k}_\perp}{\mathbf{k}_\perp^2+\chi^2(\mathbf{z})}-\frac{(\mathbf{k}_\perp-\mathbf{q}_\perp)}{(\mathbf{k}_\perp-\mathbf{q}_\perp)^2+\chi^2(\mathbf{z})}\right] \\ &\times \left[1-\cos\left(\frac{(\mathbf{k}_\perp-\mathbf{q}_\perp)^2+\chi^2(\mathbf{z})}{2x_+E}\tau\right)\right]\left(\frac{x_E}{x_+}\right)\left|\frac{dx_+}{dx_E}\right| \ , \end{aligned} \tag{5.18}$$

where χ_T and $f_{E,M}$ follows Eq. (5.11) and Eq. (5.16). We note that in the temperature range $T\sim T_c$, the coupling α_s becomes non-perturbative [236, 296, 297, 362]. Analysis of lattice data [296] suggests the following thermal running coupling form:

$$\alpha_s(Q^2)=\frac{\alpha_c}{1+\frac{9\alpha_c}{4\pi}\log(\frac{Q^2}{T_c^2})}\ , \tag{5.19}$$

with $T_c = 160$ MeV. Note that at large Q^2, Eq. (5.19) converges to vacuum running $\alpha_s(Q^2)=\frac{4\pi}{9\log(Q^2/\Lambda^2)}$; while at $Q=T_c$, $\alpha_s(T_c^2)=\alpha_c$.

5.1.5 Liberation schemes: Polyakov loop vs chiral susceptibility

As discussed in previous sections, within the semi-QGP model, the expectation value of the Polyakov loop L (note that we have redefined $L\equiv\ell$ in section 5.1.4, and we use this notation for the rest of this chapter) is the only relevant parameter for the confinement/deconfinement transition, upon proper renormalizations, L serves as a suppression factor for the colored excitations as $T\to T_c^+$. However, it is questionable whether or not L is an *order parameter* for the phase transition. Besides the fact that lattice calculations point to a $L\sim 0.1$ at T_c, Eq. (5.1)(5.2)(5.3) also indicate that to a certain degree the loop

physically characterizes the free energy of an *infinitely massive static quark*. Since (1) in the perturbative QGP phase dynamical light quarks dominate the medium transport properties; and (2) to boost v_2 in line with data, a strongly enhanced jet scattering near T_c makes decisive contributions [232]; then, the nonperturbative property of the sQGMP, in particular, the rate at which fractional chromo-electric DOFs are liberated (defined as $r_d(T) \equiv d\chi_T/dT$) in the near T_c regime will play a significant role in computing jet quenching observables within the CUJET3.0 framework and should be studied more systematically.

Another useful measure of the nonperturbative suppression of the color electric DOF is provided by the quark number susceptibilities [363–366]. Such susceptibilities quantify the quark number fluctuations that can be obtained from the QCD partition function at vanishing chemical potentials. Denote u, d, s as up, down, strange quark whose numbers are conserved charges in QCD. Starting from the pressure,

$$\frac{p}{T^4} = \frac{1}{VT^3} \ln Z(V, T, \mu_u, \mu_d, \mu_s) \ , \tag{5.20}$$

moments of charge fluctuations are defined as follows,

$$\chi^{uds}_{ijk} = \frac{\partial^{i+j+k} p/T^4}{\partial(\mu_u/T)^i \partial(\mu_d/T)^j \partial(\mu_s/T)^k} \ . \tag{5.21}$$

Concentrate on the quadratic fluctuation,

$$\chi_2^{u,d,s} = \frac{1}{VT^3} \langle N^2_{u,d,s} \rangle . \tag{5.22}$$

And $\chi_2^{u,d,s}$ is the diagonal susceptibility of u, d, s quark number density. Singlet susceptibilities of other conserved charges in QCD such as baryon number B, strangeness S and electric charge Q can be obtained from the above quark number susceptibilities [350].

The diagonal susceptibility is proposed as part of the order parameter for chiral symmetry breaking/restoration in [363]. Considering a gas of free quarks, if the quark mass m is small, then χ_2 is expected to be large since it is relatively easy to create an additional quark. For instances, if $m \ll T$, then in the continuum limit, $\chi_2 \sim N_f T$. If m is large, then it will be difficult to create a quark or antiquark, the susceptibilities will be suppressed by $\exp(-m/T)$. Realistically, in the high T phase, though strongly interacting, if the fundamental excitations of the system are low-m objects with the quantum numbers of quarks, then χ_2 is still expected to be large. Meanwhile, in the low T phase, χ_2 will be small since quarks are confined and the nonzero quark number states have large masses. Thus in the chirally symmetric phase, the quark number susceptibility is large, which is consistent with a plasma of light quarks; while in the chiral symmetry broken phase, the quark number susceptibility is small, as expected from quark confinement. It however may be noted that in the parton-hadron boundary regime, various bound states like baryons and mesons (and even other exotic composite objects) carry conserved charges and contribute to the susceptibilities. As previous studies have shown [367–369], such contributions are mostly important for the higher-order susceptibilities as well as for the off-diagonal ones. The leading order diagonal susceptibilities could therefore serve as a reasonable measure for the counting of quark degrees of freedom in the plasma.

Therefore, besides interpolating the renormalized lattice Polyakov loop as in Eq. (5.12), we parametrize the lattice diagonal susceptibility of u quark number density as

$$\chi_2^u(T) = 0.91 \times \left[\frac{1}{2}\left\{1 + \mathrm{Tanh}[15.65(T - 0.0607)]\right\}\right]^{10}. \tag{5.23}$$

Where T is the temperature in the unit of GeV. Note that at extremely high temperature, the $\chi_2^u(T)$ is not unity, so we renormalize the susceptibility by its value at $T \to \infty$ and

define a new quantity $\tilde{\chi}_2^u(T)$ as

$$\tilde{\chi}_2^u(T) = \left[\frac{1}{2}\left\{1 + \text{Tanh}[15.65(T - 0.0607)]\right\}\right]^{10} . \tag{5.24}$$

The $\tilde{\chi}_2^u(T)$ plays a similar role as properly renormalized L for quark DOFs. Let us denote the original liberation scheme, c.f. Eq. (5.11), that follows the power law of the Polyakov loop as in the semi-QGP model, as χ_T^L ($\chi_T^L \equiv \chi_T$ in Eq. (5.11)); and the new deconfinement scheme where the diagonal susceptibility of light quark number density dominates the transition, as χ_T^u ($\chi_T^u = \rho_E/\rho$):

$$\chi_T^u = c_q\, \tilde{\chi}_2^u + c_g\, L^2 \ . \tag{5.25}$$

Note that in this scheme, the magnetically charged quasi-particles, i.e. chromo-magnetic monopoles, have a density fraction of $1 - \chi_T^u = \rho_M/\rho$.

Fig. 5.1(a) shows the lattice QCD data on renormalized Polyakov loop and diagonal light quark susceptibility from the HotQCD [103] and Wuppertal-Budapest [348, 350] Collaboration, as well as the parametrization fit Eq. (5.12) and Eq. (5.23). The E and M quasi-particle density fraction in both the χ_T^L and χ_T^u scheme are plotted in the inset of Fig. 5.1(a). Note that $\rho_E/\rho = \chi_T^{L,u}$ and $\rho_M/\rho = 1 - \chi_T^{L,u}$. The two different schemes, for the rate of "quark liberation", with χ_T^L the "slow" and χ_T^u the "fast", provide useful estimates of theoretical systematic uncertainties associated with the quark component of the sQGMP model. Note that in the inset of Fig. 5.1(a) the ρ_E and ρ_M are equal at $T \sim 1.1\,T_c$ for χ_T^u scheme while at $T \sim 1.7\,T_c$ for χ_T^L scheme: these temperatures are where $r_d(T) \equiv d\chi_T^{L,u}/dT$ should peak.

As suggested in Eq. (5.16), any change in χ_T alters the electric screening mass μ_E, and one expects shifts in the magnetic screening correspondingly under electric-magnetic du-

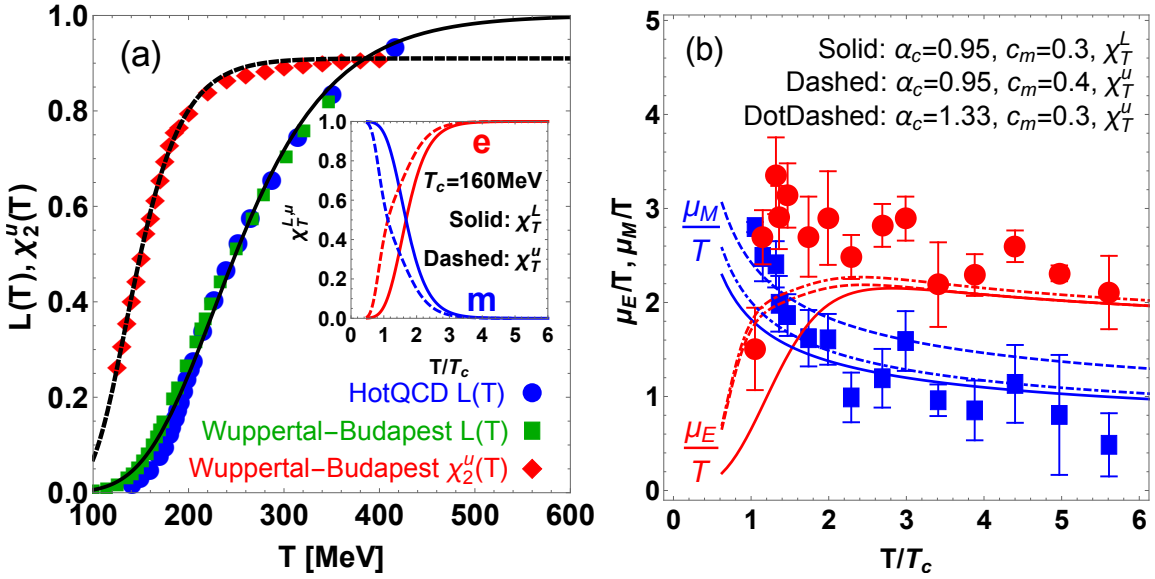

Figure 5.1: *(a) Renormalized Polyakov loop $L(T)$ (blue circle: [103], green square: [348]) and diagonal susceptibility of light quark number density $\chi_2^u(T)$ (red diamond: [350]) computed from lattice QCD, fitted with the parametrization of Eq. (5.12) and (5.23). The inset shows the the density fraction of color electric DOFs (red, $\chi_T = \rho_E/\rho$) and color magnetic DOFs (blue, $1-\chi_T = \rho_M/\rho$) within the liberation scheme χ_T^L (solid) and χ_T^u (dashed), in the temperature range $T \sim 0.6 - 6.0\ T_c$, where $T_c = 160\ MeV$. Notice that in χ_T^L, $\rho_E \approx \rho_M$ at $T \sim 1.7\,T_c$; in χ_T^u, $\rho_E \approx \rho_M$ at $T \sim 1.1\,T_c$; and these temperatures are where $r_d(T) \equiv d\chi_T/dT$ should peak in $\chi_T^{L,u}$. (b) The dimensionless electric (red) and magnetic (blue) screening mass $\mu_{E,M}/T$ in the CUJET3.0 model i.e. Eq. (5.16), for scheme (i) (5.26), (ii) (5.27), and (iii) (5.28), compared with results from Lattice QCD [275]. Note that the α_c and c_m parameters in (i)(ii)(iii) are chosen such that the high-p_T reference R_{AA} datum can be well-fitted, c.f. Fig. 5.5(a). Note that for (i) and (ii), $\mu_E/T \approx \mu_M/T$ at around the same temperature, i.e. $T \sim 1.5 - 1.6\,T_c$, while (iii)'s μ_E/T and μ_M/T intersect at $T \sim 1.1\,T_c$. In the near T_c regime, (i) and (ii)'s $\mu_E - \mu_M$ are approximately identical, both are less than (iii)'s.*

ality. In Fig. 5.1(b), lattice data of the electric and magnetic screening mass are compared

with the CUJET3.0 results in three schemes:

$$\text{(i)} \quad \alpha_c = 0.95, c_m = 0.3, \chi_T^L \,; \tag{5.26}$$

$$\text{(ii)} \quad \alpha_c = 0.95, c_m = 0.4, \chi_T^u \,; \tag{5.27}$$

$$\text{(iii)} \quad \alpha_c = 1.33, c_m = 0.3, \chi_T^u \,. \tag{5.28}$$

Note that the (α_c, c_m) parameters are chosen such that the single reference datum $R_{AA}^{h^\pm}(p_T = 12.5\text{GeV/c}) \approx 0.3$ at the LHC is well-fitted, cf. Fig. 5.5(a). Implicitly, χ_T^L and χ_T^u are determined by Eq. (5.11) and Eq. (5.25) respectively. All three schemes are in reasonable agreements with the lattice data. However, to be more careful, (i)(ii)(iii)'s $\mu_{E,M}$ do behave differently as temperature varies. (i)'s and (ii)'s μ_E/T and μ_M/T intersect at approximately the same temperature, i.e. $T \sim 1.5 - 1.6\, T_c$. Meanwhile, (iii)'s μ_E/T and μ_M/T intersect at $T \sim 1.1\, T_c$, which temperature overlaps approximately with the T where $\rho_E(T) = \rho_M(T)$ in χ_T^u. Furthermore, in the near T_c regime, (i)'s and (ii)'s $\mu_E - \mu_M$ are approximately equal, and both are less than (iii)'s.

In Section 5.2, we will focus on Scheme (i) which is our default choice of the liberation scheme for color degrees of freedom, we will study under this scheme the consistency between perfect fluidity and jet quenching in sQGMP within CUJET3.0. The robustness of the results derived in Section 5.2 to different confinement/deconfinement schemes in Eq. (5.28) will be discussed in Section 5.3.

5.2 Consistency of perfect fluidity and jet transport

Noted at the beginning of this chapter, the main motivations that stimulated the formulation of CUJET3.0 were the "high p_T v_2 puzzle" and the discrepancy between the pQCD estimate of η/s and the QGP's "perfect fluidity". We will see in this section that jet

quenching observables of high p_T light hadrons' and open heavy flavors' R_{AA} and v_2 at RHIC and the LHC computed using CUJET3.0 are in agreement with all data simultaneously withing present experimental uncertainties. And if we further calculate the jet transport parameter $\hat{q}$ and the shear viscosity to entropy density ratio η/s in CUJET3.0, we see CUJET3.0 does provide a semi-quantitative bridge between local equilibrium bulk "perfect fluidity" and high energy far from equilibrium jet transport phenomena.

5.2.1 High p_T hadrons R_{AA} and v_2 from CUJET3.0

Let us first apply CUJET3.0 to compute high p_T single inclusive hadron observables, the results are shown in Fig. 5.2, where the comparisons of data and CUJET3.0 results for mid-rapidity ($y = 0$) $R_{AA}(p_T)$ and $v_2(p_T)$ of inclusive neutral pions (π^0) and charged particles ($h^{\pm}$) in Au+Au $\sqrt{s_{NN}} = 200$ GeV and Pb+Pb $\sqrt{s_{NN}} = 2.76$ TeV semi-peripheral collisions are plotted.

There is only one parameter α_c that is fixed by a single reference data point, i.e. $R_{AA}^{h\pm}(p_T = 12.5\text{GeV}) \approx 0.3$ at the LHC, and all other parameters are already determined from lattice QCD (including the c_m in Eq. (5.16), c.f. Fig.5.1). Evidently, the CUJET3.0 framework simultaneously describes *both R_{AA} and v_2 at both RHIC and the LHC*. This finding quantitatively validates earlier arguments [295] that enhanced energy loss at later time generically increases v_2 for fixed R_{AA}.

We also predict the high p_T $R_{AA}(p_T)$ and $v_2(p_T)$ for D and B meson at the LHC semi-peripheral 20-30% Pb+Pb $\sqrt{s_{NN}} = 2.76$ TeV collisions, shown in Fig. 5.2. These results are all consistent with existing data (where available) and can be tested with future measurements.

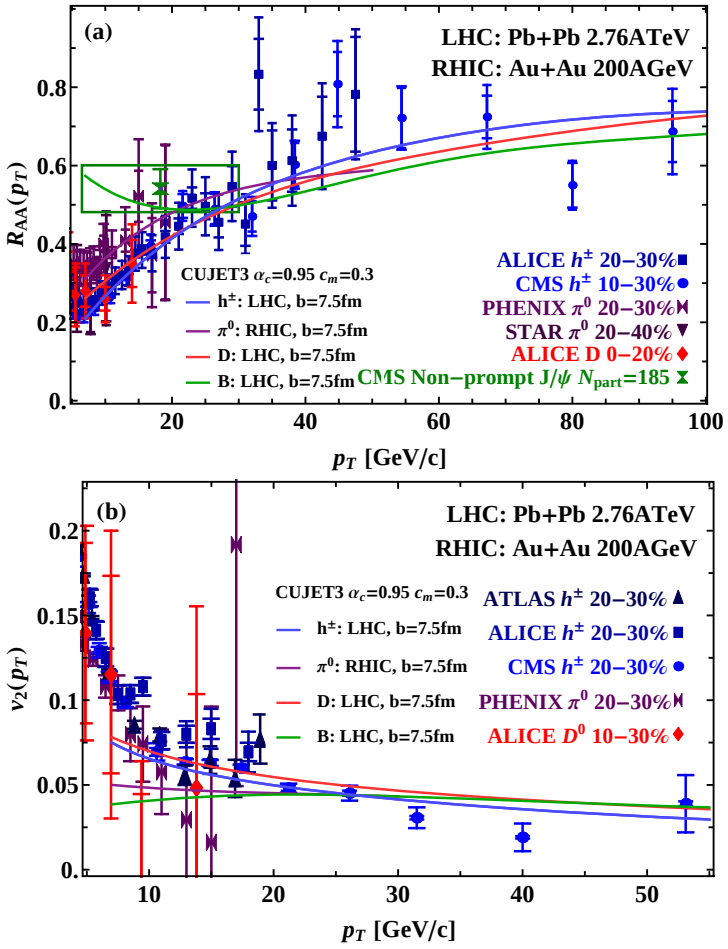

Figure 5.2: *(a) $R_{AA}(p_T)$ and (b) $v_2(p_T)$ of inclusive neutral pions (π^0) and charged particles ($h^\pm$) in Au+Au $\sqrt{s_{NN}} = 200$ GeV and Pb+Pb $\sqrt{s_{NN}} = 2.76$ TeV collisions, computed from CUJET3.0 with the impact parameter $b = 7.5$ fm, compared with corresponding data from ALICE, ATLAS, CMS, PHENIX and STAR [107, 149, 152, 272–274, 292–294]. With $(\alpha_c, c_m) = (0.95, 0.3)$, the results of CUJET3.0 are consistent with data of both R_{AA} and v_2 at both RHIC and the LHC simultaneously. CUJET3.0 ($b = 7.5$ fm) predictions of $R_{AA}(p_T)$ and $v_2(p_T)$ for open heavy flavors (D meson, red; B meson, green) at the LHC semi-peripheral Pb+Pb $\sqrt{s_{NN}} = 2.76$ TeV collisions are also plotted. The D meson results with $p_T < 20$ GeV/c agree with ALICE data of both R_{AA} and v_2 [271, 289], while the B meson R_{AA} results at $6.5 < p_T < 30$ GeV/c are in agreement with non-prompt J/ψ at CMS (green box indicates systematic errors) .*

5.2.2 Jet transport parameter

The jet transport transport parameter $\hat{q}$, which has been extensively discussed in Section 3.3, characterizes the averaged transverse momentum transfer squared per mean free path [276]. Here let us calculate the $\hat{q}$ for a quark jet (in the fundamental representation F of $SU(3)$) with initial energy E, via the following:

$$\begin{aligned}\hat{q}_F(E,T) &= \int_0^{6ET} d\mathbf{q}_\perp^2 \frac{2\pi \mathbf{q}_\perp^2}{(\mathbf{q}_\perp^2 + f_E^2\mu^2)(\mathbf{q}_\perp^2 + f_M^2\mu^2)}\rho(T) \\ &\times \left[(C_{qq}f_q + C_{qg}f_g)\alpha_s^2(\mathbf{q}_\perp^2) + C_{qm}(1-f_q-f_g)\right] . \end{aligned} \tag{5.29}$$

Here $\rho(T)$ is the total local quasi-particle number density, it is connected to the lattice pressure $p(T)$ via

$$\rho(T) = \xi\, p(T)/T , \tag{5.30}$$

with $\xi = [90\zeta(3)(16+9N_f)]/[\pi^4(16+10.5N_f)] = 1.012$ for an $N_c = 3, N_f = 2.5$ ideal gas [2]. The parameters $f_{q,g}$ are quasi-parton density fractions of quark (q) or gluon (g) type, in the χ_T^L and χ_T^u scheme, they are respectively

$$\begin{aligned} f_q &= c_q L(T),\ f_g = c_g L(T)^2,\ \text{if } \chi_T^L ; \\ f_q &= c_q \tilde{\chi}_2^u(T),\ f_g = c_g L(T)^2,\ \text{if } \chi_T^u . \end{aligned} \tag{5.31}$$

The $c_{q,g}$ and $L(T)$ are the same as in Eq. (5.11) and (5.12). The magnetically charged quasi-particle density fraction is hence $f_m(T) = 1 - f_q(T) - f_g(T)$. The color factors in

[2] The ξ near T_c may be different from the idea gas limit, the uncertainties coming from this are subject to future studies.

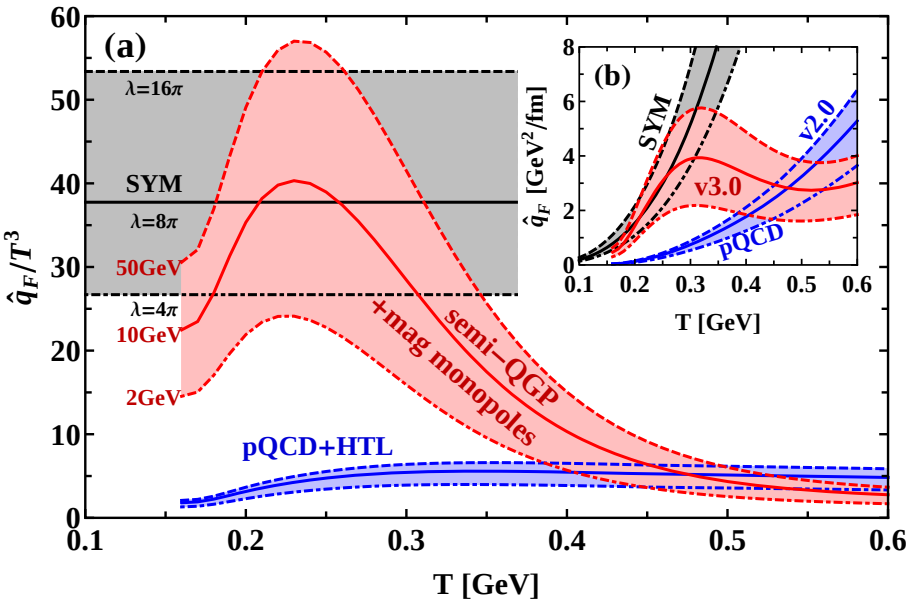

Figure 5.3: *Temperature dependence of (a) the dimensionless jet transport coefficient $\hat{q}/T^3$ and (b) the absolute $\hat{q}$ for a quark jet (F) with initial energy E = 2, 10, 50 GeV, computed from CUJET3.0 (semi-QGP + chromomagnetic monopoles) with $(\alpha_c, c_m) = (0.95, 0.3)$, compared with the result from CUJET2.0 (pQCD + HTL) [216] with $(\alpha_{max}, f_E, f_M) = (0.39, 1, 0)$, and the result from $\mathcal{N} = 4$ Supersymmetric Yang-Mills (SYM) calculations ($\hat{q} \approx 26.69\sqrt{\lambda/4\pi}T^3$) [281].*

Eq. (5.29) are given by

$$\begin{aligned} C_{qq} &= \frac{4}{9},\ C_{gg} = C_{mm} = \frac{9}{4}, \\ C_{qg} &= C_{gq} = C_{qm} = C_{mq} = 1\ . \end{aligned} \tag{5.32}$$

The scaled jet transport coefficients $\hat{q}/T^3$ of the CUJET3.0 and CUJET2.0 models are compared in Fig. 5.3. Here one sees the strong near-T_c enhancement of the sQGMP opacity as compared with the perturbative HTL model of the QGP[3]. As demonstrated

[3]In principle, at relatively large T, the $\hat{q}$ from CUJET3.0 (pQCD+sQGMP) and CUJET2.0 (pQCD+HTL) should converge because of asymptotic freedom and the vanishing of CMM component. However, compare Eq. (5.29) and Eq. (3.58)(3.59), one sees that the magnetic screening mass differs in the two models. This makes the CUJET3.0's $\hat{q}$ goes below CUJET2.0's at high T.

in Fig. 5.2, while both models of the QGP can describe the single inclusive hadron suppression (quantified by nuclear modification factor R_{AA}) data, only the nonperturbative sQGMP model with non-trivial near-T_c behavior can account well for both high p_T R_{AA} and its azimuthal anisotropy v_2. Notice that no new parameters are introduced in this analysis since the sQGMP properties are fully constrained by available lattice QCD data.

5.2.3 Shear viscosity

In the CUJET3.0 framework, once the jet transport coefficient $\hat{q}$ has been computed, the shear viscosity to entropy density ratio η/s can be calculated based on kinetic theory in a weakly-coupled quasi-particle picture[4], as proposed in [112, 282, 334]. An estimate of η/s can be derived as

$$\begin{aligned} \eta/s &= \frac{1}{s}\frac{4}{15}\sum_a \rho_a \langle p\rangle_a \lambda_a^{\perp} \\ &= \frac{4T}{5s}\sum_a \rho_a \left(\sum_b \rho_b \int_0^{\langle \mathcal{S}_{ab}\rangle/2} dq_\perp^2 \frac{4q_\perp^2}{\langle \mathcal{S}_{ab}\rangle}\frac{d\sigma_{ab}}{dq_\perp^2}\right)^{-1} \\ &= \frac{18T^3}{5s}\sum_a \rho_a/\hat{q}_a(T, E=3T) \quad . \end{aligned} \tag{5.33}$$

Note that the $\hat{q}(T,E)$ is extrapolated down to thermal energy scales $E \sim 3T$. The $\rho_a(T)$ is the quasi-parton density of type $a = q, g, m$. The mean thermal Mandelstam variable $\langle \mathcal{S}_{ab}\rangle \sim 18T^2$. The entropy density $s(T)$ is interpolated from lattice calculations [103].

[4]This picture is imposed because it is interesting to study the behavior of η/s assuming the long-short distance transport correlation built up from kinetic theory is applicable to any system.

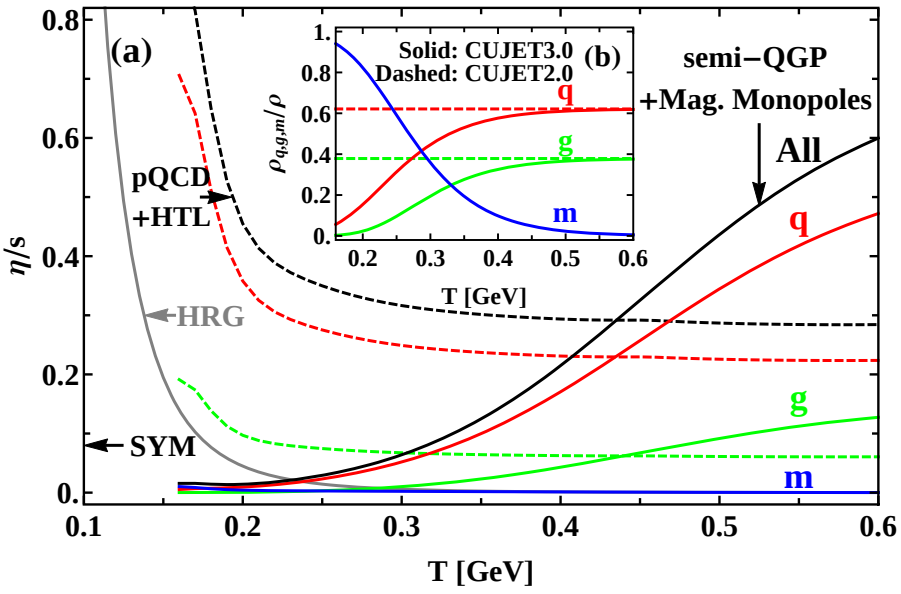

Figure 5.4: *(a) Temperature dependence of shear viscosity per entropy density (η/s) for quasi-partons of quark (q), gluon (g) and monopole (m) type, as well as their overall contribution (All). (b) The density fractions of q, g, m. Solid lines correspond to the sQGMP model (CUJET3.0), while dashed ones correspond to the pQCD+HTL model (CUJET2.0). The AdS/CFT perfect fluidity limit $\eta/s = 1/4\pi$ is marked as SYM. The shaded line is the Hadron Resonance Gas (HRG) η/s from [370]. The falling of sQGMP's η/s below $1/4\pi$ is due to the limitation of kinetic theory estimate of η/s in the low E extrapolation of $T^3/\hat{q}(E \sim 3T, T)$ [282].*

The $\hat{q}_{a=q} \equiv \hat{q}_F$ is calculated as in Eq. (5.29). The $\hat{q}_{a=g,m}$ for are computed via

$$\hat{q}_{a=g}(E,T) = \int_0^{6ET} d\mathbf{q}_\perp^2 \frac{2\pi \mathbf{q}_\perp^2}{(\mathbf{q}_\perp^2 + f_E^2\mu^2)(\mathbf{q}_\perp^2 + f_M^2\mu^2)}\rho(T) \times \left[(C_{gq}f_q + C_{gg}f_g)\alpha_s^2(\mathbf{q}_\perp^2) + C_{gm}(1 - f_q - f_g)\right] , \quad (5.34)$$

$$\hat{q}_{a=m}(E,T) = \int_0^{6ET} d\mathbf{q}_\perp^2 \frac{2\pi \mathbf{q}_\perp^2}{(\mathbf{q}_\perp^2 + f_E^2\mu^2)(\mathbf{q}_\perp^2 + f_M^2\mu^2)}\rho(T) \times \left[(C_{mq}f_q + C_{mg}f_g) + C_{mm}(1 - f_q - f_g)/\alpha_s^2(\mathbf{q}_\perp^2)\right] . \quad (5.35)$$

Clearly the η/s of the system is dominated by the component which has the largest $\rho_a/\hat{q}_a$.

We show in Fig. 5.4 the results from two models: the CUJET2.0 result assuming the

pQCD HTL model of the QGP compared to the CUJET3.0 result based on the sQGMP model. The former perturbative model clearly over-predicts the phenomenologically deduced η/s and has the wrong sign of temperature trend from RHIC to the LHC. On the other hand, the nonperturbative sQGMP model features an especially small value $\eta/s \sim 0.1$ in $T \lesssim 2T_c$ range, with a rapid increase toward high T, in line with empirical data. The sQGMP model hence provides a viable path toward perfect fluidity in contrast to all past attempts starting from perturbative jet quenching as considered in the JET collaboration summary [276].

We have seen that the CUJET3.0 jet energy loss framework, based on the semi-quark-gluon-monopole plasma (sQGMP) model that implements non-perturbative effects constrained by lattice QCD data, has led to several highly nontrivial findings: a consistent description of both bulk perfect fluidity and high p_T jet quenching phenomena; a strong increase of $\hat{q}/T^3$ accompanied by a strong decrease of η/s toward T_c; a simultaneous description of high p_T R_{AA} and v_2 data at RHIC and the LHC.

5.3 Robustness of perfect fluidity and jet quenching in CUJET3.0

We have seen in the previous section that the CUJET3.0 generated a remarkable consistency between the soft bulk "perfect fluidity" of the QGP and the hard jet transport properties in the QGP. However, it has been noted in Section 5.1.5 distinctive deconfinement schemes for color degrees of freedom that are all compatible with lattice data can be implemented in the model. Therefore, it is crucial to study the CUJET3.0's robustness to theoretical uncertainties associated with the "slow" quark liberation as suggested by $L(T)$ data compared to the "fast" quark liberation as suggested by the lattice light quark

susceptibility $\chi_u(T)$ data.

5.3.1 Implications of high p_T observables

Let us first examine jet quenching observables in scheme (i)(ii)(iii) within the CUJET3.0 framework, in particular, leading light hadrons' and open heavy flavors' $R_{AA}(p_T > 8$ GeV) (c.f. Eq. (3.55)) and $v_2(p_T > 8$ GeV) (c.f. Eq. (3.64)) in RHIC and the LHC semi-peripheral A+A collisions are of interests. The results and corresponding data are plotted in Fig. 5.5.

For high p_T light hadrons (π^0 at RHIC, $h^\pm$ at the LHC), Fig. 5.5(a) shows that all three schemes can describe the $R_{AA}(p_T)$ data at RHIC ($8 < p_T < 20\,$GeV) and the LHC ($8 < p_T < 100\,$GeV) simultaneously, but only (i) and (ii) are compatible with the high p_T single π^0 and $h^\pm$'s v_2 as illustrated in Fig. 5.5(c). Since (i) and (ii) have different liberation schemes hence r_d's, different absolute values of $\mu_{E,M}$, but approximately the same $\mu_E - \mu_M$ near T_c, this observation indicates that in boosting the π^0 or $h^\pm$'s azimuthal elliptical harmonics to be in line with data, the difference between μ_E and μ_M in the near T_c regime plays a critical role. Notice that as suggested in the magnetic scenario, when cooling down to pass $T \sim 1 - 2T_c$, the lightest hence the dominant DOFs in the medium shift from EQPs to MQPs, and the color screening mass is one of the indicators of this transition [297]. The fact that (i)(ii)'s $\mu_E(T) - \mu_M(T)$ generates a larger v_2 than (iii)'s $\mu_E(T) - \mu_M(T)$ which has a larger value and a lower zero point temperature T_0 (T_0 is defined as $\mu_E(T_0) = \mu_M(T_0)$) implies that, v_2 is sensitive to how the relative value of μ_E and μ_M inverts near T_c – the higher the T_0, the longer the path length that jets interact with the strongly coupled monopole dominated medium at later time of the evolution, the larger the azimuthal anisotropy. A further comment is on the absolute values of $\mu_{E,M}$ in (i)(ii), clearly (ii)'s are larger. This is necessary because after T drops lower than T_0,

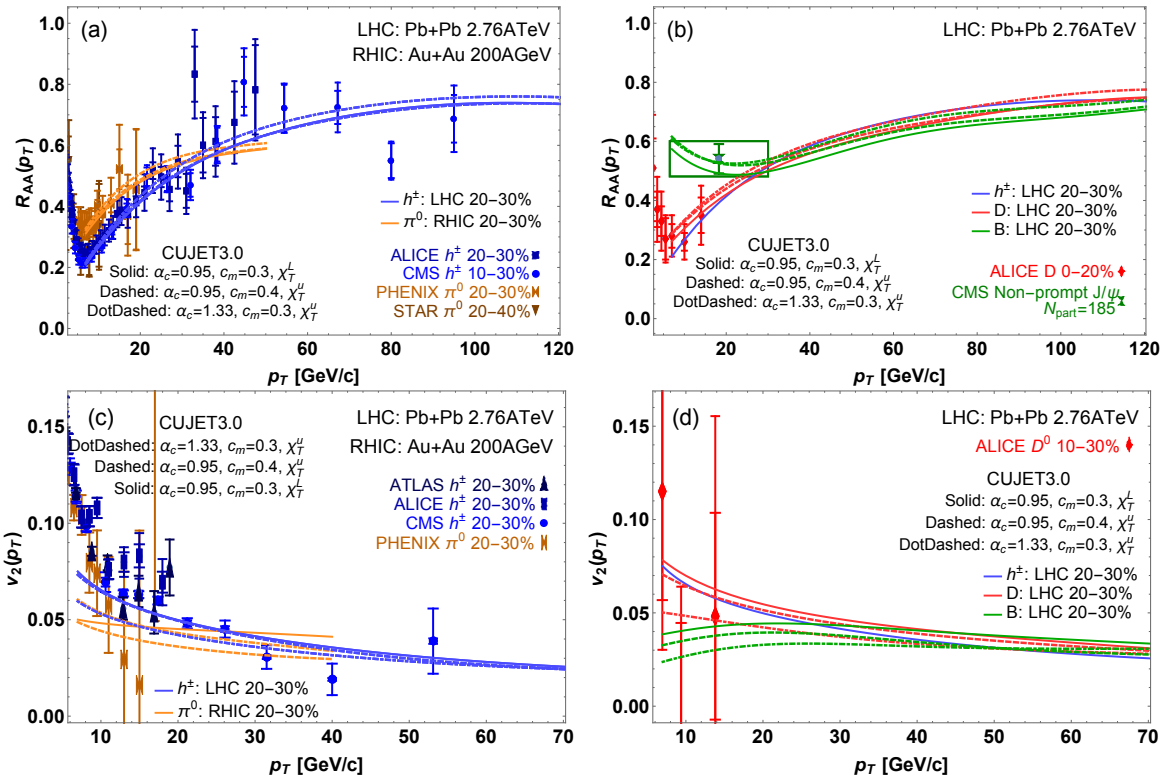

Figure 5.5: *(a) Neutral pion (π^0, brown) and charge particle ($h^\pm$, blue)'s $R_{AA}(p_T >$ 8GeV) in Au+Au 200 GeV and Pb+Pb 2.76 TeV 20-30% collisions, computed from CUJET3.0 with scheme (i)(5.26) α_c=0.95, c_m=0.3, χ_T^L (solid), (ii)(5.27) α_c=0.95, c_m=0.4, χ_T^u (dashed) and (iii)(5.28) α_c=1.33, c_m=0.3, χ_T^u (dotdashed), compared with corresponding RHIC [149, 272, 273, 294] and the LHC [107, 152, 274, 292, 293] measurements. The π^0 and $h^\pm$'s $v_2(p_T > 8$ GeV) are plotted in (c). (b) The CUJET3.0 results of D meson (red) and B meson (green)'s $R_{AA}(p_T > 8$ GeV) at the LHC in (i)(ii)(iii) compared with available data [271, 289, 371]. The D and B's $v_2(p_T > 8$ GeV) are plotted in (d). Results from all three schemes are compatible with light hadron (LH)'s R_{AA}; while for LH's v_2, (i) and (ii) can generate reasonable agreements with data, but (iii) underestimates the v_2. For open heavy flavors (HF), (ii) and (iii) have similar R_{AA} predictions, both differ from (i); while for HF's v_2, (i), (ii), and (iii)'s prediction are all different. Such differences in the predictions for jet quenching observables from (i)(ii)(iii) suggest that data on high p_T R_{AA} and v_2 can impose stringent constraints on the nonperturbative properties of the medium near T_c.*

MQPs dominates, (i)'s ρ_M is denser than (ii)'s, to get to the same magnitude of overall jet suppressions, (ii) should possess larger color screening masses, c.f. Eq. (5.10).

For open heavy flavors, specifically, high p_T D and B mesons, Fig. 5.5(b) shows their respective R_{AA} at the LHC Pb+Pb $\sqrt{s_{NN}} = 2.76$ TeV collisions, computed from CUJET3.0 with scheme (i)(ii)(iii). Differing from the light hadrons' R_{AA} where (i)(ii)(iii) have almost identical predictions, for D and B mesons, (ii) and (iii)'s R_{AA} overlap, both of which distinguish from (i)'s. One notices that (ii) and (iii) have different $\mu_{E,M}$, but the same liberation scheme χ_T^u, which is distinct from (i)'s χ_T^L. This implies the open heavy flavor's high p_T R_{AA} is critically influenced by the rate at which chromo-electric DOFs are deconfined ($r_d = d\chi_T/dT$). This connection is intrinsically embedded in the CUJET3.0 framework because the heavier masses induced dead cone effects shuffled the weights of the scattering potential (5.10) and the rest of the Eq. (5.18) in such a way that the total induced radiation became more sensitive to the deconfinement scheme r_d rather than screening masses $\mu_{E,M}$ for jet quenching in sQGMP. On the other hand, Fig. 5.5(d) shows the prediction of open heavy flavor's $v_2(p_T > 8$ GeV) at the LHC in CUJET3.0. The v_2's are all different in scheme (i), (ii), and (iii). This suggests the open charm and beauty's $v_2(p_T)$ act as good probes of the nonperturbative (r_d, μ_E, μ_M) near T_c. Let us mention in passing that for the heavy quark dynamics in low p_T region, the sQGMP model also expects a strong temperature dependence of their in-medium diffusion coefficients (specifically a "dip" near T_c), which has recently been shown as an essential ingredient toward a simultaneous description of their R_{AA} and v_2 [372, 373].

If one views the above physical connections from a different angle, the set of RHIC and the LHC heavy-ion collision data on high p_T light hadron (LH) and open heavy flavor (HF)'s R_{AA} and v_2 will provide stringent limits on the nonperturbative properties of the QCD matter near T_c in the CUJET3.0 framework. Specifically, after parameters in the model have been fixed by light quark's R_{AA} data, the rate at which color DOFs

are deconfined r_d and the color screening masses $\mu_{E,M}$ can be stringently constrained: (1) light quark's v_2 regulates $\mu_E(T) - \mu_M(T)$ near T_c; (2) heavy quark's R_{AA} determines $r_d(T)$; (3) HF's v_2 distinguishes all $r_d(T)$, $\mu_E(T)$ and $\mu_M(T)$.

5.3.2 $\hat{q}$ and η/s

As discussed above, the high p_T R_{AA} and v_2 data of light and heavy quarks can provide stringent constraints on values of the nonperturbative (r_d, μ_E, μ_M) near T_c. It is of great interests to further compare how the jet and bulk transport properties differ in varied schemes (i) (5.26), (ii) (5.27), and (iii) (5.28). This will pave the way for clarifying the temperature dependence of jet quenching and shear viscous transport properties based on available high p_T data in high-energy A+A collisions.

Fig. 5.6(a)(b)(c) shows the dimensionless jet transport coefficient $\hat{q}/T^3$ in CUJET3.0 for a quark jet with initial energy E = 20, 10, 2 GeV respectively, compared with the CUJET2.0 result [216] and the AdS/CFT limit [281]. The $\hat{q}$'s in scheme (i)(ii)(iii) are plotted. Compared with (i) which has χ_T^L "slow" quark liberation, the $\hat{q}$ in (ii) and (iii) which have χ_T^u "fast" quark liberation scheme are significantly smaller. This may be understood as follows: in the χ_T^u scheme, as temperature rises, the chromo-electric DOFs are excited faster than those in the χ_T^L scheme, and leads to a smaller fraction of magnetically charged quasi-particles in the near T_c regime. Since chromo-magnetic monopoles are the key contributors to the enhancement of jet opacity, c.f. Section 5.5.2, less monopoles thus result in a diminished $\hat{q}$ in the χ_T^u scheme compared with the one in the χ_T^L scheme. Interestingly, (ii) and (iii)'s $\hat{q}$ still get close to the Super Yang-Mills (SYM) limit near T_c. Noting that (ii) and (iii)'s $\mu_{E,M}$ behave very differently as shown in Fig. 5.1(b), then a crucial observation one can draw is that among the nonperturbative (r_d, μ_E, μ_M), the high energy jet transport property which is determined by the quenching

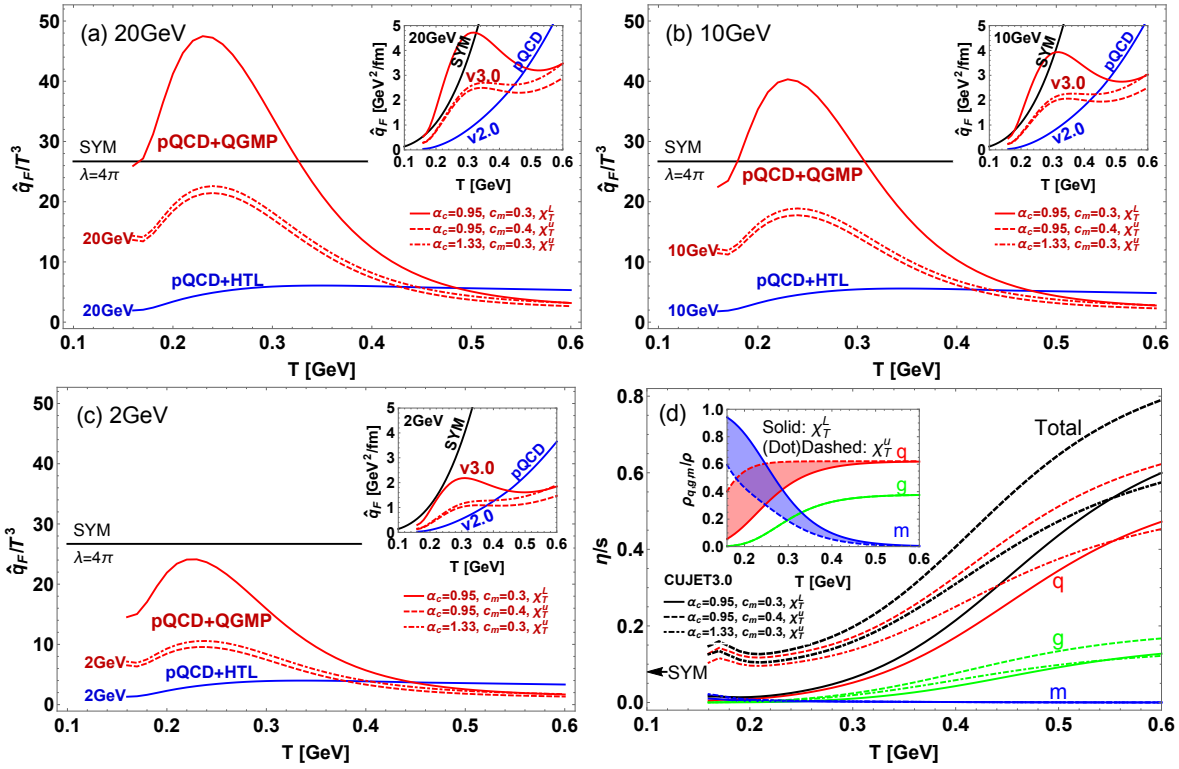

Figure 5.6: *The temperature dependence of $\hat{q}/T^3$ for a light quark jet (F) with initial energy $E =$ (a) 20 GeV, (b) 10 GeV, (c) 2 GeV in the CUJET3.0 framework (Red) with the three schemes: (i) (5.26) (solid), (ii) (5.27) (dashed), and (iii) (5.28) (dotdashed). The CUJET2.0 $\hat{q}_F/T^3$ with $(\alpha_{max}, f_E, f_M) = (0.39, 1, 0)$ (Blue) and the $\mathcal{N} = 4$ SYM $\hat{q}_{SYM}/T^3$ [281] with 't Hooft coupling $\lambda = 4\pi$ (Black) are plotted for comparisons. The insets show the corresponding absolute $\hat{q}_F$. Note that (ii) and (iii)'s $\hat{q}$ are similar, and both are smaller than (i)'s. (d) The η/s estimated in the kinetic theory using the $\hat{q}$ extrapolation Eq. (5.33) in CUJET3.0 with scheme (i) (solid) (ii) (dashed) (iii) (dotdashed), for quasi-parton type q (quark, red), g (gluon, green), and m (monopole, blue). The total η/s is plotted with black curves. The inset shows the number density fraction of q, g, m in the liberation scheme χ_T^L and χ_T^u. Note that in the near T_c regime, in the χ_T^u scheme, the total η/s is dominated by q, while in the χ_T^L "slow" quark liberation scheme the total η/s is dominated by m. In addition, there is a clear $\eta/s \sim 0.12$ minimum at $T \sim 210$ MeV in (ii) and (iii) which utilize the same χ_T^u "fast" quark liberation scheme. This $(\eta/s)_{min}$ is larger and phenomenologically more favorable than that in the "slow" quark liberation scheme.*

parameter $\hat{q}(T)$, is sensitive to r_d, i.e. the rate at which confined colors are excited near T_c. Apart from such sensitivity, the near-T_c enhancement of jet-medium interaction is a very robust feature in all schemes and is deeply tied with the nonconformal, nonperturbative dynamics near the transition temperature. It may be worth mentioning that there are studies based on holographic QCD models [374, 375] that build in near-T_c conformal-breaking effects, that have found similar near-T_c enhancement of the $\hat{q}/T^3$[5].

A surprising aspect of the comparison between CUJET2.0 and CUJET3.0 in Fig. 5.6, is that both models describe equally well the azimuthally averaged R_{AA} data (which characterize overall suppression), in spite of their rather different functional forms of $\hat{q}_F(T)$. The two models differ from each other most significantly in the near-Tc regime: the $\hat{q}_F/T^3$ of CUJET3.0 is much larger than that of CUJET2.0 for $T \sim (1-2)T_c$. Above $T \sim 3T_c$ and by $T \sim 6T_c$, the $\hat{q}_F/T^3$ of CUEJT2.0 is $\sim 50\%$ larger than that of CUJET3.0. The overall energy loss is controlled by $\hat{q}_F$ (rather than $\hat{q}_F/T^3$) and therefore more dominated by contributions from the high temperature QGP in the fireball. This explains why both CUJET2.0 and CUJET3.0 are able to fit the overall R_{AA}. The azimuthal anisotropy v_2, on the other hand, is more sensitive to the late time contributions to energy loss coming from the lower temperature $T \sim (1-2)T_c$ part of the fireball. While CUJET2.0 fails to describe v_2, the CUJET3.0 successfully describes the v_2 data precisely by virtue of the strongly enhanced near-T_c contributions due to the emergent color magnetic monopole degrees of freedom in the sQGMP. The contrast between the CUJET2.0 and CUJET3.0 demonstrates again the importance of simultaneous descriptions for both R_{AA} and v_2 data in order to differentiate energy loss models.

The fact that **remarkably different $\hat{q}(T)$ dependence could be consistent with the same R_{AA} data, demonstrates clearly the inadequacy of focusing on the**

[5]Thus the monopole density and other non-perturbative features of QCD matter may be studied using AdS/CFT.

jet path averaged quantity $\langle\hat{q}\rangle$ as the only relevant medium property to characterize jet energy loss. Evidently while the $\langle\hat{q}\rangle$ captures the important transverse "kick" factor, there are other essential factors like the actual chromo electric and magnetic composition of the plasma, the screening masses and the running couplings at multiple scales which all strongly influence jet energy loss and imprint their effects beyond just in the $\langle\hat{q}\rangle$.

In Fig. 5.6(d) the $\hat{q}$ extrapolated η/s in scheme (i)(ii)(iii) following Eq. (5.33) are plotted. Note that when $T < T_c$, as T keeps cooling down η/s rises due to the hadron resonance gas (HRG) contributions, as computed in [370, 376–378]. In terms of the total η/s near T_c, both (ii) and (iii) have a clear minimum $(\eta/s)_{min} \sim 0.12$ at $T \sim 210$ MeV, while (i) has a $(\eta/s)_{min} \sim 0.02$ which is under the $\eta/s \sim 0.08$ quantum bound. This suggests (1) the liberation scheme of color DOFs, i.e. r_d, significantly influences the lower bound of η/s; (2) $(\eta/s)_{min}$ is insensitive to the screening masses $\mu_{E,M}$. If one strictly assumes $\eta/s(T = T_c) = 0.08$, then the $r_d(T)$ should be in between $d\chi_T^L/dT$ and $d\chi_T^u/dT$. On the other hand, despite a $\Delta\eta/s \sim 0.15$ difference in the absolute magnitude, as temperature increases, (i) and (ii)'s η/s rise at about the same rate, i.e. approximately identical $d(\eta/s)/dT$, and both are larger than the one in (iii). Notice that (i) and (ii) have different r_d, μ_E and μ_M but similar $\mu_E - \mu_M$ near T_c. This implies $d(\eta/s)/dT$ is sensitive to $\mu_E - \mu_M$ but is only slightly affected by r_d and the absolute values of $\mu_{E,M}$.

Overall, the lesson that one learns from Fig. 5.6 is that r_d and $\mu_E - \mu_M$ determines $(\eta/s)_{min}$ and $d(\eta/s)/dT$ respectively. Combined with the observations that one draws from Fig. 5.5, we can arrive at the following:

- If data of high p_T light hadron (LH) and open heavy flavor (HF)'s R_{AA} and v_2 at RHIC and the LHC with sufficiently small uncertainties become available, then in the CUJET3.0 framework, after one has constrained the model parameters with LH's

R_{AA} and lattice calculations, one can use (1) LH's v_2 to estimate $\mu_E(T) - \mu_M(T)$ near T_c; (2) HF's R_{AA} to constrain $r_d(T)$; (3) HF's v_2 to limit the absolute values of μ_E and μ_M as well as to further constrain $r_d(T)$. Even if the $(r_d(T), \mu_E(T), \mu_M(T))$ are not completely fixed in CUJET3.0, insights on $\hat{q}(T)$ and $\eta/s(T)$ can be drawn within this model because for jet energy loss in sQGMP, (a) $\hat{q}(T)$ is regulated by $r_d(T)$; (b) $d(\eta/s)/dT$ is shaped by $\mu_E(T) - \mu_M(T)$ near T_c; (c) $(\eta/s)_{min}$ is bounded by $r_d(T)$.

- In addition, the investigation of how the near T_c physics affects the temperature dependence of the bulk viscosity $\zeta/s(T)$ as well as the role that $\zeta/s(T)$ plays on the experimental observables at RHIC and the LHC is a topic of significant interests, there have been studies from the soft hydro sector [243]. Investigating the importance of $\zeta/s(T)$ from the hard jet quenching sector within CUJET3.0 will be explored elsewhere.

5.3.3 Alternative determination of jet transport coefficient

The $\hat{q}$ computation above has followed the previous CUJET3.0 prescription [232] as given in Eq. (5.29), where the scattering kernel for the jet transport coefficient $\hat{q}$ is symmetric under inter-exchange of E and M in accord with E-M duality considerations. There is however a subtle ambiguity: the form of scattering potential in Eq. (5.29) differs from the scattering potential in the generalized kernel Eq. (5.10) (as given in the second line of Eq. (5.18)) that is used in the actual CUJET3.0 modeling. The $1/\mathbf{q}_\perp^2$ factors, present in Eq. (5.18) while absent in Eq. (5.29), increase the weight of soft momentum transfers in the computation of $\hat{q}$. It is important to examine the results for $\hat{q}$ and η/s determined from the following alternative $\hat{q}'$ measure of the CUJET3.0 quenching field, and compare

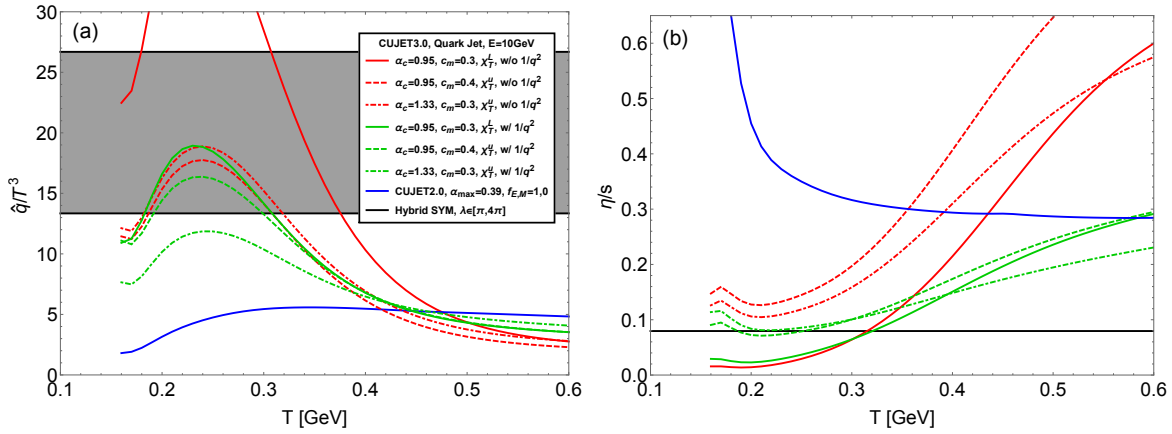

Figure 5.7: *(a) The temperature dependence of the dimensionless jet transport coefficient* $\hat{q}/T^3$ *for a light quark jet with initial energy* $E = 10$ *GeV in the CUJET3.0 framework (Red) with scheme: (i) (5.26) (solid), (ii) (5.27) (dashed), and (iii) (5.28) (dotdashed), compared with corresponding* $\hat{q}'$ *(Green) as defined in Eq. (5.36). The CUJET2.0* $\hat{q}_F/T^3$ *with* $(\alpha_{max}, f_E, f_M) = (0.39, 1, 0)$ *(Blue) and the* $\mathcal{N} = 4$ *SYM* $\hat{q}_{SYM}/T^3 = \frac{\pi^{3/2}\Gamma(\frac{3}{4})}{\Gamma(\frac{5}{4})}\sqrt{\lambda}$ *[281] with 't Hooft coupling* $\lambda \in [\pi, 4\pi]$ *(Black shaded) are plotted as references. (b) The shear viscosity to entropy density ratio* η/s *estimated in the kinetic theory using extrapolation Eq. (5.33) from* $\hat{q}$*'s in (a). Note that there is a clear* η/s *minimum at* $T \sim 210$ *MeV in the CUJET3.0 framework regardless of the schemes been chosen. The corresponding* $(\eta/s)'$ *(determined from* $\hat{q}'$*) converges to the pQCD weakly-coupled QGP limit at high temperature in (i)(ii)(iii) as expected. The* $(\eta/s)_{min}$ *in the fast liberation schemes always sits above the quantum bound while in the Polyakov liberation it does not. In the near* T_c *regime within the fast liberation schemes, the relative magnitude of* η/s*'s does not follow the naive inverse of the quark* $\hat{q}_F$*'s. This is because the computation of the* $(\eta/s)'$ *receives enhanced contributions from softer scales that have stronger electric couplings, and consequently suppressing the transverse mean free path.*

them with the computation from Eq. (5.29):

$$\begin{aligned}\hat{q}'_F(E,T) = \int_0^{6ET} d\mathbf{q}_\perp^2 \frac{2\pi}{(\mathbf{q}_\perp^2 + f_E^2\mu^2(\mathbf{z}))(\mathbf{q}_\perp^2 + f_M^2\mu^2(\mathbf{z}))}\rho(T) \\ \times \Big\{ [C_{qq}f_q + C_{qg}f_g]\cdot[\alpha_s^2(\mathbf{q}_\perp^2)]\cdot[f_E^2\mathbf{q}_\perp^2 + f_E^2 f_M^2\mu^2(\mathbf{z})] + \\ [C_{qm}(1-f_q-f_g)]\cdot[1]\cdot[f_M^2\mathbf{q}_\perp^2 + f_E^2 f_M^2\mu^2(\mathbf{z})]\Big\}. \end{aligned} \tag{5.36}$$

The "prime" generalizations of quenching parameters of gluon and monopole jets follow straightforwardly. By substituting Eq. (5.36) into Eq. (5.33), one can compute the corresponding $(\eta/s)'$ in the quasi-particle picture according to kinetic theory. Fig.5.7(a) shows the temperature dependence of both $\hat{q}/T^3$ and $\hat{q}'/T^3$ for a light quark jet with initial energy $E = 10$ GeV in the CUJET3.0 framework with scheme: (i) (5.26), (ii) (5.27), and (iii) (5.28). Fig.5.7(b) shows the corresponding comparison of η/s and $(\eta/s)'$. There is a clear η/s minimum at $T \sim 210$ MeV in the CUJET3.0 framework in both ways of determining the quenching parameter. The $(\eta/s)'$ nicely converges to the weakly-coupled HTL QGP limit at very high temperature $T > 500$ MeV in all (i)(ii)(iii) schemes, as expected from Eq. (5.18) in the $\chi_T \to 1$ limit. Interestingly, for both estimates of η/s, the $(\eta/s)_{min}$ in the "fast" quark liberation schemes stay above the quantum bound while in the "slow" quark liberation scheme it does not. The general relations between [liberation schemes + screening masses] and $[(\eta/s)_{min} + d(\eta/s)/dT]$ that one could infer from Fig. 5.6 do not alter significantly for the $(\eta/s)'$ results. Within the fast liberation schemes, in the near T_c regime, the relative magnitude of η/s's do not follow the naive inverse of the quark $\hat{q}_F$'s. This is understandable since the computation of $(\eta/s)'$ from Eq. (5.36) puts more weights on softer scales that have stronger electric couplings, given $\alpha_E \alpha_M = 1$ at all scales. Thus the important EM scattering channel is not affected while the transverse mean free path will be suppressed due to larger EE scattering channel cross sections. Consequently one gets smaller $(\eta/s)'$ values as compared with the η/s values.

5.3.4 Monopole density constraints

Thus far we have concentrated on using the total lattice QCD pressure, $p(T)$, to constrain the chromo-magnetic-monopole (CMM) density assuming an ideal gas of chromo-electric-

charged (CEC) and CMM degrees of freedom that leads to

$$\rho_m(T) = \xi_p p(T)/T - \rho_q(T) - \rho_g(T) \equiv \rho_m^{(PS)}(T) \quad . \tag{5.37}$$

Where $\xi_p = 1.012$ for a $N_c = 3, N_f = 2.5$ Stefan-Boltzmann gas as in Eq. (5.30). We refer to Eq. (5.37) as the Pressure Scheme (PS) to fix the partial pressure of magnetic monopoles from the total pressure minus the suppressed semi-QGP densities.

Such a Pressure Scheme may suffer from the potential or "bag" $B(T)$ contribution to thermodynamics whereby pressure $p = Ts/4 - B$ and energy density $\epsilon = 3Ts/4 + B$. In this case one would then have nonzero "trace anomaly" $\epsilon - 3p = 4B$ and indeed lattice QCD data have shown the existence of such a "bag" contribution. In this regard, the entropy density $s = (\epsilon + p)/T$, free from any "bag" terms, may serve as a useful "counting" scheme for quasiparticle densities. We therefore also introduce an independent Entropy Scheme (ES) for determining the total number density via $\rho(T) = \xi_s s(T)/4$, where $\xi_s = \xi_p/4 = 0.253$ for a $N_c = 3, N_f = 2.5$ Stefan-Boltzmann gas, and examine the corresponding uncertainty in our modeling.

As can be seen from Fig.5.8, in the Entropy Scheme (ES) the total quasiparticle density is higher than in the Pressure Scheme (PS) due to the bag constant:

$$\rho_m^{(ES)}(T) \equiv \xi_s s(T) - \rho_q(T) - \rho_g(T) = \rho_m^{(PS)}(T) + \xi_p B(T)/T \quad . \tag{5.38}$$

Choosing the ES vs the PS scheme to fix the monopole density would increase the monopole density near T_c by a factor of 2 and increases the $\hat{q}$ by approximately 50% near T_c. To fit the same reference path averaged R_{AA} we would need to adjust the (α_c, c_m) in CUJET3.0 and the (α_{max}, f_E, f_M) in CUJET2.0 somewhat respectively. Fig.5.10 shows the absolute $\hat{q}$ and the dimensionless $\hat{q}/T^3$ in the two schemes. After readjusted (α_c, c_m)

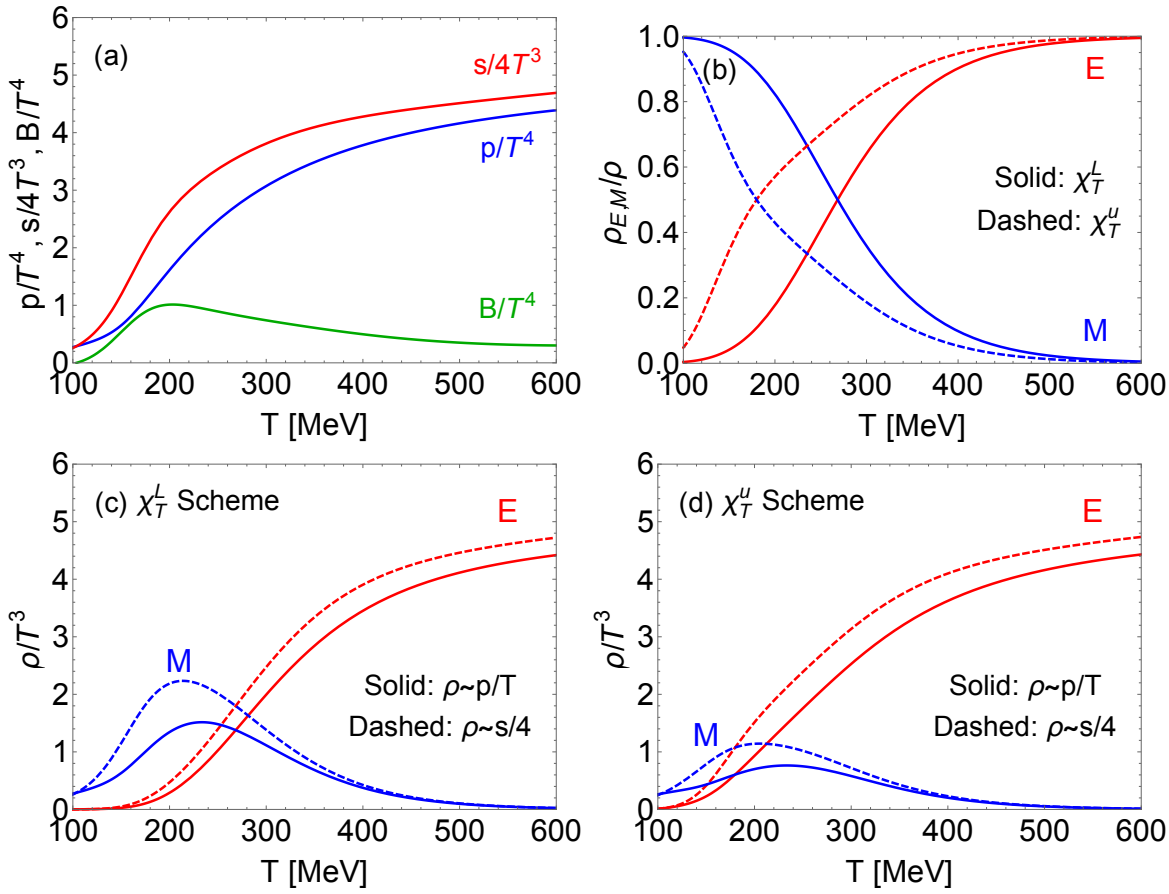

Figure 5.8: *(a) The effective ideal quasiparticle density, $\rho/T^3 = \xi_p P/T^4$, in the Pressure Scheme (PS, Blue) is compared with effective density, $\rho/T^3 = \xi_p S/4T^3$, in the Entropy Scheme (ES, Red) based on fits to lattice data from HotQCD Collaboration [44]. The difference is due to an interaction "bag" pressure $-B(T)/T^4$ (Green) that encodes the QCD conformal anomaly $\epsilon - 3p \neq 0$. (b) The density fraction of the electric (E, red) and magnetic (M, blue) degrees of freedom in the χ_T^L (solid, Eq. (5.11)) and χ_T^u (dashed, Eq. (5.25)) liberation scheme. The dimensionless E and M density ρ/T^3 in the two schemes are shown in (c)χ_T^L and (d)χ_T^u respectively, where both the ρ/T^3 in the PS (solid) and ES (dashed) are plotted. In both liberation schemes, the ρ_m in the ES near T_c is around twice the ρ_m in the PS.*

in CUJET3.0 and (α_{max}, f_E, f_M) in CUJET2.0 to $(0.6, 0.33)$ (as shown in Fig. 5.9) and $(0.35, 1, 0)$ respectively, the $\hat{q}$ near T_c in ES is around 50% larger than in the PS.

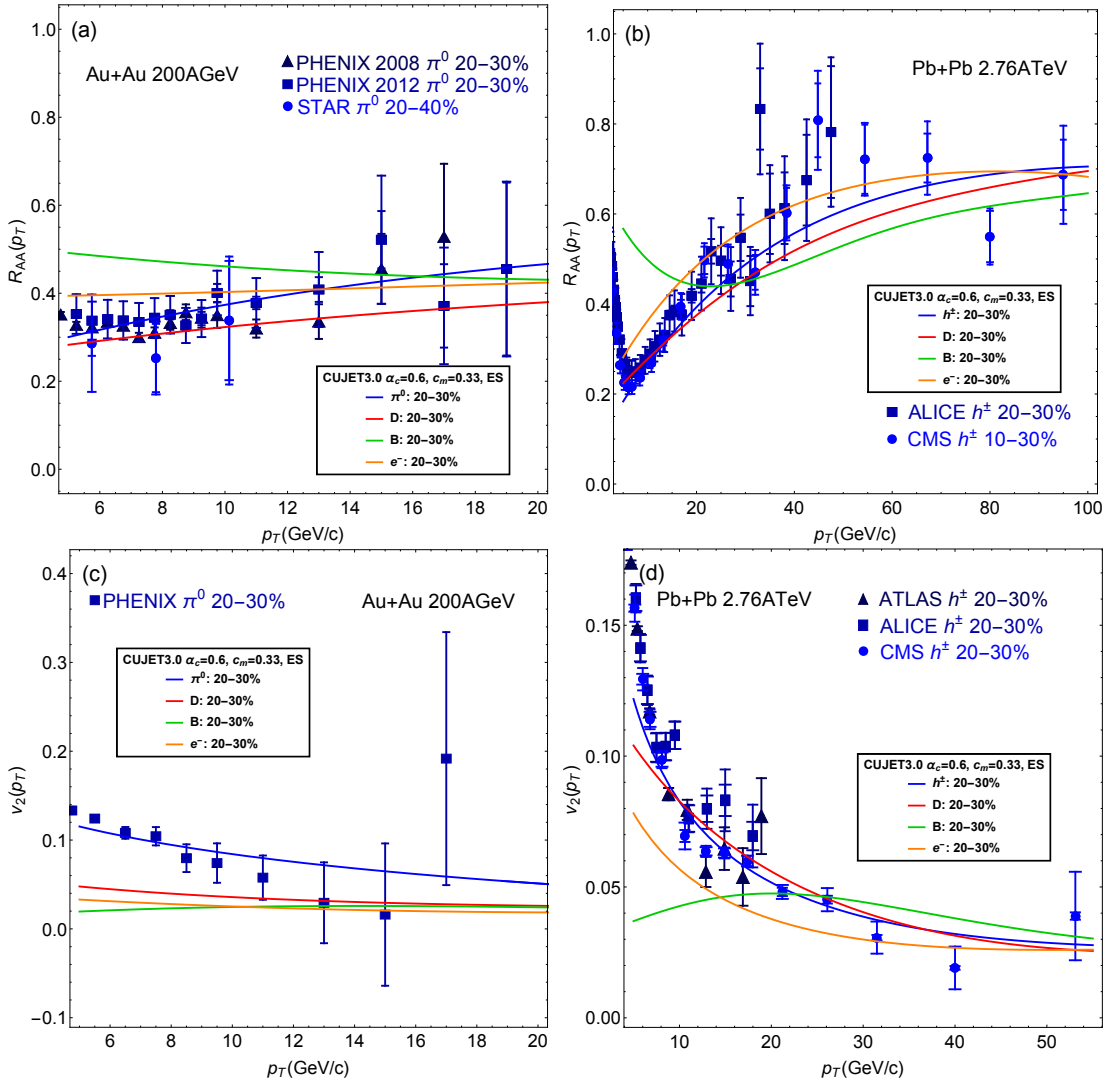

Figure 5.9: *In the CUJET3.0 model with Entropy Scheme (ES) and χ_T^L liberation, the α_c and c_m is adjusted to 0.6 and 0.33 to fit to the reference datum at the LHC $R_{AA}^{h^\pm}(p_T = 12.5\text{GeV}) \approx 0.3$ as well as the lattice μ_M ([275], c.f. Fig. 5.1(b)). With this parameter setup, the $\pi^0/h^\pm$'s high p_T R_{AA} and v_2 at RHIC Au+Au 200GeV and the LHC Pb+Pb 2.76TeV 20-30% collisions are in perfect agreements with data [107, 149, 152, 272–274, 292–294]. The result of prompt D meson, B meson, and heavy flavor decay e− results in the ES scheme is plotted in red, green, and orange, respectively.*

The η/s in CUJET2.0 and 3.0 computed from inverting the $\hat{q}/T^3$ according to Eq. (5.33) are plotted in Fig.5.11. One sees that the η/s in the ES scheme hardly deviates from its

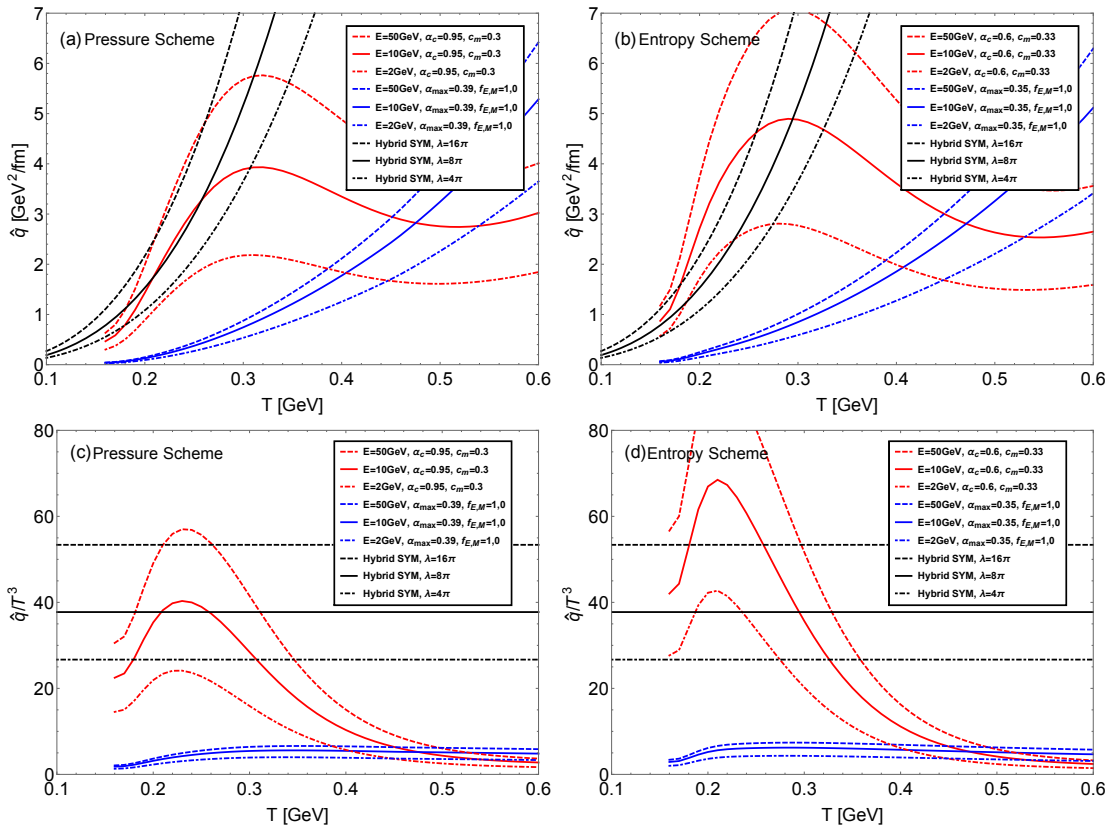

Figure 5.10: *(a) The $\hat{q}(T)$ for a quark jet with initial energy $E = 2$ GeV (dotdashed), 10 GeV (solid), 50 GeV (dashed) computed according to Eq. (5.29) in the Pressure scheme, for CUJET3.0 (red), CUJET2.0 (blue) and $\mathcal{N} = 4$ SYM (black). The dimensionless $\hat{q}(T)/T^3$ is plotted in (c). (b)(d) The counterpart of (a)(c) in the Entropy scheme. Note that (α_c, c_m) in CUJET3.0 and (α_{max}, f_E, f_M) in CUJET2.0 has been readjusted to $(0.6, 0.33)$ and $(0.35, 1, 0)$ respectively fit to the LHC reference datum (cf. Fig. 5.5). The $\hat{q}$ in the ES near T_c is $\sim 50\%$ larger than in the PS due to the "bag" contribution.*

value in the PS scheme. This is understood since η/s is dominated by the "free" quasi-quark degrees of freedom. The monopole fluid is almost viscous free in either scheme as one has already seen in Fig.5.6.

From this consideration we see that requiring the consistency of hard and soft probes can only determine a lower bound on the monopole density near T_c. Our default PS scheme is above that lower bound. We leave the search for that lower bound to a future

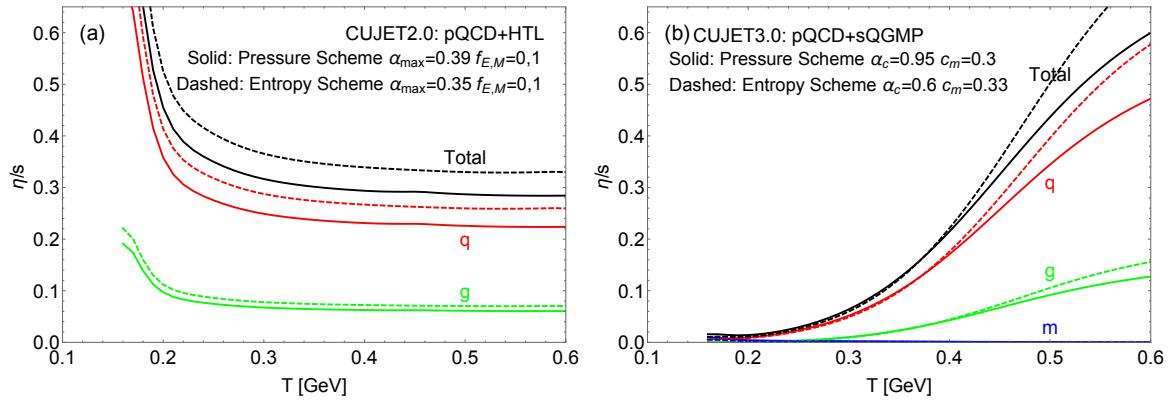

Figure 5.11: *(a) The η/s in CUJET2.0 for quasi-quarks (q, red), quasi-gluons (g, green), and its total value (black) computed from inverting the $\hat{q}/T^3$ according to Eq. (5.33). The solid lines correspond to the PS scheme, while the dashed lines correspond to the ES scheme. (b) The counterpart of (a) in CUJET3.0. Note that the addition of the monopole (m, blue) like quasi-particle degrees of freedom in sQGMP does not alter the overall η/s significantly since the strong magnetic coupling shrinks the transverse mean free path for monopoles and suppresses the shear viscosity contributions from monopoles. Since the sQGMP is dominated by monopole degrees of freedom near T_c, the total η/s in the PS and ES scheme then should naturally converge to the same value.*

study.

5.4 Path length dependence of energy loss in sQGMP

CUJET3.0 is a jet quenching framework that hybridizes the perturbative dynamical DGLV opacity expansion theory, the TG elastic energy loss, and the nonperturbative sQGMP near T_c. It is consistent with high p_T R_{AA} and v_2 data at RHC and the LHC simultaneously, and intrinsically builds a connection between high energy jet quenching and bulk perfect fluidity [232]. Beyond this phenomenological success, a crucial question to ask is how does the path length dependence of jet energy loss behave in this hybrid model. From addressing this, one can gain insights into e.g. at what temperature does the nonperturba-

tive physics enter jet quenching, why different $\hat{q}(T)$'s lead to the same suppression factor in CUJET3.0 and CUJET2.0, whether or not the beyond leading order effects change light and heavy quark energy loss identically, etc.

To obtain useful insights about the path length dependence of jet energy loss in general scenarios, one can take a step back to look at the a-b-c model [225, 291] (c.f. e.g. Section 2.3.5) where the parton energy loss is simplified as a power law of the energy E, the path length L, and the local temperature T:

$$\frac{dE}{dL} = -\kappa E^a L^b T^{2-a+b} \,. \tag{5.39}$$

Depending on the underlying energy loss mechanism, b may take quite different values (see discussions in e.g. [225, 291]: for collisional processes dominated energy loss, $b \approx 0$; at leading order (LO) in pQCD, for non-Abelian bremsstrahlung processes dominated energy loss, $b \approx 1$; as the coupling strength α_s becomes extremely strong (as well as $N_c \to \infty$) and AdS/CFT correspondence is applicable, holographic jet quenching generally has $b \approx 2$. In the following subsections, after we have interpolated $(\Delta E/E)(L)$ at various temperatures, we will further extract a "b" factor from $b = d\log(\Delta E/E)/d\log(L/L_0) - 1$. In contrast to the abc model with "global" power law dependence for the jet energy loss, our extracted "b" factor will be a sort of "local index" but it nevertheless is an informative indicator that can help achieve deeper understandings about the energy loss dynamics encoded in the computed $(\Delta E/E)(L)$ from the CUJET3.0.

5.4.1 Light quark

In the radiative sector, there have been next-to-leading order (NLO) pQCD calculations for energy loss assuming massless projectile partons [283, 285–287], and they all suggest

a double logarithmic path length dependence of the jet quenching parameter, i.e.

$$\hat{q} \propto \log \tilde{L}(1+\log^2 \tilde{L}) \ . \tag{5.40}$$

Where $\tilde{L} \equiv L/L_0$ and L_0 is a proper ultraviolet cutoff. Generally speaking, the differential jet energy loss has $dE/dL \propto \hat{q}L$. Let us assume $\log \tilde{L}$ varies much slower than $\tilde{L}$, after straightforward integrations and simplifications, one arrives at

$$\log(\Delta E/E) \propto 2\log \tilde{L} + \log\log \tilde{L} + \log(1+\log^2 \tilde{L}) + \text{const} \ . \tag{5.41}$$

This form is of course not general enough because of the $\log \tilde{L}$ approximation and it is derived at NLO in pQCD. Nevertheless, motivated by Eq. (5.41), we will use

$$\log \frac{\Delta E}{E} = A + B\log\frac{L}{L_0} + \log(1+C\log\frac{L}{L_0}) + \log(1+D\log^2\frac{L}{L_0}) \ , \tag{5.42}$$

to interpolate the path length dependence of radiative jet energy loss in sQGMP within the CUJET3.0 framework. On the other hand, combining the above with Eq. (5.39), one can easily get

$$\begin{aligned} b &\equiv \frac{d\log(\Delta E/E)}{d\log(L/L_0)} - 1 && (5.43)\\ &\overset{\text{rad}}{=} B - 1 + \frac{C}{1+C\log(L/L_0)} + \frac{D}{1+D\log^2(L/L_0)} && (5.44)\\ &\to B-1 \ (L\to\infty) \ . && (5.45) \end{aligned}$$

The upper panels of Fig. 5.12 show the path length dependence of the radiative energy loss $\Delta E/E$ of a light quark jet (mass $M = 200$ MeV) with initial energy $E = 20$ GeV traversing a brick plasma (fixed density) at varied temperatures in CUJET3.0 and in CUJET2.0. The (a)(b)(c)(d) corresponds to jet quenching in the brick medium with

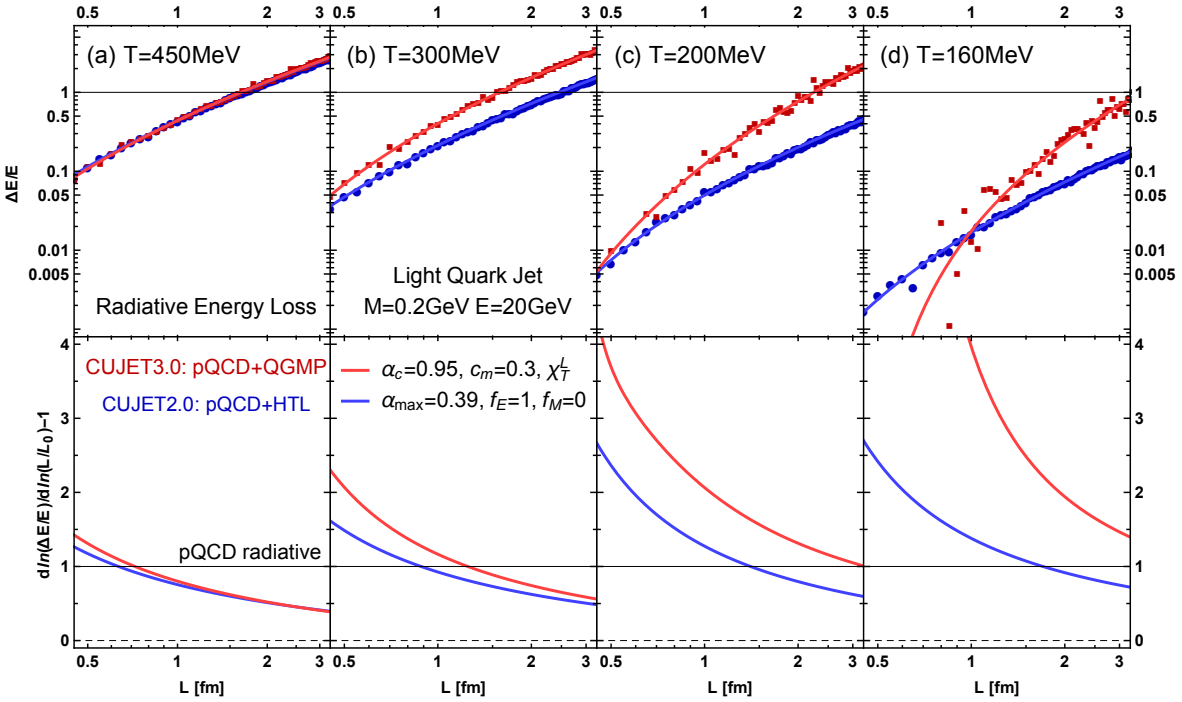

Figure 5.12: **Upper**: *The radiative energy loss ratio $\Delta E/E$ of a light quark jet ($M = 200$ MeV) with initial energy $E = 20$ GeV propagating through a brick plasma with various thicknesses L at temperature $T =$ (a) 450, (b) 300, (c) 200, (d) 160 MeV, in the CUJET3.0 $\alpha_c = 0.95$, $c_m = 0.3$, χ_T^L model (red) and in the CUJET2.0 $\alpha_{max} = 0.39$, $f_E = 1$, $f_E = 0$ model (blue). As temperature decreases, CUJET3.0's $\Delta E/E(L)$ and the stopping distance L_1 (defined in Eq. (5.46)) respectively gets steeper and larger compared with CUJET2.0's. At low and intermediate T, $(\Delta E/E)_{v3.0} < (\Delta E/E)_{v2.0}$ in the small L regime.* **Lower**: *The path length L dependence of the power b in Eq. (5.43) at different temperatures. Note that $b = 0$, 1, 2 is approximately the elastic, pQCD and AdS limit respectively. At high temperature $T \sim 400$ MeV, the $b(L)$ of CUJET3.0 and CUJET2.0 converge to around the pQCD limit. As temperature cools down, when $T \sim 300$ MeV, CUJET3.0's $b(L)$ start becoming larger than CUJET2.0's. This signals the transition from E to M dominant as well as from weak to strong coupling for the bulk. In the near T_c regime, the $b(L)$ in the CUJET3.0 framework is higher than LO pQCD, and is close to the AdS limit. This implies the model ingredients in CUJET3.0 do effectively bring in nonperturbative dynamics into the original pQCD/DGLV energy loss kernel.*

temperature $T = 450$, 300, 200, 160 MeV respectively. In the computation, Eq. (5.18) and Eq. (3.8) is used for CUJET3.0 and CUJET2.0 respectively, and the Monte-Carlo integration is iterated 1,000,000 times to enforce convergence. The brick size L is increased from 0.45 fm to 3.05 fm with 0.5 fm intervals. We fit the $\Delta E/E$ vs L in both CUJET3.0 and CUJET2.0 with Eq. (5.42). Note the phenomenon that $\Delta E/E$ exceeds 1 for some large size bricks is purely technical, since in the computation E is not dynamically updated in Eq. (5.18) and (3.8) as jets propagate through and lose energies. Nevertheless, the $\Delta E/E(L)$ at small L's[6], the slope of $\Delta E/E(L)$, the thickness where $\Delta E/E = 1$, and the relative information about jet energy loss at the four different temperatures are all meaningful.

For the CUJET2.0 model with pQCD+HTL, as temperature decreases, $d(\Delta E/E)/dL$ is altered significantly. Define the stopping distance L_1 as

$$L_1 : \Delta E/E|_{L=L_1} = 1 \ . \tag{5.46}$$

It monotonically increases in this picture. This is as expected, since in the CUJET2.0, bricks with lower temperatures have less opacities, and it takes a longer path for a jet to lose all the energy. However, for the L_1 in CUJET3.0, though it monotonically increases, its increasing rate is much less than CUJET2.0's. More importantly, the CUJET3.0's $d(\Delta E/E)/dL$ significantly grows as the temperature decreases below $T = 300$ MeV. All these observations point to the fact that, as the temperature approaches T_c, chromo-magnetic monopoles gradually dominate the medium, since $\alpha_M \gg \alpha_E$, the jet-medium interaction may weaken at a reduced rate or it may be enhanced (as indicated by Fig. 5.6(a), this is the correct picture) despite the decrease of the quasi-particle number density.

[6]Since with a smooth viscous hydro evolution background, the jet parton will stay at a certain temperature for limited time, the relevant energy loss informations are mostly at short L.

To this point, there is a critical question that one should address regarding the jet energy loss in sQGMP: if one compares the CUJET3.0 and CUJET2.0's $\hat{q}/T^3$ in Fig. 5.6(a)(b), the former is always above the latter in the temperature range of $T < 450$ MeV, then why can both of them can reasonably describe the high p_T light hadron's R_{AA} at RHIC and the LHC? The upper panels of Fig. 5.12 give one the answer: at $T = 400$ MeV, CUJET3.0 and CUJET2.0's $\Delta E/E(L)$ almost overlap; as the temperature cools down, because of the transition of the nonperturbative medium from EQPs dominate to MQPs dominate, the CUJET3.0's $\Delta E/E(L)$ becomes steeper and steeper than the CUJET2.0's, while the former's L_1 becomes less and less than the latter's; these effects lead to $(\Delta E/E)_{v3.0} < (\Delta E/E)_{v2.0}$ at small $L < L_{eq}$, where L_{eq} is defined as

$$L_{eq} : (\Delta E/E)_{v3.0}|_{L=L_{eq}} = (\Delta E/E)_{v2.0}|_{L=L_{eq}} \ , \tag{5.47}$$

and this L_{eq} keeps enlarging as T decreases. For jet suppressions in a hydrodynamically evolving smooth medium in A+A collisions, along a given jet path (let the initial production point be at the origin), if one sequentially divides it into sections with average temperature of 450, 300, 200, 160 MeV and marks the traveling time in each section as l_{450}, l_{300}, l_{200}, l_{160}, in a general estimation, the ordering is $l_{450} > l_{300} > l_{200} > l_{160}$, and $l_{160} \ll 1$ fm while $l_{200} \lesssim 0.5$ fm. Define

$$\Delta_E(\bar{T} = \frac{T_i + T_{i+1}}{2}) \equiv \frac{1}{L_> - L_<} \int_{T(L_<)=T_i}^{T(L_>)=T_{i+1}} dL \left[(\Delta E)_{v3.0} - (\Delta E)_{v2.0}\right] \ . \tag{5.48}$$

Although $\Delta_E(T = 450, 300\,\text{MeV})$ are most likely positive, $\Delta_E(T = 200, 160\,\text{MeV})$ can be nontrivially negative and thus compensate the formers. This cancellation results in the overall $\sum_{T_j} \Delta_E \approx 0$, meaning similar averaged R_{AA} predictions for CUJET3.0 and CUJET2.0.

The lower panels of Fig. 5.12 show the extracted power b ($b \equiv d\log(\Delta E/E)/d\log(L/L_0) - 1$, c.f. Eq. (5.43)) versus the brick thickness L. A first observation is that, at high temperature, the CUJET3.0's $b(L)$ is almost identical to CUJET2.0's; but as T goes down, starting from $T \sim 300$ MeV, the former gets larger than the latter. This is a clear signal showing that the chromo-magnetic monopoles begin emerging and bringing up strong coupling effects from $T \sim 300\,\mathrm{MeV} \approx 1.8\,T_c$. Let L_2 be the path length that satisfies

$$b(L = L_2) = 1\ . \tag{5.49}$$

In both CUJET2.0 and CUJET3.0, L_2 increases as the temperature decreases, this is understood as the opacity $L/\lambda = \rho\sigma L \sim T^3 L$, if T drops, a larger L is required to keep the same opacity level and hence the similar antenna structure. Meanwhile, the CUJET2.0's $db/d\tilde{L}$ does not undergo significant shifts as temperature varies, but this is not the case for CUJET3.0. Define

$$b_{1.5} \equiv b\,(L = 1.5\,\mathrm{fm})\ . \tag{5.50}$$

In CUJET2.0, $b_{1.5}$ rises from ~ 0.6 at 450 MeV to ~ 1.2 at 160 MeV, which is roughly consistent with the LO pQCD expectation of $b = 1$. In CUJET3.0, the $b_{1.5}$ rises from ~ 0.6 at 450 MeV to ~ 2.5 at 160 MeV, suggests that the sQGMP introduces some nonperturbative effects into the DGLV opacity series and effectively parameterizes the resummation of higher orders in the full QCD amplitude.

5.4.2 Heavy quarks

Let us now turn to the path length dependence of the heavy quark energy loss in the sQGMP. The upper panels of Fig. 5.13 show the $\Delta E/E(L)$ of a heavy quark jet (mass

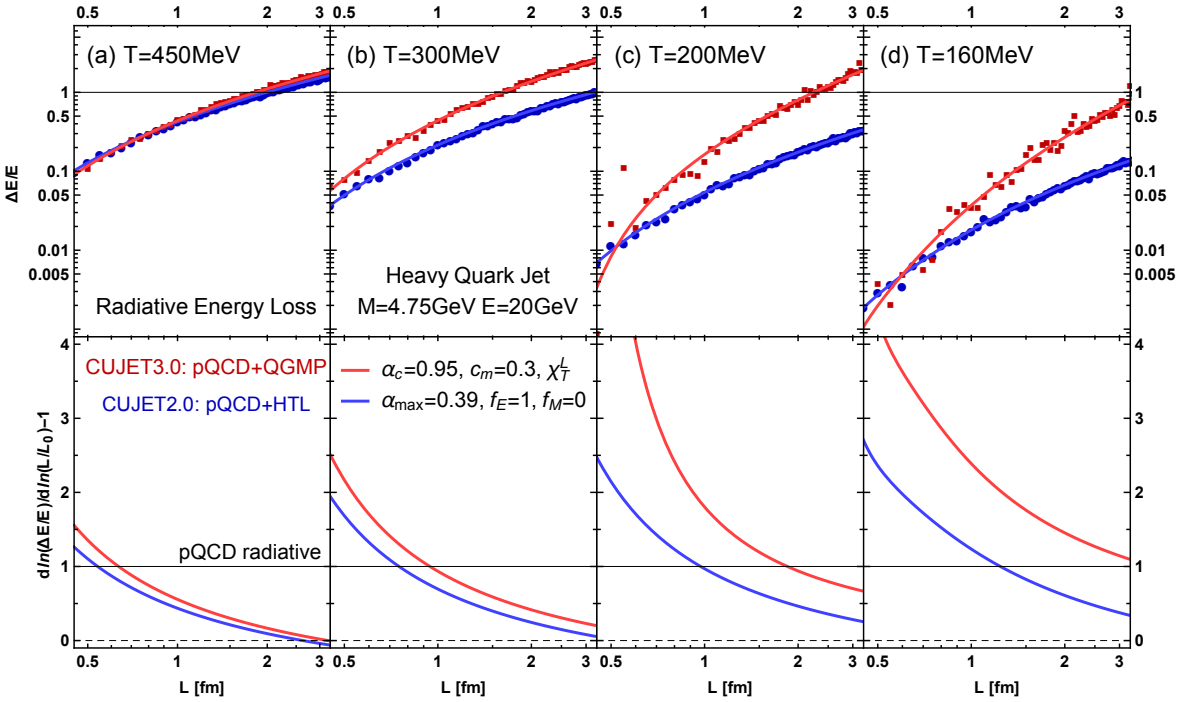

Figure 5.13: *The radiative energy loss ratio $\Delta E/E$ and the power b (c.f. Eq. (5.43)) of a heavy quark jet ($M = 4.75$ GeV) with initial energy $E = 20$ GeV traversing a brick plasma with thickness L at various temperatures in CUJET3.0 and in CUJET2.0. All marks and computational details are the same as in Fig. 5.12. Note that the heavy quark's $d(\Delta E/E)/dL$ and $b(L)$ are smaller than the light quark's as expected from the dead cone suppression. At high $T \sim 450$ MeV, both CUJET3.0 and CUJET2.0 converge at around the linear elastic energy loss limit. As T drops towards T_c, beginning from $T \sim 300$ MeV, the CUJET3.0's $b(L)$ starts deviating from CUJET2.0's because of the emergence of chromo-magnetic monopoles; the former's $\Delta E/E(L)$ gets steeper than the latter's, while L_1 (c.f. Eq. (5.46)) gets shorter. All these alternations for the heavy quark jet quenching are similar to those for the light quark, and the magnitude of the $b(L)$ deviation for the two different flavors are almost identical. This suggests that the nonperturbative effects in the near-T_c sQGMP modify the energy loss kernel of light and heavy quarks in a very similar way.*

$M = 4.75$ GeV) with initial energy $E = 20$ GeV transversing a brick plasma at $T =$ 450, 300, 200, 160 MeV, in CUJET3.0 and in CUJET2.0. Except for the jet mass M, all

technical details in this computation are the same as the in the one for the light quark energy loss. Compared with Fig. 5.12, one notices that the slopes of $\Delta E/E(L)$ in both CUJET3.0 and CUJET2.0 are more gentle for the heavy quark than for the light quark, and the L_1 (c.f. Eq. (5.46)) grows faster when cooling down. This clearly indicates the dead cone effects suppress the induced radiation regardless of whether or not the sQGMP is present. As the temperature gets lower, for heavy quarks, CUJET3.0's $\Delta E/E(L)$ and L_1 also becomes steeper and smaller than CUJET2.0's. This phenomenon has the same physical origin as for light quarks discussed in Section 5.4.1, i.e. a transition from EQPs to MQPs dominate. Interestingly, in the near T_c regime, the L_{eq} (c.f. Eq. (5.47)) for heavy quarks is smaller than for light quarks. Based on the discussions in Section 5.4.1, this will lead to the high p_T leading B meson R_{AA} predictions from CUJET3.0 being slightly lower than CUJET2.0. In fact, this is case from the comparison of the R^B_{AA} in [232] and in [216].

The lower panels of Fig. 5.13 show the extracted power b (c.f. Eq. (5.43)) versus the medium thickness L. Notice that for some temperatures at large L, the b becomes less than 1, nevertheless this can be neglected since in these regimes the $\Delta E/E$ has became larger than 1, which is unphysical. In CUJET2.0, the $b_{1.5}$ (c.f. Section 5.4.1) rises from ~ 0.3 at 450 MeV to ~ 0.6 at 160 MeV, this is weaker than the LO pQCD radiative energy loss $b = 1$, and approaches the elastic limit $b = 0$. Compared with the energy loss for light quarks, the dead cone suppression is significant for heavy quarks. In CUJET3.0, the $b_{1.5}$ rises from ~ 0.4 at 450 MeV to ~ 1.6 at 160 MeV, this suggests the strong coupling effects hence high order resummations also enter the energy loss kernel for the heavy quark jet.

At high $T \sim 450$ MeV, the CUJET3.0's and CUJET2.0's $b(L)$ overlap, as T drops, beginning from $T \sim 300$ MeV, the former starts to deviate from the latter, suggesting the commencement of monopoles taking control of the medium transport properties. This initiating temperature $T_{initial} \sim 300$ MeV for the heavy quark coincides exactly with the

$T_{initial}$ for the light quark; meanwhile, the magnitude of the deviation in $b(L)$ between CUJET3.0 and CUJET2.0 for the two different flavors resemble each other; these observations imply that the nonperturbative effects due to the sQGMP near T_c influences the light quark jet quenching and the heavy quark jet quenching in approximately the same manner within CUJET3.0.

5.5 Systematic analysis of CUJET3.0

5.5.1 Relativistic flow corrections

Generally speaking, in pQCD based energy loss models, the non-Abelian bremsstrahlung amplitudes are derived assuming a static QGP medium [144, 145, 171, 379, 380]. With a hydrodynamically evolving background, flows move at relativistic velocities in certain cells at certain times; if a light-like jet happens to pass through a unit cell flowing close to the speed of light, since the radiative formulas are applicable only in the co-moving frame, then one should boost back to the lab framework for correct predictions of jet quenching observables. Therefore, modifications on a pQCD energy loss theory are necessary if it is coupled to a hydrodynamically expanding medium.

In [234, 235], the relativistic flow corrections to $\hat{q}$ are calculated using weak and strong coupling approaches. The authors in those papers derived that in existence of hydrodynamical flows, the $\hat{q}$ should be multiplied by a factor

$$\Gamma(\vec{z}) = \frac{u_f^\mu p_\mu}{p_0} = \gamma_f(\vec{z}) \left[1 - \vec{\beta}_j(\vec{z}) \cdot \vec{\beta}_f(\vec{z})\right] . \tag{5.51}$$

Where $\vec{z}$ and $p^\mu = (p_0, \vec{p})$ are the coordinate and the four momentum of the jet parton in the lab frame, respectively. Note that $\vec{\beta}_j = \vec{p}/p_0$. The $u_f^\mu = \gamma_f(1, \vec{\beta}_f)$ is the flow four velocity.

On the other hand, from naive considerations of the jet opacity and relativistic boosts, one can get

$$\begin{aligned}\frac{L}{\lambda}\longrightarrow\frac{L'}{\lambda'} &= \rho'\cdot L'\cdot\sigma \\ &= \left\{\frac{\rho}{\gamma_f}\right\}\cdot\left\{L\gamma_f(\vec{z})\left[1-\vec{\beta}_j(\vec{z})\cdot\vec{\beta}_f(\vec{z})\right]\right\}\cdot\sigma \\ &= \left[1-\vec{\beta}_j(\vec{z})\cdot\vec{\beta}_f(\vec{z})\right]\cdot\frac{L}{\lambda}\,. \end{aligned} \tag{5.52}$$

Therefore, to systematically study the relativistic corrections to the energy loss kernel hence jet quenching observables, we compare three schemes: (1) $\Gamma=\gamma_f(1-\vec{\beta}_j\cdot\vec{\beta}_f)$; (2) $\Gamma=1-\vec{\beta}_j\cdot\vec{\beta}_f$; (3) $\Gamma=1$.

Fig. 5.14(a)(b) shows the results of high p_T charged particles' $R_{AA}(p_T)$ and $v_2(p_T)$ at the LHC Pb+Pb $\sqrt{s_{NN}}=2.76$ TeV 20-30% centrality collisions using scheme (1)(2)(3) within CUJET3.0 and CUJET2.0, compared with available data [107, 152, 274, 292, 293]. While all the six combinations generate good agreements with the R_{AA}, only the CUJET3.0 results are consistent with the v_2. It is because the nonperturbative sQGMP in the CUJET3.0 framework strongly enhances the strength of parton-medium interaction near T_c, effectively increases late time jet energy loss, and boosts the underestimated v_2 to be in line with data [232].

Surprisingly, as shown in Fig. 5.14(b), the relativistic flow correction scheme (1)(2)(3) do not alter the v_2 significantly in both CUJET3.0 and CUJET2.0, despite very different values of α_c and α_{max} (note that α_c's and α_{max}'s are adjusted to fit reasonably the reference datum $R_{AA}^{h^\pm}(p_T=12.5\text{ GeV})\approx 0.3$). Under eikonal approximation, a jet path is fixed once the initial jet production coordinate and the azimuthal jet propagation angle are specified. Therefore, the robustness of the R_{AA} and v_2 in response to relativistic flow corrections can be understood as along the fixed jet path, the number of parton-medium scatterings

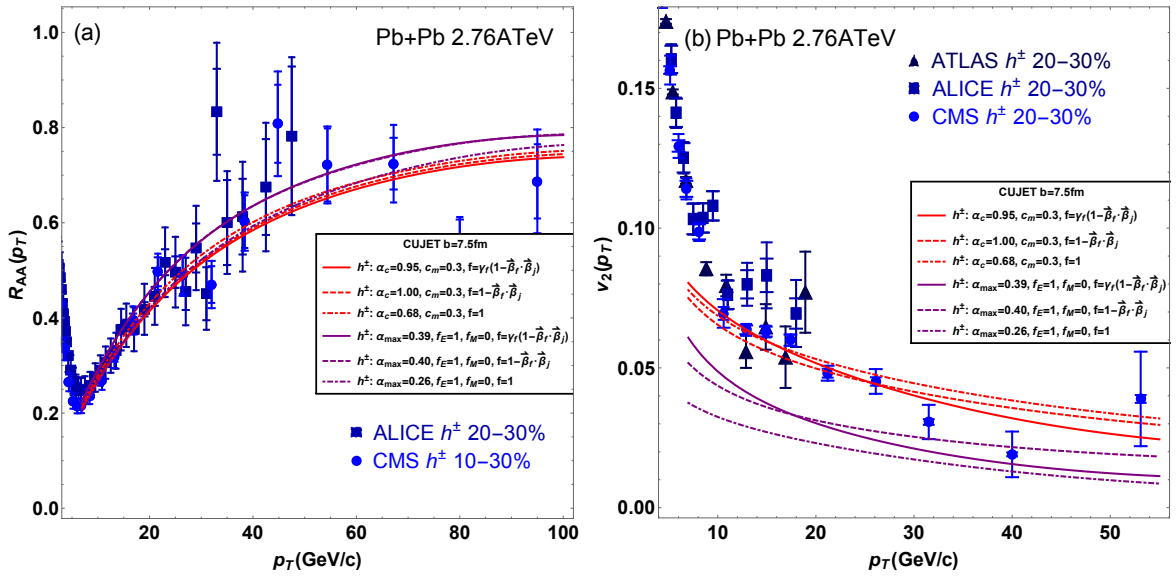

Figure 5.14: *Charged particles' (a) R_{AA} and (b) v_2 in the LHC Pb+Pb $\sqrt{s_{NN}}$=2.76TeV semi-peripheral collisions, computed from CUJET2.0 HTL $f_E = 1$, $f_M = 0$ (purple) and CUJET3.0 $c_m = 0.3$ (red) with relativistic flow corrections (1) $\Gamma = \gamma_f(1 - \vec{\beta}_j \cdot \vec{\beta}_f)$ (solid) [234, 235]; (2) $\Gamma = 1 - \vec{\beta}_j \cdot \vec{\beta}_f$ (dashed); (3) $\Gamma = 1$ (dotdashed) to the energy loss kernel, compared with relevant data [107, 152, 274, 292, 293] (blue). The parameters α_{max} (v2.0) and α_c (v3.0) are adjusted to fit to the $R_{AA}^{h^{\pm}}(p_T = 12.5\text{GeV}) \approx 0.3$ reference datum. Note that both R_{AA} and v_2 do not distinguish the different flow corrections at a measurable level. This can be partially understood as the number of parton-medium scatterings is fixed for a given jet path in any frame once the initial production coordinate and azimuthal propagation angle have been specified.*

is invariant in any frame. To be more careful, one would argue that the v_2 shifts by ~ 0.01 from scheme (3) $\Gamma = 1$ to (1) $\Gamma = \gamma_f(1 - \vec{\beta}_j \cdot \vec{\beta}_f)$, which is not "unchanged". In fact, this magnitude of variation is consistent with the conclusion of [235], where the authors argue that the corrections on ordinary jet quenching observables because of the hydro flow are too small to be measured hence can be neglected at current stage.

5.5.2 Origin of near T_c enhancement in CUJET3.0

In CUJET3.0, the dimensionless jet quenching parameter $\hat{q}/T^3$ is strongly enhanced in the near T_c regime, and several factors may contribute to this enhancement: the enlargement of $\alpha_s \to \alpha_c$ as $T \to T_c^+$ in Eq. (5.19), the separation of the electric and magnetic quasi-particle density fraction according to Eq. (5.11), and the magnetic screening mass regulator c_m in Eq. (5.16). A critical question to ask is: which factor contributes most significantly to the enhancement of the jet opacity in sQGMP? In order to answer this, a practical solution is to hybridize the CUJET2.0 running coupling scheme (denote it as α_{max}, Eq. (3.9)) with the CUJET3.0 energy loss kernel (denoted it as QGMP, Eq. (5.18)); and hybridize the CUJET3.0 running coupling scheme (denote it as α_c, Eq. (5.19)) with the CUJET2.0 energy loss kernel (denot it as HTL, Eq. (3.8)); then compare the predictions of jet quenching observables, in particular, high p_T R_{AA} and v_2 from the four models: $[\alpha_c/\alpha_{max}]+[\text{QGMP/HTL}]$.

Fig. 5.15(a) shows the running coupling used in the four models, note that the parameters are fixed by fitting the LHC $R_{AA}^{h^\pm}(p_T = 12.5 \text{ GeV}) \approx 0.3$ reference datum, c.f. Fig. 5.16(a). Note that the $[\alpha_{max}]$+[QGMP] model has a weaker chromo-electric coupling in the near T_c regime but a stronger one at large $Q > 2$ GeV than the $[\alpha_c]$+[QGMP] model. This model also has a smaller $\alpha_{max}^e = 0.24$ than the $\alpha_{max} = 0.39$ in the $[\alpha_c]$+[HTL] model. It is as expected since $[\alpha_{max}]$+[QGMP] has an extra monopole fraction with extremely strong couplings.

Fig. 5.15(b) shows the electric and magnetic screening masses in the four models compared with lattice data [275]. Both $[\alpha_{max}]$+[QGMP] and $[\alpha_c]$+[QGMP] can describe both μ_E and μ_M reasonably well. Both $[\alpha_{max}]$+[HTL] and $[\alpha_c]$+[HTL] are in agreements with μ_E, but they have $\mu_M = 0$ because $f_M = 0$ in [HTL] [219].

Fig. 5.16 show the results of high p_T light hadrons' (a) R_{AA} and (b) v_2 in the four

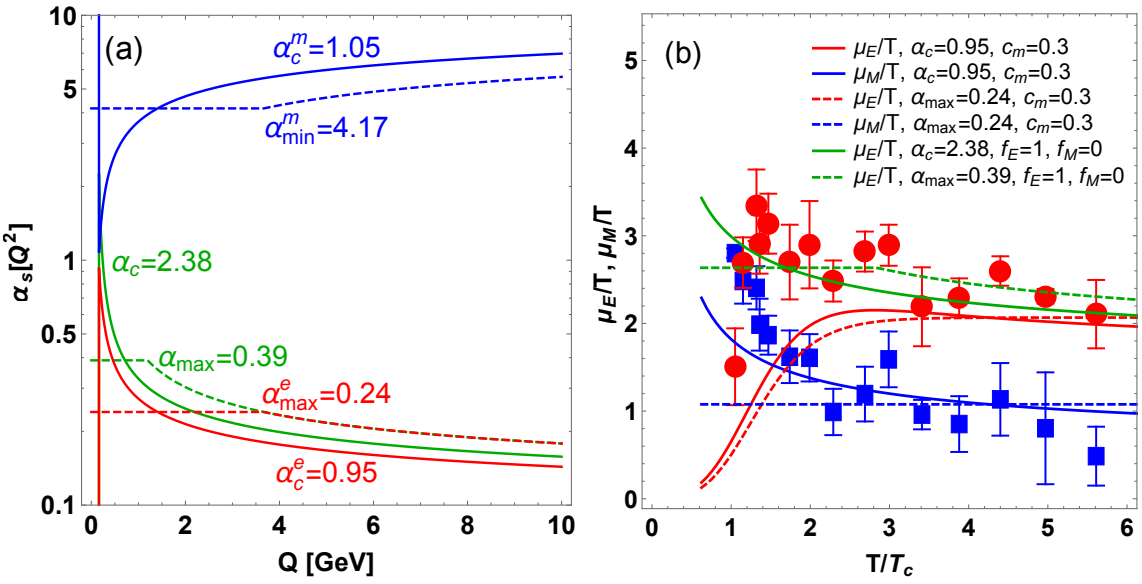

Figure 5.15: *(a) The running strong coupling $\alpha_s(Q^2)$ in four different models, $[\alpha_c/\alpha_{max}]$ + [QGMP/HTL]. Notice that α_{max} (dashed) and α_c (solid) is parametrized as in Eq. (3.9) and Eq. (5.19) respectively. Note in the CUJET3.0 energy loss kernel, i.e. Eq. (5.18) [QGMP], both chromo-electric (red) and chromo-magnetic (blue) coupling exists, while in CUJET2.0 energy loss kernel, i.e. Eq. (3.8) [HTL], only the electric coupling (green) is present. (b) The electric screening mass (μ_E) and magnetic screening mass (μ_M) as temperature varies in the four models, compared with lattice data (E, red; M, blue; [275]). Note in plotting the $[\alpha_c/\alpha_{max}]$ + [QGMP/HTL] results, the curve styles are the same as in panel (a). In $[\alpha_c]$, $T_c = 160$ MeV; In $[\alpha_{max}]$, $\Lambda_{QCD} = 200$ MeV. Note that in [HTL] the magnetic screening mass is zero because $f_M = 0$ [219].*

models, i.e. [α_c or α_{max}] + [QGMP or HTL], at the LHC Pb+Pb $\sqrt{s_{NN}} = 2.76$ TeV 20-30% collisions, compared with available data [107, 152, 274, 292, 293]. Note the model

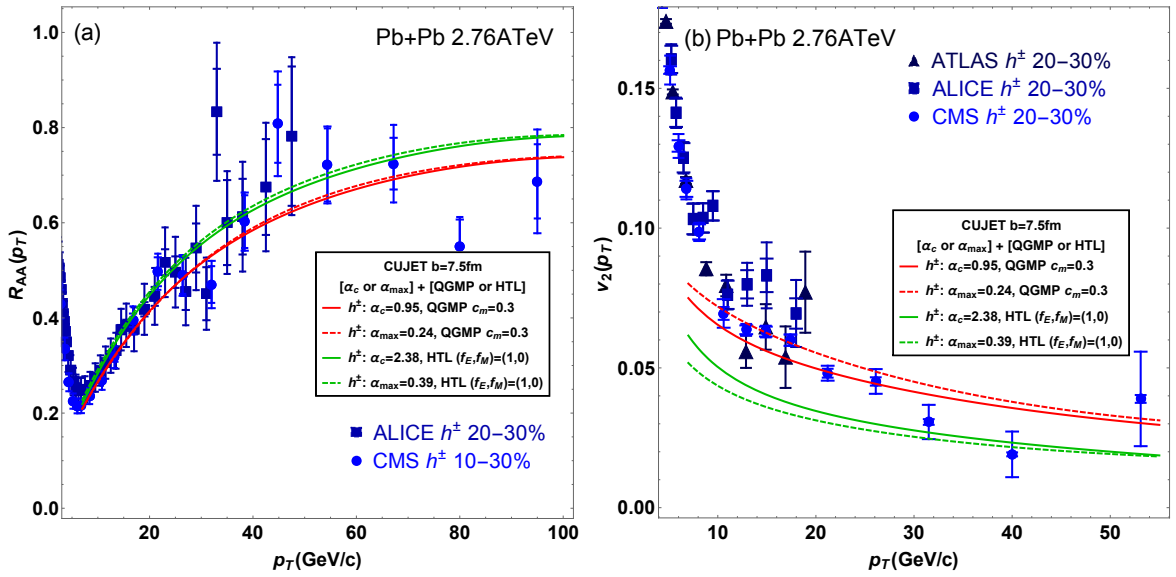

Figure 5.16: *Charged particles' (a) R_{AA} and (b) v_2 in the LHC Pb+Pb $\sqrt{s_{NN}}$=2.76 TeV semi-peripheral collisions, computed from CUJET2.0 [HTL] $f_E = 1$, $f_M = 0$ (green, Eq. (3.8)) and CUJET3.0 [QGMP] $c_m = 0.3$ (red, Eq. (5.18)) with the [α_{max}] (dashed, Eq. (3.9)) and [α_c] (solid, Eq. (5.19)) running coupling scheme, compared with available data [107, 152, 274, 292, 293] (blue). The parameter α_{max} and α_c are adjusted to fit to the $R_{AA}^{h^{\pm}}(p_T = 12.5\ \text{GeV/c}) \approx 0.3$ reference point. Note that while all four models can explain the high p_T R_{AA}, only [α_c]+[QGMP] and [α_{max}]+[QGMP] can explain the high p_T v_2. This suggests the emergence of chromo-magnetic monopoles as $T \to T_c^+$ contributes most significantly to the strongly enhanced $\hat{q}/T^3$ near T_c and generates the simultaneous description of high p_T light hadrons' R_{AA} and v_2.*

parameters in the four models are fixed as:

$$[\alpha_{\rm c}] + [\text{QGMP}]: \ \alpha_{\rm c} = 0.95, \ {\rm c_m} = 0.3\ ; \tag{5.53}$$

$$[\alpha_{\rm max}] + [\text{QGMP}]: \ \alpha_{\rm max} = 0.24, \ {\rm c_m} = 0.3\ ; \tag{5.54}$$

$$[\alpha_{\rm c}] + [\text{HTL}]: \ \alpha_{\rm c} = 2.38, \ {\rm f_E} = 1.0, \ {\rm f_M} = 0.0\ ; \tag{5.55}$$

$$[\alpha_{\rm max}] + [\text{HTL}]: \ \alpha_{\rm max} = 0.39, \ {\rm f_E} = 1.0, \ {\rm f_M} = 0.0\ . \tag{5.56}$$

While all four models are compatible with the R_{AA} data, only [α_c or α_{max}] + [QGMP] can fit to the high p_T charged particles' v_2. Note that the boost in azimuthal elliptical harmonics is contributed mainly by the enhancement of the jet opacity near T_c; [α_c]+[QGMP] and [α_{max}]+[QGMP] have different running coupling schemes as well as different μ_M's in the near T_c regime but share the same CUJET3.0 energy loss kernel; we can therefore conclude that the dividing of electric (E) and magnetic (M) fractions according to Eq. (5.11) results in the transition of the nonperturbative medium from E dominance to M dominance as temperature goes towards T_c^+, and contributes most significantly to the strongly enhanced parton-medium interaction near T_c for the jet energy loss in semi-Quark-Gluon-Monopole-Plasmas.

5.6 Conclusions

We have presented a detailed study of the jet energy loss in semi-Quark-Gluon-Monopole-Plasmas (sQGMP), within the new CUJET3.0 framework of jet quenching in bulk constrained (VISH2+1D) viscous hydrodynamic backgrounds by extending the perturbative QCD based (CUJET2.0) model to include possible non-perturbative chromodynamical features of the QCD confinement phase transition near $T_c \approx 160$ MeV. We test the robustness and consistency of this new model by comparing predictions of the leading hadron nuclear modification factor, $R_{AA}(p_T > 10$ GeV/c, $\sqrt{s})$, and its azimuthal elliptic asymmetry $v_2(p_T > 10$ GeV/c, $\sqrt{s})$ with available data from nuclear collisions at RHIC($\sqrt{s} = 0.2$ ATeV) and the LHC($\sqrt{s}$=2.76 ATeV). The sQGMP model depends on two parameters: (1) the value of the QCD running coupling $\alpha_c \approx 0.95 - 1.33$ at low $Q < T_c$ and (2) the ratio $c_m = g\mu_E/\mu_M$ of nonperturbative electric to magnetic screening scales. We study two specific cases, $c_m = 0.3, 0.4$. The value of α_c is fixed for each case by fitting a single reference datum, $R^{ch}_{PbPb}(p_T = 12$ GeV/c$) \approx 0.3$ at the LHC at 20-30% centrality. Consistency

with all available data is then tested comparing predictions of CUJET3.0 on $R^h_{AA}(p_T)$ *and* $v^h_2(p_T)$, for $h = \pi, D, B$ at both RHIC and the LHC. The emergent chromomagnetic degrees of freedom in the sQGMP model near T_c are shown to solve efficiently the long standing R_{AA} vs v_2 puzzle by leading to a broad maximum of the jet quenching parameter $\hat{q}(E,T)/T^3$ between $(1-2)T_c$. In addition and most remarkably, by extrapolation of the sQGMP $\hat{q}$ down to thermal energy $E \sim 3T$ scales one finds the shear viscosity to entropy density ratio $\eta/s \approx T^3/\hat{q} \sim 1/4\pi$ to be near the unitarity bound, in the critical $(1-2)T_c$ transition temperature range, which is consistent with viscous hydrodynamic fits to bulk azimuthal harmonics v_n at $p_T < 2$ GeV/c.

A key theoretical uncertainty of this model is the rate at which color electric degrees of freedom are liberated near the deconfinement transition temperature T_c. We have investigated three very different schemes of color liberation and found that the various rates does not alter the model's agreements with high p_T single light hadrons (LH)' R_{AA}. However, this rate ($r_d \equiv d\chi_T/dT$) considerably influences the temperature dependence of the electric screening mass. It is found that the light hadrons' $v_2(p_T > 10$ GeV) is an observable that is sensitive to the difference between the electric (E) and magnetic (M) screening mass ($\mu_{E,M}$) near T_c. For open heavy flavors (HF), r_d regulates their high p_T R_{AA}'s in CUJET3.0, and their v_2's are affected by both the screening masses and the r_d. In terms of the jet quenching parameter $\hat{q}$, it is influenced by r_d, but is insensitive to the screening masses. On the other hand, for the shear viscosity to entropy density ratio η/s, $(\eta/s)_{min}$ and $d(\eta/s)/dT$ would vary strongly if r_d and $\mu_E - \mu_M$ changes.

Therefore, for jet quenching in sQGMP from the CUJET3.0 framework, after model parameters are constrained by data of LH's R_{AA} and relevant lattice calculations, the rate of deconfinement r_d and the screening masses $\mu_{E,M}$ affect jet fragments observables in different ways: (1) $\mu_E - \mu_M$ near T_c influences LH's v_2; (2) r_d influences HF's R_{AA}; (3) r_d and absolute values of $\mu_{E,M}$ influence HF's v_2. On the other hand, the CUJET3.0's jet

transport coefficient $\hat{q}$ and the shear viscosity η/s are affected by r_d and $\mu_{E,M}$ differently: (a) $\hat{q}(T)$ is constrained by $r_d(T)$; (b) $d(\eta/s)/dT$ is constrained by $\mu_E(T) - \mu_M(T)$ near T_c; (c) $(\eta/s)_{\rm min}$ is constrained by $r_d(T)$. Given our findings of these dependences, it is expected that such model uncertainties can be significantly reduced by experimental input such as future high precision data for LH and HF's R_{AA} as well as v_2 at both RHIC and the LHC. For example, the HF's R_{AA} limits $r_d(T)$ therefore constrains $\hat{q}(T)$ and $(\eta/s)_{\rm min}$, LH's v_2 limits $\mu_E - \mu_M$ near T_c therefore constrains $d(\eta/s)/dT$, while the two can be combined to infer the functional shape of $\eta/s(T)$; in addition, HF's v_2 can be utilized to constrain the absolute magnitude of $\mu_E(T)$ and $\mu_M(T)$.

In summary, with our detailed investigations of the jet quenching phenomena in the sQGMP model, we conclude that the phenomenological consequences of the sQGMP, for both hard and soft probes in heavy ion collisions, stay very robust with respect to certain important systematic theoretical uncertainties. The phenomenological success includes simultaneous descriptions of all available high p_T R_{AA} and v_2 data at both RHIC and the LHC, as well as providing an intuitive dynamical mechanism that may explain how the shear viscosity to entropy density ratio could approach the $1/4\pi$ unitarity bound in the vicinity of T_c as required to explain the bulk low $p_T < 2$ GeV "perfect fluidity". The sQGMP model therefore provides a first model that consistently accounts for both hard and soft transport properties of the new state of QCD matter discovered in high energy nuclear collisions at RHIC and the LHC.

We end by emphasizing again the fact that remarkably different $\hat{q}(T)$ dependences could be consistent with the same R_{AA} data, demonstrates clearly the inadequacy of focusing on the jet path averaged quantity $\langle\hat{q}\rangle$ as the only relevant medium property to characterize jet energy loss. Evidently while the $\langle\hat{q}\rangle$ captures the important transverse "kick" factor, there are other essential factors like the actual chromo electric and magnetic composition of the plasma, the screening masses and the running couplings at multiple

scales which all strongly influence jet energy loss and imprint their effects beyond just $\langle \hat{q} \rangle$. It is of significant interest and importance to thoroughly exploit these multiple facets of jet physics and the opportunities they offer for progressing toward an ultimate understanding of the microscopic making of the sQGP.

Chapter 6

More results from CUJET3.0

In the previous chapter we have seen that, the long-standing "high p_T v_2 puzzle" and inconsistency between soft bulk "perfect fluidity" of the QGP and hard jet transport properties in the QGP, are both successfully solved by the CUJET3.0 jet energy loss framework through introducing a microscopic, lattice data constrained semi-quark-gluon-monopole plasma (sQGMP) into the dynamical running coupling DGLV opacity series coupled with viscous hydrodynamical backgrounds. Results from CUJET3.0 are proven to be robust to theoretical uncertainties within the model such as specific choices of the deconfinement scheme near the transition temperature T_c. In this chapter we will show more systematic results from the CUJET3.0 that can be tested with on-going measurements of jet quenching observables in RHIC and the LHC heavy-ion collisions. If they were all verified, then there will be strong phenomenological evidences for the emergence of strongly-coupled chromo-magnetic monopoles (CMM) in these experiments, though the intrinsic analytical structure for CMM within QCD is yet to be clarified.

The predictions from the CUJET3.0 model that will be presented in this chapter include: the centrality dependence of R_{AA} and R_{cp} for prompt D mesons, a systematic analysis of the suppression of open heavy flavors and heavy flavor decay electrons in A+A

collisions, and possible jet quenching effects in proton-nucleus collisions.

6.1 Centrality dependence

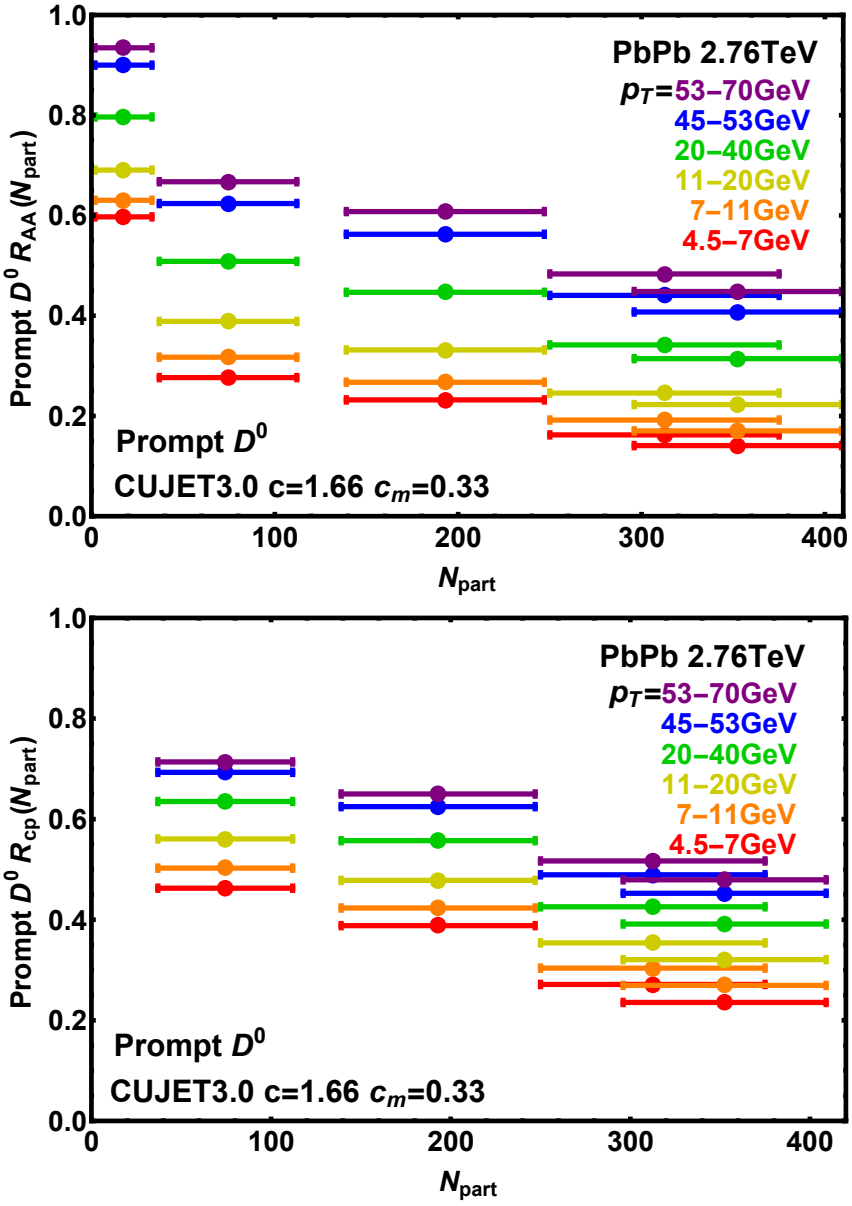

Figure 6.1: *The R_{AA} and R_{cp} of prompt D^0 at Pb+Pb 2.76 ATeV collisions computed from CUJET3.0. Different centrality and transverse momentum bins are considered.*

Fig. 6.1 shows the CUJET3.0 results of the R_{AA} and R_{cp} versus N_{part} for prompt D^0 mesons in Pb+Pb 2.76 ATeV collisions, D^0's with mean p_T of 5.75, 9, 15.5, 30, 49, 61.5 GeV are plotted. In the presence of sQGMP, its effects will be more significant in peripheral A+A collisions than in central A+A collisions. Therefore compared with energy loss models without monopoles, the CUJET3.0 should predict a more gentle slope for both $R_{AA}(N_{part})$ and $R_{cp}(N_{part})$, a smaller magnitude for $R_{AA}(N_{part})$, and a larger magnitude for $R_{cp}(N_{part})$.

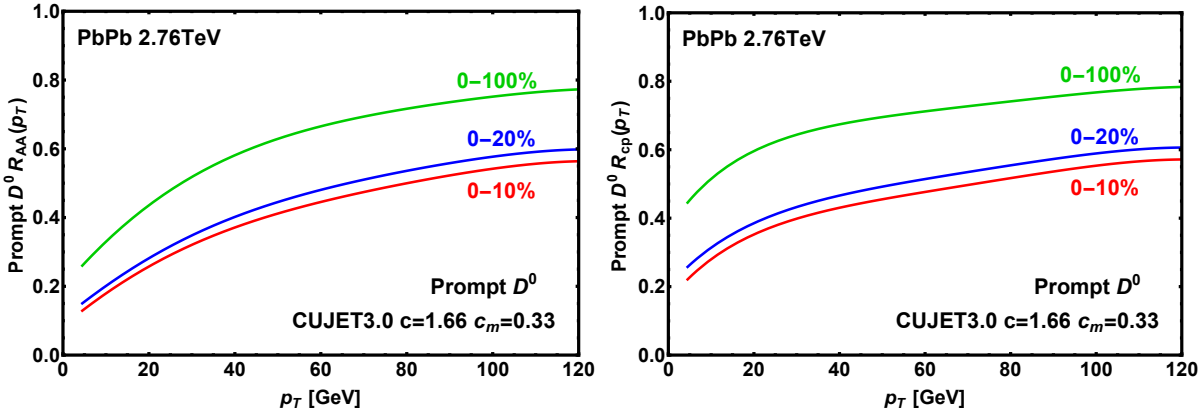

Figure 6.2: *Comparison between CUJET3.0 predictions of $R_{AA}(p_T)$ and $R_{cp}(p_T)$ for prompt D^0 at Pb+Pb 2.76 ATeV 0-10%, 0-20%, 0-100% collisions.*

For a fixed N_{part}, as p_T increases, which is more clearly shown in Fig. 6.2, the general feature that the slope of $R_{AA}(p_T)$ being larger than $R_{cp}(p_T)$ at large p_T appears. What would be interesting is to consider the quantity $(dR_{AA}/dp_T)/(dR_{cp}/dp_T)$, where the monopole effects can get enhanced in magnitude, it will be smaller for CUJET3.0 than for other energy loss models with only color electric degrees of freedom.

6.2 Heavy flavor sector

Let us move to compare the energy loss of charm, beauty and heavy flavor decay electrons within the CUJET3.0 framework. Fig. 6.3 shows the CUJET3.0 results of prompt D meson

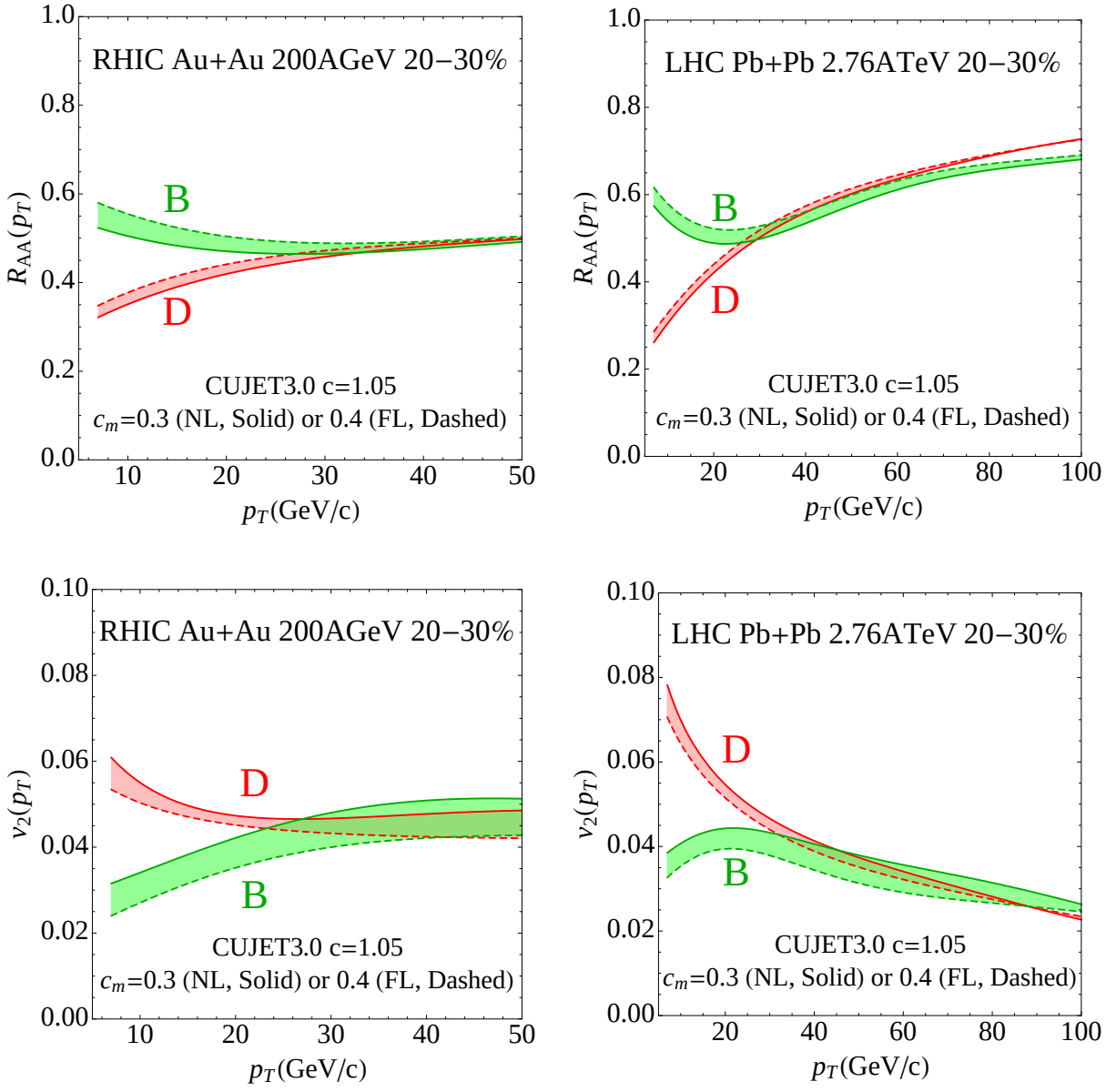

Figure 6.3: *Predictions of prompt D meson and B meson $R_{AA}(p_T)$ and $v_2(p_T)$ from CUJET3.0 at Au+Au 200 AGeV and Pb+Pb 2.76 ATeV 20-30% collisions.*

and B meson's $R_{AA}(p_T)$ and $v_2(p_T)$ in semi-peripheral 20-30% A+A collisions at RHIC and LHC energies. For $R_{AA}(p_T)$, the LHC results at relative low p_T are well constrained by data. One sees that $R^D_{AA}(p_T)$ and $R^B_{AA}(p_T)$ becomes comparable at approximately the same $p_T \sim 30$ GeV at both RHIC and the LHC. Generally speaking, the existence of monopoles will enhance the energy loss ratio between D and B at fixed p_T, therefore bringing down the p_T at which $R^D_{AA}(p_T)$ and $R^B_{AA}(p_T)$ intersect.

For $v_2(p_T)$, an interesting observation is that $v^D_2(p_T)$ and $v^B_2(p_T)$ intersect at approximately the same p_T as $R^D_{AA}(p_T)$ and $R^B_{AA}(p_T)$ at both RHIC and the LHC. $v^B_2(p_T)$ has a maximum at $p_T \sim 20$ GeV at the LHC.

To gain more insights about the relative energy loss between D and B, one can plot their R_{AA} ratio, this is shown in Fig. 6.4. One notices that the $R^D_{AA}(p_T)/R^B_{AA}(p_T) \to 1$ at around the same $p_T \sim 30$ GeV at RHIC and the LHC, this confirms our previous observation. Since this ratio is more sensitive to specific jet-medium interaction mechanisms than the R_{AA}'s alone, it can serve as a good quantitative constraint on the energy loss models. For comparisons, the partonic charm/bottom quark $R^c_{AA}(p_T)/R^b_{AA}(p_T)$ ratios at RHIC and the LHC are also plotted in this figure. The larger $R^D_{AA}(p_T)/R^B_{AA}(p_T)$ compared to $R^c_{AA}(p_T)/R^b_{AA}(p_T)$ suggests a harder fragmentation for b than c.

Fig. 6.5 shows the CUJET3.0 predictions of $R_{AA}(p_T)$ and $v_2(p_T)$ for electrons from different heavy flavor decay channels. They provide rich quantitative information about the heavy quark energy loss in the presence of emergent magnetic monopoles. A notable feature is that while the inclusive HF electrons have lower R_{AA}'s than the semi-exclusive ones, their v_2's are relatively larger.

The fundamental differences between the jet quenching mechanism in the HTL QGP and the sQGMP can be studied from comparisons of CUJET2.0 and CUJET3.0's $R_{AA}(p_T)$. This is shown in Fig. 6.6. One first notices that the CUJET2.0's v_2 is inconsistent with experimental measurements. Therefore only CUJET3.0's $v_2(p_T)$'s are suitable for com-

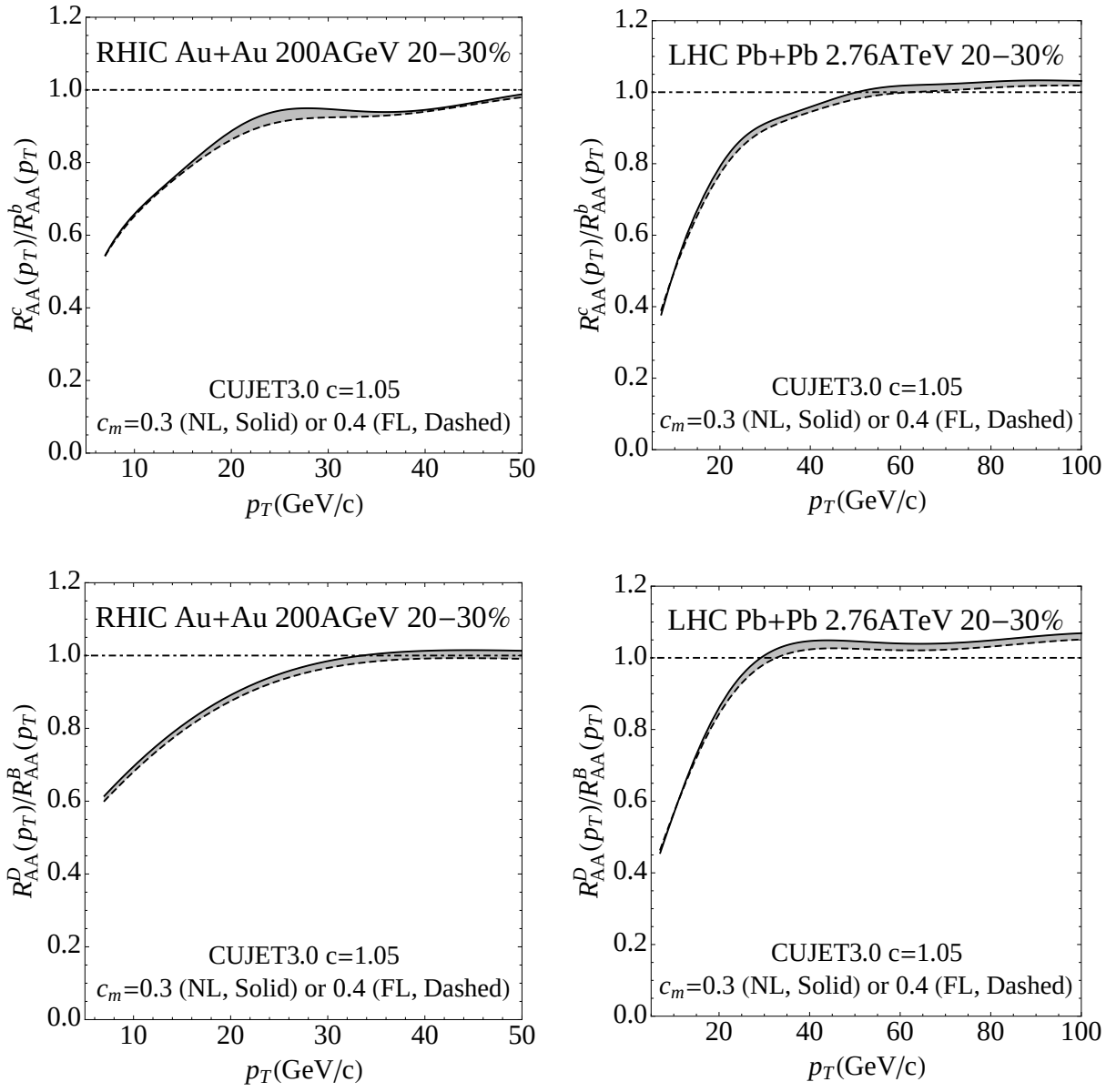

Figure 6.4: *CUJET3.0 predictions of the charm/bottom quark's $R^c_{AA}(p_T)/R^b_{AA}(p_T)$ and D/B meson's $R^D_{AA}(p_T)/R^B_{AA}(p_T)$ at RHIC and LHC semi-peripheral collisions.*

parisons with data.

Let us focus on comparing the $R_{AA}(p_T)$ of CUJET3.0 and CUJET2.0 for different flavors. Note that the parameters in these two models are all constrained using the

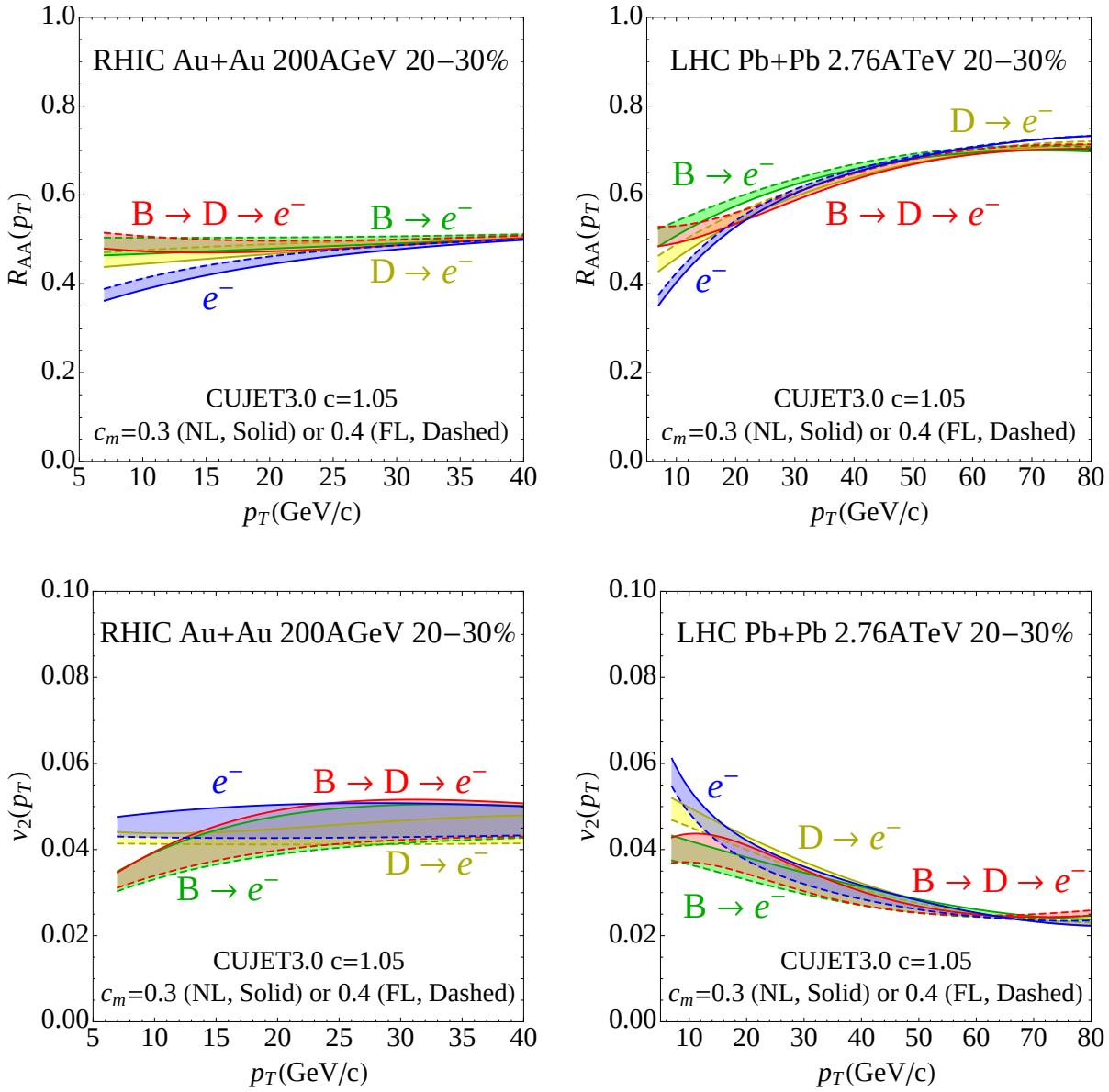

Figure 6.5: *The $R_{AA}(p_T)$ and $v_2(p_T)$ for electrons from different heavy flavor decay channels at RHIC and the LHC computed in CUJET3.0.*

same LHC reference $R_{AA}^{h^\pm}$ at $p_T \sim 12.5$ GeV. Focusing on light hadrons, because of the emergent monopoles, it is clear that the sQGMP generates a stronger quenching effect than the HTL QGP and hence leads to a smaller R_{AA}. In fact, this stronger suppression

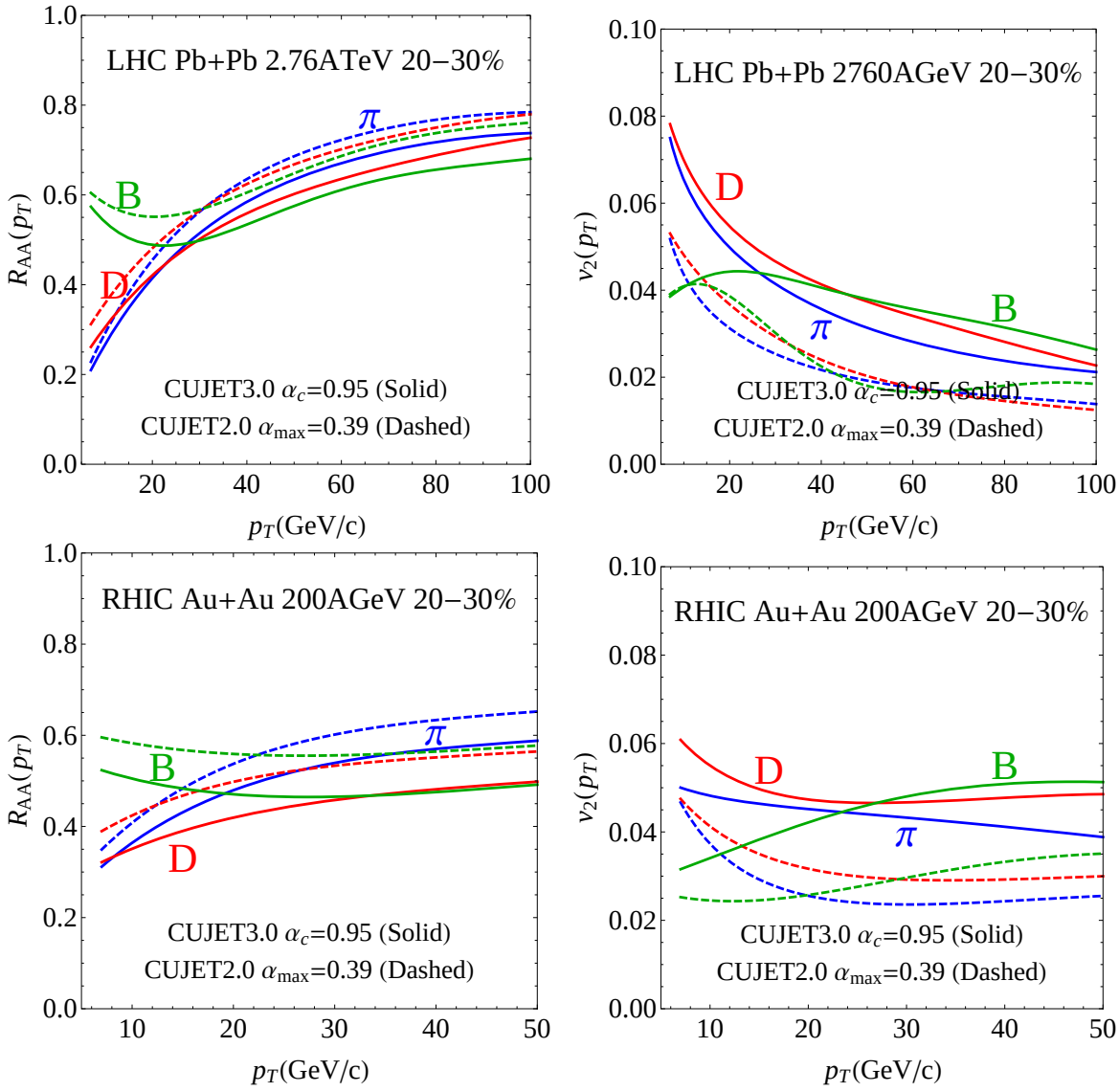

Figure 6.6: *Comparisons of CUJET3.0 and CUJET2.0's $R_{AA}^{\pi,D,B}(p_T)$ and $v_2^{\pi,D,B}(p_T)$ at RHIC and LHC 20-30% collisions.*

because of monopoles extends to extremely high p_T at both RHIC and the LHC, this suggests a universal influence of monopoles on the hard parton scattering regardless of its virtuality, i.e. $\hat{q}$ will get modified by emergent CMM regardless of the initial energy of the jet.

For open heavy flavor D and B, they also get suppressed more in the presence of

monopoles compared to purely electric plasmas, and the p_T's at which R^{π}_{AA}, R^{D}_{AA}, R^{B}_{AA} intersect are universally smaller. To gain insights from this and to perform more quantitative tests for the sQGMP, the comparison between the joint π, D, B $\chi^2/d.o.f.$ in CUJET3.0 and in other HTL QGP based energy loss models can serve as a good indicator.

6.3 R_{pA} in CUJET3.0 assuming a small QGP droplet

The recent studies of collective signatures in high multiplicity $p+p$ and $p+A$ collisions has stimulated broad discussions about the size of the smallest droplet of QGP [381–383]. If a hot deconfined plasma does form in such a small colliding systems, regardless of its size, jet quenching effects must be present and hard parton transport properties in such a medium must be consistent with the "perfect fluidity" of the QGP[1].

To explore this question, one can gain insights from the comparison between very peripheral A+A collisions and the p+A collision systems with comparable multiplicities. For this reason, let us apply CUJET3.0 to study the charged particle $R^{h^{\pm}}_{PbPb,pPb}(p_T)$ in the two configurations, the result is plotted in Fig. 6.7. Note that the bulk hydro evolution profiles at both collisions are generated via the iEBE-VISHNU simulations from the McGill group that fits the low p_T particle spectra [384]. It has MC-Glauber initial conditions, lattice s95p-v0-PCE165 EOS, $\eta/s = 0.08$ for $T > 180$ MeV, and the dS/dy is 12.9-16.9 for pPb 0-1%, 0.2-42.8 for PbPb 50-100%, 266.3-418.2 for PbPb 0-10%[2], a typical event is plotted in the right panel of Fig. 6.7. It has an explosive profile that has strong transverse expansions (even forms a nutshell like shape at later time).

One sees that in central $p+Pb$ collisions one has a smaller multiplicity than peripheral

[1] Although the quenching effect may be small on length scales less than 1 fm.

[2] A complete list of $(dS/dy, N^{min}_{part}$–$N^{max}_{part})$ from the McGill viscous hydro simulations: pPb 0.1% (16.9, 6-27), pPb 1% (12.9, 6-26), pPb 99% (16.9, 2-7), PbPb 0.1% (418.2, 374-414), PbPb 10% (266.3, 250-375), PbPb 50% (42.8, 37-112), PbPb 99% (0.17, 2-10).

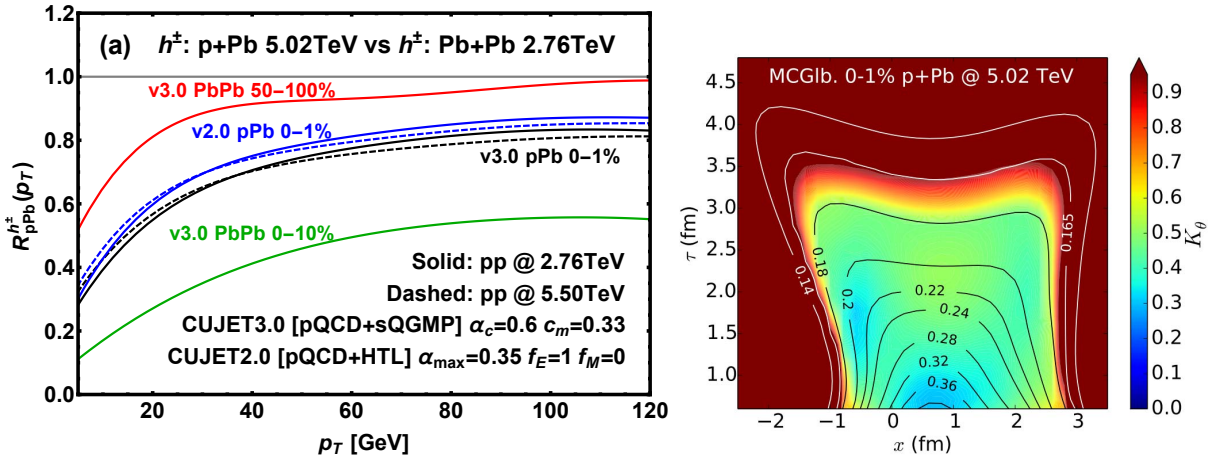

Figure 6.7: *Left: The CUJET3.0's $R_{pPb}(p_T > 5$ GeV$)$ vs $R_{PbPb}(p_T > 5$ GeV$)$ results at different centralities* **assuming the medium is thermalized in high multiplicity p+A collisions**. *Right: Color contour plot for the space-time evolution of the Knudsen number in 0-1% p+Pb collisions at 5.02 TeV from [384]. Note that $K_\theta = \frac{\lambda_{\rm mfp}}{L_{\rm hydro}} = \tau_\pi \theta = 5\frac{\eta\theta}{sT}$ [238].*

$Pb+Pb$ collisions, its suppression factor is anomalously smaller, this suggest if there is QGP formation in $p+Pb$ collisions, it must possess a extremely high temperature profile upon thermalization, and be followed by strong explosions. Note that R_{pPb} never reaches 1 because in a hot deconfined QGP the consistency between jet transport and shear viscous transport within CUJET3.0 is strictly obeyed, i.e. $\hat{q}/T^3 \sim (\eta/s)^{-1} \neq 0$.

Of course in such small colliding systems cold nuclear matter effects may dominate and cancel out the suppression coming from the QGP droplet. The competition between initial and final state interactions in such systems will require further studies.

Moving on to flavor tomography, $R_{dAu,HeAu,AuAu,pPb,PbPb}(p_T > 5$ GeV$)$ of π^0, $h^{\pm}$, Prompt D, B or non-prompt J/ψ, heavy flavor decay e^- are plotted in Fig. 6.8. The nuclear suppression factor in $0-100\%$ & $50-100\%$ centrality $Au+Au$ $\sqrt{s_{NN}} = 200$ GeV & $Pb+Pb$ $\sqrt{s_{NN}} = 2.76$ TeV collisions are compared with $0-100\%$ centrality $d+Au$ $\sqrt{s_{NN}} = 200$ GeV, $He+Au$ $\sqrt{s_{NN}} = 200$ GeV, $p+Pb$ $\sqrt{s_{NN}} = 5.02$ TeV collisions. At very high

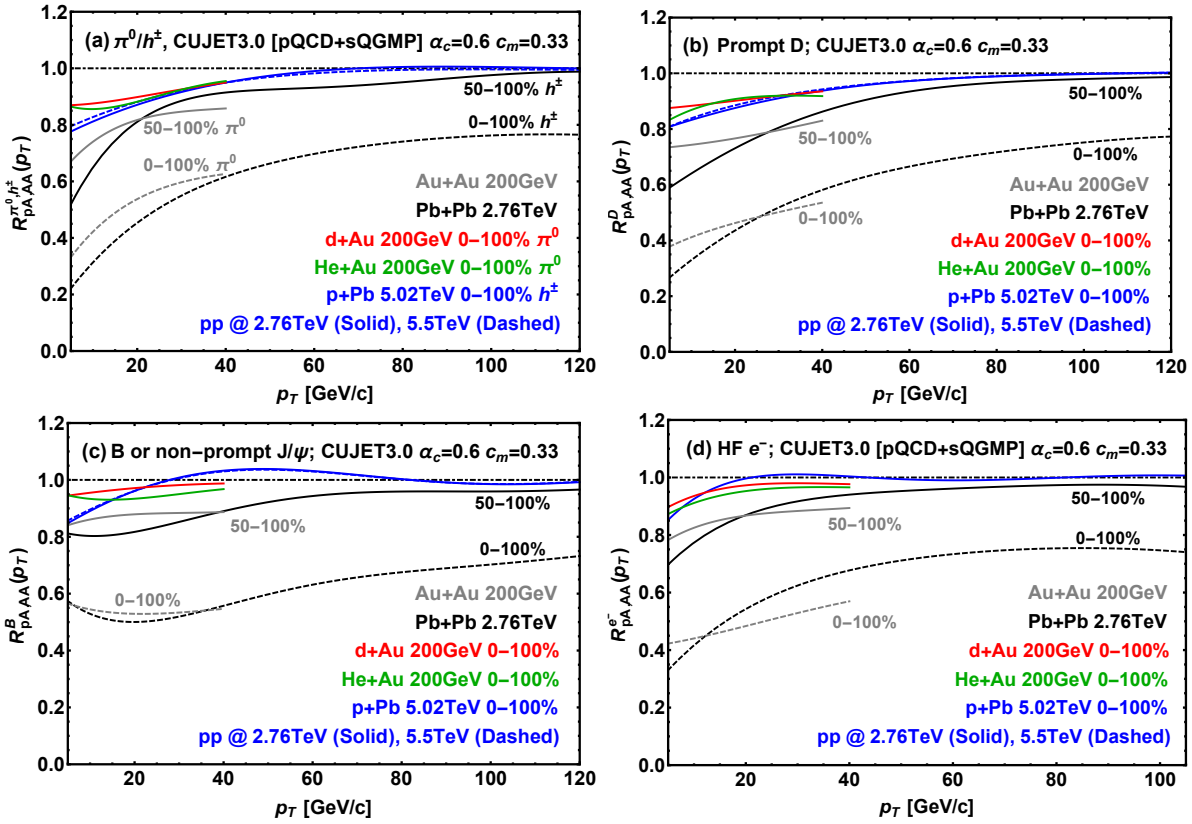

Figure 6.8: *The CUJET3.0's* $R_{dAu,HeAu,AuAu,pPb,PbPb}(p_T > 5$ GeV$)$ *results for* π^0, $h^{\pm}$, *Prompt* D, B *or non-prompt* J/ψ, *heavy flavor decay* e^- *at different centralities* **assuming the medium is thermalized in high multiplicity p+A collisions**.

p_T, $R_{pA} \sim 1$.

The way R_{pA} is calculated is as follows: in the code, pp spectra at 2.76 TeV are used; one gets normalized AA spectra after the run has completed; the two are compared and $\Delta E/E$ vs E for different flavors are extracted; one then plugs in pp spectra at 5.5 TeV and gets the R_{pA}. Note that through doing so the energy loss mechanism $\Delta E/E$ vs E is physical for a certain incoming jet with initial energy E, only the suppression factors will be shifted because of different pp references.

Fig. 6.9 shows the results of CUJET2.0 and CUJET3.0's $R_{dAu,HeAu,pPb}(p_T > 5$ GeV$)$ of π^0, $h^{\pm}$, Prompt D, B or non-prompt J/ψ, heavy flavor decay e^-. $d + Au$ $\sqrt{s_{NN}} =$

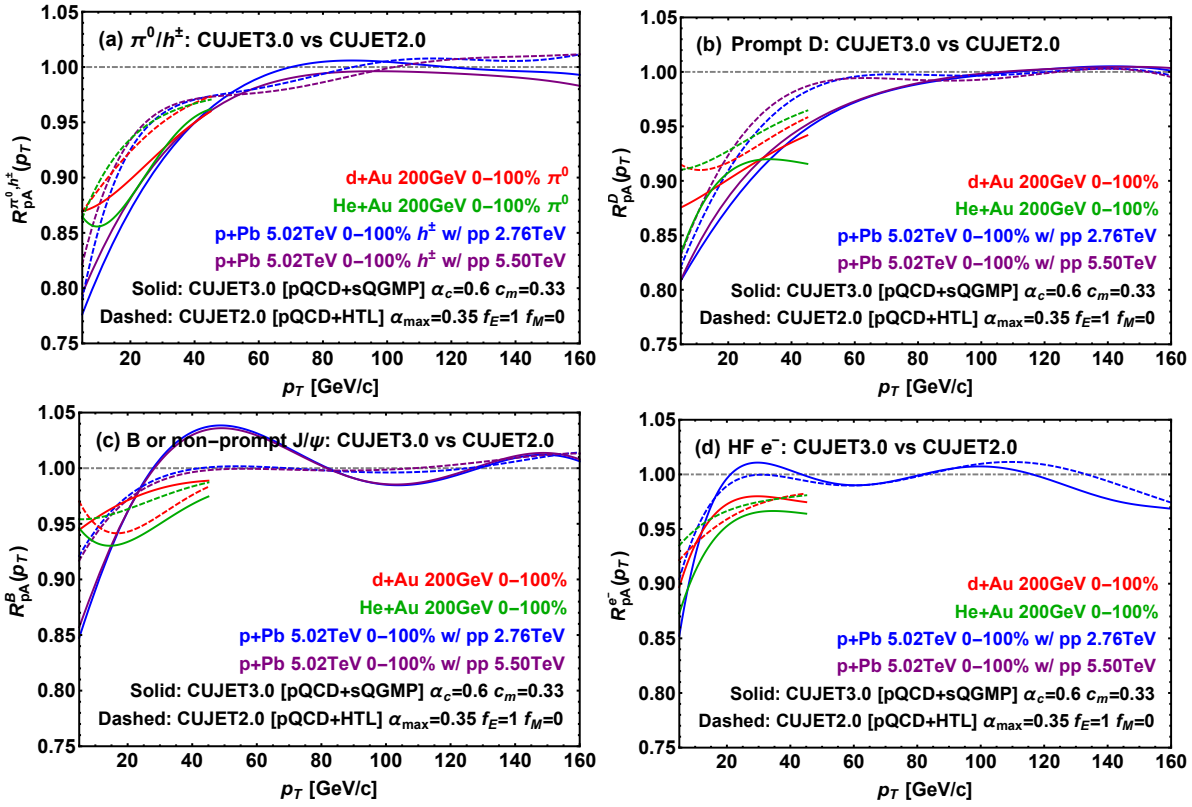

Figure 6.9: *Comparison between CUJET3.0 and CUJET2.0's results of* $R_{dAu,HeAu,pPb}(p_T > 5 \text{ GeV})$ *of* π^0, $h^{\pm}$, *Prompt D, B or non-prompt* J/ψ, *heavy flavor decay* e^- *at different centralities* **assuming the medium is thermalized in high multiplicity p+A collisions**.

200 GeV, $He + Au$ $\sqrt{s_{NN}} = 200$ GeV, $p + Pb$ $\sqrt{s_{NN}} = 5.02$ TeV collisions all have $0 - 100\%$ centrality. For CUJET3.0, $(\alpha_c, c_m) = (0.6, 0.33)$; for CUJET2.0, $(\alpha_{max}, f_E, f_M) = (0.35, 1, 0)$.

The rising of CUJET3.0's $R_{pA}(p_T)$ is slower than CUJET2.0's as expected from the strong scattering because of emergent chromo-magnetic monopoles. In principle, if there is no jet quenching hence no formation of QGP in pA, then the CUJET3.0 and CUJET2.0's results should not differ from each other. Again this effect may be smeared out by cold nuclear matter effects and more careful considerations are required.

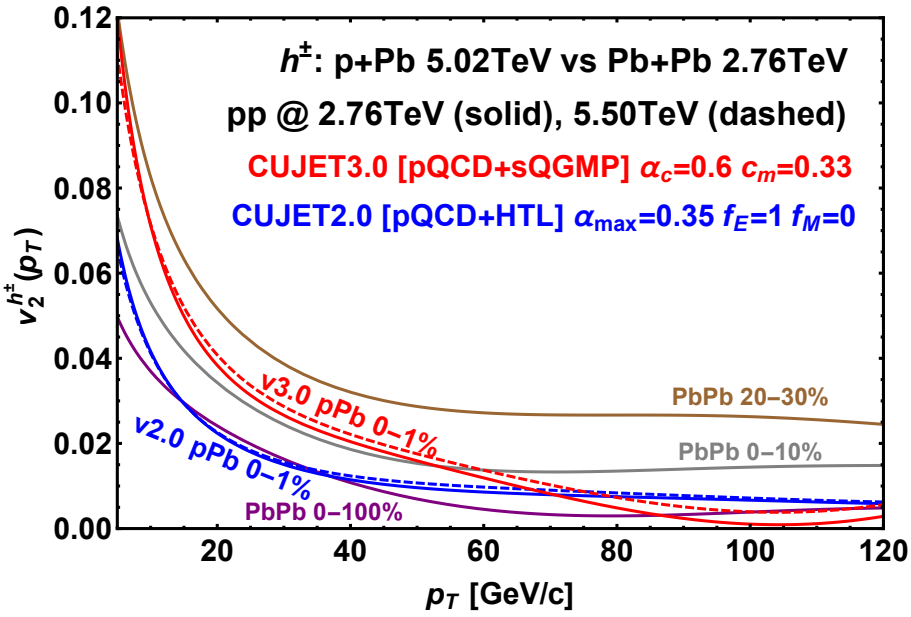

Figure 6.10: *The CUJET3.0 and CUJET2.0's results of* $v_2^{h^{\pm}}(p_T > 5 \text{ GeV})$ **assuming the medium is thermalized in high multiplicity p+A collisions** *compared with* v_2 *in some A+A collisions.*

6.4 Single particle v_2 in p+A collisions

Even if cold nuclear matter effects in p+A reactions may suppress the visibility of hot QGP effects in R_{AA} at high p_T, for generating azimuthal anisotropies, in particular v_2 at high $p_T > 10$ GeV, the latter may be dominating.

For this reason it is interesting to study the single particle azimuthal elliptic anisotropy v_2 within the CUJET3.0 as well as the CUJET2.0 model, because the azimuthally averaged absolute magnitude of the particle spectrum will be factored out.

Fig. 6.10 shows the results of CUJET2.0 and CUJET3.0's $v_2^{h^{\pm}}(p_T > 5 \text{ GeV})$ in $p + Pb$ $\sqrt{s_{NN}} = 5.02$ TeV collisions with $0 - 1\%$ centrality compared with the v_2 in $Pb + Pb$ $\sqrt{s_{NN}} = 2.76$ TeV collisions with $0 - 10\%$, $20 - 30\%$, $0 - 100\%$ centrality. Complications may come about because the iEBE-VISHNU hydro backgrounds implemented

MC-Glauber initial conditions that may somehow exaggerate the size of the medium. If one ignores these technical details and focuses on the results alone, one can gain interesting observations.

First of all, the high p_T v_2 in p+Pb collisions is significant. It reaches the magnitude of v_2 in Pb+Pb 20-30% collisions at $p_T \sim 10$ GeV and fall off to the value of v_2 in Pb+Pb 0-10% collisions and stays comparable with it until $p_T \sim 60$ GeV. Such a large v_2 can easily be proved or disproved by measurements at the LHC.

Secondly, compared to non-central A+A collisions whose v_2 is non-zero at $p_T \sim 100$ GeV, the 0-1% p+Pb v_2 does go to zero at such a high p_T. Assuming that high p_T leading hadrons are initially produced mostly at the edge of the fireball, the phenomenon can be understood if the transverse expansion in p+Pb is so explosive that it is more isotropic than the A+A case, and the momentum anisotropy of outer shells is smaller than inner ones.

Lastly, compare the CUJET3.0 and CUJET2.0 result, in the presence of emergent chromo-magnetic monopoles, for $p + Pb$ 0-1% collisions, the v_2 in the former gets significantly boosted compared with the latter. Recall that in Pb+Pb collisions, the CUJET2.0 20-30% v_2 (c.f. Section 3.4) has approximately the same magnitude as the CUJET3.0 0-10% v_2, one thus see that the enhancement in high p_T v_2 because of the sQGMP is approximately the same in $p + Pb$ 5.02 TeV 0-1% collisions as in $Pb + Pb$ 2.76 TeV 20-30% collisions. The more explosive expansion in $p + Pb$ collisions is one of the contributors to this phenomenon.

6.5 Conclusions

In this chapter, we have provided predictions of high p_T $R_{AA,pA}$ and v_2 for light hadrons, open heavy flavors and heavy flavor decay electrons from the CUJET3.0 model that

can be systematically tested by future or ongoing measurements at RHIC and the LHC. Differences between the CUJET3.0 and CUJET2.0 results provide additional checkpoints for examining the existence of semi-Quark-Gluon-Monopole Plasmas in the near T_c regime through jet quenching studied in ultra-relativistic nucleus-nucleus collisions.

Although more careful considerations for the suppression factors in high multiplicity p+A collisions are required because of cold nuclear matter effects, a non-zero/zero high p_T azimuthal anisotropy v_2 in such systems can be a powerful indicator of the existence/nonexistence of hot deconfined QGP droplets in these p+A reactions. What is more, the magnitude of high p_T v_2 in high multiplicity p+A events can be an exclusive determinant of emergent chromo-magnetic monopoles in near-critical QGPs.

Concluding Remarks

In the first part of this thesis, a perturbative QCD (pQCD) based azimuthal jet flavor tomography model, CUJET2.0 (Chapter 3), is developed. This development follows the objectives of the US Department of Energy Topical JET Collaboration [228] to design quantitative tools to analyze jet probes at RHIC and the LHC. CUJET2.0 features dynamical running coupling DGLV opacity series (Section 2.3 and 3.1.1) coupled with QGP bulk data constrained viscous hydrodynamical backgrounds (Section 3.1.3). Within the CUJET2.0 framework:

1. A solution to the "heavy quark energy loss puzzle" at RHIC, i.e. the anomalously strong suppression of heavy flavor decay electrons observed in central Au+Au collisions, is derived, through considerations of dynamical QCD medium effects, realistic geometric fluctuations, elastic scatterings, and energy loss fluctuations. (Section 3.2.1).

2. An explanation to the "surprising transparency of the QGP" at the LHC, i.e. the jet opacity scales weaker than linearly with the medium density, is gained, through considerations of multi-scale running strong couplings in the DGLV opacity expansion theory. (Section 3.2.2).

3. The jet transport coefficient $\hat{q}$, a critical parameter that characterizes the mean transverse momentum transfer squared per unit length for hard partons traversing

the hot deconfined QGP, is calculated from CUJET2.0. Utilizing this information and those from 4 other pQCD based models in the JET Collaboration fitting to the same set of experimental hadron suppression factors at RHIC and LHC central A+A collisions, the value of $\hat{q}$ is determined to an unprecedented accuracy. (Section 3.3).

4. A universal "high p_T v_2 puzzle" exists in pQCD based energy loss models, i.e. the high transverse momentum p_T light hadrons and open heavy flavors azimuthal elliptic anisotropy v_2 (c.f. Section 1.2.3 and 3.4.1) will be underestimated by $\sim 50\%$ after one has constrained all parameters with the nuclear modification factor R_{AA} (c.f. Section 1.2.6) data. It is found within CUJET2.0 that if one allows the path averaged coupling strength $\langle \alpha_s \rangle_P$ to be enhanced by 10% from in reaction plane to out-of reaction plane paths, one can get a 100% boost in the high p_T hadrons v_2, bringing theoretical results to be in line with data. This extreme sensitivity of $v_2(p_T > 10$ GeV/c) on $\langle \alpha_s \rangle_P$ suggests the jet-medium interaction has a non-trivial dependence on local QGP temperature that originates from nonperturbative aspects of QCD. (Section 3.4).

One qualitative solution to the "high p_T v_2 puzzle" suggests an enhanced jet-medium coupling in the nonperturbative regime near the critical transition temperature T_c (Section 3.4.4). Such an enhancement can naturally rise from a "magnetic scenario of the strongly-coupled QGP" (Chapter 4). This magnetic scenario however does not take into account the effects of the Polyakov loop in the presence of non-trivial holonomy that result in "semi-QGP" suppressions (Section 4.4 and 5.1.2).

To explore the full nonperturbative chromo-electric and chromo-magnetic structure of the "perfect fluid" like QGP near T_c, in the second part of this thesis, a microscopic semi-Quark-Gluon-Monopole Plasma (sQGMP) model, that includes Polyakov loop sup-

pressed semi-QGP chromo-electric charges (Section 5.1.2) and emergent chromo-magnetic monopoles (Section 5.1.3), is built and implemented in generalized CUJET2.0 (Section 5.1.4). This lead to a new CUJET3.0 jet quenching framework that quantitatively incorporates both perturbative and nonperturbative aspects of QCD (Section 5.1). It is found within the CUJET3.0 framework that:

1. After fixing (1) the value of the QCD running coupling α_c at low $Q < T_c$ and (2) the ratio $c_m = g\mu_E/\mu_M$ of nonperturbative electric to magnetic screening scales by fitting reference R^{ch}_{PbPb} data at the LHC, the CUJET3.0 results are in perfect agreements with all available RHIC and the LHC data on $R^h_{AA}(p_T)$ and $v^h_2(p_T)$ for $h = \pi, D, B$ *simultaneously*. CUJET3.0 therefore solves the "high p_T v_2 puzzle". (Section 5.2.1).

2. The emergent chromo-magnetic degrees of freedom in the sQGMP model near T_c lead to a broad maximum of the scaled jet quenching parameter $\hat{q}(E,T)/T^3$ between $(1-2)T_c$ within CUJET3.0. It smoothly bridges the $\mathcal{N}=4$ SYM limit close to T_c and the pQCD limit at high temperature. (Section 5.2.2).

3. Most remarkably, by extrapolating the CUJET3.0's $\hat{q}(E,T)$ down to thermal energy $E \sim 3T$ scales, one finds the shear viscosity to entropy density ratio $\eta/s \sim T^3/\hat{q} \sim 1/4\pi$ to be near the unitarity bound in the $T \sim (1-2)T_c$ critical transition temperature range. This is consistent with viscous hydrodynamic fits to bulk azimuthal harmonics v_n at $p_T < 2$ GeV/c. It indicates that CUJET3.0 provides a novel quantitative connection between the long distance bulk "perfect fluidity" of the QGP and the short distance jet transport in the QGP. (Section 5.2.3).

To apply CUJET3.0 to perform quantitative analysis of both perturbative and nonperturbative properties of the QGP, and more fundamentally color confinement/deconfinement

transition using jet probes, key theoretical uncertainties in this framework must be investigated. They come from different interpretations of the lattice QCD data on the color electric and magnetic components in the nonperturbative regime. Among them the deconfinement transition rate $r_d \equiv d\chi_T/dT$ and the electric (E) and magnetic (M) screening mass $\mu_{E,M}$ near T_c are most critical ones. (Section 5.1.5).

After CUJET3.0 model parameters are constrained by data of high p_T light hadrons (LH) R_{AA} and relevant lattice calculations, it is found that: (1) $\mu_E - \mu_M$ near T_c influences LH v_2; (2) r_d influences open heavy flavors (HF) R_{AA}; (3) r_d and absolute values of $\mu_{E,M}$ influence HF v_2. On the other hand, the CUJET3.0's $\hat{q}$ and η/s are affected by r_d and $\mu_{E,M}$ differently: (a) $\hat{q}(T)$ is constrained by $r_d(T)$; (b) $d(\eta/s)/dT$ is constrained by $\mu_E(T) - \mu_M(T)$ near T_c; (c) $(\eta/s)_{\rm min}$ is constrained by $r_d(T)$. (Section 5.3).

In addition to all the above, findings within the CUJET3.0 jet quenching framework also include:

1. Different relativistic corrections from viscous hydrodynamical flows which are found not to affect either R_{AA} or v_2 for light hadrons. This is expected from the eikonal approximation that, the number of parton-medium scatterings is fixed in any frame once the initial jet production coordinate and the azimuthal jet propagation angle are specified. (Section 5.5.1).

2. Among the various ingredients in CUJET3.0 that contribute toward obtaining a quantitative description of the high p_T hadrons v_2 data, the emergent chromomagnetic monopoles play the decisive role. As long as monopoles are present in the near T_c regime, v_2 is insensitive to the detailed form of the running coupling $\alpha_s(Q^2)$, provided that lattice screening masses can be reasonably described. (Section 5.5.2).

3. It is reassuring from the energy loss's path length L dependence that both CU-

JET3.0 and CUJET2.0 converge to the pQCD/elastic limit at high temperatures $T \gtrsim 400$ MeV. However as T drops, starting from $T \sim 300$ MeV, chromo-magnetic monopoles gradually dominate the medium. Consequently the CUJET3.0's energy loss dependence on L starts to deviate from pQCD/elastic toward the AdS/CFT-like strong coupling limit. (Section 5.4.1).

4. It is noteworthy that the "dead cone" suppression is not altered by the nonperturbative sQGMP near T_c. It is also found that the modification on the L dependence of light and heavy quark energy loss caused by the transition from high-T QGP to near-T_c sQGMP are similar. (Section 5.4.2).

5. Remarkably different $\hat{q}(T)$ dependence could be consistent with the same R_{AA} data. This demonstrates clearly the inadequacy of focusing on the jet path averaged quantity $\langle\hat{q}\rangle$ as the only relevant medium property to characterize jet energy loss. Evidently while the $\langle\hat{q}\rangle$ captures the important transverse "kick" factor, there are other essential factors like the actual chromo-electric and chromo-magnetic composition of the plasma, the screening masses and the running couplings at multiple scales which all strongly influence jet energy loss and imprint their effects beyond just in the $\langle\hat{q}\rangle$. It is of significant interest and importance to thoroughly exploit these multiple facets of jet physics and the opportunities they offer for progressing toward an ultimate understanding of the microscopic make-up of the sQGP. (Section 5.3.3).

With detailed investigations of jet quenching in the sQGMP, one sees that the phenomenological consequences for both hard and soft probes in heavy ion collisions, stay very robust with respect to important systematic theoretical uncertainties. The phenomenological success includes simultaneous descriptions of all available high p_T R_{AA} and v_2 data at both RHIC and the LHC, as well as providing an intuitive dynamical mechanism that explains how the shear viscosity to entropy density ratio could approach the

$1/4\pi$ unitarity bound in the vicinity of T_c as required to explain the bulk low $p_T < 2$ GeV long wavelength "perfect fluidity". CUJET3.0 therefore provides a first model that consistently accounts for both short and long distance transport properties of the new state of QCD matter discovered in high energy nuclear collisions at RHIC and the LHC. (Section 5.6).

Predictions from CUJET3.0 are also made (Chapter 6), including: the centrality dependence of R_{AA} and R_{cp} for prompt D mesons; systematic results of the suppression of charm, beauty and heavy flavor decay electrons in A+A collisions; and possible jet quenching effects in proton-nucleus collisions. They can all be tested by RHIC and LHC measurements in the future. If these are verified, CUJET3.0 will be a robust framework to perform quantitative jet quenching studies of both perturbative and nonperturbative aspects of QCD.

Bibliography

[1] M. Gell-Mann and Y. Ne'eman, *The Eightfold Way*. Westview Press, 2000.

[2] V. Barnes, P. Connolly, D. Crennell, B. Culwick, W. Delaney et al., *Observation of a Hyperon with Strangeness -3*, *Phys. Rev. Lett.* **12** (1964) 204–206.

[3] M. Gell-Mann, *A Schematic Model of Baryons and Mesons*, *Phys. Lett.* **8** (1964) 214–215.

[4] G. Zweig, *An SU(3) model for strong interaction symmetry and its breaking*, *CERN-TH-401* (1964) .

[5] M. Han and Y. Nambu, *Three Triplet Model with Double SU(3) Symmetry*, *Phys. Rev.* **139** (1965) B1006–B1010.

[6] H. Fritzsch and M. Gell-Mann, *Current algebra: Quarks and what else?*, *eConf* **C720906V2** (1972) 135–165, [hep-ph/0208010].

[7] M. Breidenbach, J. I. Friedman, H. W. Kendall, E. D. Bloom, D. Coward et al., *Observed Behavior of Highly Inelastic electron-Proton Scattering*, *Phys. Rev. Lett.* **23** (1969) 935–939.

[8] E. D. Bloom, D. Coward, H. DeStaebler, J. Drees, G. Miller et al., *High-Energy Inelastic e p Scattering at 6-Degrees and 10-Degrees*, *Phys. Rev. Lett.* **23** (1969) 930–934.

[9] TASSO collaboration, R. Brandelik et al., *Evidence for Planar Events in e+ e- Annihilation at High-Energies*, *Phys. Lett.* **B86** (1979) 243.

[10] J. Christenson, G. Hicks, L. Lederman, P. Limon, B. Pope et al., *Observation of massive muon pairs in hadron collisions*, *Phys. Rev. Lett.* **25** (1970) 1523–1526.

[11] C. Chang, K. Chen, D. Fox, A. Kotlewski, P. F. Kunz et al., *Observed Deviations from Scale Invariance in High-Energy Muon Scattering*, *Phys. Rev. Lett.* **35** (1975) 901.

[12] D. Gross and F. Wilczek, *Asymptotically Free Gauge Theories. 1*, *Phys. Rev.* **D8** (1973) 3633–3652.

[13] H. D. Politzer, *Reliable Perturbative Results for Strong Interactions?*, *Phys. Rev. Lett.* **30** (1973) 1346–1349.

[14] G. 't Hooft, *Unpublished* (1972) .

[15] R. D. Field, *Applications of perturbative QCD*. Addison-Wesley, 1989.

[16] Particle Data Group collaboration, J. Beringer et al., *Review of Particle Physics (RPP)*, *Phys. Rev.* **D86** (2012) 010001.

[17] Y. Nambu and G. Jona-Lasinio, *Dynamical Model of Elementary Particles Based on an Analogy with Superconductivity. 1.*, *Phys. Rev.* **122** (1961) 345–358.

[18] Y. Nambu and G. Jona-Lasinio, *Dynamical Model of Elementary Particles Based on an Analogy with Superconductivity. II*, *Phys. Rev.* **124** (1961) 246–254.

[19] T. Hatsuda and T. Kunihiro, *QCD phenomenology based on a chiral effective Lagrangian*, *Phys. Rept.* **247** (1994) 221–367, [hep-ph/9401310].

[20] S. Weinberg, *Phenomenological Lagrangians*, *Physica* **A96** (1979) 327.

[21] J. Gasser and H. Leutwyler, *Chiral Perturbation Theory to One Loop*, *Annals Phys.* **158** (1984) 142.

[22] J. Gasser and H. Leutwyler, *Chiral Perturbation Theory: Expansions in the Mass of the Strange Quark*, *Nucl. Phys.* **B250** (1985) 465.

[23] M. A. Shifman, A. Vainshtein and V. I. Zakharov, *QCD and Resonance Physics. Sum Rules*, *Nucl. Phys.* **B147** (1979) 385–447.

[24] P. Colangelo and A. Khodjamirian, *QCD sum rules, a modern perspective*, *At the frontier of particle physics* **3** (2000) 1495–1576, [hep-ph/0010175].

[25] K. G. Wilson, *Confinement of Quarks*, *Phys. Rev.* **D10** (1974) 2445–2459.

[26] J. M. Maldacena, *The Large N limit of superconformal field theories and supergravity*, *Adv. Theor. Math. Phys.* **2** (1998) 231–252, [hep-th/9711200].

[27] S. Gubser, I. R. Klebanov and A. M. Polyakov, *Gauge theory correlators from noncritical string theory*, *Phys. Lett.* **B428** (1998) 105–114, [hep-th/9802109].

[28] E. Witten, *Anti-de Sitter space and holography*, *Adv. Theor. Math. Phys.* **2** (1998) 253–291, [hep-th/9802150].

[29] O. Aharony, S. S. Gubser, J. M. Maldacena, H. Ooguri and Y. Oz, *Large N field theories, string theory and gravity*, *Phys. Rept.* **323** (2000) 183–386, [hep-th/9905111].

[30] J. Casalderrey-Solana, H. Liu, D. Mateos, K. Rajagopal and U. A. Wiedemann, *Gauge/String Duality, Hot QCD and Heavy Ion Collisions*. Cambridge University Press, 2014.

[31] Y. Nambu, *Strings, Monopoles and Gauge Fields*, *Phys. Rev.* **D10** (1974) 4262.

[32] A. Chodos, R. Jaffe, K. Johnson, C. B. Thorn and V. Weisskopf, *A New Extended Model of Hadrons*, *Phys. Rev.* **D9** (1974) 3471–3495.

[33] A. Chodos, R. Jaffe, K. Johnson and C. B. Thorn, *Baryon Structure in the Bag Theory*, *Phys. Rev.* **D10** (1974) 2599.

[34] T. A. DeGrand, R. Jaffe, K. Johnson and J. Kiskis, *Masses and Other Parameters of the Light Hadrons*, *Phys. Rev.* **D12** (1975) 2060.

[35] E. V. Shuryak, *The QCD vacuum, hadrons and the superdense matter*, *World Sci. Lect. Notes Phys.* **71** (2004) 1–618.

[36] H. Satz, *Color deconfinement in nuclear collisions*, *Rept. Prog. Phys.* **63** (2000) 1511, [hep-ph/0007069].

[37] J. Bardeen, L. Cooper and J. Schrieffer, *Theory of superconductivity*, *Phys. Rev.* **108** (1957) 1175–1204.

[38] Y. Nambu, *Axial vector current conservation in weak interactions*, *Phys. Rev. Lett.* **4** (1960) 380–382.

[39] J. Goldstone, *Field Theories with Superconductor Solutions*, *Nuovo Cim.* **19** (1961) 154–164.

[40] I. Aitchison and A. Hey, *Gauge theories in particle physics: A practical introduction. Vol. 2: Non-Abelian gauge theories: QCD and the electroweak theory.* Bristol, UK: IOP, 2004.

[41] K. Yagi, T. Hatsuda and Y. Miake, *Quark-gluon plasma: From big bang to little bang*, *Camb. Monogr. Part. Phys. Nucl. Phys. Cosmol.* **23** (2005) 1–446.

[42] E. V. Shuryak, *Two Scales and Phase Transitions in Quantum Chromodynamics*, *Phys. Lett.* **B107** (1981) 103.

[43] R. D. Pisarski, *Phenomenology of the Chiral Phase Transition*, *Phys. Lett.* **B110** (1982) 155.

[44] HotQCD collaboration, A. Bazavov et al., *Equation of state in (2+1)-flavor QCD*, *Phys. Rev.* **D90** (2014) 094503, [1407.6387].

[45] C. Bonati, P. de Forcrand, M. D'Elia, O. Philipsen and F. Sanfilippo, *Constraints on the two-flavor QCD phase diagram from imaginary chemical potential*, *PoS* **LATTICE2011** (2011) 189, [1201.2769].

[46] R. D. Pisarski and F. Wilczek, *Remarks on the Chiral Phase Transition in Chromodynamics*, *Phys. Rev.* **D29** (1984) 338–341.

[47] R. Gupta, *Introduction to lattice QCD: Course*, in *Probing the standard model of particle interactions. Proceedings, Summer School in Theoretical Physics, NATO Advanced Study Institute, 68th session, Les Houches, France, July 28-September 5, 1997. Pt. 1, 2*, pp. 83–219, 1997. hep-lat/9807028.

[48] F. Karsch, *Lattice QCD at high temperature and density*, *Lect. Notes Phys.* **583** (2002) 209–249, [hep-lat/0106019].

[49] Y. Iwasaki, *Renormalization Group Analysis of Lattice Theories and Improved Lattice Action: Two-Dimensional Nonlinear O(N) Sigma Model*, *Nucl. Phys.* **B258** (1985) 141–156.

[50] D. B. Kaplan, *A Method for simulating chiral fermions on the lattice*, *Phys. Lett.* **B288** (1992) 342–347, [hep-lat/9206013].

[51] V. Furman and Y. Shamir, *Axial symmetries in lattice QCD with Kaplan fermions*, *Nucl. Phys.* **B439** (1995) 54–78, [hep-lat/9405004].

[52] M. Creutz, *Quarks, gluons and lattices*. Cambridge University Press, 1985.

[53] I. Montvay and G. Munster, *Quantum fields on a lattice*. Cambridge University Press, 1997.

[54] P. Hasenfratz and F. Karsch, *Chemical Potential on the Lattice*, *Phys. Lett.* **B125** (1983) 308.

[55] "How Low Can RHIC Go?." http://www.bnl.gov/newsroom/news.php?a=21870.

[56] F. Gelis, *The Early Stages of a High Energy Heavy Ion Collision*, *J. Phys. Conf. Ser.* **381** (2012) 012021, [1110.1544].

[57] L. McLerran, *The CGC and the Glasma: Two Lectures at the Yukawa Insitute*, *Prog. Theor. Phys. Suppl.* **187** (2011) 17–30, [1011.3204].

[58] G. Altarelli and G. Parisi, *Asymptotic Freedom in Parton Language*, *Nucl. Phys.* **B126** (1977) 298.

[59] V. Gribov and L. Lipatov, *Deep inelastic e p scattering in perturbation theory*, *Sov. J. Nucl. Phys.* **15** (1972) 438–450.

[60] Y. L. Dokshitzer, *Calculation of the Structure Functions for Deep Inelastic Scattering and e+ e- Annihilation by Perturbation Theory in Quantum Chromodynamics.*, *Sov. Phys. JETP* **46** (1977) 641–653.

[61] L. N. Lipatov, *Reggeization of the Vector Meson and the Vacuum Singularity in Nonabelian Gauge Theories*, *Sov. J. Nucl. Phys.* **23** (1976) 338–345.

[62] E. A. Kuraev, L. N. Lipatov and V. S. Fadin, *The Pomeranchuk Singularity in Nonabelian Gauge Theories*, *Sov. Phys. JETP* **45** (1977) 199–204.

[63] I. I. Balitsky and L. N. Lipatov, *The Pomeranchuk Singularity in Quantum Chromodynamics*, *Sov. J. Nucl. Phys.* **28** (1978) 822–829.

[64] ZEUS AND H1 collaboration, F. D. Aaron et al., *Combined Measurement and QCD Analysis of the Inclusive e+- p Scattering Cross Sections at HERA*, *JHEP* **01** (2010) 109, [0911.0884].

[65] H1 collaboration, F. D. Aaron et al., *A Precision Measurement of the Inclusive ep Scattering Cross Section at HERA*, *Eur. Phys. J.* **C64** (2009) 561–587, [0904.3513].

[66] F. Gelis, E. Iancu, J. Jalilian-Marian and R. Venugopalan, *The Color Glass Condensate*, *Ann. Rev. Nucl. Part. Sci.* **60** (2010) 463–489, [1002.0333].

[67] L. Gribov, E. Levin and M. Ryskin, *Semihard Processes in QCD*, *Phys. Rept.* **100** (1983) 1–150.

[68] A. H. Mueller and J.-W. Qiu, *Gluon Recombination and Shadowing at Small Values of x*, *Nucl. Phys.* **B268** (1986) 427.

[69] E. Iancu, K. Itakura and L. McLerran, *Geometric scaling above the saturation scale*, *Nucl. Phys.* **A708** (2002) 327–352, [hep-ph/0203137].

[70] A. Mueller and D. Triantafyllopoulos, *The Energy dependence of the saturation momentum*, *Nucl. Phys.* **B640** (2002) 331–350, [hep-ph/0205167].

[71] E. Iancu, K. Itakura and S. Munier, *Saturation and BFKL dynamics in the HERA data at small x*, *Phys. Lett.* **B590** (2004) 199–208, [hep-ph/0310338].

[72] D. Boer et al., *Gluons and the quark sea at high energies: Distributions, polarization, tomography*, *SLAC-R-995* (2011) , [1108.1713].

[73] L. D. McLerran and R. Venugopalan, *Computing quark and gluon distribution functions for very large nuclei*, *Phys. Rev.* **D49** (1994) 2233–2241, [hep-ph/9309289].

[74] L. D. McLerran and R. Venugopalan, *Gluon distribution functions for very large nuclei at small transverse momentum*, *Phys. Rev.* **D49** (1994) 3352–3355, [hep-ph/9311205].

[75] E. Iancu, A. Leonidov and L. D. McLerran, *The Renormalization group equation for the color glass condensate*, *Phys. Lett.* **B510** (2001) 133–144, [hep-ph/0102009].

[76] K. Fukushima, F. Gelis and L. McLerran, *Initial Singularity of the Little Bang*, *Nucl. Phys.* **A786** (2007) 107–130, [hep-ph/0610416].

[77] D. Kharzeev, E. Levin and M. Nardi, *The Onset of classical QCD dynamics in relativistic heavy ion collisions*, *Phys. Rev.* **C71** (2005) 054903, [hep-ph/0111315].

[78] J. L. Albacete, *Particle multiplicities in Lead-Lead collisions at the LHC from non-linear evolution with running coupling*, *Phys. Rev. Lett.* **99** (2007) 262301, [0707.2545].

[79] J. L. Albacete, A. Dumitru and Y. Nara, *CGC initial conditions at RHIC and LHC*, *J. Phys. Conf. Ser.* **316** (2011) 012011, [1106.0978].

[80] D. Kharzeev, Y. V. Kovchegov and K. Tuchin, *Cronin effect and high p(T) suppression in pA collisions*, *Phys. Rev.* **D68** (2003) 094013, [hep-ph/0307037].

[81] J. L. Albacete, N. Armesto, A. Kovner, C. A. Salgado and U. A. Wiedemann, *Energy dependence of the Cronin effect from nonlinear QCD evolution*, *Phys. Rev. Lett.* **92** (2004) 082001, [hep-ph/0307179].

[82] J. L. Albacete and C. Marquet, *Single Inclusive Hadron Production at RHIC and the LHC from the Color Glass Condensate*, *Phys. Lett.* **B687** (2010) 174–179, [1001.1378].

[83] D. Kharzeev, E. Levin and L. McLerran, *Jet azimuthal correlations and parton saturation in the color glass condensate*, *Nucl. Phys.* **A748** (2005) 627–640, [hep-ph/0403271].

[84] J. L. Albacete and C. Marquet, *Azimuthal correlations of forward di-hadrons in d+Au collisions at RHIC in the Color Glass Condensate*, *Phys. Rev. Lett.* **105** (2010) 162301, [1005.4065].

[85] A. Dumitru, K. Dusling, F. Gelis, J. Jalilian-Marian, T. Lappi et al., *The Ridge in proton-proton collisions at the LHC*, *Phys. Lett.* **B697** (2011) 21–25, [1009.5295].

[86] T. Lee, *Report of the workshop on BeV/nucleon collisions of heavy ions – how and why*, in *Bear Mountain, New York, Nov. 29 – Dec. 1, 1974*, *BNL-AUI* (1975).

[87] T. Lee and G. Wick, *Vacuum Stability and Vacuum Excitation in a Spin 0 Field Theory*, *Phys. Rev.* **D9** (1974) 2291.

[88] J. C. Collins and M. Perry, *Superdense Matter: Neutrons Or Asymptotically Free Quarks?*, *Phys. Rev. Lett.* **34** (1975) 1353.

[89] "A new state of matter created at CERN." http://newstate-matter.web.cern.ch/newstate-matter/Experiments.html.

[90] BRAHMS collaboration, I. Arsene et al., *Quark gluon plasma and color glass condensate at RHIC? The Perspective from the BRAHMS experiment*, *Nucl. Phys.* **A757** (2005) 1–27, [nucl-ex/0410020].

[91] PHENIX collaboration, K. Adcox et al., *Formation of dense partonic matter in relativistic nucleus-nucleus collisions at RHIC: Experimental evaluation by the PHENIX collaboration*, *Nucl. Phys.* **A757** (2005) 184–283, [nucl-ex/0410003].

[92] B. Back, M. Baker, M. Ballintijn, D. Barton, B. Becker et al., *The PHOBOS perspective on discoveries at RHIC*, *Nucl. Phys.* **A757** (2005) 28–101, [nucl-ex/0410022].

[93] STAR collaboration, J. Adams et al., *Experimental and theoretical challenges in the search for the quark gluon plasma: The STAR Collaboration's critical assessment of the evidence from RHIC collisions*, *Nucl. Phys.* **A757** (2005) 102–183, [nucl-ex/0501009].

[94] M. Gyulassy and L. McLerran, *New forms of QCD matter discovered at RHIC*, *Nucl. Phys.* **A750** (2005) 30–63, [nucl-th/0405013].

[95] PHOBOS collaboration, B. Back et al., *Charged-particle pseudorapidity distributions in Au+Au collisions at* $s(NN)^{1/2}$ *= 62.4-GeV*, *Phys. Rev.* **C74** (2006) 021901, [nucl-ex/0509034].

[96] ALICE collaboration, B. Abelev et al., *Charged-particle multiplicity density at mid-rapidity in central Pb-Pb collisions at* $\sqrt{s_{NN}} = 2.76$ *TeV*, *Phys. Rev. Lett.* **105** (2010) 252301, [1011.3916].

[97] J. Bjorken, *Highly Relativistic Nucleus-Nucleus Collisions: The Central Rapidity Region*, *Phys. Rev.* **D27** (1983) 140–151.

[98] PHENIX collaboration, S. Adler et al., *Identified charged particle spectra and yields in Au+Au collisions at S(NN)**1/2 = 200-GeV*, *Phys. Rev.* **C69** (2004) 034909, [nucl-ex/0307022].

[99] R. Glauber and G. Matthiae, *High-energy scattering of protons by nuclei*, *Nucl. Phys.* **B21** (1970) 135–157.

[100] P. Huovinen and P. Ruuskanen, *Hydrodynamic Models for Heavy Ion Collisions*, *Ann. Rev. Nucl. Part. Sci.* **56** (2006) 163–206, [nucl-th/0605008].

[101] P. B. Arnold, G. D. Moore and L. G. Yaffe, *Transport coefficients in high temperature gauge theories. 1. Leading log results*, *JHEP* **0011** (2000) 001, [hep-ph/0010177].

[102] P. B. Arnold, G. D. Moore and L. G. Yaffe, *Transport coefficients in high temperature gauge theories. 2. Beyond leading log*, *JHEP* **0305** (2003) 051, [hep-ph/0302165].

[103] A. Bazavov, T. Bhattacharya, M. Cheng, N. Christ, C. DeTar et al., *Equation of state and QCD transition at finite temperature*, *Phys. Rev.* **D80** (2009) 014504, [0903.4379].

[104] W. Reisdorf and H. Ritter, *Collective flow in heavy-ion collisions*, *Ann. Rev. Nucl. Part. Sci.* **47** (1997) 663–709.

[105] B. Mller, *Investigation of Hot QCD Matter: Theoretical Aspects*, *Phys. Scripta* **T158** (2013) 014004, [1309.7616].

[106] ATLAS collaboration, G. Aad et al., *Measurement of the azimuthal anisotropy for charged particle production in $\sqrt{s_{NN}} = 2.76$ TeV lead-lead collisions with the ATLAS detector*, *Phys. Rev.* **C86** (2012) 014907, [1203.3087].

[107] CMS collaboration, S. Chatrchyan et al., *Azimuthal anisotropy of charged particles at high transverse momenta in PbPb collisions at $\sqrt{s_{NN}} = 2.76$ TeV*, *Phys. Rev. Lett.* **109** (2012) 022301, [1204.1850].

[108] STAR collaboration, J. Adams et al., *Azimuthal anisotropy in Au+Au collisions at s(NN)**(1/2) = 200-GeV*, *Phys. Rev.* **C72** (2005) 014904, [nucl-ex/0409033].

[109] T. Hirano, U. W. Heinz, D. Kharzeev, R. Lacey and Y. Nara, *Hadronic dissipative effects on elliptic flow in ultrarelativistic heavy-ion collisions*, *Phys. Lett.* **B636** (2006) 299–304, [nucl-th/0511046].

[110] P. Huovinen, *Hydrodynamical description of collective flow. Chapter 1.*, *Quark gluon plasma* (2003) 600–633, [nucl-th/0305064].

[111] P. F. Kolb and U. W. Heinz, *Hydrodynamic description of ultrarelativistic heavy ion collisions*, *Quark gluon plasma* (2003) 634–714, [nucl-th/0305084].

[112] T. Hirano and M. Gyulassy, *Perfect fluidity of the quark gluon plasma core as seen through its dissipative hadronic corona*, *Nucl. Phys.* **A769** (2006) 71–94, [nucl-th/0506049].

[113] D. Teaney, *The Effects of viscosity on spectra, elliptic flow, and HBT radii*, *Phys. Rev.* **C68** (2003) 034913, [nucl-th/0301099].

[114] P. Kovtun, D. Son and A. Starinets, *Viscosity in strongly interacting quantum field theories from black hole physics*, *Phys. Rev. Lett.* **94** (2005) 111601, [hep-th/0405231].

[115] M. Luzum and P. Romatschke, *Conformal Relativistic Viscous Hydrodynamics: Applications to RHIC results at s(NN)**(1/2) = 200-GeV*, *Phys. Rev.* **C78** (2008) 034915, [0804.4015].

[116] STAR collaboration, B. Abelev et al., *Centrality dependence of charged hadron and strange hadron elliptic flow from s(NN)**(1/2) = 200-GeV Au + Au collisions*, *Phys. Rev.* **C77** (2008) 054901, [0801.3466].

[117] P. B. Arnold, G. D. Moore and L. G. Yaffe, *Transport coefficients in high temperature gauge theories. 1. Leading log results*, *JHEP* **0011** (2000) 001, [hep-ph/0010177].

[118] C. Gale, S. Jeon and B. Schenke, *Hydrodynamic Modeling of Heavy-Ion Collisions*, *Int. J. Mod. Phys.* **A28** (2013) 1340011, [1301.5893].

[119] T. Matsui and H. Satz, *J/ψ Suppression by Quark-Gluon Plasma Formation*, *Phys. Lett.* **B178** (1986) 416.

[120] P. Koch, B. Muller and J. Rafelski, *Strangeness in Relativistic Heavy Ion Collisions*, *Phys. Rept.* **142** (1986) 167–262.

[121] V. Greco, C. Ko and P. Levai, *Parton coalescence and anti-proton / pion anomaly at RHIC*, *Phys. Rev. Lett.* **90** (2003) 202302, [nucl-th/0301093].

[122] R. Fries, B. Muller, C. Nonaka and S. Bass, *Hadronization in heavy ion collisions: Recombination and fragmentation of partons*, *Phys. Rev. Lett.* **90** (2003) 202303, [nucl-th/0301087].

[123] A. Andronic, P. Braun-Munzinger and J. Stachel, *Hadron production in central nucleus-nucleus collisions at chemical freeze-out*, *Nucl. Phys.* **A772** (2006) 167–199, [nucl-th/0511071].

[124] D. Zschiesche, S. Schramm, J. Schaffner-Bielich, H. Stoecker and W. Greiner, *Particle ratios at RHIC: Effective hadron masses and chemical freezeout*, *Phys. Lett.* **B547** (2002) 7–14, [nucl-th/0209022].

[125] R. C. Hwa and C. Yang, *Scaling distributions of quarks, mesons and proton for all p(T), energy and centrality*, *Phys. Rev.* **C67** (2003) 064902, [nucl-th/0302006].

[126] D. Molnar and S. A. Voloshin, *Elliptic flow at large transverse momenta from quark coalescence*, *Phys. Rev. Lett.* **91** (2003) 092301, [nucl-th/0302014].

[127] STAR collaboration, J. Adams et al., *Particle type dependence of azimuthal anisotropy and nuclear modification of particle production in Au + Au collisions at s(NN)**(1/2) = 200-GeV*, *Phys. Rev. Lett.* **92** (2004) 052302, [nucl-ex/0306007].

[128] CTEQ collaboration, R. Brock et al., *Handbook of perturbative QCD: Version 1.0*, *Rev. Mod. Phys.* **67** (1995) 157–248.

[129] R. K. Ellis, W. J. Stirling and B. Webber, *QCD and collider physics*, *Camb. Monogr. Part. Phys. Nucl. Phys. Cosmol.* **8** (1996) 1–435.

[130] B. A. Kniehl, G. Kramer and B. Potter, *Fragmentation functions for pions, kaons, and protons at next-to-leading order*, *Nucl. Phys.* **B582** (2000) 514–536, [hep-ph/0010289].

[131] F. Cooper and G. Frye, *Comment on the Single Particle Distribution in the Hydrodynamic and Statistical Thermodynamic Models of Multiparticle Production*, *Phys. Rev.* **D10** (1974) 186.

[132] J. C. Collins, D. E. Soper and G. F. Sterman, *Factorization of Hard Processes in QCD*, *Adv. Ser. Direct. High Energy Phys.* **5** (1988) 1–91, [hep-ph/0409313].

[133] J. D. Bjorken, *Energy Loss of Energetic Partons in Quark - Gluon Plasma: Possible Extinction of High p(t) Jets in Hadron - Hadron Collisions*, *FERMILAB-PUB-82-059-THY* (1982) .

[134] M. Arneodo, *Nuclear effects in structure functions*, *Phys. Rept.* **240** (1994) 301–393.

[135] N. Armesto, *Nuclear shadowing*, *J. Phys.* **G32** (2006) R367–R394, [hep-ph/0604108].

[136] X.-N. Wang and M. Gyulassy, *Gluon shadowing and jet quenching in A + A collisions at s**(1/2) = 200-GeV*, *Phys. Rev. Lett.* **68** (1992) 1480–1483.

[137] S.-y. Li and X.-N. Wang, *Gluon shadowing and hadron production at RHIC*, *Phys. Lett.* **B527** (2002) 85–91, [nucl-th/0110075].

[138] M. Hirai, S. Kumano and M. Miyama, *Determination of nuclear parton distributions*, *Phys. Rev.* **D64** (2001) 034003, [hep-ph/0103208].

[139] K. Eskola, V. Kolhinen and P. Ruuskanen, *Scale evolution of nuclear parton distributions*, *Nucl. Phys.* **B535** (1998) 351–371, [hep-ph/9802350].

[140] BRAHMS collaboration, I. Arsene et al., *On the evolution of the nuclear modification factors with rapidity and centrality in d + Au collisions at s(NN)**(1/2) = 200-GeV*, *Phys. Rev. Lett.* **93** (2004) 242303, [nucl-ex/0403005].

[141] J. Cronin, H. J. Frisch, M. Shochet, J. Boymond, R. Mermod et al., *Production of Hadrons with Large Transverse Momentum at 200-GeV, 300-GeV, and 400-GeV*, *Phys. Rev.* **D11** (1975) 3105.

[142] M. Lev and B. Petersson, *Nuclear Effects at Large Transverse Momentum in a QCD Parton Model*, *Z. Phys.* **C21** (1983) 155.

[143] J. Gunion and G. Bertsch, *Hadronization by Color Bremsstrahlung*, *Phys. Rev.* **D25** (1982) 746.

[144] M. Gyulassy, I. Vitev, X.-N. Wang and B.-W. Zhang, *Jet quenching and radiative energy loss in dense nuclear matter*, *Quark gluon plasma* (2003) 123–191, [nucl-th/0302077].

[145] R. Baier, D. Schiff and B. Zakharov, *Energy loss in perturbative QCD*, *Ann. Rev. Nucl. Part. Sci.* **50** (2000) 37–69, [hep-ph/0002198].

[146] M. Cacciari, G. P. Salam and G. Soyez, *The Anti-k(t) jet clustering algorithm*, *JHEP* **04** (2008) 063, [0802.1189].

[147] STAR collaboration, J. Adams et al., *Transverse momentum and collision energy dependence of high p(T) hadron suppression in Au+Au collisions at ultrarelativistic energies*, *Phys. Rev. Lett.* **91** (2003) 172302, [nucl-ex/0305015].

[148] D. d'Enterria, *Jet quenching*, *Landolt-Bornstein* **23** (2010) 471, [0902.2011].

[149] PHENIX collaboration, A. Adare et al., *Suppression pattern of neutral pions at high transverse momentum in Au + Au collisions at s(NN)**(1/2) = 200-GeV and constraints on medium transport coefficients*, *Phys. Rev. Lett.* **101** (2008) 232301, [0801.4020].

[150] PHENIX collaboration, K. Adcox et al., *Suppression of hadrons with large transverse momentum in central Au+Au collisions at* $\sqrt{s_{NN}}$ *= 130-GeV*, *Phys. Rev. Lett.* **88** (2002) 022301, [nucl-ex/0109003].

[151] BRAHMS collaboration, I. Arsene et al., *Transverse momentum spectra in Au+Au and d+Au collisions at s**(1/2) = 200-GeV and the pseudorapidity dependence of high p(T) suppression*, *Phys. Rev. Lett.* **91** (2003) 072305, [nucl-ex/0307003].

[152] CMS collaboration, S. Chatrchyan et al., *Study of high-pT charged particle suppression in PbPb compared to pp collisions at* $\sqrt{s_{NN}} = 2.76$ *TeV*, *Eur. Phys. J.* **C72** (2012) 1945, [1202.2554].

[153] ALICE collaboration, K. Aamodt et al., *Suppression of Charged Particle Production at Large Transverse Momentum in Central Pb–Pb Collisions at* $\sqrt{s_{NN}} = 2.76$ *TeV*, *Phys. Lett.* **B696** (2011) 30–39, [1012.1004].

[154] PHENIX collaboration, S. Adler et al., *Nuclear modification of electron spectra and implications for heavy quark energy loss in Au+Au collisions at s(NN)**(1/2) - 200-GeV*, *Phys. Rev. Lett.* **96** (2006) 032301, [nucl-ex/0510047].

[155] M. H. Thoma, *Collisional energy loss of high-energy jets in the quark gluon plasma*, *Phys. Lett.* **B273** (1991) 128–132.

[156] M. G. Mustafa and M. H. Thoma, *Quenching of hadron spectra due to the collisional energy loss of partons in the quark gluon plasma*, *Acta Phys. Hung.* **A22** (2005) 93–102, [hep-ph/0311168].

[157] M. G. Mustafa, *Energy loss of charm quarks in the quark-gluon plasma: Collisional versus radiative*, *Phys. Rev.* **C72** (2005) 014905, [hep-ph/0412402].

[158] S. Wicks, *Fluctuations with small numbers: Developing the perturbative paradigm for jet physics in the QGP at RHIC and LHC*, *PhD Dissertation, Columbia University Academic Commons* (2008) .

[159] M. H. Thoma and M. Gyulassy, *Quark damping and energy loss in the high temperature QCD*, *Nucl. Phys.* **B351** (1991) 491–506.

[160] E. Braaten and M. H. Thoma, *Energy loss of a heavy fermion in a hot plasma*, *Phys. Rev.* **D44** (1991) 1298–1310.

[161] E. Braaten and M. H. Thoma, *Energy loss of a heavy quark in the quark - gluon plasma*, *Phys. Rev.* **D44** (1991) 2625–2630.

[162] S. Peigne and A. Peshier, *Collisional energy loss of a fast heavy quark in a quark-gluon plasma*, *Phys. Rev.* **D77** (2008) 114017, [0802.4364].

[163] A. Peshier, *Running coupling and screening in the (s)QGP*, *arXiv: hep-ph* (2006) , [hep-ph/0601119].

[164] M. Djordjevic and U. Heinz, *Radiative heavy quark energy loss in a dynamical QCD medium*, *Phys. Rev.* **C77** (2008) 024905, [0705.3439].

[165] Y. L. Dokshitzer and D. Kharzeev, *Heavy quark colorimetry of QCD matter*, *Phys. Lett.* **B519** (2001) 199–206, [hep-ph/0106202].

[166] M. Gyulassy and X.-N. Wang, *Multiple collisions and induced gluon Bremsstrahlung in QCD*, *Nucl. Phys.* **B420** (1994) 583–614, [nucl-th/9306003].

[167] X.-N. Wang, M. Gyulassy and M. Plumer, *The LPM effect in QCD and radiative energy loss in a quark gluon plasma*, *Phys. Rev.* **D51** (1995) 3436–3446, [hep-ph/9408344].

[168] A. Ficnar, *Holographic jet quenching*, *PhD Dissertation, Columbia University Academic Commons* (2014) .

[169] H. Bethe and W. Heitler, *On the Stopping of fast particles and on the creation of positive electrons*, *Proc. Roy. Soc. Lond.* **A146** (1934) 83–112.

[170] M. Djordjevic and M. Gyulassy, *Heavy quark radiative energy loss in QCD matter*, *Nucl. Phys.* **A733** (2004) 265–298, [nucl-th/0310076].

[171] N. Armesto, B. Cole, C. Gale, W. A. Horowitz, P. Jacobs et al., *Comparison of Jet Quenching Formalisms for a Quark-Gluon Plasma 'Brick'*, *Phys. Rev.* **C86** (2012) 064904, [1106.1106].

[172] A. Majumder and M. Van Leeuwen, *The Theory and Phenomenology of Perturbative QCD Based Jet Quenching*, *Prog. Part. Nucl. Phys.* **A66** (2011) 41–92, [1002.2206].

[173] S. A. Bass, C. Gale, A. Majumder, C. Nonaka, G.-Y. Qin et al., *Systematic Comparison of Jet Energy-Loss Schemes in a realistic hydrodynamic medium*, *Phys. Rev.* **C79** (2009) 024901, [0808.0908].

[174] R. Baier, Y. L. Dokshitzer, S. Peigne and D. Schiff, *Induced gluon radiation in a QCD medium*, *Phys. Lett.* **B345** (1995) 277–286, [hep-ph/9411409].

[175] R. Baier, Y. L. Dokshitzer, A. H. Mueller, S. Peigne and D. Schiff, *Radiative energy loss of high-energy quarks and gluons in a finite volume quark - gluon plasma*, *Nucl. Phys.* **B483** (1997) 291–320, [hep-ph/9607355].

[176] R. Baier, Y. L. Dokshitzer, A. H. Mueller, S. Peigne and D. Schiff, *Radiative energy loss and p(T) broadening of high-energy partons in nuclei*, *Nucl. Phys.* **B484** (1997) 265–282, [hep-ph/9608322].

[177] R. Baier, Y. L. Dokshitzer, A. H. Mueller and D. Schiff, *Radiative energy loss of high-energy partons traversing an expanding QCD plasma*, *Phys. Rev.* **C58** (1998) 1706–1713, [hep-ph/9803473].

[178] R. Baier, Y. L. Dokshitzer, A. H. Mueller and D. Schiff, *Quenching of hadron spectra in media*, *JHEP* **0109** (2001) 033, [hep-ph/0106347].

[179] B. Zakharov, *Fully quantum treatment of the Landau-Pomeranchuk-Migdal effect in QED and QCD*, *JETP Lett.* **63** (1996) 952–957, [hep-ph/9607440].

[180] B. Zakharov, *Radiative energy loss of high-energy quarks in finite size nuclear matter and quark - gluon plasma*, *JETP Lett.* **65** (1997) 615–620, [hep-ph/9704255].

[181] B. Zakharov, *Light cone path integral approach to the Landau-Pomeranchuk-Migdal effect*, *Phys. Atom. Nucl.* **61** (1998) 838–854, [hep-ph/9807540].

[182] B. Zakharov, *Transverse spectra of radiation processes in-medium*, *JETP Lett.* **70** (1999) 176–182, [hep-ph/9906536].

[183] R. Baier, Y. L. Dokshitzer, A. H. Mueller and D. Schiff, *Medium induced radiative energy loss: Equivalence between the BDMPS and Zakharov formalisms*, *Nucl. Phys.* **B531** (1998) 403–425, [hep-ph/9804212].

[184] B. Zakharov, *Transverse spectra of radiation processes in-medium*, *JETP Lett.* **70** (1999) 176–182, [hep-ph/9906536].

[185] N. Armesto, C. A. Salgado and U. A. Wiedemann, *Medium induced gluon radiation off massive quarks fills the dead cone*, *Phys. Rev.* **D69** (2004) 114003, [hep-ph/0312106].

[186] U. A. Wiedemann, *Gluon radiation off hard quarks in a nuclear environment: Opacity expansion*, *Nucl. Phys.* **B588** (2000) 303–344, [hep-ph/0005129].

[187] N. Armesto, C. A. Salgado and U. A. Wiedemann, *Measuring the collective flow with jets*, *Phys. Rev. Lett.* **93** (2004) 242301, [hep-ph/0405301].

[188] N. Armesto, A. Dainese, C. A. Salgado and U. A. Wiedemann, *Testing the color charge and mass dependence of parton energy loss with heavy-to-light ratios at RHIC and CERN LHC*, *Phys. Rev.* **D71** (2005) 054027, [hep-ph/0501225].

[189] X.-N. Wang and X.-F. Guo, *Multiple parton scattering in nuclei: Parton energy loss*, *Nucl. Phys.* **A696** (2001) 788–832, [hep-ph/0102230].

[190] X.-F. Guo and X.-N. Wang, *Multiple scattering, parton energy loss and modified fragmentation functions in deeply inelastic e A scattering*, *Phys. Rev. Lett.* **85** (2000) 3591–3594, [hep-ph/0005044].

[191] X.-N. Wang, *Dynamical screening and radiative parton energy loss in a quark gluon plasma*, *Phys. Lett.* **B485** (2000) 157–161, [nucl-th/0003033].

[192] E. Wang and X.-N. Wang, *Parton energy loss with detailed balance*, *Phys. Rev. Lett.* **87** (2001) 142301, [nucl-th/0106043].

[193] B.-W. Zhang, E. Wang and X.-N. Wang, *Heavy quark energy loss in nuclear medium*, *Phys. Rev. Lett.* **93** (2004) 072301, [nucl-th/0309040].

[194] P. B. Arnold, G. D. Moore and L. G. Yaffe, *Photon and gluon emission in relativistic plasmas*, *JHEP* **0206** (2002) 030, [hep-ph/0204343].

[195] P. B. Arnold, G. D. Moore and L. G. Yaffe, *Effective kinetic theory for high temperature gauge theories*, *JHEP* **0301** (2003) 030, [hep-ph/0209353].

[196] S. Jeon and G. D. Moore, *Energy loss of leading partons in a thermal QCD medium*, *Phys. Rev.* **C71** (2005) 034901, [hep-ph/0309332].

[197] S. Turbide, C. Gale, S. Jeon and G. D. Moore, *Energy loss of leading hadrons and direct photon production in evolving quark-gluon plasma*, *Phys. Rev.* **C72** (2005) 014906, [hep-ph/0502248].

[198] G.-Y. Qin, J. Ruppert, S. Turbide, C. Gale, C. Nonaka et al., *Radiative jet energy loss in a three-dimensional hydrodynamical medium and high pT azimuthal asymmetry of pi0 suppression at mid and forward rapidity in Au+Au collisions at sNN=200 GeV*, *Phys. Rev.* **C76** (2007) 064907, [0705.2575].

[199] G.-Y. Qin, J. Ruppert, C. Gale, S. Jeon, G. D. Moore et al., *Radiative and collisional jet energy loss in the quark-gluon plasma at RHIC*, *Phys. Rev. Lett.* **100** (2008) 072301, [0710.0605].

[200] R. D. Pisarski, *Scattering Amplitudes in Hot Gauge Theories*, *Phys. Rev. Lett.* **63** (1989) 1129.

[201] E. Braaten and R. D. Pisarski, *Resummation and Gauge Invariance of the Gluon Damping Rate in Hot QCD*, *Phys. Rev. Lett.* **64** (1990) 1338.

[202] E. Braaten and R. D. Pisarski, *Soft Amplitudes in Hot Gauge Theories: A General Analysis*, *Nucl. Phys.* **B337** (1990) 569.

[203] E. Braaten and R. D. Pisarski, *Calculation of the gluon damping rate in hot QCD*, *Phys. Rev.* **D42** (1990) 2156–2160.

[204] E. Braaten and R. D. Pisarski, *Deducing Hard Thermal Loops From Ward Identities*, *Nucl. Phys.* **B339** (1990) 310–324.

[205] E. Braaten and R. D. Pisarski, *Simple effective Lagrangian for hard thermal loops*, *Phys. Rev.* **D45** (1992) 1827–1830.

[206] M. Gyulassy, P. Levai and I. Vitev, *Jet quenching in thin quark gluon plasmas. 1. Formalism*, *Nucl. Phys.* **B571** (2000) 197–233, [hep-ph/9907461].

[207] M. Gyulassy, P. Levai and I. Vitev, *Reaction operator approach to nonAbelian energy loss*, *Nucl. Phys.* **B594** (2001) 371–419, [nucl-th/0006010].

[208] M. Gyulassy, P. Levai and I. Vitev, *NonAbelian energy loss at finite opacity*, *Phys. Rev. Lett.* **85** (2000) 5535–5538, [nucl-th/0005032].

[209] M. Gyulassy, I. Vitev and X. Wang, *High p(T) azimuthal asymmetry in noncentral A+A at RHIC*, *Phys. Rev. Lett.* **86** (2001) 2537–2540, [nucl-th/0012092].

[210] M. Gyulassy, P. Levai and I. Vitev, *Reaction operator approach to multiple elastic scatterings*, *Phys. Rev.* **D66** (2002) 014005, [nucl-th/0201078].

[211] M. Djordjevic and M. Gyulassy, *The Ter-Mikayelian effect on QCD radiative energy loss*, *Phys. Rev.* **C68** (2003) 034914, [nucl-th/0305062].

[212] S. Wicks, W. Horowitz, M. Djordjevic and M. Gyulassy, *Elastic, inelastic, and path length fluctuations in tomography*, *Nucl. Phys.* **A784** (2007) 426–442, [nucl-th/0512076].

[213] M. Gyulassy, P. Levai and I. Vitev, *Jet tomography of Au+Au reactions including multigluon fluctuations*, *Phys. Lett.* **B538** (2002) 282–288, [nucl-th/0112071].

[214] P. B. Arnold, *Simple Formula for High-Energy Gluon Bremsstrahlung in a Finite, Expanding Medium*, *Phys. Rev.* **D79** (2009) 065025, [0808.2767].

[215] A. Buzzatti, *Jet quenching in quark gluon plasma: flavor tomography at rhic and lhc by the cujet model*, *PhD Dissertation, Columbia University Academic Commons* (2013) .

[216] J. Xu, A. Buzzatti and M. Gyulassy, *Azimuthal jet flavor tomography with CUJET2.0 of nuclear collisions at RHIC and LHC*, *JHEP* **1408** (2014) 063, [1402.2956].

[217] B. Betz, M. Gyulassy and G. Torrieri, *Fourier Harmonics of High-pT Particles Probing the Fluctuating Intitial Condition Geometries in Heavy-Ion Collisions*, *Phys. Rev.* **C84** (2011) 024913, [1102.5416].

[218] B. Betz and M. Gyulassy, *Examining a reduced jet-medium coupling in Pb+Pb collisions at the Large Hadron Collider*, *Phys. Rev.* **C86** (2012) 024903, [1201.0281].

[219] M. Djordjevic and U. W. Heinz, *Radiative energy loss in a finite dynamical QCD medium*, *Phys. Rev. Lett.* **101** (2008) 022302, [0802.1230].

[220] M. Djordjevic, *Theoretical formalism of radiative jet energy loss in a finite size dynamical QCD medium*, *Phys. Rev.* **C80** (2009) 064909, [0903.4591].

[221] A. Buzzatti and M. Gyulassy, *Jet Flavor Tomography of Quark Gluon Plasmas at RHIC and LHC*, *Phys. Rev. Lett.* **108** (2012) 022301, [1106.3061].

[222] A. Buzzatti and M. Gyulassy, *Dynamical magnetic enhancement of light and heavy quark jet quenching at RHIC*, *Nucl. Phys.* **A855** (2011) 307–310, [1012.0614].

[223] A. Buzzatti and M. Gyulassy, *A running coupling explanation of the surprising transparency of the QGP at LHC*, *Nucl. Phys.* **A904-905** (2013) 779c–782c, [1210.6417].

[224] W. Horowitz and M. Gyulassy, *The Surprising Transparency of the sQGP at LHC*, *Nucl. Phys.* **A872** (2011) 265–285, [1104.4958].

[225] B. Betz and M. Gyulassy, *Sensitivity of Pion versus Parton-Jet Nuclear Modification Factors to the Path-Length Dependence of Jet-Energy Loss at RHIC and LHC*, *Chin. Phys. Lett.* **32** (2015) 121204, [1503.07671].

[226] Wikipedia, "Tomography — Wikipedia, the free encyclopedia." https://en.wikipedia.org/wiki/Tomography, 2015.

[227] "X-ray imaging and computed tomography." http://media.wiley.com/product_data/excerpt/63/04712376/0471237663.pdf.

[228] "Topical Collaboration on Jet and Electromagnetic Tomography of Extreme Phases of Matter in Heavy-ion Collisions." http://jet.lbl.gov/.

[229] "The ALICE Collaboration." http://alice-collaboration.web.cern.ch/.

[230] J. C. Collins, *Light cone variables, rapidity and all that*, hep-ph/9705393.

[231] J. Xu, A. Buzzatti and M. Gyulassy, *The tricky azimuthal dependence of jet quenching at RHIC and LHC via CUJET2.0*, *Nucl. Phys.* **A932** (2014) 128–133, [1404.0384].

[232] J. Xu, J. Liao and M. Gyulassy, *Consistency of Perfect Fluidity and Jet Quenching in semi-Quark-Gluon Monopole Plasmas*, *Chin. Phys. Lett.* **32** (2015) 092501, [1411.3673].

[233] J. Xu, J. Liao and M. Gyulassy, *Bridging Soft-Hard Transport Properties of Quark-Gluon Plasmas with CUJET3.0*, *arXiv: hep-ph* (2015) , [1508.00552].

[234] H. Liu, K. Rajagopal and U. A. Wiedemann, *Wilson loops in heavy ion collisions and their calculation in AdS/CFT*, *JHEP* **0703** (2007) 066, [hep-ph/0612168].

[235] R. Baier, A. H. Mueller and D. Schiff, *How does transverse (hydrodynamic) flow affect jet-broadening and jet-quenching?*, *Phys. Lett.* **B649** (2007) 147–151, [nucl-th/0612068].

[236] B. Zakharov, *Jet quenching with running coupling including radiative and collisional energy losses*, *JETP Lett.* **88** (2008) 781–786, [0811.0445].

[237] B. Zakharov, *Parton energy loss in an expanding quark-gluon plasma: Radiative versus collisional*, *JETP Lett.* **86** (2007) 444–450, [0708.0816].

[238] C. Shen, Z. Qiu, H. Song, J. Bernhard, S. Bass and U. Heinz, *The iEBE-VISHNU code package for relativistic heavy-ion collisions*, *Comput. Phys. Commun.* **199** (2016) 61–85, [1409.8164].

[239] C. Gale, S. Jeon, B. Schenke, P. Tribedy and R. Venugopalan, *Event-by-event anisotropic flow in heavy-ion collisions from combined Yang-Mills and viscous fluid dynamics*, *Phys. Rev. Lett.* **110** (2013) 012302, [1209.6330].

[240] T. Hirano and K. Tsuda, *Collective flow and two pion correlations from a relativistic hydrodynamic model with early chemical freezeout*, *Phys. Rev.* **C66** (2002) 054905, [nucl-th/0205043].

[241] H. Song and U. W. Heinz, *Causal viscous hydrodynamics in 2+1 dimensions for relativistic heavy-ion collisions*, *Phys. Rev.* **C77** (2008) 064901, [0712.3715].

[242] B. Schenke, S. Jeon and C. Gale, *Elliptic and triangular flow in event-by-event (3+1)D viscous hydrodynamics*, *Phys. Rev. Lett.* **106** (2011) 042301, [1009.3244].

[243] S. Ryu, J. F. Paquet, C. Shen, G. S. Denicol, B. Schenke, S. Jeon et al., *Importance of the Bulk Viscosity of QCD in Ultrarelativistic Heavy-Ion Collisions*, *Phys. Rev. Lett.* **115** (2015) 132301, [1502.01675].

[244] H. Song and U. W. Heinz, *Multiplicity scaling in ideal and viscous hydrodynamics*, *Phys. Rev.* **C78** (2008) 024902, [0805.1756].

[245] P. Huovinen and P. Petreczky, *QCD Equation of State and Hadron Resonance Gas*, *Nucl. Phys.* **A837** (2010) 26–53, [0912.2541].

[246] T. Renk, H. Holopainen, U. Heinz and C. Shen, *A Systematic comparison of jet quenching in different fluid-dynamical models*, *Phys. Rev.* **C83** (2011) 014910, [1010.1635].

[247] W. Israel and J. M. Stewart, *Transient relativistic thermodynamics and kinetic theory*, *Annals Phys.* **118** (1979) 341–372.

[248] C. Shen, U. Heinz, P. Huovinen and H. Song, *Systematic parameter study of hadron spectra and elliptic flow from viscous hydrodynamic simulations of Au+Au collisions at* $\sqrt{s_{NN}} = 200$ *GeV*, *Phys. Rev.* **C82** (2010) 054904, [1010.1856].

[249] X.-N. Wang, *Private communication* (2013) .

[250] M. L. Mangano, P. Nason and G. Ridolfi, *Heavy quark correlations in hadron collisions at next-to-leading order*, *Nucl. Phys.* **B373** (1992) 295–345.

[251] M. Cacciari, M. Greco and P. Nason, *The P(T) spectrum in heavy flavor hadroproduction*, *JHEP* **9805** (1998) 007, [hep-ph/9803400].

[252] M. Cacciari, S. Frixione and P. Nason, *The p(T) spectrum in heavy flavor photoproduction*, *JHEP* **0103** (2001) 006, [hep-ph/0102134].

[253] P. Nason, S. Dawson and R. K. Ellis, *The Total Cross-Section for the Production of Heavy Quarks in Hadronic Collisions*, *Nucl. Phys.* **B303** (1988) 607.

[254] P. Nason, S. Dawson and R. K. Ellis, *The One Particle Inclusive Differential Cross-Section for Heavy Quark Production in Hadronic Collisions*, *Nucl. Phys.* **B327** (1989) 49–92.

[255] W. Beenakker, W. van Neerven, R. Meng, G. Schuler and J. Smith, *QCD corrections to heavy quark production in hadron hadron collisions*, *Nucl. Phys.* **B351** (1991) 507–560.

[256] M. Cacciari and M. Greco, *Large p_T hadroproduction of heavy quarks*, *Nucl. Phys.* **B421** (1994) 530–544, [hep-ph/9311260].

[257] A. Adil and I. Vitev, *Collisional dissociation of heavy mesons in dense QCD matter*, *Phys. Lett.* **B649** (2007) 139–146, [hep-ph/0611109].

[258] I. Vitev, A. Adil and H. van Hees, *Novel heavy flavor suppression mechanisms in the QGP*, *J. Phys.* **G34** (2007) S769–774, [hep-ph/0701188].

[259] C.-Y. Wong, *Heavy quarkonia in quark-gluon plasma*, *Phys. Rev.* **C72** (2005) 034906, [hep-ph/0408020].

[260] RBC-Bielefeld collaboration, P. Petreczky, P. Hegde and A. Velytsky, *Quark number fluctuations at high temperatures*, *PoS* **LAT2009** (2009) 159, [0911.0196].

[261] C. Peterson, D. Schlatter, I. Schmitt and P. M. Zerwas, *Scaling Violations in Inclusive e+ e- Annihilation Spectra*, *Phys. Rev.* **D27** (1983) 105.

[262] M. Djordjevic, M. Gyulassy, R. Vogt and S. Wicks, *Influence of bottom quark jet quenching on single electron tomography of Au + Au*, *Phys. Lett.* **B632** (2006) 81–86, [nucl-th/0507019].

[263] M. Cacciari, P. Nason and R. Vogt, *QCD predictions for charm and bottom production at RHIC*, *Phys. Rev. Lett.* **95** (2005) 122001, [hep-ph/0502203].

[264] H. Song, S. A. Bass, U. Heinz, T. Hirano and C. Shen, *200 A GeV Au+Au collisions serve a nearly perfect quark-gluon liquid*, *Phys. Rev. Lett.* **106** (2011) 192301, [1011.2783].

[265] A. Majumder and C. Shen, *Suppression of the High p_T Charged Hadron R_{AA} at the LHC*, *Phys. Rev. Lett.* **109** (2012) 202301, [1103.0809].

[266] Z. Qiu, C. Shen and U. Heinz, *Hydrodynamic elliptic and triangular flow in Pb-Pb collisions at $\sqrt{s} = 2.76 ATeV$*, *Phys. Lett.* **B707** (2012) 151–155, [1110.3033].

[267] C. Shen, U. Heinz, P. Huovinen and H. Song, *Radial and elliptic flow in Pb+Pb collisions at the Large Hadron Collider from viscous hydrodynamic*, *Phys. Rev.* **C84** (2011) 044903, [1105.3226].

[268] C. Shen and U. Heinz, *Collision Energy Dependence of Viscous Hydrodynamic Flow in Relativistic Heavy-Ion Collisions*, *Phys. Rev.* **C85** (2012) 054902, [1202.6620].

[269] PHENIX collaboration, A. Adare et al., *Heavy Quark Production in $p+p$ and Energy Loss and Flow of Heavy Quarks in Au+Au Collisions at $\sqrt{s_N N} = 200$ GeV*, *Phys. Rev.* **C84** (2011) 044905, [1005.1627].

[270] STAR collaboration, B. Abelev et al., *Erratum: Transverse momentum and centrality dependence of high-p(T) non-photonic electron suppression in Au+Au collisions at $\sqrt{s_{NN}} = 200$ GeV*, *Phys. Rev. Lett.* **98** (2007) 192301, [nucl-ex/0607012].

[271] ALICE collaboration, B. Abelev et al., *Suppression of high transverse momentum D mesons in central Pb-Pb collisions at $\sqrt{s_{NN}} = 2.76$ TeV*, *JHEP* **1209** (2012) 112, [1203.2160].

[272] PHENIX collaboration, A. Adare et al., *Neutral pion production with respect to centrality and reaction plane in Au+Au collisions at $\sqrt{s_{NN}}$=200 GeV*, *Phys. Rev.* **C87** (2013) 034911, [1208.2254].

[273] STAR collaboration, B. Abelev et al., *Neutral Pion Production in Au+Au Collisions at s(NN)**(1/2) = 200-GeV*, *Phys. Rev.* **C80** (2009) 044905, [0907.2721].

[274] ALICE collaboration, B. Abelev et al., *Centrality Dependence of Charged Particle Production at Large Transverse Momentum in Pb–Pb Collisions at* $\sqrt{s_{\rm NN}} = 2.76$ *TeV*, *Phys. Lett.* **B720** (2013) 52–62, [1208.2711].

[275] A. Nakamura, T. Saito and S. Sakai, *Lattice calculation of gluon screening masses*, *Phys. Rev.* **D69** (2004) 014506, [hep-lat/0311024].

[276] JET collaboration, K. M. Burke et al., *Extracting the jet transport coefficient from jet quenching in high-energy heavy-ion collisions*, *Phys. Rev.* **C90** (2014) 014909, [1312.5003].

[277] W.-T. Deng and X.-N. Wang, *Multiple Parton Scattering in Nuclei: Modified DGLAP Evolution for Fragmentation Functions*, *Phys. Rev.* **C81** (2010) 024902, [0910.3403].

[278] A. Majumder, *Calculating the jet quenching parameter q in lattice gauge theory*, *Phys. Rev.* **C87** (2013) 034905, [1202.5295].

[279] M. Panero, K. Rummukainen and A. Schfer, *Lattice Study of the Jet Quenching Parameter*, *Phys. Rev. Lett.* **112** (2014) 162001, [1307.5850].

[280] S. Caron-Huot, *O(g) plasma effects in jet quenching*, *Phys. Rev.* **D79** (2009) 065039, [0811.1603].

[281] H. Liu, K. Rajagopal and U. A. Wiedemann, *Calculating the jet quenching parameter from AdS/CFT*, *Phys. Rev. Lett.* **97** (2006) 182301, [hep-ph/0605178].

[282] A. Majumder, B. Muller and X.-N. Wang, *Small shear viscosity of a quark-gluon plasma implies strong jet quenching*, *Phys. Rev. Lett.* **99** (2007) 192301, [hep-ph/0703082].

[283] T. Liou, A. Mueller and B. Wu, *Radiative* $p_\perp$*-broadening of high-energy quarks and gluons in QCD matter*, *Nucl. Phys.* **A916** (2013) 102–125, [1304.7677].

[284] J.-P. Blaizot, F. Dominguez, E. Iancu and Y. Mehtar-Tani, *Probabilistic picture for medium-induced jet evolution*, *JHEP* **06** (2014) 075, [1311.5823].

[285] Z.-B. Kang, E. Wang, X.-N. Wang and H. Xing, *Next-to-Leading QCD Factorization for Semi-Inclusive Deep Inelastic Scattering at Twist-4*, *Phys. Rev. Lett.* **112** (2014) 102001, [1310.6759].

[286] E. Iancu, *The non-linear evolution of jet quenching*, *JHEP* **1410** (2014) 95, [1403.1996].

[287] J.-P. Blaizot and Y. Mehtar-Tani, *Renormalization of the jet-quenching parameter*, *Nucl. Phys.* **A929** (2014) 202–229, [1403.2323].

[288] W. A. Horowitz, *Large observed v(2) as a signature for deconfinement*, *Acta Phys. Hung.* **A27** (2006) 221–225, [nucl-th/0511052].

[289] ALICE collaboration, B. B. Abelev et al., *Azimuthal anisotropy of D meson production in Pb-Pb collisions at* $\sqrt{s_{\rm NN}} = 2.76$ *TeV*, *Phys. Rev.* **C90** (2014) 034904, [1405.2001].

[290] S. Voloshin and Y. Zhang, *Flow study in relativistic nuclear collisions by Fourier expansion of Azimuthal particle distributions*, *Z. Phys.* **C70** (1996) 665–672, [hep-ph/9407282].

[291] B. Betz and M. Gyulassy, *Constraints on the Path-Length Dependence of Jet Quenching in Nuclear Collisions at RHIC and LHC*, *JHEP* **1408** (2014) 090, [1404.6378].

[292] ALICE collaboration, B. Abelev et al., *Anisotropic flow of charged hadrons, pions and (anti-)protons measured at high transverse momentum in Pb-Pb collisions at* $\sqrt{s_{NN}}$*=2.76 TeV*, *Phys. Lett.* **B719** (2013) 18–28, [1205.5761].

[293] ATLAS collaboration, G. Aad et al., *Measurement of the pseudorapidity and transverse momentum dependence of the elliptic flow of charged particles in lead-lead collisions at* $\sqrt{s_{NN}} = 2.76$ *TeV with the ATLAS detector*, *Phys. Lett.* **B707** (2012) 330–348, [1108.6018].

[294] PHENIX collaboration, A. Adare et al., *Azimuthal anisotropy of neutral pion production in Au+Au collisions at* $\sqrt{(s_N N)} = 200$ *GeV: Path-length dependence of jet quenching and the role of initial geometry*, *Phys. Rev. Lett.* **105** (2010) 142301, [1006.3740].

[295] J. Liao and E. Shuryak, *Angular Dependence of Jet Quenching Indicates Its Strong Enhancement Near the QCD Phase Transition*, *Phys. Rev. Lett.* **102** (2009) 202302, [0810.4116].

[296] J. Liao and E. Shuryak, *Magnetic Component of Quark-Gluon Plasma is also a Liquid!*, *Phys. Rev. Lett.* **101** (2008) 162302, [0804.0255].

[297] J. Liao and E. Shuryak, *Strongly coupled plasma with electric and magnetic charges*, *Phys. Rev.* **C75** (2007) 054907, [hep-ph/0611131].

[298] P. A. Dirac, *Quantized Singularities in the Electromagnetic Field*, *Proc. Roy. Soc. Lond.* **A133** (1931) 60–72.

[299] J. Liao, *Magnetic component of strongly coupled quark-gluon plasma*, *PhD Dissertation, Stony Brook University* (2008) .

[300] G. 't Hooft, *Topology of the Gauge Condition and New Confinement Phases in Nonabelian Gauge Theories*, *Nucl. Phys.* **B190** (1981) 455.

[301] S. Mandelstam, *Vortices and Quark Confinement in Nonabelian Gauge Theories*, *Phys. Rept.* **23** (1976) 245–249.

[302] N. Seiberg, *Exact results on the space of vacua of four-dimensional SUSY gauge theories*, *Phys. Rev.* **D49** (1994) 6857–6863, [hep-th/9402044].

[303] N. Seiberg and E. Witten, *Monopoles, duality and chiral symmetry breaking in N=2 supersymmetric QCD*, *Nucl. Phys.* **B431** (1994) 484–550, [hep-th/9408099].

[304] N. Seiberg and E. Witten, *Electric - magnetic duality, monopole condensation, and confinement in N=2 supersymmetric Yang-Mills theory*, *Nucl. Phys.* **B426** (1994) 19–52, [hep-th/9407087].

[305] G. S. Bali, *QCD forces and heavy quark bound states*, *Phys. Rept.* **343** (2001) 1–136, [hep-ph/0001312].

[306] A. Bazavov and P. Petreczky, *Static meson correlators in 2+1 flavor QCD at non-zero temperature*, *Eur. Phys. J.* **A49** (2013) 85, [1303.5500].

[307] A. M. Polyakov, *Thermal Properties of Gauge Fields and Quark Liberation*, *Phys. Lett.* **B72** (1978) 477–480.

[308] O. Kaczmarek and F. Zantow, *Static quark anti-quark free and internal energy in 2-flavor QCD and bound states in the QGP*, *PoS* **LAT2005** (2006) 192, [hep-lat/0510094].

[309] J. Liao and E. V. Shuryak, *Polymer chains and baryons in a strongly coupled quark-gluon plasma*, *Nucl. Phys.* **A775** (2006) 224–234, [hep-ph/0508035].

[310] E. V. Shuryak and I. Zahed, *Towards a theory of binary bound states in the quark gluon plasma*, *Phys. Rev.* **D70** (2004) 054507, [hep-ph/0403127].

[311] S. Datta, F. Karsch, P. Petreczky and I. Wetzorke, *Charmonium systems after the deconfinement transition*, *J. Phys.* **G30** (2004) S1347–S1350, [hep-lat/0403017].

[312] M. Asakawa and T. Hatsuda, *J / psi and eta(c) in the deconfined plasma from lattice QCD*, *Phys. Rev. Lett.* **92** (2004) 012001, [hep-lat/0308034].

[313] G. S. Bali, *The Mechanism of quark confinement*, in *Quark confinement and the hadron spectrum III. Proceedings, 3rd International Conference, Newport News, USA, June 7-12, 1998*, pp. 17–36, 1998. hep-ph/9809351.

[314] Y. Koma, M. Koma, E.-M. Ilgenfritz, T. Suzuki and M. I. Polikarpov, *Duality of gauge field singularities and the structure of the flux tube in Abelian projected SU(2) gauge theory and the dual Abelian Higgs model*, *Phys. Rev.* **D68** (2003) 094018, [hep-lat/0302006].

[315] M. Baker, J. S. Ball and F. Zachariasen, *Dual QCD: A Review*, *Phys. Rept.* **209** (1991) 73–127.

[316] E. V. Shuryak, *Quantum Chromodynamics and the Theory of Superdense Matter*, *Phys. Rept.* **61** (1980) 71–158.

[317] J. Liao and E. Shuryak, *Electric Flux Tube in Magnetic Plasma*, *Phys. Rev.* **C77** (2008) 064905, [0706.4465].

[318] C. P. Korthals Altes, *Magnetic monopoles in hot QCD*, in *Continuous advances in QCD. Proceedings, 7th Workshop, QCD 2006, Minneapolis, USA, May 11-14, 2006*, pp. 266–272, 2006. hep-ph/0607154.

[319] T. C. Kraan and P. van Baal, *Exact T duality between calorons and Taub - NUT spaces*, *Phys. Lett.* **B428** (1998) 268–276, [hep-th/9802049].

[320] K.-M. Lee and P. Yi, *Monopoles and instantons on partially compactified D-branes*, *Phys. Rev.* **D56** (1997) 3711–3717, [hep-th/9702107].

[321] C. Gattringer, E. M. Ilgenfritz and S. Solbrig, *Cooling, smearing and Dirac eigenmodes: A Comparison of filtering methods in lattice gauge theory*, in *Sense of Beauty in Physics: Miniconference in Honor of Adriano Di Giacomo on his 70th Birthday Pisa, Italy, January 26-27, 2006*, 2006.

[322] P. Gerhold, E. M. Ilgenfritz and M. Muller-Preussker, *An SU(2) KvBLL caloron gas model and confinement*, *Nucl. Phys.* **B760** (2007) 1–37, [hep-ph/0607315].

[323] R. D. Pisarski and L. G. Yaffe, *THE DENSITY OF INSTANTONS AT FINITE TEMPERATURE*, *Phys. Lett.* **B97** (1980) 110–112.

[324] E. Shuryak, *Gauge topology and confinement: an update*, *PoS* **CPOD2014** (2015) 044, [1502.06251].

[325] E. Poppitz and M. Unsal, *Seiberg-Witten and 'Polyakov-like' magnetic bion confinements are continuously connected*, *JHEP* **07** (2011) 082, [1105.3969].

[326] R. D. Pisarski, *Effective Theory of Wilson Lines and Deconfinement*, *Phys. Rev.* **D74** (2006) 121703, [hep-ph/0608242].

[327] Y. Hidaka and R. D. Pisarski, *Suppression of the Shear Viscosity in a "semi" Quark Gluon Plasma*, *Phys. Rev.* **D78** (2008) 071501, [0803.0453].

[328] Y. Hidaka and R. D. Pisarski, *Hard thermal loops, to quadratic order, in the background of a spatial 't Hooft loop*, *Phys. Rev.* **D80** (2009) 036004, [0906.1751].

[329] Y. Hidaka and R. D. Pisarski, *Small shear viscosity in the semi quark gluon plasma*, *Phys. Rev.* **D81** (2010) 076002, [0912.0940].

[330] D. Molnar and M. Gyulassy, *Saturation of elliptic flow and the transport opacity of the gluon plasma at RHIC*, *Nucl. Phys.* **A697** (2002) 495–520, [nucl-th/0104073].

[331] J. Noronha, M. Gyulassy and G. Torrieri, *Conformal Holography of Bulk Elliptic Flow and Heavy Quark Quenching in Relativistic Heavy Ion Collisions*, *Phys. Rev.* **C82** (2010) 054903, [1009.2286].

[332] D. Molnar and D. Sun, *High-pT suppression and elliptic flow from radiative energy loss with realistic bulk medium expansion*, *arXiv: nucl-th* (2013) , [1305.1046].

[333] A. Hosoya and K. Kajantie, *Transport Coefficients of QCD Matter*, *Nucl. Phys.* **B250** (1985) 666.

[334] P. Danielewicz and M. Gyulassy, *Dissipative Phenomena in Quark Gluon Plasmas*, *Phys. Rev.* **D31** (1985) 53–62.

[335] M. H. Thoma, *Viscosity coefficient of the quark - gluon plasma in the weak coupling limit*, *Phys. Lett.* **B269** (1991) 144–148.

[336] P. Kovtun, D. T. Son and A. O. Starinets, *Viscosity in strongly interacting quantum field theories from black hole physics*, *Phys. Rev. Lett.* **94** (2005) 111601, [hep-th/0405231].

[337] T. Lee, *The strongly interacting quark-gluon plasma and future physics*, *Nucl. Phys.* **A750** (2005) 1–8.

[338] E. V. Shuryak, *What RHIC experiments and theory tell us about properties of quark-gluon plasma?*, *Nucl. Phys.* **A750** (2005) 64–83, [hep-ph/0405066].

[339] E. V. Shuryak, *The Azimuthal asymmetry at large p(t) seem to be too large for a 'jet quenching'*, *Phys. Rev.* **C66** (2002) 027902, [nucl-th/0112042].

[340] A. M. Polyakov, *Quark Confinement and Topology of Gauge Groups*, *Nucl. Phys.* **B120** (1977) 429–458.

[341] J. Liao and E. Shuryak, *Static $\bar{Q}Q$ Potentials and the Magnetic Component of QCD Plasma near T_c*, *Phys. Rev.* **D82** (2010) 094007, [0804.4890].

[342] J. Liao and E. Shuryak, *Effect of Light Fermions on the Confinement Transition in QCD-like Theories*, *Phys. Rev. Lett.* **109** (2012) 152001, [1206.3989].

[343] C. Ratti and E. Shuryak, *The Role of monopoles in a Gluon Plasma*, *Phys. Rev.* **D80** (2009) 034004, [0811.4174].

[344] X. Zhang and J. Liao, *Hard probe of geometry and fluctuations in heavy ion collisions at sNN=0.2 , 2.76, and 5.5 TeV*, *Phys. Rev.* **C89** (2014) 014907, [1208.6361].

[345] X. Zhang and J. Liao, *Event-by-event azimuthal anisotropy of jet quenching in relativistic heavy ion collisions*, *Phys. Rev.* **C87** (2013) 044910, [1210.1245].

[346] X. Zhang and J. Liao, *Jet Quenching and Its Azimuthal Anisotropy in AA and possibly High Multiplicity pA and dA Collisions*, *arXiv: nucl-th* (2013) , [1311.5463].

[347] S. Borsanyi, Z. Fodor, C. Hoelbling, S. D. Katz, S. Krieg et al., *Full result for the QCD equation of state with 2+1 flavors*, *Phys. Lett.* **B730** (2014) 99–104, [1309.5258].

[348] Wuppertal-Budapest collaboration, S. Borsanyi et al., *Is there still any Tc mystery in lattice QCD? Results with physical masses in the continuum limit III*, *JHEP* **1009** (2010) 073, [1005.3508].

[349] HotQCD collaboration, A. Bazavov et al., *Fluctuations and Correlations of net baryon number, electric charge, and strangeness: A comparison of lattice QCD results with the hadron resonance gas model*, *Phys. Rev.* **D86** (2012) 034509, [1203.0784].

[350] S. Borsanyi, Z. Fodor, S. D. Katz, S. Krieg, C. Ratti et al., *Fluctuations of conserved charges at finite temperature from lattice QCD*, *JHEP* **1201** (2012) 138, [1112.4416].

[351] S. Lin, R. D. Pisarski and V. V. Skokov, *Zero interface tension at the deconfining phase transition for a matrix model of a $SU(\infty)$ gauge theory*, *Phys. Rev.* **D87** (2013) 105002, [1301.7432].

[352] S. Lin, R. D. Pisarski and V. V. Skokov, *Collisional energy loss above the critical temperature in QCD*, *Phys. Lett.* **B730** (2014) 236–242, [1312.3340].

[353] C. Gale, Y. Hidaka, S. Jeon, S. Lin, J.-F. Paquet et al., *Production and Elliptic Flow of Dileptons and Photons in a Matrix Model of the Quark-Gluon Plasma*, *Phys. Rev. Lett.* **114** (2015) 072301, [1409.4778].

[354] Y. Hidaka, S. Lin, R. D. Pisarski and D. Satow, *Dilepton and photon production in the presence of a nontrivial Polyakov loop*, *JHEP* **10** (2015) 005, [1504.01770].

[355] M. N. Chernodub and V. I. Zakharov, *Magnetic component of Yang-Mills plasma*, *Phys. Rev. Lett.* **98** (2007) 082002, [hep-ph/0611228].

[356] B. G. Zakharov, *Radiative parton energy loss in an expanding quark-gluon plasma with magnetic monopoles*, *JETP Lett.* **101** (2015) 587–592, [1412.6287].

[357] Y. Jiang, X.-G. Huang and J. Liao, *Chiral vortical wave and induced flavor charge transport in a rotating quark-gluon plasma*, *Phys. Rev.* **D92** (2015) 071501, [1504.03201].

[358] M. Djordjevic and M. Djordjevic, *Generalization of radiative jet energy loss to non-zero magnetic mass*, *Phys. Lett.* **B709** (2012) 229–233, [1105.4359].

[359] A. Dumitru, Y. Guo, Y. Hidaka, C. P. K. Altes and R. D. Pisarski, *How Wide is the Transition to Deconfinement?*, *Phys. Rev.* **D83** (2011) 034022, [1011.3820].

[360] G. Ripka, *Dual superconductor models of color confinement*, *Lect. Notes Phys.* **639** (2004) 1, [hep-ph/0310102].

[361] K.-I. Kondo, S. Kato, A. Shibata and T. Shinohara, *Quark confinement: Dual superconductor picture based on a non-Abelian Stokes theorem and reformulations of YangMills theory*, *Phys. Rept.* **579** (2015) 1–226, [1409.1599].

[362] L. Randall, R. Rattazzi and E. V. Shuryak, *Implication of exact SUSY gauge couplings for QCD*, *Phys. Rev.* **D59** (1999) 035005, [hep-ph/9803258].

[363] L. D. McLerran, *A Chiral Symmetry Order Parameter, the Lattice and Nucleosynthesis*, *Phys. Rev.* **D36** (1987) 3291.

[364] S. A. Gottlieb, W. Liu, D. Toussaint, R. Renken and R. Sugar, *Fermion Number Susceptibility in Lattice Gauge Theory*, *Phys. Rev.* **D38** (1988) 2888–2896.

[365] R. Gavai, J. Potvin and S. Sanielevici, *Quark Number Susceptibility in Quenched Quantum Chromodynamics*, *Phys. Rev.* **D40** (1989) 2743.

[366] S. A. Gottlieb, W. Liu, D. Toussaint, R. Renken and R. Sugar, *The Quark Number Susceptibility of High Temperature QCD*, *Phys. Rev. Lett.* **59** (1987) 2247.

[367] J. Liao and E. V. Shuryak, *What do lattice baryonic susceptibilities tell us about quarks, diquarks and baryons at $T > T_c$?*, *Phys. Rev.* **D73** (2006) 014509, [hep-ph/0510110].

[368] K.-Y. Kim and J. Liao, *On the Baryonic Density and Susceptibilities in a Holographic Model of QCD*, *Nucl. Phys.* **B822** (2009) 201–218, [0906.2978].

[369] S. Shi and J. Liao, *Conserved Charge Fluctuations and Susceptibilities in Strongly Interacting Matter*, *JHEP* **06** (2013) 104, [1304.7752].

[370] N. Christiansen, M. Haas, J. M. Pawlowski and N. Strodthoff, *Transport Coefficients in Yang–Mills Theory and QCD*, *Phys. Rev. Lett.* **115** (2015) 112002, [1411.7986].

[371] CMS collaboration, C. Collaboration, *J/psi results from CMS in PbPb collisions, with 150mub-1 data*, *CMS-PAS-HIN-12-014* (2012) .

[372] R. Rapp and H. van Hees, *Heavy Quarks in the Quark-Gluon Plasma*, in *Quark Gluon Plasma 4, World Scientific, 111 (2010)*. 0903.1096.

[373] S. K. Das, F. Scardina, S. Plumari and V. Greco, *Toward a solution to the R_{AA} and v_2 puzzle for heavy quarks*, *Phys. Lett.* **B747** (2015) 260–264, [1502.03757].

[374] D. Li, J. Liao and M. Huang, *Enhancement of jet quenching around phase transition: result from the dynamical holographic model*, *Phys. Rev.* **D89** (2014) 126006, [1401.2035].

[375] R. Rougemont, A. Ficnar, S. Finazzo and J. Noronha, *Energy loss, equilibration, and thermodynamics of a baryon rich strongly coupled quark-gluon plasma*, *arXiv: hep-th* (2015) , [1507.06556].

[376] J. Noronha-Hostler, J. Noronha and C. Greiner, *Transport Coefficients of Hadronic Matter near T(c)*, *Phys. Rev. Lett.* **103** (2009) 172302, [0811.1571].

[377] H. Niemi, G. S. Denicol, P. Huovinen, E. Molnar and D. H. Rischke, *Influence of the shear viscosity of the quark-gluon plasma on elliptic flow in ultrarelativistic heavy-ion collisions*, *Phys. Rev. Lett.* **106** (2011) 212302, [1101.2442].

[378] J. Noronha-Hostler, J. Noronha and C. Greiner, *Hadron Mass Spectrum and the Shear Viscosity to Entropy Density Ratio of Hot Hadronic Matter*, *Phys. Rev.* **C86** (2012) 024913, [1206.5138].

[379] A. Kovner and U. A. Wiedemann, *Gluon radiation and parton energy loss*, *Quark gluon plasma* (2003) 192–248, [hep-ph/0304151].

[380] P. Jacobs and X.-N. Wang, *Matter in extremis: Ultrarelativistic nuclear collisions at RHIC*, *Prog. Part. Nucl. Phys.* **54** (2005) 443–534, [hep-ph/0405125].

[381] P. Boek and W. Broniowski, *Hydrodynamic approach to p-Pb*, *Nucl. Phys.* **A926** (2014) 16–23, [1401.2367].

[382] A. Bzdak, B. Schenke, P. Tribedy and R. Venugopalan, *Initial state geometry and the role of hydrodynamics in proton-proton, proton-nucleus and deuteron-nucleus collisions*, *Phys. Rev.* **C87** (2013) 064906, [1304.3403].

[383] K. Werner, B. Guiot, I. Karpenko and T. Pierog, *Analysing radial flow features in p-Pb and p-p collisions at several TeV by studying identified particle production in EPOS3*, *Phys. Rev.* **C89** (2014) 064903, [1312.1233].

[384] C. Shen, J. F. Paquet, G. S. Denicol, S. Jeon and C. Gale, *Thermal Photon Radiation in High Multiplicity p+Pb Collisions at the Large Hadron Collider*, *arXiv: nucl-th* (2015) , [1504.07989].

[385] R. Vogt, *Ultrarelativistic heavy-ion collisions*. Elsevier, 2007.

[386] P. Romatschke, *New Developments in Relativistic Viscous Hydrodynamics*, *Int. J. Mod. Phys.* **E19** (2010) 1–53, [0902.3663].

[387] M. L. Miller, K. Reygers, S. J. Sanders and P. Steinberg, *Glauber modeling in high energy nuclear collisions*, *Ann. Rev. Nucl. Part. Sci.* **57** (2007) 205–243, [nucl-ex/0701025].

[388] R. D. Woods and D. S. Saxon, *Diffuse Surface Optical Model for Nucleon-Nuclei Scattering*, *Phys. Rev.* **95** (1954) 577–578.

[389] W.-T. Deng, X.-N. Wang and R. Xu, *Hadron production in p+p, p+Pb, and Pb+Pb collisions with the HIJING 2.0 model at energies available at the CERN Large Hadron Collider*, *Phys. Rev.* **C83** (2011) 014915, [1008.1841].

[390] M. Gyulassy, I. Vitev, X.-N. Wang and P. Huovinen, *Transverse expansion and high p(T) azimuthal asymmetry at RHIC*, *Phys. Lett.* **B526** (2002) 301–308, [nucl-th/0109063].

[391] M. Luzum and P. Romatschke, *Viscous Hydrodynamic Predictions for Nuclear Collisions at the LHC*, *Phys. Rev. Lett.* **103** (2009) 262302, [0901.4588].

[392] G. Baym and D. Mermin, *Determination of Thermodynamic Green's Functions*, *J. Math. Phys.* **2** (1961) 232.

[393] R. Mills, *Propagators for Many-Particle Systems*. New York: Gordon and Breach, 1969.

[394] J.-P. Blaizot and E. Iancu, *The Quark gluon plasma: Collective dynamics and hard thermal loops*, *Phys. Rept.* **359** (2002) 355–528, [hep-ph/0101103].

Appendix A

Statistical mechanics & relativistic hydrodynamics

In this appendix some basic results from statistical physics that are useful in the course of this thesis will be derived. The basics of relativistic hydrodynamics will also be discussed.

A.1 Basic results from statistical physics

The massless ideal gas limit (StefanBoltzmann limit) for fermions and bosons is a useful reference of quark-gluon plasmas at high temperature. This section will be concentrated on deducing its energy and particle number density.

Denote by $n_\pm$ the particle number density of an ideal, massless, Bosonic $(-)$/Fermionic $(+)$ gas with degeneracy g, then

$$dn_\pm = g_\pm \frac{d^3k}{(2\pi)^3} f_\pm(k)\,, \tag{A.1}$$

where k is the particle momentum and $f_\pm(k)$ is the Bose-Einstein (BE, $-$) or Fermi-Dirac (FD, $+$) distribution,

$$f_\pm(k) = \frac{1}{e^{\beta k} \pm 1}\,, \tag{A.2}$$

where $\beta = 1/T$. The chemical potential is assumed to be zero implicitly. After integrations, one gets

$$n_{\rm BE} = g_- \frac{\zeta(3)}{\pi^2} T^3\,, \qquad n_{\rm FD} = g_+ \frac{3\zeta(3)}{4\pi^2} T^3\,, \tag{A.3}$$

where $\zeta(3) \approx 1.202$. The energy density is obtained from integrating $d\varepsilon = kdn$. One has

$$\varepsilon_{\rm BE} = g_- \frac{\pi^2}{30} T^4 \,, \qquad \varepsilon_{\rm FD} = g_+ \frac{7\pi^2}{240} T^4 \,. \tag{A.4}$$

As discussed in Section 1.1.2 and indicated by Eq. (1.14), for gluons, the degeneracy factor $g_- = 2(N_c^2 - 1) = 16$; while for quarks, $g_+ = 12N_f$. Therefore, for a quark-gluon plasma in StefanBoltzmann limit:

$$\begin{aligned} n_{\rm QGP} &= \frac{\zeta(3)}{\pi^2}(16 + 9N_f)T^3 \,, \\ \varepsilon_{\rm QGP} &= \frac{\pi^2}{30}(16 + 10.5N_f)T^4 \,. \end{aligned} \tag{A.5}$$

Note that non-vanishing chemical potential μ will lead to additional terms in (A.5) (more details can be found in e.g. [385]).

A.2 Basics of relativistic hydrodynamics

In this section some basic concepts in relativistic hydrodynamics will be outlined as a supplementary to Section 3.1.3. For reviews of relativistic hydrodynamics and the applications to relativistic heavy ion collisions, one can refer to e.g. [118] and [386].

Generally speaking, hydrodynamics is a classical theory that is applicable in the limit of low frequency and long wavelength[1]. The equations of motion controlling the evolution of hydro fields include the conservation of energy and momentum as well as the conservation of various transport currents J^μ:

$$\partial_\mu T^{\mu\nu} = 0 \,, \qquad \partial_\mu J^\mu = 0 \,. \tag{A.6}$$

Where $T_{\mu\nu}$ is the energy-momentum tensor. For isotropic ideal fluids in the local rest frame,

$$T^{\mu\nu}_{\rm ideal} = {\rm diag}(\varepsilon, p, p, p) \,. \tag{A.7}$$

The ε and p are the energy density and pressure respectively. Here the four-velocity $u^\mu = dx^\mu/d\tau$, and it is constrained by $u^2 = u^\mu u_\mu = 1$. In a general Lorentz frame, one can construct $T^{\mu\nu}_{\rm ideal}$ from available scalars (ε, p), vectors (u^μ) and tensors (the metric $g_{\mu\nu}$),

[1] Hydro fields are expectation values of quantum operators.

and enforce that $T^{\mu\nu}_{\text{ideal}}$ being symmetric and reducing back to Eq. (A.7) in the local rest frame:

$$T^{\mu\nu}_{\text{ideal}} = (\varepsilon + p)u^\mu u^\nu - pg^{\mu\nu} \,. \tag{A.8}$$

For non-ideal (-perfect) fluid, dissipative (viscous) effects are present, a viscous stress tensor $\Pi^{\mu\nu}$ must be added to Eq. (A.8):

$$T^{\mu\nu} = T^{\mu\nu}_{\text{ideal}} + \Pi^{\mu\nu} \,. \tag{A.9}$$

One can reorder Eq. (A.9) and view it as a gradient expansion in u^μ such that $T^{\mu\nu}_{\text{ideal}}$ contains no velocity gradients and $\Pi^{\mu\nu}$ contains them all. In this way, if one is only interested in the dynamics of the system at length/time scales greater than those set by the gradients in $\Pi^{\mu\nu}$, the $\Pi^{\mu\nu}$ term can be dropped and the ideal fluid limit is restored. The applicability of hydrodynamics in time is regulated by the isotropization scale τ_{iso} and the thermalization scale τ_{eq}: after the former time, $T^{\mu\nu}$ becomes diagonal in the rest frame (Eq. (A.7)); after the latter time, there is no more entropy being produced. In a conformal fluid, the trace of $T^{\mu\nu}$ vanishes, i.e. $T^\mu{}_\mu = 0$. According to Eq. (A.8), this implies that $\varepsilon = 3p$, one thus arrives at the simplest equation of state (EOS) for ideal fluids. Of course more realistic EOS can be calculated using lattice QCD (cf. e.g. Fig. 1.3). The EOS and the initial ε distribution constitute the major inputs for hydrodynamical simulations.

By allowing first order gradients in $\Pi^{\mu\nu}$, first order dissipative effects are introduced to the ideal fluid. This limit is called the first order dissipative hydrodynamics. The form of the first order Navier-Stokes $\Pi^{\mu\nu}$ is

$$\Pi^{\mu\nu} = 2\eta\sigma^{\mu\nu} + \zeta\Delta^{\mu\nu}\nabla\cdot u \,, \tag{A.10}$$

where $\Delta^{\mu\nu} = g^{\mu\nu} - u^\mu u^\nu$, $\nabla^\mu \equiv \Delta^{\mu\nu}\partial_\nu$ ∇_μ, $\sigma^{\mu\nu} \equiv \nabla^{\langle\mu}u^{\nu\rangle}$. In (A.10), η and ζ are the shear and bulk viscosity respectively. For a conformal fluid, $\Pi^\mu{}_\mu = 0$ hence $\zeta = 0$, but η is not necessarily zero (since $\sigma^{\mu\nu}$ is traceless). For a complete set of equations of motion, in addition to the constitutive relations Eq. (A.6), thermodynamic relations are needed. In all of them, η and ζ appear in the form of η/s and ζ/s, where s is the entropy density. This is the reason why η/s and ζ/s are key transport variables governing the hydrodynamical evolution of quark-gluon plasmas rather than the η and ζ themselves. More details about the discussions in this section can be found in [386].

Appendix B

Simple modeling of QGP

In this appendix a simple model for the profile of the quark-gluon plasma (QGP) in heavy-ion collisions will be developed. Specifically, the initial transverse profile of the QGP (the Glauber model) and its subsequent spacetime evolution (the Bjorken expansion) will be studied.

B.1 The Glauber model

The Glauber model [99] is a simple framework to account for the initial conditions for the quark-gluon plasma created in relativistic heavy-ion collisions For reviews, one can refer to e.g. [387] and [385]. The Glauber model is of optical type or Monte Carlo type, the former assumes a continuous distribution for nucleons in the colliding nuclei thus simple and analytical formulae are possible, the latter considers collisions event-by-event and the positions of nucleons are sampled according to certain distributions. This section will concentrate on the former.

To begin, the density profile of a nucleus with mass number A is described by Woods-Saxon parametrization [388]:

$$\rho_A(\vec{r} \equiv (z, \mathbf{x})) = \frac{\mathcal{N}_\mathcal{A}}{1 + \exp\left\{(|\vec{r}| - R)/a\right\}} \quad . \tag{B.1}$$

Where $R \approx 1.1A^{1/3}$ fm is the mean radius of the nucleus, a is the surface thickness for which the standard choice is $a = 0.535$ fm. $\rho_A(\vec{r})$ is normalized to mass number A. The thickness function, that gives the number of nucleons per unit area in the plane transverse

to the beam axis, of the nucleus A is defined as

$$T_A(\mathbf{x}) = \int dz\ \rho_A(z, \mathbf{x}) \ . \tag{B.2}$$

Considering a collision where nucleus A and B collide with impact parameter $\mathbf{b}$ (a vector in the transverse plane) in the high energy limit, diffractive and elastic processes can be neglected, nucleon trajectories are eikonal and distributions in the nuclei are smooth. The initial jet production probability is distributed according to the number density of binary collisions that is given by

$$\begin{aligned} \rho_{binary}(\mathbf{x}, \mathbf{b}) =& \sigma_{in}\ T_A(\mathbf{x} + \mathbf{b}/2)\ T_B(\mathbf{x} - \mathbf{b}/2) \ , \\ N_{binary}(\mathbf{b}) =& \int d\mathbf{x}\ \rho_{binary}(\mathbf{x}, \mathbf{b}) \ . \end{aligned} \tag{B.3}$$

Where σ_{in} is the inelastic nucleon-nucleon scattering cross section.

For the distribution of participants in such a collision, one needs to find the number of wounded nucleons per unit area that is given by $T_A \times P_B$ $(+T_B \times P_A)$, where P_B is the probability that one of nucleons the in nucleus B has at least one interaction. P_B has the form

$$P_B = 1 - \left(1 - \frac{T_B}{B}\sigma_{in}\right)^B \longrightarrow 1 - \exp\left(-\sigma_{in} T_B\right) \ . \tag{B.4}$$

The limit is taken as $B \to \infty$. Following this, the Glauber participant nucleon density profile is given by

$$\begin{aligned} \rho_{part}(\mathbf{x}, \mathbf{b}) =& T_A(\mathbf{x} + \mathbf{b}/2)\left(1 - \mathrm{e}^{-\sigma_{in} T_B(\mathbf{x} - \mathbf{b}/2)}\right) \\ &+ T_B(\mathbf{x} - \mathbf{b}/2)\left(1 - \mathrm{e}^{-\sigma_{in} T_A(\mathbf{x} + \mathbf{b}/2)}\right) \\ N_{part}(\mathbf{b}) =& \int d\mathbf{x}\ \rho_{part}(\mathbf{x}, \mathbf{b}) \ , \end{aligned} \tag{B.5}$$

where σ_{in} is the inelastic nucleon-nucleon cross section. The A, R, a, σ_{in} parameters chosen for Au+Au (RHIC) and Pb+Pb (LHC) collisions in Eq. (B.1)(B.3)(B.5) are listed in Table B.1.

	A	R (fm)	a (fm)	σ_{in} (mb)
Au	197	6.37	0.535	42
Pb	207	6.48	0.535	63

Table B.1: *Woods-Saxon parameters used in CUJET. A is the mass number of the nucleus, R is the nuclear radius, a is the surface thickness and σ_{in} is the inelastic nucleon-nucleon cross section.*

B.2 The Bjorken expansion

The evolution of the QGP temperature in spacetime can be modeled using a simple phenomenological Bjorken expansion [97]. The Bjorken model assumes that the system is thermalized rapidly after the initial collision, and the macroscopic quantities such as the energy density ε and pressure p, are longitudinally boost invariant in the hydrodynamical evolution[1].

A convenient set of coordinates can be chosen, consisting of the spacetime rapidity y (Eq. (1.34)) and proper time τ:

$$y = \frac{1}{2}\log\left(\frac{t+z}{t-z}\right), \qquad \tau = \sqrt{t^2 - z^2}\,. \tag{B.6}$$

Boost invariance suggests that ε and p are functions of proper time only, i.e. $\varepsilon(\tau)$ and $p(\tau)$. Assuming the system is homogeneous in the transverse plane and neglecting transverse expansions, it is convenient to solve the Euler's equation (A.6) for the energy-momentum tensor,

$$\tilde{\nabla}_\mu T^{\mu\nu} = 0\,, \tag{B.7}$$

in the $y-\tau$ coordinates, i.e. $\tilde{x}^\mu = (\tau, y, \mathbf{x})$. From Eq. (B.6) one can easily get the transformation matrix $M^\mu{}_\nu = \partial\tilde{x}^\mu/\partial x^\nu$, where $x^\mu = (t, z, \mathbf{x})$, and subsequently, one can get the metric and the four-velocity:

$$\begin{aligned} \tilde{u}^\mu &= (1,0,0,0)\,, \\ \tilde{g}^{\mu\nu} &= \mathrm{diag}(1,-1,-1,-1/\tau^2)\,, \end{aligned} \tag{B.8}$$

[1]This approximation is valid at high energies in the mid-rapidity regime, because longitudinal boosts that are much smaller than the beam energy do not affect the results (since boosts are additive in rapidity). This invariance can be interpreted as the evolution of the system looks the same in all reference frames near the center-of-mass frame.

The only non-vanishing Christoffel symbols (entering the covariant derivative $\tilde{\nabla}_\mu$) of this metric are

$$\Gamma^y_{\tau y} = \frac{1}{\tau}, \qquad \Gamma^\tau_{yy} = \tau\,. \tag{B.9}$$

The energy momentum tensor is

$$\begin{aligned} \tilde{T}^{\mu\nu} &= (\varepsilon + p)\tilde{u}^\mu \tilde{u}^\nu - p\tilde{g}^{\mu\nu} \\ &= \mathrm{diag}\left(\varepsilon, p, p, \frac{p}{\tau^2}\right)\,. \end{aligned} \tag{B.10}$$

Plugging this into the $\nu = \tau$ component of Eq. (B.7), one gets:

$$\frac{d\varepsilon}{d\tau} + \frac{\varepsilon + p}{\tau} = 0\,. \tag{B.11}$$

On the other hand, one knows that for a system with constant volume, $d\varepsilon = Tds$, where s is the entropy density. Combined with $\varepsilon + p = Ts$, Eq. (B.11) becomes

$$\frac{ds}{d\tau} + \frac{s}{\tau} = 0\,. \tag{B.12}$$

It has a simple solution,

$$s(\tau)\tau = \text{const.} \tag{B.13}$$

To solve for T from Eq. (B.11), firstly, one notices that:

$$\frac{d\varepsilon}{d\tau} = \frac{d\varepsilon}{dp}\frac{dp}{dT}\frac{dT}{d\tau}\,, \tag{B.14}$$

where $T(\tau)$ is the temperature. At constant volume, $s = dp/dT$ (since $\varepsilon + p = Ts$ and $d\varepsilon = Tds$). Note that the speed of sound:

$$c_s^2(T) \equiv \frac{dp}{d\varepsilon} = \frac{sdT}{Tds} = \frac{d\log T}{d\log s}\,. \tag{B.15}$$

Therefore, Eq. (B.11) now becomes

$$\int_{T_0}^{T} \frac{dT'}{T' c_s^2(T')} = \log\left(\frac{\tau_0}{\tau}\right)\,. \tag{B.16}$$

The speed of sound for QCD matter at finite temperature can be computed from lattice

QCD. This information is contained in the trace anomaly of the energy-momentum tensor (cf. e.g. Fig. 1.14), i.e.

$$\Theta(T) \equiv T^{\mu}{}_{\mu} = \varepsilon - 3p = T\frac{dp}{dT} - 4p = T^5 \frac{d}{dT}\left(\frac{p}{T^4}\right) . \tag{B.17}$$

Once $c_s^2(T)$ is known, Eq. (B.16) can be solved to get $T(\tau)$. If in some regime one can approximate the speed of sound to be a constant, i.e. $c_s^2(T) = c_s^2$, then Eq. (B.16) can solved analytically:

$$T(\tau) = T_0 \left(\frac{\tau_0}{\tau}\right)^{c_s^2} . \tag{B.18}$$

On the other hand, Eq. (B.11) becomes

$$\frac{d\varepsilon}{d\tau} = -(1 + c_s^2)\frac{\varepsilon}{\tau} . \tag{B.19}$$

If the system is scale-invariant (conformal), then $\varepsilon \propto T^4 \propto \tau^{-4c_s^2}$. Substitute this relation into Eq. (B.19), one gets $c_s^2 = 1/3$. This gives one the temperature evolution that is referred to as the "Bjorken expansion":

$$T(\tau) \propto \tau^{-1/3} . \tag{B.20}$$

B.3 The relation to experimental observables

In this section the thermodynamic quantities from early times in the evolution of the quark-gluon plasma (QGP) phase will be related to the quantities that are observable in the experiments. For a massless ideal gas, $p = \epsilon/3$ and $s = \frac{4\varepsilon}{3T}$. Denote by ξ the proportionality factor between s and n, i.e.

$$s = \xi n . \tag{B.21}$$

One has for the QGP

$$\xi_{\mathrm{QGP}} = \frac{\pi^4}{45\zeta(3)} \frac{32 + 21N_f}{16 + 9N_f} . \tag{B.22}$$

Here $\xi_{\mathrm{QGP}} \approx 3.92$ for $N_f = 2$, and $\xi_{\mathrm{QGP}} \approx 3.98$ for $N_f = 3$. N_f is the number of flavors that are considered to be part of the thermal medium, it is determined by the temperature scale. Meanwhile, for a massless pion (boson) gas one has the degeneracy factor $g_\pi = 3$

in Eq. (A.4), therefore,

$$\xi_\pi = \frac{2\pi^4}{45\zeta(3)} \approx 3.6\,. \tag{B.23}$$

The entropy of the system at proper time τ is

$$S(\tau) = \int d^3x\,\sqrt{h}\,s(\tau) = \int d\mathbf{x}_\perp dy\,s(\tau)\tau\,, \tag{B.24}$$

where h is the determinant of the spatial part of metric (B.8). Since $s(\tau)\tau$ is a constant from Eq. (B.13), the differential entropy with respect to rapidity is also a constant, i.e.

$$\frac{dS}{dy} = \text{const.} \tag{B.25}$$

One notices from Eq. (B.21) that S is proportional to the number of particles. At some later time τ_f when the system has gone through the phase transition to a hadron gas state, assuming that the observed particle multiplicity dN/dy is pion dominance, i.e. $dN/dy = dN_\pi/dy$, one has from Eq. (B.21):

$$\left.\frac{dS}{dy}\right|_{\tau_f} = \xi_\pi \frac{dN_\pi}{dy}\,, \tag{B.26}$$

On the other hand, at τ_0,

$$\left.\frac{dS}{dy}\right|_{\tau_0} = \xi_{\rm QGP}\tau_0 \int d\mathbf{x}\,n_{\rm QGP}(\tau_0,\mathbf{x})\,. \tag{B.27}$$

From Eq. (B.25), one thus has

$$\frac{dN_\pi}{dy} f(\mathbf{x}) = \frac{\xi_{\rm QGP}}{\xi_\pi}\tau_0\,n_{\rm QGP}(\tau_0,\mathbf{x})\,. \tag{B.28}$$

Where f describes the non-uniform transverse density profile of the medium, it is normalized to 1. A reasonable choice for f is the normalized participant density from Eq. (B.5)[2],

$$f(\mathbf{x}) = \frac{\rho_{\rm part}(\mathbf{x})}{N_{\rm part}}\,. \tag{B.29}$$

[2]This is because the "soft" QGP bulk is at thermal scales. Note that the binary collision density Eq. (B.3) determines the probability distribution of the initial hard jet production.

Combining Eq. (A.5), (B.18) and (B.20), one can express the temperature as[3]

$$T = \left[\frac{\pi^2}{\zeta(3)}\frac{1}{16+9N_f}n_{\rm QGP}(\tau_0,\mathbf{x})\frac{\tau_0}{\tau}\right]^{1/3}. \tag{B.30}$$

Substituting Eq. (B.28) and (B.29) into the above, one gets the temperature profile of the plasma[4]:

$$T_{\rm QGP}(\tau,\mathbf{x}) = \left[\frac{\pi^2}{\zeta(3)}\frac{\xi_\pi}{\xi_{\rm QGP}}\frac{1}{16+9N_f}\frac{dN_\pi}{dy}\frac{\rho_{\rm part}(\mathbf{x})}{N_{\rm part}}\frac{1}{\tau}\right]^{1/3}. \tag{B.31}$$

Note that $\xi_\pi/\xi_{\rm QGP} \approx 1$ for $N_f = 0, 1, 2, 3$.

The experimentally measured multiplicity is usually $dN_{\rm ch}/d\eta$ (cf. e.g. Fig. 1.12), i.e. the multiplicity of charged particles with respect to the pseudorapidity (η defined in Eq. (1.32)). One sees from Eq. (1.36) that the order $\mathcal{O}(m_\pi^2/p^2)$ difference between y and η is negligible at high momenta, while lower energy pions, a good estimate will be $d\eta/dy \approx 1.1$. Assuming that the number of π^+, π^- and π^0 is approximately equal, one has

$$\frac{dN_\pi}{dy} \approx \frac{3}{2}\frac{dN_{\rm ch}}{d\eta}\frac{d\eta}{dy}. \tag{B.32}$$

At the center of an $N_f = 3$ QGP ($\mathbf{x} = \mathbf{0}$) created in central A+A collisions ($b = 0$), at the initial time $\tau_0 = 0.6$ fm/c, Eq. (B.31) gives $T_{\text{RHIC, Au+Au 200 A·GeV}} \approx 370$ MeV and $T_{\text{LHC, Pb+Pb 2.76 A·TeV}} \approx 470$ MeV.

[3] It is questionable if the conformal proper time dependence of the temperature $T \propto \tau^{-1/3}$ is valid when T is close to the QCD transition temperature where the system seems highly non-conformal, as suggested by trace anomaly (cf. e.g. Fig. 1.14). In fact, there is a simple numerical calculation shows that the temperature evolution is very similar to $\sim \tau^{-1/3}$ in this regime [168].

[4] To simulate the transverse expansion of the QGP, one can use a simple blast wave dilation factor [225, 390]: $r_{\rm bl}(\tau) = \sqrt{1+\left(\frac{v_T\tau}{R}\right)^2}$. Where R is the mean nuclear radius, the transverse velocity is usually chosen as $v_T = 0.6$. This dilation factor changes $\rho_{\rm part}$ in Eq. (B.31): $\rho_{\rm part}(\vec{x}_\perp) \to \rho_{\rm part}(\vec{x}_\perp/r_{\rm bl})/r_{\rm bl}^2$. Besides this, a wider range of more realistic transverse expansion models are available, including viscous RL hydro [115, 391], VISH2+1 [238, 241, 244], and others.

Appendix C

Basics of finite temperature QFT

The key concept that allows the definition of a quantum field theory at $T \neq 0$ is switching Minkowski to Euclidean metric via a rotation in the complex temporal plane, $t \to -i\tau$. In such a way the grand-canonical partition function Z can be redefined as a path-integral over the fields and their conjugate momenta. The inverse temperature is defined as the temporal span of the integration, i.e. $\tau_f = 1/T$, while periodic boundary conditions imposed on the fields ensure that initial and final states coincide. More details about the discussions in this appendix can be found in [215, 394].

C.1 General formalism

In the Euclidean space, the expression of the partition function Z can be simplified if one integrates over the conjugate momenta , leading to

$$Z = \int \mathcal{D}\phi \, \exp\left(- \int_0^{1/T} d\tau \int d^3x \, \mathcal{L}(\phi(\tau, \mathbf{x}), \partial\phi(\tau, \mathbf{x})) \right) \quad , \tag{C.1}$$

where $\mathcal{L}$ is the Lagrangian density and ϕ is the field of interests ($\phi(0, \mathbf{x}) = \phi(1/T, \mathbf{x})$).

With a finite temporal size and periodic boundary conditions, the temporal component of the four-momentum is the discretized , and the fields can be Fourier decomposed:

$$\phi(\tau, \mathbf{x}) = T \sum_n \int \frac{d^3k}{(2\pi)^3} \mathrm{e}^{i(\omega_n \tau + \mathbf{k}\cdot\mathbf{x})} \phi(\omega_n, \mathbf{k}) \quad , \tag{C.2}$$

$$\omega_n = \begin{cases} 2n\pi T & \text{for gluons} \\ (2n+1)\pi T & \text{for quarks} \end{cases} . \tag{C.3}$$

For a free field theory, the above is sufficient to compute explicitly the partition function, after which the desired thermodynamic quantities can be extracted. If one turns on interactions, the Lagrangian can be split into a free and interaction part, the action therefore becomes

$$S = S_0 + S_I \equiv \int_0^{1/T} d\tau \int d^3x \ (\mathcal{L}_0 + \mathcal{L}_I) \quad , \tag{C.4}$$

and the partition function can be written as

$$Z = \sum_n \frac{1}{n!} \int \mathcal{D}\phi \ (-S_I)^n \mathrm{e}^{-S_0} \quad . \tag{C.5}$$

Expressions for the Feynman vertices can be read off from the interaction Lagrangian, while free propagators are obtained as functional derivatives of Z_0. As a glimpse, in the covariant gauge, the gluon propagator becomes

$$\Delta_{\mu\nu}(Q) = \frac{1}{Q^2}[\delta_{\mu\nu} - (1-\xi)\frac{Q_\mu Q_\nu}{Q^2}] \quad , \tag{C.6}$$

where $Q_\mu = (\omega_n, \mathbf{q})$.

The interaction theory defined in Euclidean space is useful to compute static properties of the system such as thermodynamic potentials. However for dynamical quantities, real-time Green's functions are necessary. They can be extracted as real continuations of their imaginary time counterparts [392], or formulated directly by choosing an appropriate path for the temporal integration on the complex plane ($\mathrm{Re}\, t, \mathrm{Re}\, \tau$) [393].

C.2 Hard thermal loop gluon propagator

As an application of thermal perturbation theory, results relative to the gluon propagator at finite T will be discussed in this section. The changes resulting from the presence of a thermal medium explain the origin of some key properties of the QGP, such as the Debye screening mass (cf. e.g. Section 2.2.6).

The self-energy of the gluon, Π, is computed in the Hard Thermal Loop (HTL) frame-

work developed by Pisarski [200], Braaten and Pisarski [201–205], in which the temperature T is assumed to dominate over all the other scales in the loop diagrams. Implicitly, only contributions proportional to g^2T^2 are considered. In contrast to the $T = 0$ theory where the unphysical polarizations that appear in the covariant gauge are canceled by the ghost loops, here the gluon propagator develops a longitudinal polarization in addition to the transverse one. After analytically continuing the Green's function to real time and Minkowski spacetime, the propagator in the HTL approximation becomes

$$\Delta_{\mu\nu} = \frac{(P_L)_{\mu\nu}}{Q^2 - \Pi_L} + \frac{(P_T)_{\mu\nu}}{Q^2 - \Pi_T} + \xi \frac{Q_\mu Q_\nu}{Q^2} \quad . \tag{C.7}$$

The four-momentum $Q_\mu = (\omega, \mathbf{q})$. $(P_{T,L})_{\mu\nu}$ represent the usual transverse and longitudinal projection operators. The transverse and longitudinal gluon self-energies are

$$\begin{aligned} \Pi_L(x \equiv \frac{\omega}{q}) &= \mu_D^2 \left\{ 1 - x^2 - \frac{x(1-x^2)}{2} \left[\log\left(\frac{x+1}{x-1} \right) - i\pi\theta(1-|x|) \right] \right\} \\ \Pi_T(x \equiv \frac{\omega}{q}) &= \mu_D^2 \left\{ \frac{x^2}{2} + \frac{x(1-x^2)}{4} \left[\log\left(\frac{x+1}{x-1} \right) - i\pi\theta(1-|x|) \right] \right\} \quad . \end{aligned} \tag{C.8}$$

Here $q \equiv |\mathbf{q}|$, and the Debye screening mass μ_D is

$$\mu_D = gT\sqrt{1 + \frac{N_f}{6}} \quad . \tag{C.9}$$

In the limit of $q = 0$, within the time-like region $\omega > q$, both the longitudinal and transverse propagators develop a pole for

$$\omega^2 = \frac{\mu_D^2}{3} \equiv \omega_{pl}^2 \quad . \tag{C.10}$$

The characteristic frequency of the plasma is then identified with ω_{pl}. For collective modes with soft momenta $q \ll \mu_D$ $(q \neq 0)$, the above relation becomes:

$$\begin{aligned} \omega^2 &\simeq \omega_{pl}^2 + \frac{3}{5}q^2 \qquad \text{for longitudinal modes} \quad , \\ \omega^2 &\simeq \omega_{pl}^2 + \frac{6}{5}q^2 \qquad \text{for transverse modes} \quad . \end{aligned} \tag{C.11}$$

For hard momenta, $q \gg \mu_D$, one has instead

$$\begin{aligned} \omega^2 &\simeq q^2\left[1+4\exp\left(\frac{2q^2}{3\omega_{pl}^2}-2\right)\right] \qquad \text{for longitudinal} \ , \\ \omega^2 &\simeq q^2+\frac{3}{2}\omega_{pl}^2 \qquad\qquad\qquad\qquad\quad \text{for transverse} \ . \end{aligned} \tag{C.12}$$

One immediately sees that ω_{pl} plays the role of an effective mass for a gluon propagating in the QGP. These plasma oscillations, or quasi-particles, are called plasmons.

If one switches to the space-like region $\omega < q$, one notices that the self-energies Eq. (C.8) develop an imaginary part responsible for what is called Landau damping, which is an effect related to the energy transfer between the collective modes and the plasma constituents. Near the static limit $\omega \ll q$ where the field configuration can be represented by time-independent gauge potentials, the longitudinal and transverse gluon propagators are

$$\begin{aligned} \Delta_L(\omega,q) &= \left(q^2+\mu_D^2+i\frac{\pi\mu_D^2}{2}\frac{\omega}{q}\right)^{-1} \ , \\ \Delta_T(\omega,q) &= \left(q^2-i\frac{\pi\mu_D^2}{2}\frac{\omega}{q}\right)^{-1} \ . \end{aligned} \tag{C.13}$$

For purely static fields, $\omega = 0$, the longitudinal gluon propagator develops an effective mass term that is equal to μ_D.

This is precisely the Debye mass that is responsible for the screening of the color-electric field in the plasma. It leads to a Yukawa potential between a heavy $q\bar{q}$ pair seen in Eq. (1.16). In this limit, the transverse gluon is massless and magnetic interactions are unscreened hence being long-range. However due to Landau damping, the magnetic interactions become dynamically screened for finite values of ω. The transverse propagator squared that appears in the computation of the cross section in fact takes the form

$$|\Delta_T(\omega,q)|^2 \simeq \left[q^4-\left(\frac{\pi\mu_D^2\omega}{4q}\right)^2\right]^{-1} \ , \tag{C.14}$$

which shows that the imaginary part of the propagator acts as a frequency-dependent infrared cutoff at momenta $p \sim (\omega\mu_D^2)^{1/3}$. The dynamical screening of the soft momenta plays an important role in taming the singularities in the scattering processes with the exchange of transverse gluons [215].

An equivalent approach to derive the HTL gluon self-energy using the perturbative

expansion is given by kinetic theory as well as the solution of the coupled set of Vlasov equations [394]. In this semi-classical approach, one considers a relativistic plasma composed of charged particles whose spacetime-dependent density distribution function is given by $n_{\pm}(\mathbf{p}, \mathbf{x}, t)$. The system is subject to the effects of an external source (ext) and an induced electromagnetic field (ind):

$$\partial_{\mu} F^{\mu\nu}(\mathbf{x}, t) = j^{\nu}_{ind}(\mathbf{x}, t) + j^{\nu}_{ext}(\mathbf{x}, t) \ , \tag{C.15}$$

$$j^{\mu}_{ind}(\mathbf{x}, t) = 2g \int \frac{d^3p}{(2\pi)^3} v^{\mu} \left[n_{+}(\mathbf{p}, \mathbf{x}, t) - n_{-}(\mathbf{p}, \mathbf{x}, t) \right] \ , \tag{C.16}$$

$$\left\{ \frac{\partial}{\partial t} + \mathbf{v} \cdot \frac{\partial}{\partial \mathbf{x}} \pm \left[\mathbf{E}(\mathbf{x}, t) + \mathbf{v} \times \mathbf{B}(\mathbf{x}, t) \right] \cdot \frac{\partial}{\partial \mathbf{p}} \right\} n_{\pm}(\mathbf{p}, \mathbf{x}, t) = 0 \ . \tag{C.17}$$

Here $v^{\mu} = (1, \mathbf{v})$. The last equation represents the time-evolution of the distribution $n_{\pm}(\mathbf{p}, \mathbf{x}, t)$. Through linearizing

$$n_{\pm}(\mathbf{p}, \mathbf{x}, t) = n_0(\mathbf{p}) + \delta n(\mathbf{p}, \mathbf{x}, t) \ , \tag{C.18}$$

($n_0(\mathbf{p})$ is the density distribution in the absence of an induced field) and expressing

$$j^{\mu}_{ind}(\mathbf{x}, t) = \int d^4y \ \Pi^{\mu\nu}(x - y) A_{\nu}(y) \ , \tag{C.19}$$

one can derive the same expressions for the gluon self-energy (Eq. (C.8)) after solving explicitly for $j^{\mu}_{ind}(\mathbf{x}, t)$. More details about this approach can be found in [394].